Interpretable Machine Learning trained on Experimental Data for Novel Insights into Complex Compositional Alloy Corrosion Phenomena in Molten Salts

By

Bonita Goh

A dissertation submitted in partial fulfillment of

the requirements for the degree of

Doctor of Philosophy

(Nuclear Engineering & Engineering Physics)

at the

University of Wisconsin – Madison

2023

Date of final oral examination: 05/19/ 2023

The dissertation is approved by the following members of the Final Oral Committee:

Adrien Couet , Associate Professor, Nuclear Engineering & Engineering Physics, UW Madison
Kumar Sridharan, Professor, Nuclear Engineering & Engineering Physics, UW Madison
Yongfeng Zhang, Assistant Professor, Nuclear Engineering & Engineering Physics, UW Madison
Jason Hattrick-Simpers, Professor, Materials Science & Engineering, University of Toronto
Dimitris Papailiopoulos, Associate Professor, Electrical & Computer Engineering, UW Madison

Abstract

Next-generation advancements in molten salt-based technologies demand structural properties for which materials do not yet exist, lacking the necessary corrosion resistance for these applications, such as in molten salt nuclear reactors. Compositionally Complex Alloys (CCAs), sometimes also called High-Entropy Alloys (HEAs), are a novel class of structural materials that promises to yield alloys with the necessary corrosion resistance in the molten salt environment at high temperature, but the compositional space is quasi-infinite, and the corrosion mechanism unclear. This thesis presents a parametric experimental investigation of the corrosion in molten LiCl-KCl of novel CCAs in the CrFeMnNi composition space, as well as methods for high-throughput corrosion testing of novel CCAs, chemical analysis and quantification of corrosion products. This thesis also presents a methodology for implementing machine learning and materials informatics techniques to gain mechanistic insights of material degradation of CCAs in molten salts.

Acknowledgments

The prodigious capacity to learn has provided us humans with the ability to devise ever more sophisticated means of survival. The human is driven to learn by the desire to find meaning in the world outside of ourselves. The drive then to understand how we learn and why we see the world in the ways that we do is propelled by the desire to understand the self. It is no wonder then that we should desire to reverse-engineer the mechanisms of cognition as Artificial Intelligence (AI) in order to study it externally from all sides - like Raphael sculpting the human form down to the very anatomically-correct sinew - to perfectly reproduce is to perfectly understand.

This thesis may be about how I built an AI that figured out that noble-element diffusion mediated dealloying is the primary mechanism of chemical degradation in compositionally complex alloys in high temperature molten salt, but it is also a story of how thought processes are examined as machines (to scrutinize the “cog” in “cognition”, if you will), why they were built the way they were, and what this reflects about the humanity of the builders.

In other words, this thesis is ultimately a story of the human condition. And despite the fantasies we might hold about using AI to devise closed-loop autonomous experimentation processes independent of human intervention, I humbly maintain that scientific discoveries would not be quite as beautiful if they were merely the inevitable conclusion of an infinite iteration. The beauty of a genius idea lies in its rarity, and so rendering it a mundane product of a mass-production line dulls its luster.

All this is to say the discoveries described in this thesis are very much not genius, for they were in fact conclusions reached by an iterative thought process of an artificial brain, that is my Random Forest

Regressor Model for predicting corrosion behavior in a multi-variate system. ChatGPT, however, took no part in the crafting of these words. I have far too much pride for that.

What good is this thesis then, really?

Christoph Molnar said in his book A Guide to Interpretable Machine Learning, that “the effectiveness of an explanation hinges on the relationship between the one providing the explanation and the one receiving it”; herein lies the profound wisdom at the very foundations of scientific endeavor, for what is science if not an unbroken series of explanations between scientists through the generations and the shared moments between them of mutual appreciation for an elegant idea?

On this note I would like to extend my deepest gratitude to the following dramatis personae of the story without whom this thesis would not be possible:

Firstly my father, who provided the spark of intellectual curiosity to me when I was but 14, who embodies the virtue of the lifelong learner. Perhaps in another universe you’d have had the privilege and means to pen a dissertation in your own hand. But in this universe, please consider this thesis as much yours as it is mine.

Secondly, to my mother, without whose financial sacrifices my pursuing higher education would not have been possible.

To Adrien, thank you for your consistent patience and guidance throughout this journey; thank you for embodying a good example of a PhD advisor.

To all the members of my committee, thank you for your insights on my research problems.

To Yafei, thank you for your sage advice in navigating the path to be a successful academic professional.

To Will Doniger, Cody Falconer, Michael Moorehead, thank you for teaching me various aspects of being a well-rounded engineer.

To Ricardo, thank you for being my ride-or-die buddy in the EP Dept.

To Isabelle, thank you for being an awesome intern. Your diligence has restored my faith in undergrads.

To Kailee & Shae, thank you for your invaluable support on the Synchrotron experiment.

To Dr Marlene Malavasi & Dr Ubirajara Malavasi thank you for your kindness, empathy and emotional support in this journey.

To Dr Katie Crimmins & Dr Uni Choi, omg we did it.

And finally to Dr Leticia Malavasi, the guardian angel of my entire PhD life.

Contents

1 List of Figures

2 List of Tables

3 Background

3.1 The Importance of Gen IV Molten Salt Reactors

If you are not reading this thesis on a screen, you most certainly printed it with an electric-powered printer. Such is the utter ubiquity of energy as a commodity in modern life. We need this commodity from the moment we wake up to check our phones, brew our coffee and travel to work, to the moment we lay our heads down in bed and check our phones again before dropping off to sleep - energy commodity consumption has permeated our every waking second.

Global consumption of energy by source is shown in Figure 1. It is evident that nuclear power (green) is not a large part of it. Evidently, fossil fuels (purple, pink, red) remain an overwhelmingly large part of it. We cannot assume this is a stable state of affairs for the decades to come - quite the opposite in fact, over-reliance on fossil fuel has become untenable for the following reasons:
A) fossil fuels are a primary source of anthropogenic climate change as well as environmental pollution [1]–[3] and the need to slow the degradation of our planet earth should be self-evident,
B) its global supply is dependent on an oligopoly of suppliers called the Organization of Petroleum Exporting Countries (OPEC). Their price-fixing decisions are a constant source of socio-political anxiety for every country dependent on the product, including the United States, since energy is a significant component of the Consumer Price Index. These price flutterings in the winds of global politics might be less of a problem if fossil fuels were not as energy-inefficient as they are, so any country that would emancipate itself from dependency on petroleum as a primary source of energy would undeniably be taking a step towards economic stability.

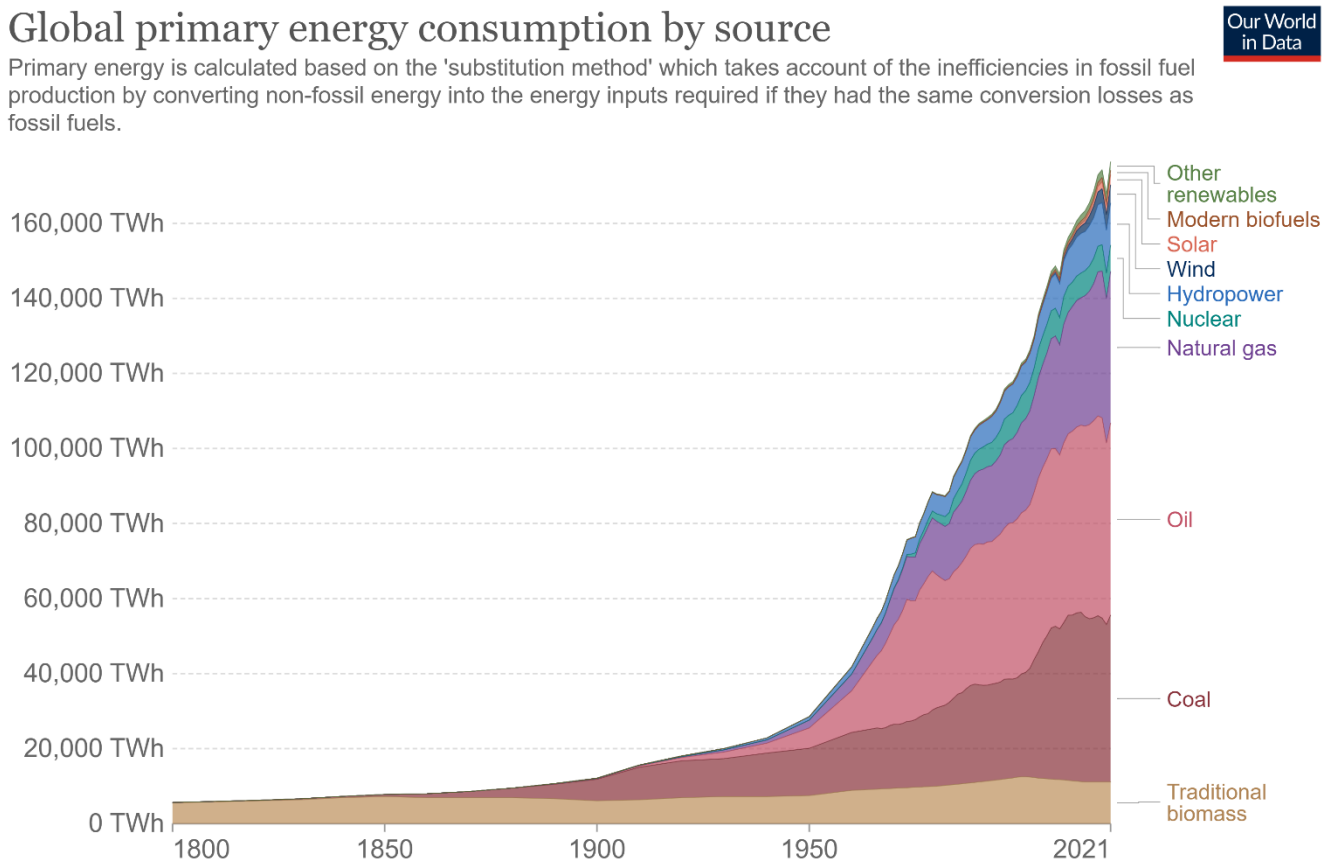

Figure 1: Global primary energy consumption by source, primary energy calculated by 'substitution method [4]

The figure shows that nuclear power does not constitute a huge part of the global energy consumption portfolio. A coordinated and focused national policy is necessary for a country to shift away from legacy fossil fuel systems in the power grid to install newer nuclear-powered systems on it. France leads with 70% of its national power production coming from nuclear power. The US only has 20% of its national power production coming from nuclear power.

Nuclear power is poised to grow in its assumption of the global energy consumption burden. A 6g pellet of reactor grade uranium produces the same amount of energy as 126 gallons of oil [5]the

Chicago Reactor Pile led by Enrico Fermi in 1942 [6] as the proof-of-concept for nuclear power as a viable source for civil consumption, it has been 80 years of tireless technological development supported by governments of the wealthiest and most populous nations, both in cooperation with and in parallel to one another. The result in the burgeoning of nuclear reactors into the mature technology of the present day.

At the time of this writing in 2023, the nuclear industry is currently embarking on the 4th generation of nuclear reactor designs. The simplified schematic of a generalized 3rd generation reactor based on light water reactors (LWR) system which are the most common type of nuclear reactor (~80% of all reactors in the world) currently in commercial use for civilian energy production Figure 2 illustrates that a nuclear reactor functions by generating heat via controlled fission reactions in the (usually uranium) fuel elements within the core (red, yellow). In correctly-operating conditions, core temperature reaches about 700-800 ^{o}C. Water is used as a medium of heat transfer from the core to a steam generator where the heat energy is converted into kinetic energy which is in turn converted into electric energy via a turbine. For a quick reference, the thermal-to-electric conversion efficiency is generally 3:1.

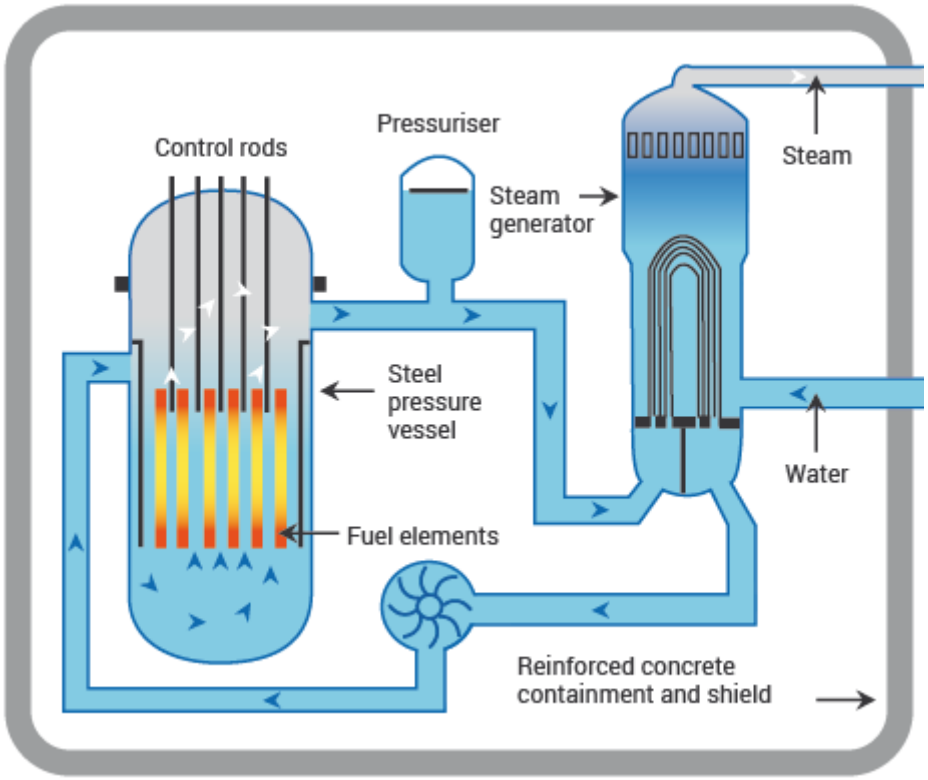

Figure 2: Basic schematic of LWR design concept [7]

With this simplified illustration we can already see two obvious aspects in which the nuclear reactor design can be improved. Firstly, there is much room for improvement for thermal-to-electric energy conversion efficiency at ~33%. .

On average 2.4 neutrons are born per fission reaction, generally at faster-than-thermal speeds (aka “fast neutrons”). A sufficient flux of thermal neutrons is necessary to perpetuate enough fission reactions for self-sustaining power generation. Neutron moderation entails slowing the neutron to thermal speeds via inelastic scattering and the high density of hydrogen atoms present in water also makes it an effective neutron moderator. Core reactivity is directly impacted by moderator temperature, measured as reactivity feedback coefficient with respect to moderator temperature. NRC 10 CFR 50 mandates that all reactors must be designed to operate with negative core reactivity feedback coefficient with respect to moderator temperature.

Two significant nuclear reactor accidents in history highlight the significant vulnerabilities in relying on water as coolant and moderator in a nuclear reactor, one at Three Mile Island, USA and the other at Fukushima Daiichi, Japan.

In the case of Three Mile Island, the root cause of the accident was a leakage on one of the valves controlling flow in the heat transfer system and water entering air lines, causing a series of interconnected valves to malfunction and mistakenly trip the turbine, resulting in a Loss of Coolant Accident (LOCA). The nuclear reactor core was emergency-shut down ("safety control rod activation mechanism", known colloquially in industry as a "scram") automatically as it was designed to, however the loss of coolant meant that residual heat from the reactor could not be removed at the rate necessary to prevent buildup of heat in the reactor core, resulting in a reactor core meltdown.

In the case of Fukushima Daiichi, the tsunami damaged the active pumps necessary to remove residual heat from the scrammed reactor core which also resulted in a partial meltdown of the core. More details on the play-by-play of both accidents are included in the supplemental materials of this chapter. The primary concerns with a meltdown are the escape of high-dosage radiation from containment and shielding which are hazardous to human health and the environment.

The cases of Three Mile Island and Fukushima Daiichi serve as evidence that the stability of water-mediated heat transfer systems is inherently not robust which brings us to the second aspect in which a design update for the next generation of nuclear reactors is necessary: alternative media of heat transfer systems.

The Molten Salt Reactor (MSR) is a 4th generation nuclear reactor design concept poised to solve the problems mentioned. Table 1 summarizes some pertinent thermophysical properties of particular salts of interest, with the properties of water included for comparison to LWR systems.

The MSR design concept is attractive because molten halide salts are feasible as coolant for MSR applications since they possess [8]:

I. high heat capacity, which makes them efficient as heat transfer media;

II. low viscosity, which means they can be pumped in a coolant loop with minimal power input;

III. low vapor pressure at reactor operating temperatures and high boiling point, which eliminates the need for pressure-containing systems which only add to the instability of the overall system;

Molten salts show promise to replace water as heat transfer medium because they are liquid in the reactor operating temperature range of interest (500-800 ^{o}C) but they are solid at room temperature and atmospheric pressure (rtp). Therefore one could conceive that if there were a leakage in a coolant line, the salt is expected to quickly freeze at rtp, forming a plug to avoid immediate escalation of damage before a permanent solution can be found. In this way, the MSR concept has some inherent safety features by design [9], [10]

Another attractive point of the MSR design concept is that fluoride and chloride salts are mostly radiolytically and thermally stable to over 1000^{o}C [11] which qualifies them as candidates for fuel salt in the MSR design. Extensive studies have shown generally inhomogeneous power generation across solid-pin fuel cores of currently-operating Gen III nuclear reactor designs, indicating high burnup in the center but low burnup towards the edges [12].The MSR concept proposes FLiBe (67mol% LiF, 33mol% BeF_2) as a candidate salt for the primary coolant loop in thermal MSR for its favorable neutronic properties, as Be is fairly transparent to neutrons [13], [14] in addition to its favorable thermophysical properties. A molten salt core with dissolved uranium or thorium [15]–[17] has the potential to improve fuel burnup efficiency over the traditional solid oxide fuel-pin core designs of LWRs because it would be self-homogenizing, thereby improving the total end-of-fuel cycle burnup efficiency.

An example of a salt mixture considered for coolant is FLiNaK, a eutectic mixture of NaF,

LiF and KF (46.5mol% LiF-11.5mol% NaF-42 mol% KF). In addition, chloride eutectics (such as 59mol% LiCl- 41mol% KCl) [18], [19] are of interest as coolants in low temperature process loops. Chlorides in particular also present favorable characteristics because: i) they have lower melting points (< 200 ^{o}C) and higher boiling points (> 800 ^{o}C) , ii) chlorides have higher abundance in nature)[8], and iii) comparatively low production cost [8]. Some of their favorable thermophysical properties of these eutectics of interest are summarized in Table 1.

Table 1: Some examples of salt eutectic compositions of interest for the Gen IV Molten Salt Reactor concept [19]

Table 1: Some examples of salt eutectic compositions of interest for the Gen IV Molten Salt Reactor concept [19]

Molten Salt Coolant	Composition (mol %)	Melting Point (^{o}C)	Vaporization point (^{o}C)	Specific heat capacity ($Jkg^{-1}K^{-1}$)	Reference
FLiBe	67% LiF, 33% BeF_2	459	1430 (boiling)	2414.17	[19]
FLiNaK	46.5% LiF, - 11.5% NaF - 42% KF	454	1570 (boiling)	1882.8	[19]
LiCl-KCl	41% KCl, 59% LiCl	357	>1400 (boiling)	1340	[8], [20], [21]
H_2O @ 20^{o}C	-	0	100	4184	-

As described in this section, LOCAs are especially dangerous scenarios for nuclear reactor cores. Even under emergency shutdown scenarios, the system must be able to remove residual heat quickly to avoid a reactor core meltdown. Ideally this system would be a passive one. While the MSR is theoretically less susceptible to LOCAs as previously described, under expected reactor operating conditions in the absence of natural disasters or hostile agents, the primary risk of LOCAs can still come from material degradation. The Silver Bridge Collapse of 1967 is a testament that a crack due to material degradation on the order of millimeters due to exposure to environmental corrodants can propagate to a million times its length in a matter of seconds resulting in complete structural failure [22]. This serves to illustrate the importance of having suitable structural materials that are resistant to degradation under the operating conditions for the entire planned lifetime of the reactor. The primary sources of concern for degradation of structural materials in an MSR are irradiation [23]and corrosion in the molten halide.

The viability of the MSR concept has been demonstrated by the success of the Aircraft Reactor Experiment (AER) [24]and the Molten Salt Breeder Reactor (MSBR) [11] with no detectable degradation of the salts by radiolysis and thermolysis.

Despite the demonstrated viability, there are still major obstacles to the scale-up commercialization of MSRs, chief of which is corrosion [19], [25]. There are presently scant viable options for suitable structural materials for MSRs, which hinders its commercial-scale deployability. Current ASME Sec III Div 5 code certified alloys up to 700°C (Alloy 800H, 316SS, IN 617) are not well-suited for molten salts because they contain high Cr content (>15%). This is because corrosion occurs primarily by elemental dissolution because any corrosion products formed in the form of mainly metal oxides and fluorides are highly soluble in the salt [26].

This thesis is primarily concerned with addressing alloy design to optimize corrosion resistance in molten halides. The next section discusses in detail the current understanding of the molten salt chemistry behind corrosion mechanisms of alloys in molten salts. This understanding of the chemistry forms the

basis for the work demonstrated in this thesis to probe these corrosion mechanisms in depth in order to inform a recommendation for alloy design bases.

3.2 Complex Compositional Alloys (CCAs) as structural materials of interest

In Molten Salt Reactor Experiment (MSRE) was a test reactor run from 1965-1969 to demonstrate the feasibility of the molten salt reactor design concept [27], [28]. As part of this experiment, Ni-based candidate alloys (Table 2 [29]) were experimental alloys proposed and tested for feasibility as structural materials for the MSRE.

Ni was considered as the foremost candidate as an alloy base for its high temperature strength and thermodynamic unfavourability to forming stable halides. Mo was considered as the second major component because of its impartation of solid-solution strengthening at high temperatures as well as its thermodynamic nobility against forming stable halides. W was considered as a minor additive for the same reasons as Mo. Despite the fact that the formation of Cr(II) and Cr(III) fluorides is relatively favorable thermodynamically (Figure 1), the inclusion of Cr in the alloy compositions at concentrations of 5-7 at% is necessary to maintain oxidation resistance in ambient conditions [30]. At the time Ti and Nb were considered as additives to mitigate the formation of embrittling tellurides in the structural material which form as a result of the migration of the fission product tellurium [29].

Table 2: Compositions of alloys tested for MSRE, balance is Ni [29]

Alloy	Mo	Cr	Fe	Ti	Al	Nb	W
INOR-1	30						
INOR-2	16	5					
INOR-3	16			1.5	1		
INOR-4	16			1.5	2		
INOR-5	15					2	2
INOR-6	16	5		1.5	1		
INOR-7	16	6			1	1	
INOR-8	16	6	5				
INOR-9	17		5			3	

INOR-9, presently rebranded by Haynes as Hastelloy-N emerged as the prime candidate from this matrix of 9 alloys that were investigated for the MSRE. It exhibited satisfactory corrosion resistance during the MSRE [29], [31] it still possesses some weaknesses that might present challenges to its application in the MSR: firstly, it lacks sufficient creep rupture strength at the required conditions [32]; secondly irradiation-induced embrittlement by a) He bubble formation by the reaction $^{59}Ni(n,\alpha)^{56}Fe$ [33] and b) deposition of the fission product tellurium at the sample surface leading to telluride formation at grain boundaries [34]

In addition, another limitation to the application of Ni-rich alloys in scaled-up MSR

deployment is supply-side scarcity due to the prohibitively high cost of production [29].

Therefore, since the Hastelloy-N leaves some properties to be desired, there remains a berth for the introduction of novel alloys that have the potential to surpass its performance as an MSR structural material.

Commercially available alloys proposed as structural materials for MSRs consist primarily of the elements Ni, Mo, Cr, Fe, Mn, Ti, Nb and W. These form an 8-dimensional space in which 8 alloy compositions have been proposed in the original MSRE and tested [29] .This implies that beyond these 8 alloys there is a quasi-infinite 8-dimensional space of which a mere 8 points have been studied at all.

How can we know for sure that there does not exist a composition within this space that exceeds the 8 tested ones in corrosion resistance? In a quasi-infinite space, is there an efficient way to search the space in order to find out?

It becomes apparent then that a significant subspace within this elemental hyperspace comprises compositions that do not consist of any one particular element as a base. This space, “the central region of the multicomponent alloy phase space” was termed by Miracle & Senkov as the space of Compositionally Complex Alloys (CCAs) [35]. This is an alloy composition space of immense scientific interest in recent years for their potential practical applications, and it is of interest in this thesis for their potential as MSR structural materials.

Multiprincipal component alloys were first introduced in 2004 independently by Yeh et al [36], [37] and Cantor et al [38] when they demonstrated metallurgical preparations of equiatomic CrCoFeMnNi and CrCuFeMnNi respectively with simple crystal structures among other equiatomic or near-equiatomic compositions in their respective studies. The atoms of each element were found to be randomly distributed throughout the lattice with no single matrix element. These demonstrations pioneered a new class of alloys known variously in the field as Multiprincipal Component Alloys

(MPEAs), Compositionally Complex Alloys (CCAs) or High Entropy Alloys (HEAs), where previously it was believed that a single matrix element as a base was necessary to stabilize a homogeneous composition and structure throughout the bulk.

In this thesis we refer to the space of interest, "the central region of the multicomponent alloy phase space" termed by Miracle & Senkov as Compositionally Complex Alloy (CCA). This definition is adopted as most inclusive since it is not overly constraining unlike definitions according to entropy or single-phase-space [35]

Within the last 20 years, research interest in CCAs for their potential practical applications has grown rapidly, with their metallurgy [39]–[41] and their microstructures [42], [43] investigated in detail.

CCAs have been explored for their electromagnetic properties [44]–[46] hardness [42], [47] irradiation resistance [23], [48]–[52].

Atomistic effects unique to CCAs have been studied for their impact on macro-properties such as the contribution of lattice distortion in CCAs to solid solution strengthening [53]–[56] the impact of electronic structure on bond strength [57] the impact of chemical disorder on heat and electrical conductivity [58], [59]. The impact of configurational entropy on solid solution phase stability has been extensively studied [60]–[63] generally found not to contribute significantly to microstructural stabilization of an alloy as a single phase [35], [63], [64]. Therefore, by extension, configurational entropy is not expected to contribute significantly to material properties that depend on microstructure, such as corrosion. The findings of this thesis work are consistent with that observation. In general elevated configurational entropy in an alloy is balanced by a correspondingly weaker (less negative) enthalpy [35] which is an additional reason the term CCAs is preferred in this thesis to refer to the class of alloys studied.

Corrosion behavior of CCAs in harsh aqueous media (elevated temperature & strongly oxidizing environment) have been extensively investigated [65], [66], [75]–[78], [67]–[74] with results being as varied as the compositions of the CCAs studied. It is difficult to compare results across a corpus of literature to glean coherent macro-trends if the data are not standardized in solvent condition and CCA class (eg. 3d transition metal alloys, refractory metal alloys, etc)[35].

3.3 Theory of Corrosion of Alloys in Molten Salts

Corrosion in fluorides and chlorides occurs primarily by elemental dissolution at the alloy-salt interface, assuming the salts are fairly pure enough [79] that the thermodynamic favorability of oxidation and dissolution of the element into salt dictates how fast the element depletes at the surface, and the kinetics of its diffusion from the bulk to the surface dictates how fast the element replenishes at the surface dictates how much of it is available to be continuously lost over the corrosion period. Since metal oxides are generally soluble in molten fluorides [80], any passivating oxide layer (for example Cr_2O_3 or Al_2O_3) preexisting on the alloy surface due to prior exposure in air or high-temperature water would quickly dissolve in the molten halide shortly upon initial exposure to the salt [81].

Corrosion in molten chlorides largely results from the formation of alloy-element chlorides [79] , which are soluble [80]. These elements are then dissolved from the alloy into the salt. It is generally assumed that carbide and oxide precipitation on the surface of the alloy is insufficient to form a continuous or even substantially detectable layer between the alloy and the salt, in fact, so far studies have shown that these are generally soluble in molten halides [26], [80]. Assuming no solute saturation and corrosion kinetics controlled by surface reactions, the mass of metal corroded from an alloy, W_M is given by Faraday's Law:

$$W = \frac{\int I(t)dt\, M_A}{nF} \qquad (1)$$

Where $\int I(t)dt$ is the total charge exchanged over the corrosion period t [s], M_A is the atomic weight of the element, F is the faraday constant [$C \cdot mol^{-1}$] and n is the number of equivalents electrons transferred during the oxidation reaction of metal. The total mass loss W is converted to units of total concentration of elements corroded in [ppm] into the salt as a standard metric to quantify the extent of corrosion in the alloys tested in our study.

Assuming constant vapor pressure of $Cl_2(g)$ in thermodynamic equilibrium with dissolved Cl_2 in the salt, the net reaction describing the dissolution of an element M from the surface of the alloy can be expressed by the Nernst equation:

$$\Delta E_{M/MCl_2} = \Delta E^{o}_{M/MCl_2} - \frac{RT}{nF} ln\left(\frac{a_{MCl_2} \cdot P_{Cl_2}}{a_{M,surf}}\right) \quad (2)$$

Where $\Delta E^{o}_{M/MCl_2}$ is the standard reduction potential of corrosion reaction of metal M (by formation of soluble MCl_2) from the alloy. T is the temperature in K, R is the ideal gas constant in [$J \cdot K^{-1} \cdot mol^{-1}$], $a_{M,surf}$ is the activity of M at the surface, and P_{Cl_2} is the partial pressure of chlorine in the atmosphere.

In a well-controlled system the standard value of P_{Cl_2} is assumed to be constant. a_{MCl_2} is the activity of MCl_2 dissolved in the molten salt *before* the reaction initiates. Since the thermodynamic favorability of initial onset of elemental dissolution into pure salt is of interest, a nominally dilute concentration of corrosion product MCl_2 is often assumed of $a_{MCl_2} = 10^{-6}$ [mol/cm^3]. The reduction potential of this corrosion reaction can be converted to the free energy of the same reaction by the relation:

$$\Delta G_{M/MCl_2} = -nF\Delta E_{M/MCl_2} \quad (3)$$

Like $\Delta E^{o}_{M/MCl_2}$ the free energy of a reaction indicates the thermodynamic favorability of the corrosion reaction; the more negative the ΔG value of a reaction, the more thermodynamically favorable it is. The thermodynamics of the corrosion mechanism can then be parametrized by the Gibbs free energies of the product formation $\Delta G_{M/MCl_2}$ and the activities of the alloying elements $a_{M,surf}$ at the interface. The Gibbs free energy of formation of the alloy also provides an indicator of corrosion resistance.

The Ellingham Diagram (Figure 3) shows the standard reduction potentials of the corrosion reaction in fluoride for several common elements of interest (Fe, Cr, Mn, Ni, Mo, Al, Ti, Co, Mo, W) for their respective reactions expressed in Equation (1). The more negative the E^{o} value is, the less noble the metal in the fluoride media and the more stable the metal fluoride. Evidently, the thermodynamic favorability of dissolution varies widely across different elements.

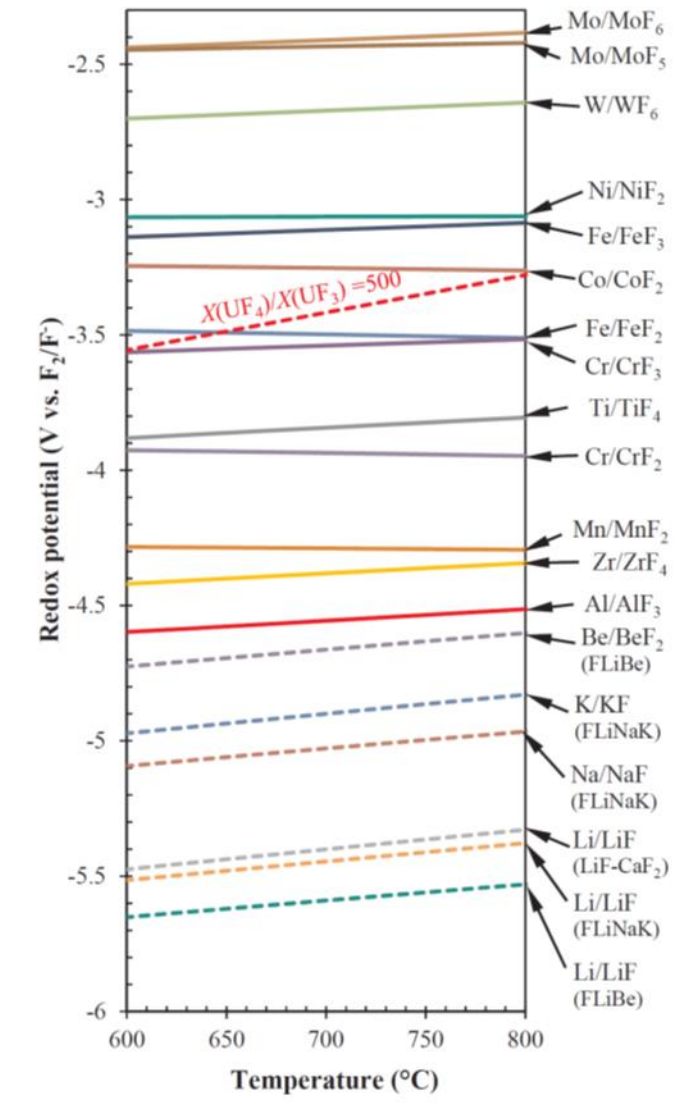

Figure 3 Ellingham diagram [82] *showing standard reduction potentials of various common alloying elements of interest as a function of temperature in fluoride salts, assuming activity of metal fluoride = 10^{-6} [mol/cm^3].. The more negative the reduction potential of a metal is, the more stable the fluoride and therefore the less noble it is in fluoride media.*

The development of a corrosion model begins by considering mass transport along the depth of the alloy for each element from the interface, described by Fick's Second Law:

$$\frac{\delta C_{SS,M}(x,t)}{\delta t} = D_{SS,M}\frac{\delta^2 C_{SS,M}(x,t)}{\delta x^2} \qquad (4)$$

Where $C_{SS,M}(x,t)$ is the local instantaneous concentration of the element M (aka the analyte) in solid solution of the alloy [moles/m^3] as a function of depth from the metal alloy interface into the alloy, x [m] and time, t in [s]. $D_{SS,M}$ is the effective solid solution diffusion coefficient of the element M in the lattice in [m^2/s]. Applying the following to Equation (4),

i) Dirichlet boundary conditions:

   a) $C_{SS,M}$ (x $-\infty$, t) = 0, ie. The concentration of the analyte at the alloy surface is 0; Applying this boundary condition assumes a volume of molten salt which is large enough that it does not become saturated with the analyte within the corrosion period, and that, once dissolved, the diffusion of the analyte away from the surface into the bulk is extremely fast. A comparison of solid solution diffusion coefficient for Fe in Table 2 with its diffusion coefficient in molten chloride in Table 9 shows that the diffusion of Fe in molten salt is 7 orders of magnitude faster than in solid solution, so this assumption is valid;

   b) $C_{SS,M}$ (x ∞, t) = C_0 (alloy bulk concentration of the element), ie the concentration of the analyte in the bulk alloy is equal to the original concentration;

ii) Initial Condition: $C_{SS,M}$ (x , t = 0) = C_0;

iii) Dimensional scaling: $\theta(x) = \frac{C_{SS,M}(x)}{C_0}$; and

iv) The similarity transformation: $\xi = \frac{x}{2\sqrt{D_{SS,M}t}}$

The concentration profile of the element along the depth into the alloy from the molten salt/alloy

interface, x [m] at time t [s] can therefore be given by the analytical solution to Equation (4):

$$\frac{C_{SS,M}(x,t)}{C_0} = \text{erf}\left(\frac{x}{2\sqrt{D_{SS,M}t}}\right) \qquad ; 0 < t < \tau \qquad (5)$$

This concentration profile can be used to estimate elemental depletion depth. An example of the concentration profile as a result of this corrosion model is shown in Figure 2. The elemental depletion depth can indicate the extent to which corrosion has altered the alloy chemistry at subsurface regions: higher depletion depths can imply greater effects of corrosion attack.

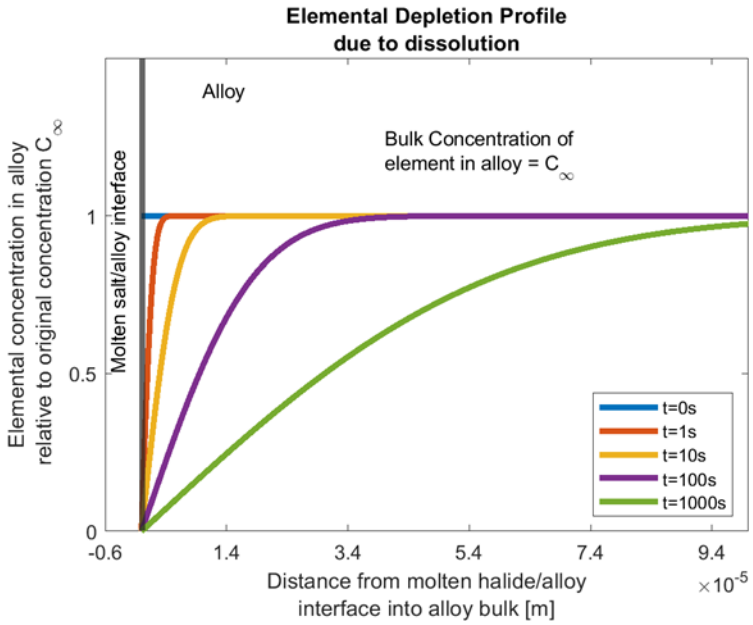

Figure 4 An illustration of the elemental depletion profile due to dissolution based on the analytical solution to the diffusion equation found in Equation (8) assuming surface concentration of analyte at molten salt/alloy interface = 0, and temperature T = 500°C where solid solution diffusion coefficient, $D_{SS,M} = 10^{-15}[m^2/s]$.

Surface corrosion rate (indicated by I in equation (1) of an element M) affects the value of

C_0 in the initial condition as well as the left boundary condition in the Model, and solid state diffusion coefficient $D_{SS,M}$ determine the concentration gradients that result in a shift in local composition of the alloy near the surface region. Diffusion coefficients of alloying elements can determine the steepness of their concentration gradients at any point in time during the corrosion period, as illustrated in Figure 4. It is therefore apparent how these kinetic parameters I_M and $D_{SS,M}$ affect corrosion. It was observed by Elbakhshwan et al [83] that at high temperatures, the combination of fast diffusion to the surface and favorable thermodynamics of corrosion at the surface resulted in Mn corroding rapidly enough to apparently suppress the corrosion of Cr, demonstrating how a combination of particular kinetic and thermodynamic parameters can give rise to novel phenomenon. As an example of the order of magnitude for diffusion coefficients in Ni-based alloys at high temperature some values for Hastelloy N are provided:

The rate at which an element M participates in a corrosion reaction at the surface depends on the abundance of element M at the surface. The depletion of M at the surface sets up concentration gradients which initiate the diffusion of M to the surface from the bulk. Diffusion of M through the bulk to the surface is described by Fick's Second Law:

$$\frac{\delta C_{ss,\mathrm{M}}(x,t)}{\delta t} = D_M^c \nabla^2 C_{ss,M}(x,t) \qquad (6)$$

Where $C_{SS,M}$ is the local concentration of the element M in solid solution in the alloy [moles/m^3] at a given exposure time and depth from the metal alloy interface. $D_{ss,M}^c$ is the chemical diffusion coefficient of a specific element in the lattice in [m^2/s] (in the case of multiple phases being present, an effective chemical diffusion coefficient was defined as the phase fraction weighted sum). In an alloy under corrosion in molten salt, the chemical diffusion coefficients D_{M}^c may be more relevant than tracer diffusion coefficient D_{M}^t.

The diffusion coefficient represents the speed at which M diffuses in the bulk, and it is dependent on the energetic favorability of the migration of one atom of M to a vacancy site within the bulk, as described mathematically by the Einstein Diffusion Equation:

$$D_{SS,M} = \frac{1}{6} r^2 \nu Z \exp\left(\frac{-Q}{RT}\right) \qquad (7)$$

Where $D_{SS,M}$ is the diffusion coefficient of a species M in the solid, r is the "jump" radius (distance) of an atom between sites (~0.3 nm), ν is the vibrational frequency of the diffusing atom (~ 10^{13} Hz), Z is the number of available neighboring sites, Q is the activation energy for the diffusion in [J/mol] (as an example, the Q-value for Ni in $FeCoCrMn_{0.5}Ni$ HEA is ~315 [kJ/mol] [84], R is the ideal gas constant in [$J \cdot K^{-1} \cdot mol^{-1}$], and T is the temperature in [K]. It is therefore apparent from the Z term in the equation how processes that increase the number of neighboring sites, such as the injection of vacancies by surface corrosion, can affect the diffusion constant in the bulk of the alloy. It is also apparent that migration activation energy Q and temperature T can affect the rate at which a species diffuses within the bulk of the alloy.

Table 3: Examples of solid solution diffusion coefficients of analytes of interest

Element	Temperature (°C)	Diffusion Coefficient [cm^2/s]	Ref
Cr	700	8.72×10^{-15}	[85]
Cr	850	2.31×10^{-12}	[79]
Fe	850	5.56×10^{-12}	[86]

These values are useful benchmarks to know what rate of corrosion to expect.

We can therefore see how kinetic parameters can impact the mechanisms of corrosion : elements with faster dissolution kinetics at the interface but insufficiently quick solid state diffusion kinetics within the alloy deplete more quickly in the near-surface regions and the depletion of some elements results in the relative localized enrichment of others, giving rise to phase instabilities which can affect corrosion.

The chemical model described provides the basis for commonly-used quantitative methods of evaluating corrosion extent and corrosion rate: weight loss from alloy as in Eqn (1), elemental depletion depth and quantity of element lost from the surface which can be derived from the integration of eqn 7. In addition, the kinetics of the surface reaction rate can be measured by potentiodynamic polarization which will be discussed in more detail in the later section on theory of analytical techniques for quantifying corrosion products.

However quantitative metrics for measuring extent of corrosion are insufficient to completely describe material degradation these materials undergo. It is possible for a material to have lost a comparatively small amount of weight, but if all this weight loss was due to a crack that had formed at the material grain boundary, this can propagate leading to rapid structural failure. Therefore qualitative analysis of corrosion is often necessary. The following corrosion-related modalities of material degradation have been codified as distinct in literature, distinguished from one another by the specific interplay between thermodynamics/kinetics of the surface interaction of constituent elements of the structural alloy and the kinetics of their diffusion to the surface that give rise to the distinct degradation phenomenologies:

The mechanism of galvanic corrosion can occur where there is enough local potential difference present between two regions on the surface of an alloy for the more positive region to act as a local anode where the oxidation reaction occurs and the more negative region to function as the local

cathode where the reduction reaction occurs . This pair of local anode/cathode can be separated by distances as small as 2.5 um [75]. Local potential differences can observed in mixed phase regions where one phase is at a higher potential than the other, attributed to the higher-potential phase having a relatively elevated enrichment of a more noble element than the lower-potential phase [65], [75].

Where a galvanic couple arises, there also arises the possibility for anodic dissolution [87] where elements oxidized at the anode dissolve into the molten salt. This can occur even with elements considered noble [88] in that environment. Fundamentally, galvanic corrosion is limited by thermodynamic parameters.

Pitting is the phenomenon where microscopic depressions spontaneously initiate on the alloy surface due to local dissolution. As mentioned earlier, local corrosion by dissolution can occur on the spatial order of a few microns, but pitting occurs without the need of local potential differences. These pits become sites for local concentration of chemically-attacking species, thus exacerbating corrosion. Pitting is a significant phenomenon in corrosion of alloys in molten salts [89]. Fundamentally, pitting is a thermodynamic phenomenon limited by the morphological availability of pitting initiation sites.

Intergranular corrosion is where particularly corrodible elements are preferentially corroded at sites between grains at the alloy-salt interface [90], [91] . This phenomenon is more pronounced in systems where there are driving forces to accelerate the diffusion of elements from the grain bulk to the grain boundary [92] where diffusion tends to be faster, facilitating the exposure of the element to the alloy-salt interface. A related phenomenon is grain boundary corrosion – defined as faster diffusion coefficient along the grain boundaries - which, if significant, can cause premature failures even at low weight loss values [8] by mechanisms such as accelerated stress corrosion cracking at the grain boundaries [93], [94]. Fundamentally, intergranular corrosion is limited by kinetics of thermo-dynamically corrodible elements; it is a corrosion modality which accelerates stress corrosion cracking.

Dealloying [95] is the phenomenon where a more thermodynamically corrodible element is continuously dissolved from the alloy leaving the more thermodynamically noble element behind resulting in a distinctively nano-porous structure. This resulting morphology distinguishes the process of dealloying from intergranular corrosion. Two of the three major mechanisms of dealloying rely on a sufficient abundance of the noble element in the alloy (expressed by the “parting limit" which is the minimum fraction in the alloy of less noble elements which is required for dealloying to be observed at a particular temp [96] balanced by sufficiently quick diffusion kinetics of the noble element to competitively fill vacancies injected by the departure of corrodible element atoms [97], [98]. These two mechanisms are distinguished from one another by the subtle differences in the resulting morphologies - 3D bicontinuous vs negative dendrite porous morphology. The third major mechanism of dissolution/redeposition [98] in which the alloying elements are generally both noble and their thermodynamics of dissolution are close together. Molten Salt Dealloying (MSD) has been demonstrated for binary NiCr alloys [90], [99] and even ternary NiCrFe alloys [100]. In general, dealloying mechanisms are limited by the solid state mobility of the thermodynamically more noble element.

Those previously mentioned mechanisms are of primary concern if the salt is absolutely free of impurities. However, since even the most aggressive purification processes such as the bubbling of halide-acid gas through the halide salt to react away any oxygen bearing impurities [101] rely on L’Hopital’s equilibrium rule, absolute purity is impossible to achieve and therefore most salt will contain even miniscule amounts of impurities, even if it is close to or below the detectable limits of the most sensitive state-of-the-art analytical techniques. Therefore impurity driven corrosion cannot be completely eliminated from consideration. Oxide (O^{2-}), water (H_2O), sulfate (SO_4^{2-}) and phosphate (PO_4^{3-}) are the primary anionic culprits of impurity-driven corrosion. Under the Lux-Flood model of acids/bases oxygen-bearing impurities spontaneously release the O^{2-} anion into the molten salt under most conditions where they attack metal elements on the surface of the alloy to form soluble metal cations [102]–[104] . On the

other hand, metal oxides formed which are insoluble in the melt can precipitate on the alloy surface. Carbides and Tellurides are other notable insoluble impurities whose precipitation on the alloy surface accelerates degradation. The grain growth of these insoluble impurity precipitates can cause intergranular cracking on the alloy [91], [105]. Metal cations in the salt that are not the base cations can alter the surface activity of the alloy elements and thus impact corrosion mechanisms. While impurity-driven corrosion is a legitimate engineering concern, the primary task at hand is to understand the processes of material degradation of alloys by the primary anion in the solvent environment - halides.

Investigating the interplay between these mechanisms is the primary focus of this thesis, and the question of whether one process in particular predominates the degradation of alloys in molten halides is the central line of inquiry herein.

3.4 Analytical Techniques for Quantifying Corrosion Products in MS

In order to study corrosion mechanisms, it is necessary to determine the rate at which the various alloy constituent elements corrode differentially into the salt. The suitability of the chemical analysis technique to quantify corrosion products is highly dependent on a) the state of matter of the analytes (solid/liquid/gas), b) the chemical form of the analytes expected, c) the expected concentration of the analytes within the sample. The next chapter includes a comparative study of common chemical analysis techniques employed in the molten salt research community. This study serves to highlight the importance of correctly estimating the correct chemical form of corrosion products/

This section provides a brief overview of the theory behind chemical analysis techniques used to quantify corrosion products in molten salts used in this thesis, as well as the framework for the quantification analysis. These techniques are commonly used by the molten salt corrosion community.

3.4.1 Inductively Coupled Plasma Mass Spectrometry & various techniques in Optical Emissions Spectroscopy

Several chemical analysis techniques used in this thesis used to quantify corrosion products such as Inductively-Coupled Plasma Optical Emissions Spectroscopy (ICPOES), Laser Induced Breakdown Spectroscopy (LIBS) and Glow Discharge Optical Emission Spectroscopy (GDOES) have in common that they are all destructive techniques in which a small amount of sample on the order of mg is atomized by a plasma (thousands of degrees K) which also serves to energetically excite the electrons in the analyte such that upon relaxation, they emit light usually in the optical spectrum that can be quantified by a detector. Quantifying the intensity of the emitted light allows the analyst to infer the concentration of analyte in the atomized sample by a calibration curve. A schematic of the commonalities between ICPOES, LIBS and GDOES is shown in Figure 5.

Plasma Atomization

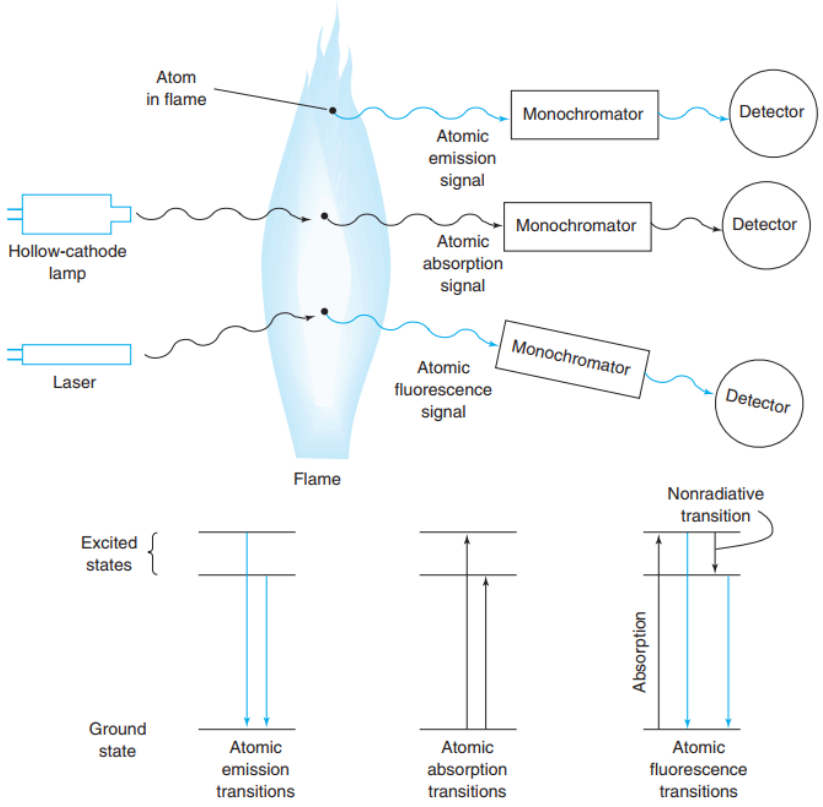

Figure 5 Infographic from Chapter 20 of [106]. *Emission, absorption and fluorescence by atoms in a flame or plasma. In atomic absorption, atoms absorb part of the light from the source and the remainder of the light reaches the detector. Atomic emission comes from atoms that are in an excited state because of the high thermal energy of the flame. To observe atomic fluorescence, atoms are excited by an external lamp or laser. An excited atom can fall to a lower state and emit radiation.*

Inductively-Coupled Plasma (ICP) is a conventional technique used to atomize samples in order to analyze the constituent elements in the sample. For atomization by ICP, a sample must first be completely digested by acid (generally about ~1g amounts are digested) such that all of it dissolves into aqueous solution thereby homogenizing it. Sample masses of milligrams may be used if the analyte of interest to be quantified constitutes the bulk of the sample. Otherwise, if the analyte of interest is in trace

amounts (1-1000ppm) in the sample, at least 1g of sample is required for analysis.

It is then volumetrically diluted [107] before the aqueous digest is loaded onto the ICP instrument. The aqueous digest needs to be volumetrically diluted such that the anticipated analyte concentration is within the dynamic range of the detector (ie. The range of detector sensitivity). This is generally ~0.1-10,000ppm [108] for detectors coupled to ICP. With this understanding, it then becomes clear why samples ~5g or greater become difficult to analyze by ICP-related methods - they have to be diluted by >5000x at which point uncertainties compounded by serial dilution become non-negligible.

The sample chamber of an ICP instrument only has room for a volume of ~10mL of aqueous sample [108]. The aqueous sample is aspirated into an inductively coupled plasma produced by applying high voltage across a chamber of argon gas. The ionization energy of Ar is 15.8eV, which exceeds the ionization energy of most elements except He, Ne and F [106], so most elements are ionized with the Ar. Analyte elements can be ionized by collisions with Ar+ or energetic electrons [102]. A plasma torch in a typical Agilent instrument is about 8cm in length, 1cm in diameter. The plasma, reaching temperatures as high as 5500 - 6500 K [109], atomizes the sample digest.

Another possible method of atomization of the sample is by Laser Induced Breakdown in which a laser of spot size ~0.5mm [110] is pulsed directly onto a sample, usually a solid, and a very localized plasma is produced such that the local temperature on the sample can go as high as 10,000-20,000K[102] and the surface atoms on the sample in proximity are thereby atomized (Figure 6.) The laser is produced directly on the solid sample, laborious sample preparation is eschewed. Method development for LIBS to replace ICP-MS/OES in quantifying corrosion product ex-situ for the accelerated quantification of high-throughput CCA corrosion tests was performed as part of this thesis

In the case of Glow Discharge, the sample functions as a cathode and is placed opposite an anode. A high voltage and a steady supply of Ar is placed between them. The plasma is formed locally on the sample by the ionization of the Ar atoms. Sputtering of the sample occurs, which is the ejection of sample atoms following the impact of energetic ions (and neutral atoms) in the plasma on the surface. An incoming ion suffers a binary collision with a target atom. This is illustrated in Figure 7.

In the case of solid samples, depth profiling can be performed by successive pulses probing increasingly deeper to measure elemental concentrations as a function of depth [102].

After the sample has been atomized, it is quantified according to the coupled detection method.

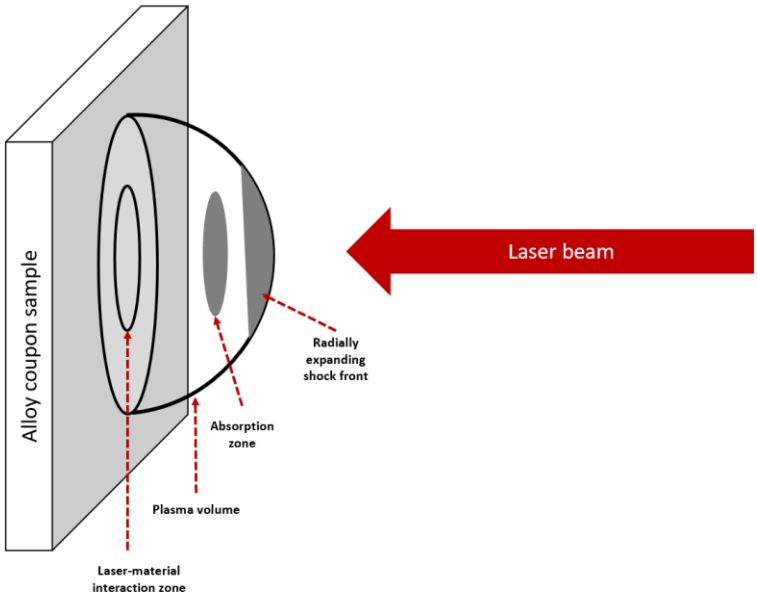

Figure 6: Schematic of plasma formation for Laser Induced Breakdown analysis adapted from [111]

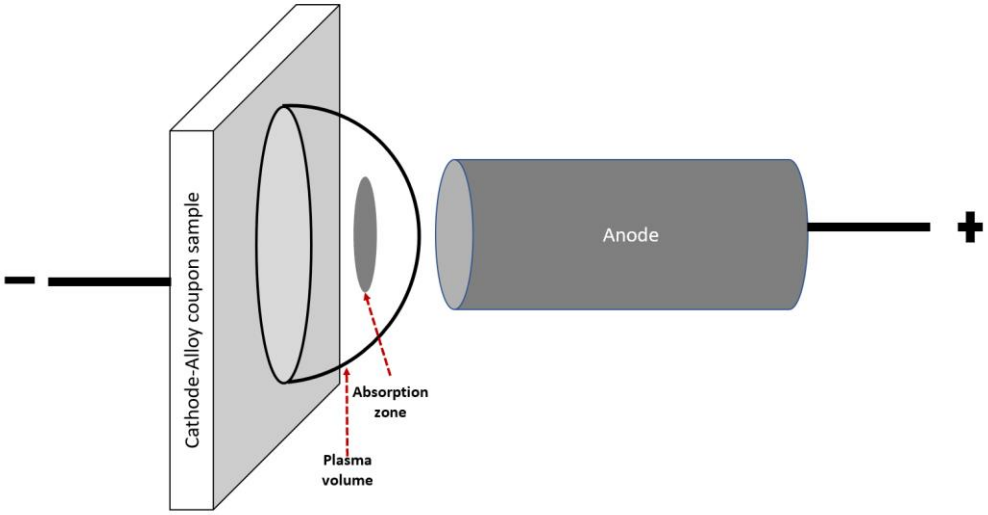

Figure 7: Schematic of plasma formation for Glow Discharge Optical Emission Spectroscopy, adapted from [112]

Mass Spectrometry

The plasma produced by ICP can be directed into a mass spectrometer. Atoms are generally singly-ionized in a plasma. The hardware of a mass spectrometer (eg. Magnetic sector or alternating current quadrupoles are common ones) enables the separation of analytes by mass-to-charge ratio to be discriminated by Faraday cup detectors [102]. The analytes are thereby identified by mass number. The mass spectrum of a sample is essentially an histogram of the elements in the sample detected over the analysis period. The height of the histogram corresponds to analyte concentration in the sample according to a linear calibration curve of the form H = bC

Where H is the element intensity on the mass spectrum, C is the concentration of the analyte in the sample and b is the linear calibration constant dependent on ionization efficiency and detector efficiency of the mass spectrometer.

(Optical Emissions) Spectroscopy

Electrons on the atoms within the plasma get energetically excited. Upon their de-excitation, they emit photons at wavelengths characteristic to their element. The series emission wavelengths (λ) can be predicted by eqn (8) for m =3,4,5… and each element with proton number Z and L_{series} is an empirical constant depending on the region of electromagnetic spectrum of interest: L_{series} = 3645.6A for the Balmer series in the visible spectrum. As m—> infinity, the series converges to the value L_{series} indicating that $L_{series} = 1/Z^2$ is the lowest wavelength theoretically observable from an element, which corresponds to its first ionization energy.

$$\lambda = L_{series}\frac{m^2}{m^2 - 2^2}\cdot\frac{1}{Z^2} \qquad (8)$$

An illustration electronic transitions resulting in optical emission is provided [113].

Many elements heavier than Hydrogen with multiple valence and tightly-bound core electrons will exhibit deviations from their expected emission lines based on this analytic formula, due to the mutual interactions of their electrons.

Quantum selection rules determine the probabilities with which each transition and its associated emission can occur.

The emission rate density at a particular wavelength I(λ) is linearly related to the number of analyte atoms n_0 in the plasma:

$I(\lambda) = Cn_o$

Where I = detected emission intensity, n_o is concentration of analyte atoms in the matrix and C is a constant determined by:

I. The transition probability of an electron between energy levels
II. The energy of the upper level
III. The partition function
IV. Signal transmission efficiency of the detector
V. Temperature
VI. Matrix effects

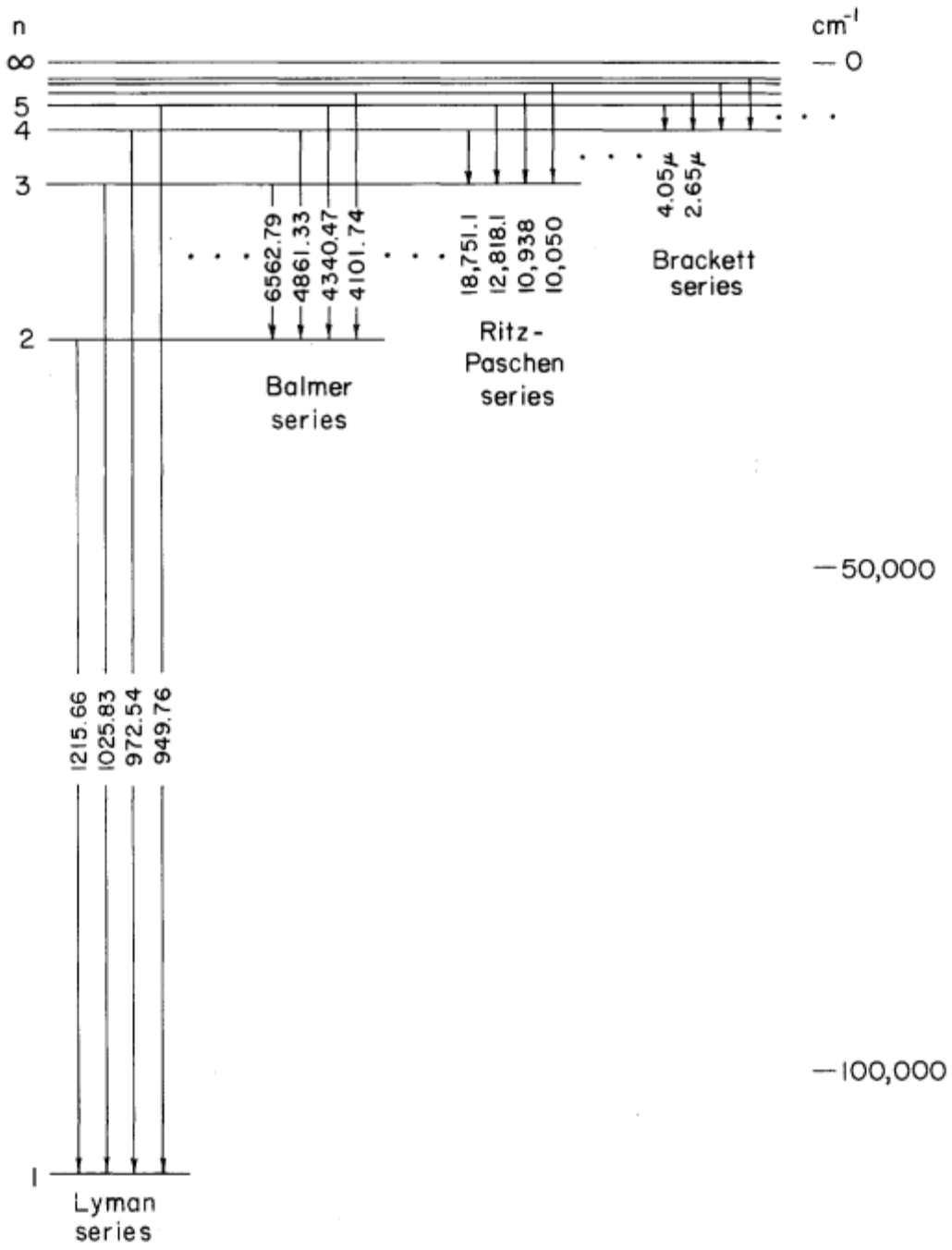

Figure 8 Illustration of electronic transitions resulting in optical emission of the hydrogen atom [109]

The selection rules governing the emission energies and their expected intensities of each element are more complex than can be discussed by the scope of this thesis. In practice, only a small subset of emission wavelengths (aka “lines”) has sufficient intensity to enable adequate instrument sensitivity for quantifying the analyte. For more details on the quantum mechanical theory governing optical emissions spectra the reader is directed to Chapter 2 of [113]. For more details on considerations regarding the quantification precision by OES such as a)peak width, b) background correction, c)determining detection limits for a particular sample-matrix pair, d) how to address spectral interference, the reader is directed to Chapter 20 of [102].Moreover, depending on atomization technique (ICP vs. GD vs. LIB), analyte atoms may or may not be in local thermodynamic equilibrium, so the best emission lines for a particular analyte in one atomization technique may not be the best emission lines for the same analyte with a different analytical technique. Due to all these considerations, generally in practice it is necessary to establish a calibration curve for the dynamic range of one’s samples for every optical emissions technique and matrix-analyte pair.

A direct comparison of analytical performance between OES techniques (represented by ICP-OES) and ICP-MS is provided in Table 4. Example figures for the analyte Ni+ ion at 231nm is provided for illustration [114] . For Ni, we note that these values are generally in the ppb range meaning they are sensitive to incredibly minute concentrations of Ni+, and by extension, common alloying cations in alloy corrosion experiments.

Table 4 Comparison of analytical figures of merit for ICPOES and ICPMS [102].

	ICP-OES	ICP-MS
Detection limits (ng/g)	0.1-10 (eg. 3-50 [ng/g] for Ni^+ @231nm [114]	10^{-5} – 10^{-4} (eg. 0.001-0.2 [ng/g] for Ni^+ @231nm [114])
Linear range	10^5	10^8
Precision, short term (5-10min)	0.1-2%	0.5-2%
Precision, long term (hours)	1-5%	<5%
Sources of interference	Many spectral interferences, few chemical interferences	Some chemical interference, many mass interferences, especially isotopic interference
Sample throughput	6-60 elements/min	All elements in 2-5min

ICP-MS and ICP-OES are common analytical techniques used to quantify ex-situ metal corrosion products dissolved into salt in the molten salt community. They have the disadvantage of being destructive techniques which require a comparatively elaborate sample preparation procedure. In addition they are ex-situ techniques so they preclude the capability to obtain time-resolved analyte quantification data. In this thesis, ICP-OES/MS, GDOES and LIBS are critically evaluated and implemented with awareness of their limitations in Chapter 2.

3.4.2 Theory behind Some Commonly-used Electrochemical Techniques to study corrosion in molten salts

Beyond showing results consistent to those from traditional gravimetric experiments, polarization studies of alloys in molten salts can also be used to probe element-wise reaction kinetics. Ai et al [115] have used polarization studies of W and Mo in FLiNaK at 800°C to observe that the i_{corr} of Mo is twice that of W in the molten salt. They made further observations with corrosion tests of Ni-based Mo & W-bearing alloys that are consistent with Mo diffusing more rapidly through the Ni matrix relative to W. This suggests we can expect the corrosion kinetics of Mo to be higher than W. This finding is significant because the thermodynamic nobility of both Mo and W against corrosion have made it difficult to study their corrosion kinetics with ex-situ analytical methods, but with in-situ electrochemical methods, this has now become a possibility. This is a major advantage of electrochemical methods over gravimetry.

Within the last 10 years, in-situ electrochemical techniques to study the corrosion performance of alloys in molten salts have been favored because they present the following benefits [116], [117]:

i) instantaneous corrosion rate can be obtained in minutes in a polarization study;

ii) instantaneous corrosion rates at intermediate time steps across the corrosion period;

iii) corrosion conditions can be well-controlled in a polarization experiment;

iv) the in-situ nature of the electrochemical measurements has the potential for scaling up to handle a high-throughput experimental process or in-reactor online monitoring.

An example of a setup to perform polarization studies on an alloy is shown below in Figure 9 [118]. The alloy to be studied is connected to the working electrode (WE).

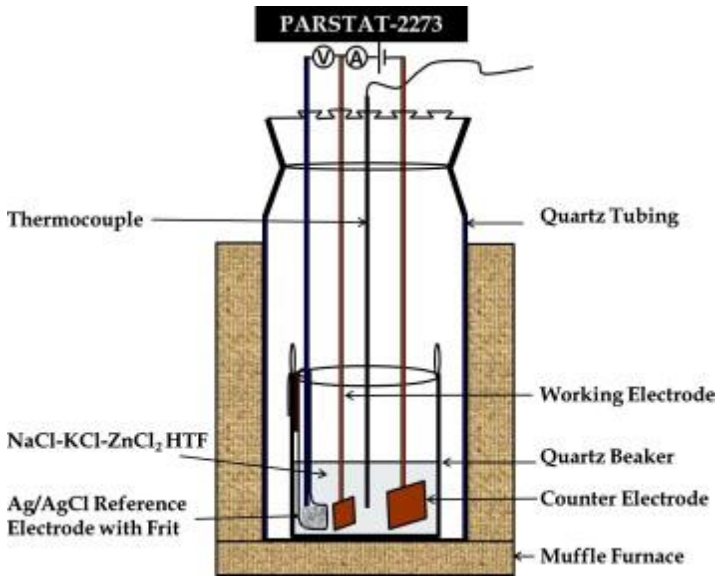

Figure 9 An example of a setup to perform polarization studies on an alloy [118]. *The salt medium is NaCl-KCl-$ZnCl_2$. The alloy to be studied is connected to the working electrode (WE). The reference electrode (RE) is the Ag/AgCl couple. A counter electrode (CE) is present as a source of electrons. Quartz is used as insulation and containment material such that the salt bath provides the only route of electrical conductivity between all electrodes. Parstat-2273 refers to the potentiostat.*

With the setup, the potentiostat is used to electrically polarize the alloy sample over a range of values and the current crossing the WE is measured. The polarization window is selected such that the following Tafel plot (Figure 8) can be obtained:

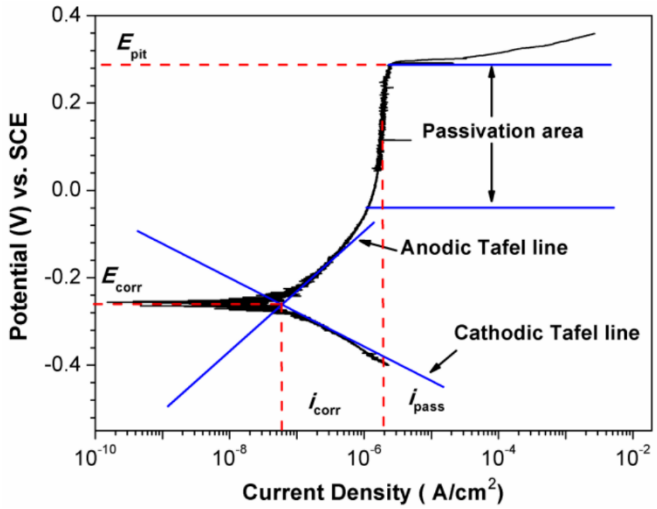

Figure 10: An example of a Tafel plot with parameters of interest marked out [118]. *E_{corr}: corrosion potential, i_{corr}: corrosion current density, Passivation area indicates a range of potentials in which a protective film (often consisting of oxide) has formed over the alloy to prevent continual dissolution of metal, i_{pass} is the current density in the passivation area , E_{pit} : critical pitting potential.*

E_{corr} indicates the overall nobility of the alloy with respect to the RE, and the value for an alloy is typically in between the E_{corr} of its most noble and least noble elements. Potentiodynamic polarization experiment can provide both kinetic (i_{corr}) and thermodynamic (E_{corr}) information about the system. The corrosion current density can be converted to corrosion rate in [mm/yr] by the Stearn-Geary Equation [119]

$$Corrosion\ Rate = \frac{i_{corr} \cdot K \cdot EW}{\rho} \qquad (9)$$

Where K is a conversion constant 3272 [$mmA^{-1}cm^{-1}year^{-1}$], EW is the Equivalent Weight of the alloy in [$g\ mole^{-1}\ e^{-1}$], calculated by the following relationship [120]:

$$EW = \left(\sum \frac{f_i n_i}{MW_i}\right)^{-1} \quad (10)$$

Where f_i is the weight fraction of the i^{th} alloy constituent, n_i is the number of electrons being transferred in the oxidation of the i^{th} species, and MW_i is the atomic weight of the i^{th} alloy constituent.

Tafel plots from Keny et al [117] (Figure 10) show that i_{corr} of alloys of interest is lowest for Hastelloy N and Incoloy 800HT, compared to the Inconels studied and Incoloy 800. This corroborates the large volume of experimental support, obtained from gravimetric measurements, for Hastelloy N as a prime candidate structural material for MSR among commercial alloys in Table 3 and Table 4 , and lends support for the efficacy of potentiodynamic polarization over gravimetry.

In order to accelerate the throughput of corrosion product quantification, in-situ electrochemical probe to quantify dissolved cations of interest, in particular Fe and Mn was developed. Cyclic voltammetry-based electrochemical probes in molten salts have been demonstrated as a robust concept in the literature spanning decades.

The setup to perform CV in a salt to determine the concentration of dissolved analyte (for example Fe^{2+}) is shown in Figure 11:

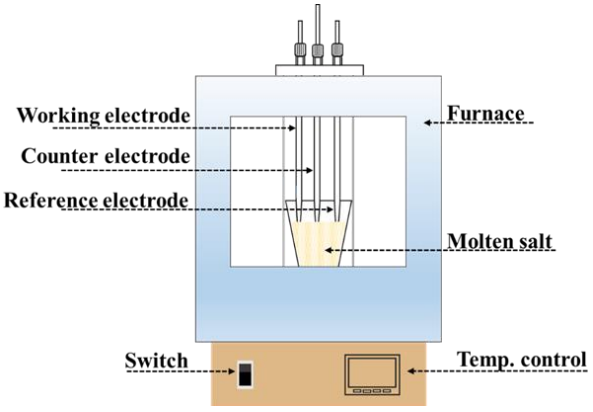

Figure 11: A typical cyclic voltammetry setup to measure the concentration of a dissolved cationic analyte in molten salt at >500°C [121]*. The Reference Electrode (RE) and Counter Electrode (CE) material is usually a noble metal like Pt whose potential remains stable in the salt over the course of the*

study. The Working Electrode (WE) material selected to be a noble metal like Pt or W which is more noble than the analyte to be studied (ie. When the potential is swept in the positive direction the analyte will oxidize much more quickly than the electrode material does). All three electrodes are controlled by the potentiostat. All electrodes must be electrically insulated from one another and the crucible material. The crucible material is usually chosen to be a material that is impervious to corrosion by the molten salt media to be studied to avoid corrosion effects such as dissimilar materials corrosion from complicating the system. ***The major difference between the CV setup shown here and the Polarization study setup shown in Figure 9 is that in the Polarization study, the alloy to be studied is connected to the WE, however, in a CV study, the WE is in direct contact with the salt to study the bulk analyte concentration in the salt.***

A potential is applied by the potentiostat at the WE, and swept from one end of a potential widow to the other while the current density (I) crossing the WE is measured by the potentiostat. When the potential at the WE crosses the apparent reduction potential of a species during the cathodic scan, reduction of the analyte at the WE initiates. When the potential at the WE passes the apparent reduction potential of a species during the anodic scan, oxidation of the analyte at the WE initiates. The apparent reduction potential of an analyte (for example Cr) in a particular cell, $E_{Cr,cell}$ is given by

$$E_{Cr,cell} = \mathrm{E}_{\mathrm{Cr0/Cr2+}} - E_{ref} \qquad (11)$$

Where E_{ref} is the half-cell reduction potential of the RE and the half-cell reduction potential of a metallic analyte Cr, $E_{Cr0/Cr2+}$, is given by the Nernst equation for the reduction of a pure metal:

$$\mathrm{E}_{\mathrm{Cr0/Cr2+}} = \Delta\mathrm{E}^{o}_{\mathrm{Cr0/Cr2+}} - \frac{RT}{nF} ln(\frac{1}{[Cr^{2+}]}) \qquad (12)$$

(recalling that in ideal solutions, activity coefficient can be assumed to be constant such that the change in

the activity of an analyte in solution is approximated by the change in concentration in solution).

For dissolved metallic cations in molten fluorides, charge transport due to oxidizing/reducing analyte at the surface of the electrode for a Nernstian, soluble-insoluble reaction takes the form derived by Berzins & Delahay [122]

$$i_{BD,M}(t) = -C_{bulk,Cr} n^{3/2} F^{3/2} A \left(\frac{D_{o,M} v}{RT}\right)^{\frac{1}{2}} exp\left(-\frac{nF}{RT} \cdot \eta\right) erf\left[\left(\frac{nF}{RT} \cdot \eta\right)^{\frac{1}{2}}\right] \quad (13)$$

Where $i_{BD,M}(t)$ is the Berzins-Delahay solution for current density crossing the surface of the electrode for the metal M in [A/cm^2] at overpotential, η (the difference between the measured potential at the WE and the half-cell potential of the reaction of interest ie. $\eta = E_{measured} - E_{M0/M2+}$) ; $C_{bulk,M}$ is the bulk concentration in [mol/cm^3] of the metal analyte M *dissolved in the molten salt*; n is the number of electrons exchanged in the reaction, F is the Faraday constant in [C/mol]; A is the electrode surface area in [cm^2] ; D_o is the diffusion coefficient of the dissolved oxidized species in the molten salt [cm^2/s] ; v is the potential scan rate in [V/s]; R is the ideal gas constant in [J·K^{-1}·mol^{-1}]; T is the absolute temperature in [K]. An example of a CV curve is shown in Figure 1

The directly proportional relationship of the redox peaks to the bulk concentration of the analyte is therefore derived (8]:

$$i_p = 0.61 A C_{bulk,Cr} \sqrt{\frac{F^3 n^3 D_{Cr2+} v}{RT}} \quad (14)$$

An example of a calibration study to use CV as a quantification technique for dissolved Cr in FLiBe at 500-700ºC is shown in Figure 12, illustrating how if one has knowledge of the D_o value, with a constant potential sweep rate v, one can determine the C_{bulk} in a system using CV.

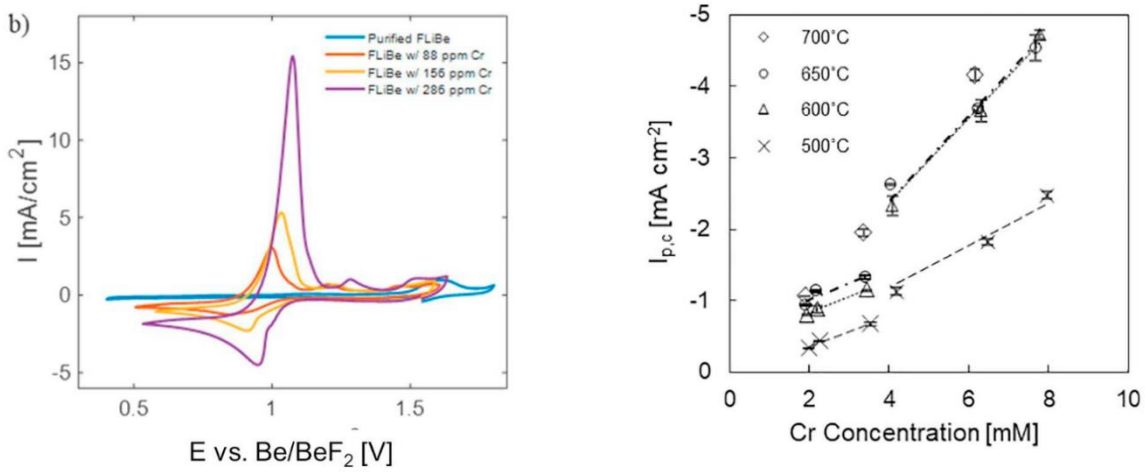

Figure 12 From [123] *(a,left) Cyclic Voltammetry to quantify dissolved Cr in molten FLiBe at 700°C with a series of calibration concentrations of dissolved Cr: 0ppm, 88ppm, 156ppm, 285ppm. The higher the dissolved concentration, the larger the amplitudes of the redox scan peaks; (b,right) the directly proportional relationship between the cathodic peak potentials of the Cr/Cr2+ couple with respect to the log of concentration at 500-700 °C.*

Diffusion coefficients for common analytes in molten fluorides and chlorides have been widely studied using electrochemical techniques, and some representative values of analytes of interest are summarized in Table 5:

Table 5 Examples of diffusion coefficients of analytes of interest in molten halides.

Analyte	System	Diffusion coefficient [cm^2/s]	Reference
Cr^{2+}	FLiBe, 600°C	1.2×10^{-5}	[123]
Fe^{2+}	LiCl-KCl, 500°C	1.5×10^{-4}	[124]
Co^{2+}	LiCl-KCl, 500°C	1.16×10^{-4}	[124]

CV-based sensors for quantifying metallic analytes in molten FLiBe [123] FLiNaK [121], [125] and LiCl-KCl [126] have been developed with some success in recent years.
The development and testing of a miniaturized CV-based Fe probe in molten halides as well as data reduction tools for the automated CV analysis was developed as part of this thesis.

3.4.3 Synchrotron X-ray Absorption Analysis

The electronic structure and chemical environment of an analyte can be probed by X-ray Absorption Spectroscopy (XAS); information regarding the site symmetry, chemical bonding, oxidation state, interatomic distance, and coordination number can be obtained [127] Our samples of diameter 6mm are each exposed to a monochromatic X-ray beam a few microns (~3um) in diameter.

Depending on the analyte of interest, an incident X-ray beam is scanned in energy in the neighborhood of the excitation energy (E_0) of a core electron (K denotes a 1s electron and L3 denotes a 2p electron, illustrated in Figure 13) for the analyte (eg. Cr, K= 5989 eV, Ni, K=8340 eV, Eu, L3~6970 eV). The core electron is excited to an unoccupied energetic state of the atom (aka “quasi-bound” state) , leaving a hole in its place [127] .The absorption spectrum is obtained from a measurement is a superposition various photon absorption events that are characteristic of analyte (for example Cr, Ni or Eu), oxidation state, orbitals of transition, and chemical coordination (eg. Ligands) in the vicinity of the analyte atom [128]. Even though theoretically the species present in the analyte can thereby be identified on an X-ray Absorption Near Edge Structural (XANES) spectrum, due to the complexity of the of absorption/transmission/emission events allowed by selection rules, definitive identification of the chemistry of the analyte studied based on its XANES spectrum often needs to be accompanied by computational modeling of the expected spectrum.

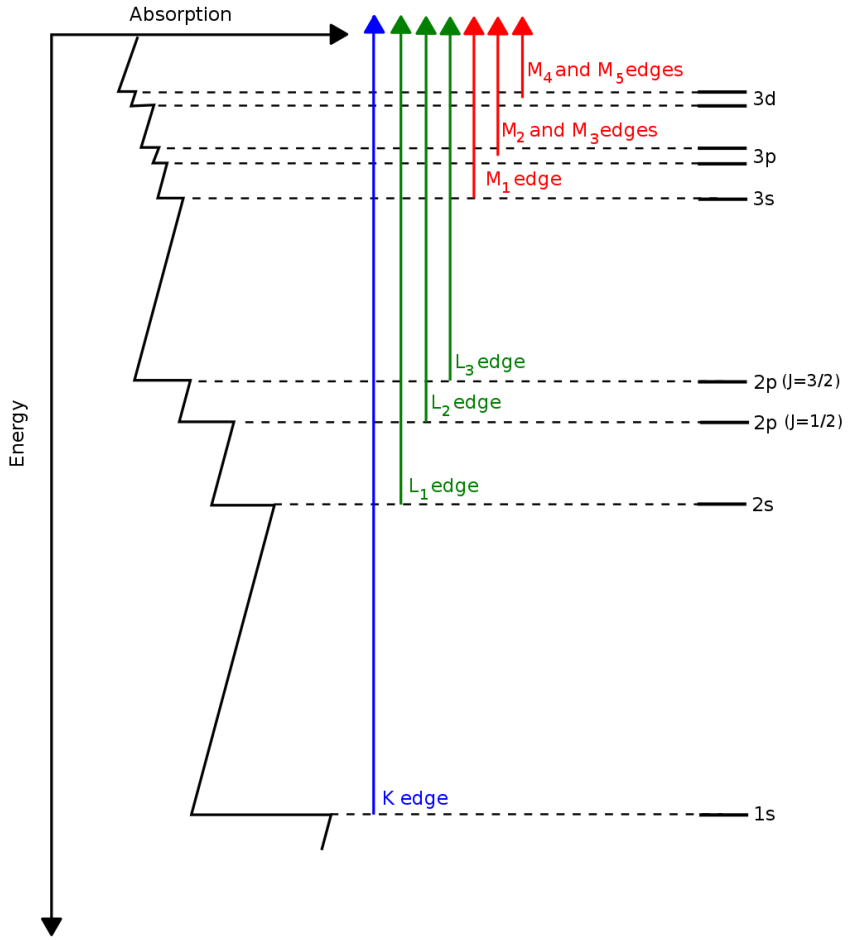

Figure 13 Absorption transitions illustrated by [129]

Synchrotron XAS have been identified as a powerful method for measuring the elemental concentration and chemical state of reaction products at micro- and nanoscale at low ppm-level concentrations, which can reveal the type of chemical reaction and the corrosion mechanism [130]. Feasibility studies to analyze the Cr^{2+} ion in molten chloride [131] and Ni^{2+} in molten FLiNaK [132] provide benchmark XANES spectra for what can be expected from in-situ analysis of Cr or Ni-bearing alloys corroding in molten halides.

3.5 Literature review: Corrosion Studies of Commercially Available Alloys & CCAs in Molten Salt

Commercially available Fe-based alloys and Ni-based alloys have been extensively investigated for their corrosion performance in molten halides. This research goes as far back as the 1950s [24]. The interest has only accelerated in the last 20 years. This provides a wide base of benchmark metrics and qualitative understanding for the corrosion performance of molten salts the state-of-the-art in commercial alloys, to direct the research and development in advanced structural alloys. Corrosion rate of Hastelloy N and Incoloy 800HT have shown lower corrosion rates than Inconels 600, 617, 625 and Incoloy 800 (compositions provided in Table 7) via potentiodynamic polarization [117]

Table 6: Weight % compositions of "conventional" Fe-based alloys, in decreasing order of Fe content

Material	Fe	C	Mn	Si	Cr	Ni	Mo	Nb	Ta	Ref
T91	**90.06**	**0.105**	**0**	**0.43**	**8.26**	**0.13**	**0.74**	**0.075**	**0**	[31]
SS 347	**67.096**	**0.08**	**2**	**1**	**18**	**11**	**0**	**0.8**	**0.024**	
SS 304	**65.92**	**0.08**	**2**	**1**	**20**	**11**	**0**	**0**	**0**	
SS 316L	**65.638**	**0.002**	**1.8**	**0.46**	**17.5**	**12.3**	**2.3**	**0**	**0**	
SS 310	**50.75**	**0.25**	**2**	**1.5**	**25**	**20.5**	**0**	**0**	**0**	

Table 7 : Weight % compositions of Ni-based considered as candidates for MSR applications, in decreasing order of Ni content.

Material	Fe	C	Mn	Si	Cr	Ni	Mo	Al	W	Nb	Ti	Co	Ta	Ref
Nimonic 80A	**0.12**	**0**	**0.23**	**<0.01**	**19.0**	**76.60**	**<0.01**	**1.42**	**<0.01**	**<0.05**	**2.44**	**0.024**	**0**	[133]
Alloy 600	**6**	**0.15**	**1**	**0.5**	**17**	**75.35**	**0**	**0**	**0**	**0**	**0**	**0**	**0**	[31]
Hastelloy N	**6**	**0.8**	**0**	**0**	**8**	**68.2**	**17**	**0**	**0.1**	**0**	**0**	**0**	**0**	
Hastelloy B3	**1.5**	**0.01**	**3**	**0.1**	**1.5**	**65**	**28.5**	**0.5**	**3**	**0**	**0**	**3**	**0**	[134]
Haynes 242	**2**	**0.03**	**0.8**	**0**	**8**	**65**	**25**	**0.5**	**0**	**0**	**0**	**2.5**	**0**	
Haynes-230	**1.8**	**0.1**	**0.5**	**0**	**22.5**	**59**	**1.2**	**0.3**	**14.1**	**0**	**0**	**0.3**	**0**	[135]

Haynes-263	**0.6**	**0.05**	**0**	**0**	**20**	**52**	**6**	**0.6**	**0.6**	**0**	**0**	**2.5**	**0**	[134]
Inconel 625	**5**	**0**	**0**	**0**	**21.5**	**58**	**9**	**0.46**	**0**	**0**	**0**	**0**	**3.55**	[119]
Hastelloy C-276	**3**	**0.01**	**1**	**0.08**	**16**	**57**	**16**	**0**	**4**	**0**	**0**	**1**	**0**	[118]
Alloy 690	**11**	**0.05**	**0.5**	**0.5**	**31**	**56.95**	**0**	**0**	**0**	**0**	**0**	**0**	**0**	[31]
Hastelloy C-22	**5**	**0.01**	**0.5**	**0.08**	**22**	**56**	**13**	**0**	**3**	**0**	**0**	**2.5**	**0**	
Inconel 718	**11.47**	**0.08**	**0.35**	**0.35**	**21**	**55**	**3.3**	**0.8**	**0**	**5.5**	**1.15**	**1**	**0**	
Inconel 617	**1.1**	**0.1**	**0.1**	**0**	**22.1**	**52.9**	**9.6**	**1.1**	**0**	**0**	**0.4**	**12.4**	**0**	[135]
Hastelloy X	**19.3**	**0.1**	**0.5**	**0**	**21.3**	**47.5**	**8.8**	**0**	**0.4**	**0**	**0**	**1.4**	**0**	
Incoloy 800H	**41.3**	**0.1**	**0**	**0**	**23**	**35**	**0**	**0**	**0**	**0**	**0.6**	**0**	**0**	[31]

The next two subsections summarize findings from a survey of literature on the current frontier of knowledge on the corrosion performance of candidate alloys, first by the conventional method of gravimetry that measures the total ions lost to solution during corrosion over a fixed corrosion period, and second by electrochemical techniques to determine an alloy's nobility and the kinetics of the surface reaction. The body of literature consistently finds that the greater the alloy content of (Ni + Mo + W), especially over 70%, the more corrosion-resistant the alloy is in molten halides. Conversely, a consistent finding is that Cr is the primary corrosion product corroded from the alloy into molten halides. These findings suggest that designing an optimally corrosion-resistant alloy would involve maximizing (Ni + Mo + W) content and minimizing Cr content.

Measurements of corrosion performance of commercially-available Fe-based and Ni-based alloys in molten salts by gravimetry

A large volume of literature in the field comparing the corrosion performance of commercially-available Fe-based and Ni-based alloys' corrosion performance in chlorides and fluorides by gravimetry generally point to Hastelloy-N being most suitable among them for MSR applications. A selection of representative data from the literature is summarized in Table 8 and Table 9.

Table 8 summarizes the corrosion performance of commercially available Fe-based alloys in molten fluorides, chlorides and HITEC. The thickness loss rate is at best 10 μm/yr for SS 316L in FLiBe, and at worst 7.5 mm/yr for SS 347 in chloride.

Table 8: A summary of studies on corrosion performance of commercially available Fe-based alloys in descending order of Fe content, in molten salt systems of interest.

Material	Thickness loss rate (mm/yr)	condition	ref
SS 347	7.49 ± 0.32	NaCl-LiCl, 650 °C	[119]
	0.12	HITEC at 538 °C	[136]
316L	0.01	FLiBe, 700 °C	[89]
	0.015	FLIBe, 650 °C	[137]
	2	LiF-LiCl-LiBr, 530 °C	[137]
	0.34	HITEC 570 °C	[136]
SS 310	6.427 ± 0.40	NaCl-LiCl, 650 °C	[119]
	0.36	HITEC 570 °C	[136]

Table 9 summarizes the corrosion performance of commercially available Ni-based alloys, generally showing that thickness loss in Ni-based alloys is far less than in Fe-based alloys. However, there is a notable zone of Cr depletion in the subsurface region of alloys with Cr as a constituent. This is expected, considering the thermodynamic favorability of chromium fluoride formation as shown in the Ellingham Diagram (Figure 3).

Table 9: A summary of studies on corrosion performance of commercially available Ni-based alloys of interest in descending order of Ni content, in molten salt systems of interest.

Material	Thickness loss rate (mm/yr)	condition	ref
Hastelloy N	negligible, with Cr depletion ingress of 0.020 mm/yr*	FLiBe, 700 °C	[89]
	negligible, with Cr depletion ingress of 0.050 mm/yr*	FLiNaK, 850 °C	[135]
IN 625	2.80 ± 0.38	NaCl-LiCl, 650 °C	[119]
IN 800H	5.947 ± 0.33	NaCl-LiCl, 650 °C	[119]
Haynes-230	Negligible	FLiNaK, 850 °C	[135]
Inconel 600	0.2	FLiBe, 650 °C	[138]
Inconel 617	negligible, with Cr depletion ingress of 0.100 mm/yr*	FLiNaK, 850 °C	[135]
Hastelloy C-276	0.01	NaCl–KCl–ZnCl2 , 500°C	[118]
Hastelloy C-22	0.03		
Hastelloy X	negligible, with grain boundary attack primarily associated with Cr depletion ingress of 0.300 mm/yr*	FLiNaK, 850 °C	[135]

* - extrapolated

It is the general consensus that Fe-based alloys suffer rapid elemental dissolution in molten fluorides that disqualifies them for MSR applications, an expected conclusion given the comparatively high thermodynamic stability of Fe fluorides in fluoride media according to the Ellingham Diagram (Figure 3). It is also generally understood that the presence of Ni and Mo in the Hastelloy N impart

corrosion resistance to it by 1) the low thermodynamic stability of their fluorides in fluoride media and 2) forming diffusion barriers within the alloy that prevent more active elements such as Fe and Cr from diffusing to the surface; such diffusion barriers form in Ni-Fe alloys where the surface concentration of Fe depletes and Ni becomes relatively enriched at the surface [89], [135].

Thickness loss rate must be reported with microstructural analysis to give a comprehensive understanding of the corrosion incurred by an alloy exposed to molten salt because intergranular corrosion can cause premature failures even at low weight loss values [8] by mechanisms such as accelerated stress corrosion cracking at the grain boundaries[93], [94]. In terms of microstructural changes incurred by alloys upon corrosion by FLiNaK at 850 ^{o}C,. Hastelloy X, Inconel 617, Haynes 230 and Incoloy 800H show significant Cr depletion at depths of ~100 μm throughout the grains but more severely at the grain boundaries. It is expected that these four alloys would suffer more significant Cr mass transport (dissolution and solid-state diffusion) than Hastelloy N because they contain ~20% Cr content, which is 2.5x higher than the 8% Cr content in Hastelloy N. The significant Cr mass transport was also seen with 60-75%Ni, ~20% Cr alloys in FLiNaK at 580 ^{o}C [133].

These recent detailed studies into the corrosion resistance of Hastelloy N in molten fluorides are consistent with the finding from the MSRE which deemed Hastelloy N to be adequate over the duration of the experiment [29], although post-decommission examination revealed significant surface cracking [139], suggesting that there is room for improvement in performance in terms of irradiation-induced embrittlement.

In general, fluoride salts are more corrosive than chloride salts [140]. To compare the corrosion performances of these commercially available alloys in fluoride to their performance in chloride [140], [141], Hastelloy-N, Hastelloy-X, Haynes-230, and Inconel-617 and Incoloy-800H in KCl-$MgCl_2$ at 850^{o}C had less intergranular void formation [140], [142], less surface pitting, less intergranular attack, less Cr depletion and shallower Cr depletion depth in chlorides than in fluorides. As with fluorides, Cr

depletion by corrosion in chlorides increases with increasing Cr content in the alloy [143].

The top performers in corrosion resistance according to the data summarized in Table 9 in decreasing order, Hastelloy N, Inconel 617 and Hastelloy X, are also in order of decreasing (Ni + Mo + W) content. This observation is expected from the thermodynamic perspective since these three elements form the least stable fluorides (Figure 3). Hastelloy N has much less Cr content at 8% than does Inconel 617 and Hastelloy X at ~22%, therefore the elevated activity of Cr in the latter two alloys can account for the fact that they suffer higher depletion depths of Cr than Hastelloy N after the corrosion period.

However, there are three major challenges with gravimetry: first, it is difficult to determine from gravimetric measurements alone whether an alloy's corrosion resistance is due to the thermodynamic properties of its elements, or whether it is due to surface reaction kinetics of the alloy constituents. Second, the corrosion period required to perform gravimetric measurements is constrained by the need to have sufficient mass loss to obtain precise measurements which means instantaneous corrosion rates at short time intervals cannot be measured by this method. Third, gravimetry is an ex-situ technique, requiring down-time to transfer the sample from the experiment apparatus to the measurement apparatus.

High-temperature potentiodynamic polarization of the alloy samples in molten salt is an in-situ electrochemical technique that is able to indicate the nobility of the alloy to corrosion by measuring the corrosion potential E_{corr} [V] and the overall kinetics of corrosion of the alloy by measuring the corrosion current density i_{corr} [A/cm^2]. High-temperature cyclic voltammetry in molten salt is an in-situ electrochemical technique that allows us to measure the dissolved concentration in the molten salt of elements corroded from the alloy, facilitating a time-resolved study of elements as they corrode from the alloy into the molten salt over the corrosion period.

The following section summarizes the state-of-the-art in polarization and cyclic voltammetry to study corrosion of alloys in molten salts.

An effort was made to summarize as best as possible the broad trends observed over the large body of literature investigating corrosion performance of molten salts in Table 8, Table 9. One quickly finds that the corpus of literature is very unstandardized [144]with studies on an average of 3-4 alloys being performed in various different salt mixtures (common anions are fluorides, chlorides, nitrates, carbonates, sulfates; common cations are Li, Na, K, Be, Mg), temperature conditions, presence of inert cover gas. Furthermore, the literature do not all use the same techniques for chemically quantifying corrosion products. Several commonly used analytical techniques for chemically quantifying corrosion products are detailed in the section on Analytical Techniques for Quantifying Corrosion Products. In addition, the majority of the content each of these corrosion investigation studies is a *qualitative* analysis of the corrosion modalities, often through microscopy images (with Scanning Electron Microscopy, SEM, or Transmission Electron Microscopy, TEM) coupled to elemental distribution maps from Electron Dispersive X-Ray Spectroscopy (EDS).

All these factors make it quite impossible to understand large-scale trends in corrosion behavior of alloys as a function of composition simply from collating and comparing all the data in the body of literature. The literature collated in Table 8, Table 9 are static corrosion studies in molten halides at 500-800 ^{o}C, they were selected for their quantitative corrosion analysis to highlight macro-trends consistent throughout the entire body of literature.

The most obvious macro-trend observable from Table 8, Table 9 is that Ni-based alloys have 1 order of magnitude lower corrosion in mm/year compared to Fe-based alloys. This is expected because Ni is far more thermodynamically noble against halide formation than Fe is in molten halides. Another obvious macro-trend is that corrosion is generally higher in the same salt for the same alloy at higher temperatures. This is also expected from a thermodynamic perspective as the Ellingham diagram shows that the halide-forming side of the equilibrium is favored with increased temperature. The third most obvious macro-trend is that increasing more noble additives to the alloy composition at the expense

of the less-noble base element - in Table 11 W is increased at the expense of Ni - serves to decrease corrosion rate, as expected [117]–[119], [133]. Overall the body of literature generally tends to use thermodynamics to justify most of the quantitative corrosion data.

However thermodynamics does not explain everything. Table 10 shows that Hastelloy C-22 was observed to exceed Hastelloy N in corrosion performance because while they both have (Mo+W) ~16-17%, Hastelloy C-22 contains a larger proportion of the less noble element W at 3% than Hastelloy-N at 0.1%. Nevertheless, the reason behind the superior corrosion performance of Hastelloy C-22 over Hastelloy-N can be explained from the kinetics standpoint, as it was noted by [115] that the surface reaction kinetics of Mo are 3x faster than W. From this comparison we can see that either thermodynamics (Hastelloy C-276) or kinetics (Hastelloy C-22) can be just as much responsible for the thickness loss rate in [mm/yr] observed by gravimetry

Table 10: Comparison of some Ni-based alloys in their corrosion performance in FLiNaK at 680^{o}C as determined by potentiodynamic polarization [133]

Alloy	**Salt**	**Condition**	**Icorr (μA/cm^2)**	**Ecorr (vs. ref)**	**Ref**
Nimonic 80A (< 1% Mo, W)	FLiNaK	680^{o}C	660	-0.278	[133]
Inconel 718 (3.3% Mo, 0% W)		680 ^{o}C	140	-0.303	
Hastelloy C-276 (16% Mo, 4% W)		680 ^{o}C	2.9	-0.206	

Table 11: Comparison of some Ni-based alloys in their corrosion performance in chloride salts at high temperatures as determined by potentiodynamic polarization.

Alloy	**Salt**	**Condition**	**Icorr (uA/cm^2)**	**Ecorr (vs. ref)**	**Corrosion Rate [mm/yr]**	**Ref**
HEA	Na_2SO_4- 45 NaCl (mol%)	700 °C	388	-1.34	3.85	[145]
Inconel 600			191	-1.03	3.1	
Inconel 718			150	-0.98	2.525	
SS 447	34% NaCl, 66% LiCl	650 °C	710	-0.85	7.5	[119]
SS 310			630	-0.9	6.4	
Incoloy 800H			570	-0.91	5.9	
Inconel 625			230	-0.86	2.8	
SS 310		700 °C	1200	-0.57	12	
Incoloy 800H			1400	-0.474	14	
Hastelloy C276 (16% Mo, 4% W)	NaCl–KCl–$ZnCl_2$ halide	250 °C	1.4	-0.2	0.01	[118]
Hastelloy C-22 (17% Mo, 3% W)			2.0	-0.26	0.02	
Hastelloy N			4.4	-0.35	0.04	
Hastelloy C276 (16% Mo, 4% W)		500 °C	4.1	0.05	0.04	
Hastelloy C-22 (17% Mo, 3% W)			4.35	-0.14	0.04	
Hastelloy N			16.9	-0.2	0.15	

By contrast, corrosion behavior of CCAs in molten salts at high temperatures have not been as thoroughly investigated but this avenue of inquiry is promising. Refractory equimolar TaTiVWZr and HfTaTiVZr have been demonstrated by [146], [147] to be more corrosion resistant than their benchmark commercially available alloys Table 12. Conversely, some CCAs such as equiatomic AlCoCrFeNi [145], [147] is more easily corroded than their commercially available alloy benchmarks (Table 12).These results are consistent with an understanding of thermodynamic nobility-driven corrosion resistance. However, it has been demonstrated by [83] using $Fe_{27.5}Cr_{18}Mn_{27}Ni_{27.5}$ CCA - consisting of fairly corrodible elements from the thermodynamic perspective - that it formed Cr-precipitates that hindered the corrosion of Cr. Other studies have also noted complex interactions that either curtail or exacerbate corrosion [85], [117], [135].

This behavior opens the question of whether high-temperature precipitation is a mechanism which may be leveraged to design corrosion-resistant alloys for MSR conditions. The observation of the phenomenon also opens the question as to what alloy compositions and conditions are necessary for the optimization of this mechanism in such a way that it confers corrosion resistance on the alloy. Juxtaposing the elevated corrosion resistance of the near-equiatomic CCA of [83] with the depressed corrosion resistance of [145], [146], [148]'s equiatomic CCA serves to illustrate that being in the central region of the composition space is not enough to predict whether a CCA is more corrodible than commercially available alloys - corrosion resistance is dependent on many factors and it is a research goal of this thesis to find out what these factors are by systematic, parametric analysis.

We must qualify that this quick comparison of corrosion from the thermodynamic perspective between these different studies is not completely straightforward because the occurred in differing salt media, temperature and impurity conditions. The comparison was made simply to highlight the potential of CCAs to exhibit novel mechanisms that may confer corrosion protection. As mentioned in the earlier section the corpus of literature on corrosion of commercially available alloys in molten salts is

highly unstandardized [144] and this issue only compounds when we desire to compare novel CCAs' corrosion performance to what is known in the community.

Table 12 serves to illustrate that it is incredibly difficult to observe meaningful macro-trends by collating and comparing the existing corpus of literature on CCA corrosion performance in molten salts because:

A) inert atmosphere is necessary. Only the minority of studies summarized here used inert atmosphere [83], [148]. The rest did so in air. This is problematic because air introduces O^{2-} ions into the salt which tends to form a multitude of oxide corrosion products. For MSR applications, a large amount of dissolved O^{2-} cannot be tolerated by the flow system because these can form precipitates that clog lines which can lead to reactor failure modes (see supplemental material A). Therefore this already disqualifies many of the existing studies of CCAs in molten salts from a comparison of their validity as MSR structural alloys. The CCA needs to be corroded in an environment where the impact of O^{2-} is negligible or at least minimal.

B) on average, 1-2 CCAs are studied and compared to 1-2 commercially available alloys and a qualitative binary evaluation is made on which corroded more. This is not very useful to give an overall picture of macro-trends on the impact of perturbations to the CCA composition on its corrosion resistance in molten salt. As demonstrated in the previous section, the body of literature on commercial alloys corrosion performance in molten salt is itself not standardized, so there is not a single widely consistent basis for comparison of one CCA in isolation. Therefore there is a gap in the corpus of knowledge ready to be filled by a broad study with many samples distributed over the same composition space in the same corrosion conditions ie. a large standardized experimental dataset.

C) these studies are not standardized in total corrosion period with one another, therefore a comparison *between* different studies is made difficult by the need to consider whether the relevant studies were

performed in the linear-approximate region of corrosion rate or close to the plateau-region ie. Saturation region of corrosion.

D) material degradation modes beyond thermodynamics and kinetics are in general not systematically studied in these collated studies. An isolated study on pitting potential (E_{pit}) has been determined for a few CCAs in molten salts by [149] was done, but this is insufficient to draw macro trends about the susceptibility of CCAs to pitting corrosion.

There are also other physical parameters hypothesized to be predictors of corrosion resistance which have yet to be systematically studied, for example, elemental solid solution mobility, as hypothesized by Elbakhshwan et al [83]. In the preliminary studies for this project, low surface energy and high work function of an alloy were also hypothesized to be predictors of elevated corrosion resistance. Knowing the strongest predictor of corrosion resistance amongst an alloy's physical parameters is undoubtedly the most efficient way to optimize the corrosion resistance of an alloy designed. Therefore ***a primary goal*** *of this project's approach to designing corrosion-resistant alloys is to determine the primary predictor of corrosion resistance in an alloy.*

Table 12 A summary of corrosion performance of CCAs evaluated in MS.

Alloy	**Salt**	**Temp**	**Corrosion performance compared to commercially available alloys**	**Reference**
$AlCoCrFeNi_{2.1}$	NaCl-KCl-$MgCl_2$	450 °C and 650 °C	CCA exhibited lower corrosion than stainless steel 2205 (DS2205).	[147]
$Fe_{65.7}Ni_{11.7}Ti_1Mo_{6.6}Co_{15}$	NaCl and Na_2SO_4	650 °C	N/A	[150]
near-equimolar CrCoFeMnNi	in pure NaCl and Na_2SO_4+NaC	800 °C and 1000 ◦C	N/A	[81]
equimolar TaTiVWZr and HfTaTiVZr	33NaCl–22KCl–45$MgCl_2$ (wt. %) eutectic salt at	450 °C and 600 °C	corrosion rates for HEAs generally one order of magnitude lower than SS304 measured by potentiodynamic polarization	[148]
equimolar TaTiVWZr and HfTaTiVZr	FLINAK	650 °C	corrosion rates for CCAs one order of magnitude lower compared with Inconel 718 and SS316, measured by potentiodynamic polarization and EIS	[146]

Y, Hf-codoped AlxCoCrFeNi (Alx, x = 0.7, 1.0, and 1.3) high-entropy alloys (HEAs)	under Na_2SO_4 + 25 % NaCl molten salts at 900 ◦C	900 °C	N/A	[76]
equimolar CoCrFeMnNi	$NaNO_3$-KNO3	500 °C	higher passive current density compared with Inconel 718, 800H and SS316, measured by potentiodynamic polarization, attributed to the presence of Cr and Mn	[151]
$Fe_{27.5}Cr_{18}Mn_{27}Ni_{27.5}$	FLIBe	700 °C	more weight loss than SS316, due to high Mn content, but was surprising that not much Cr was lost	[83]
equiatomic AlCoCrFeNi (HEA), UNS N06600 and UNS N07718 in a	molten NaCl-Na_2SO_4 eutectic	700 °C	HEA was less noble and exhibited a higher corrosion rate than UNS N07718 and UNS N06600. Aluminum	[145]
Ni–16Mo–7Cr–4Fe superalloy	FLiNaK	850C	N/A	[152]

In order to observe meaningful macro-trends in CCA corrosion performance in molten salts that will inform corrosion-resistant CCA alloy design, a parametric study is necessary in a salt under standardized conditions.

The work of Wang et al [153] an example of a small-scale parametric study in the effects of Cr content on the corrosion performance of an Ni-Cr (Table 13). Their results show generally that alloy corrosion kinetics, indicated by i_{corr}, increase with Cr content, and alloy nobility, indicated by E_{corr}, decrease with increasing Cr content. This finding is consistent with the body of literature on commercial alloys, which observe that when two alloy components are considered, the higher the content of the less noble element the less noble the alloy will be to corrosion. Parametric studies such as this one by Wang et al [153] are informative, but unfortunately are exceedingly rare in the body of literature, perhaps hindered by the laborious and time-consuming process of producing novel alloys for corrosion-testing. This thesis will demonstrate a parametric study expanded from 2 into 4-element composition space with the use of additive manufacturing techniques to overcome the obstacle of long downtimes for alloy fabrication in order to perform parametric corrosion studies.

Table 13:Summary of parametric polarization studies on binary Ni-Cr in various compositions [153]

Alloy	**Salt**	**Condition**	**Icorr ($\mu A/cm^2$)**	**Ecorr (vs. ref)**	**Ref**
Ni	FLINAK	700	19	-0.77	[153]
Ni 5-Cr (binary)			89	-0.155	
Ni-10Cr (binary)			115	-0.175	
Ni-15Cr (binary)			245	-0.287	
Cr			494	-0.507	

3.5.1 Project Goal & Approach

This thesis presents a platform that couples high-throughput parametric alloy testing coupled to machine learning to narrow the search space of interest in such a way as to simultaneously address the 4 major technological advancement needs highlighted by [154].

1) “the biggest challenge in the field of exploring the enormous number of HEA and CCA compositions and their microstructures” - in this project 110 alloys are printed, heat treated, polished and corrosion tested in 3 weeks’ worth of man-hours. As part of the project they are microstructurally characterized.

2) “New high throughput experiments are needed, especially for structural materials.” - a process for testing 25 alloys simultaneously each in mutually isolated environments in a footprint of 10cm x 10cm is presented

3) “new strategies are needed to quickly navigate the winding, narrow path between properties that depend on composition, and those that depend sensitively on both composition and exquisitely designed microstructures” - each alloy is featurized by kinetic, thermodynamic and microstructural properties to train a machine learning model. This thesis will demonstrate the ML model can be interpreted to glean physical meaning so that the winding path to understanding physical mechanisms of CCA properties can be straightened out.

4) “Acquiring new fundamental data is also essential because the current lack of data for new physical models and new predictive capabilities in CCAs is a barrier to future scientific progress and collecting this data is expected to lead to new scientific discoveries.” - these studies were designed to be parametric to facilitate acquiring new fundamental data.

The investigation of the viability of CCAs as MSR structural materials will take a parametric approach, so the scope was bounded to a quaternary alloy space. Based on the experience from

the INOR series, prime elements considered for the parametric study would be Fe, Cr, Ni and Mo - it is expected that the quaternary space of CrFeMoNi would be the intuitive domain to search for halide-corrosion resistant alloys. However Mo presents the disadvantages of being a refractory metal which is difficult to process metallurgically in concert with the other alloying elements Fe, Cr and Ni. Mo is also expensive. A limited set of ~25 CCAs in the CrFeMoNi space were printed for feasibility testing and it was found that tuning parameters were difficult to scale up for a large number of compositions. It was concluded that a study in which, say 100 Mo-containing alloys were processed and corrosion-tested would be beyond the financial and time resources bounding this project.

Mn was chosen to replace Mo in the composition space for its potential to contribute high temperature hardness, despite the thermodynamic favorability of Mn to form stable halides.

It was mentioned in the preceding section that even a crack not a few microns in length in a nuclear reactor structural material has the potential to have a multitude of catastrophic implications which could result in millions of dollars in damage and loss of life. Therefore it is of paramount importance to develop structural alloys with sufficient degradation resistance under the conditions of the nuclear reactor operating environment.

Table 14 summarizes some properties justifying the inclusion of the elements in the search (advantages) and some properties that are disadvantages to its inclusion. This space has been explored in the last 10 years, with studies generally focusing on comparing single CCA compositions to commercially-available alloys.

Table 14: Summary of advantages and disadvantages of some elements of interest to the development of structural materials for MSR.

Element	Advantages	Disadvantages
Fe	inexpensive	forms stable halide that is soluble in molten salt
Cr	imparts corrosion-resistance in air by formation of passivating oxide on the surface	forms stable halide that is soluble in molten salt
Mn	imparts high-temperature hardness to the alloy	forms stable halide that is soluble in molten salt
Ni	noble against corrosion by halides, imparts high-temperature strength to the alloy	expensive, susceptible to irradiation-induced embrittlement
Mo	noble against corrosion by halides, high temperature hardness, solid solution strengthening	expensive, refractory metal
W	noble against corrosion by halides, high temperature hardness	expensive, refractory metal

With this conventional intuition that corrosion kinetics and thermodynamics can be superficially predicted using composition as demonstrated by the binary parametric studies of Wang et al [153] it is desired to expand the parametric search to a quaternary elemental space (CrFeMnNii) in search of corrosion-resistant compositions.

3.6 Accelerating the search through Compositionally Complex Alloys in Molten Salts

3.6.1 Literature Review: Accelerated Electrochemical methods to study corrosion phenomena in molten salts

This section comprises content from the following journal articles co-authored by the PhD candidate,

Y Wang, B Goh, M Moorehead, J Hattrick-Simpers, A Couet, **High-Throughput Electrochemistry to Study Materials Degradation in Extreme Environments**, Anal Chem, (2022), 94, 48, 16528-16537

Abstract

Electrochemistry has been used for decades to study materials' degradation in-situ in corrosive environments, whether it is in room temperature chemically aggressive solutions containing halide ions or in high-temperature oxidizing media such as pressurized water, liquid metals, or molten salts. Thus, following the recent surge in high-throughput techniques in materials science, it seems quite natural that high-throughput electrochemistry is being considered to study materials' degradation in extreme environment, with the objective to reduce corrosion resistant alloy development time by orders of magnitude and identify complex degradation mechanisms. However, while there has been considerable interest in the development of high-throughput methods for accelerating the discovery of corrosion resistant materials in different environments, these extreme environments propose formidable and exciting challenges for high-throughput electrochemical instrumentation, characterization, and data analysis. It is the objective of this paper to highlight those challenges, to present relatively new efforts to tackle them, and to develop research perspectives on the future of this exciting field. This perspective paper is articulated around four main inter-connected topics, which must be conjointly considered to enable corrosion resistant alloys design using high-throughput

electrochemical methods: (1) high-throughput processing methods to develop material libraries, (2) high-throughput electrochemical methods for corrosion testing and evaluation, (3) high-throughput machine-learning augmented electrochemical data analysis and (4) high-throughput autonomous electrochemistry representing the future of accelerated electrochemistry research.

1. Introduction and motivation

The term, "high-throughput," (HTP) is inherently a relative and contemporary term much like "high-speed" or "advanced" in that it compares the throughput of a proposed process to a current standard. What is considered HTP today may not be tomorrow. However, in addition to the comparative function, the term also connotes parallelization, automation, and often major gains in speed and efficiency, potentially at the cost of fidelity or completeness. HTP methodologies also tend to embody the Pareto principle, whereby 80 % of the problem can be solved with 20% of the total required effort while the remaining 20% of the problem will consume 80% of the total required effort. As such, HTP methodologies are best suited for screening applications where a large array of samples can be quickly examined to determine macroscopic trends and be able to make informed down-selections before more labor-intensive and time-consuming techniques are applied. The prototypical example of the HTP methodology in action is the high-throughput screening (HTS) technique developed by the pharmaceutical industry to search for potentially effective drug candidates. Beginning in the 1980s, automated screening techniques were developed using 96-well plates, each containing a mixture of human cells and unique chemical compound to test the interactions between them.[155] Initial HTS techniques were limited to less than 10,000 test a day, were prone to robotics/automation reliability issues, and their output datasets still required substantial human involvement to process. Shortly after the turn of the century, the HTS process had become fully automated, was able to screen millions of compounds with little to no human oversight, to produce dozens of leads, and to bring multiple drugs to market.[156] As such, it became a fully industrialized process. Automated research will always remain imperfect, but the many orders of magnitude increase in speed and efficiency is generally seen to outweigh the marginal gains in accuracy or reductions in false positives/negatives afforded by more meticulous testing performed by humans – who are also imperfect.

The success of the HTP methodology championed by the pharmaceutical industry has caught the attention of other industries and communities who also wish to accelerate their processing and screening techniques, including the

electrochemistry community. Indeed, and as will be discussed later, electrochemical techniques are now quite mature and standardized such that HTP instrumentation and electrochemical data analysis are relatively trivial. For instance, HTP electrochemistry is now used for HTP materials synthesis (i.e. electrosynthesis) to develop combinatorial arrays of materials[157]. As will be detailed later, there has also been an increased interest in HTP materials' characterization using electrochemical methods. Indeed, HTP characterization techniques can significantly decrease the material design and optimization timeline (see for instance the Materials Genome Initiative)[158]. Thus, as highlighted in the rest of this study, HTP electrochemical processing and characterization methods have the potential to significantly shorten the materials design timeline, as well as improving our understanding of complex degradation mechanisms.

Electrochemistry has been used for decades to study materials' degradation in-situ in corrosive environments, whether it is in room temperature chemically aggressive solutions containing halide ions or in high-temperature oxidizing media such as pressurized water, liquid metals, or molten salts. Thus, following the recent surge in HTP techniques in materials science, it seems quite natural that HTP electrochemistry is being considered to study materials' degradation in extreme environment, with the objective to reduce corrosion resistant alloy development time by orders of magnitude. However, while there has been considerable interest in the development of HTP methods for accelerating the discovery of corrosion resistant materials in different environments, these extreme environments propose formidable and exciting challenges for HTP electrochemical instrumentation, characterization, and data analysis. It is the objective of this paper to highlight those challenges, to present relatively new efforts to tackle them, and to develop research perspectives on the future of this exciting field. The rest of the paper will be articulated around four main inter-connected topics, which must be conjointly considered to enable corrosion resistant alloys design using HTP electrochemical methods: (1) HTP processing methods to develop material libraries, (2) HTP electrochemical methods for corrosion testing and evaluation, (3) HTP electrochemical data analysis and (4) HTP autonomous electrochemistry.

2. High-Throughput Alloy Processing Methods

In extreme environments, such as gas turbines or liquid metal and molten salt cooled systems, structural materials are primarily concerned by corrosion issues. Thus, HTP methods for metal alloy synthesis will be mainly discussed in this section. HTP electrochemical techniques are closely correlated to HTP alloy processing, since the latter

inherently sets boundary conditions on the shape and morphologies of the alloys to be studied using the former. To date, HTP alloy synthesis techniques have mostly relied on producing compositional gradients, such that a wide range of alloy compositions can be processed rapidly. Among those, diffusion multiples are likely the most used.[159], [160] This technique uses an assembly of three or more different metal blocks in interfacial contact and subjects this system to relatively high temperature in an inert atmosphere to allow for thermal interdiffusion, which results in solute gradients and intermetallic compounds nucleation and growth. Diffusion multiples originates from the traditional diffusion couples and diffusion triples.[161] As an example, Figure 14(a) shows a diffusion multiple schematics of five different metal elements A, B, C, D, and E. The diffusion multiple was made of a base metal disk, E, with a slot cut in the center for the placement of another 4 different metal foils which are arranged in a bricklaying geometry. The arrangement allows for the formation of different diffusion couples, triples, and quadruples. Through exposing the diffusion multiple to high temperature, the thermal interdiffusion occurs and a wide range of solute gradients and intermetallic compositions consisting of elements A, B, C, D, and E can be created. While scanning micropipette contact methods by electrochemical techniques can be utilized to study the corrosion behaviors of different compositions in diffusion multiples[162], the composition and microstructure dictated by thermodynamics and kinetics processes are out of control, and the surface is often in metastable conditions. Consequently, this technique is of limited use in HTP corrosion studies, especially for high-temperature applications. Combinatorial gradients can also be obtained with thin film deposition from multiple magnetron sputter sources as shown in Figure 14(b).[163], [164] The co-sputtering from different sputter sources on a wafer substrate creates a two-dimensional gradient in the compositional ratio of alloy system of interest. This technique has the advantage of allowing a very precise compositional control across the wafer. However, the microstructure is often composed of nano-grains, which is not quite representative of structural materials, and can have significant repercussions on the electrochemical response.[165] In addition, the films are usually a couple micrometers thick at most, which make them very susceptible to internal stresses (such as the ones induced by oxide volume expansion, or differential thermal expansion) and spallation. Additive manufacturing is another promising HTP method to generate compositional gradients. For instance, by employing laser engineered net shaping (LENS) approach[166], premixed powder blends can be directed into the focal point of a laser beam with the help of a carrier gas. The laser focal point is located at the build surface, and a compositional gradient can be obtained by varying the powder feeding rates, as shown in Figure 14(c). This

HTP synthesis technique has led to significant decrease in the time necessary to explore various alloy systems. However, like the diffusion multiples, a single composition of interest typically only exists in a vanishingly thin 1D line or 2D plane, limiting the capability to characterize the electrochemical response as function of well controlled composition/microstructure features. At the same time, the utility of the produced material for high temperatures has been limited because of the element diffusion resulting from the thermodynamically unstable phases of the chemically graded structures. To solve those challenges, the LENS system has been recently used to print multiple arrays of compositionally homogenous bulk alloys by in-situ alloying as shown in Figure 14(d).[167], [168] In this approach, the ratios of elemental powders can be varied from one alloy build to another by controlling the RPM of the augers on each powder hopper containing elemental or pre-mixed powders. This technique is particularly attractive since it produces homogeneous alloys across length scales conducive to the use of HTP electrochemical techniques, such as a scanning droplet cell. In addition, the processing time is orders of magnitude faster than traditional approaches such as rapid alloy prototyping using arc-melting[169]. Finally, any heterogeneities in the build, such as un-melted powders, can be removed using surface laser re-glazing, without the powder flowing, between each path. Rapid cooling rate associated with metal printing creates dendritic microstructures, quite different from typical microstructure used in structural materials. Heat treatment at high temperature in inert atmosphere can be performed to remove the dendritic compositional segregation and possible residual stresses to obtain a thermodynamically stable alloy surface suitable for further HTP electrochemical characterization. On the other hand, another challenge exists in alloy additive manufacturing with the formation of pores during the printing process because of keyholes or entrapped gas. It is well known that surface defects, such as pores, are often preferred sites for significant electrochemical reactivity resulting in well-known phenomena such as pitting. It is quite challenging to eliminate pores in printed parts by post processing and further efforts are needed in the future to unveil the dynamics and mechanisms of pore evolution and elimination. For instance, the use of in-situ diagnosis, such as synchrotron X-Ray imaging, are promising techniques to understand the parameters of importance in pore formation during printing.[168]

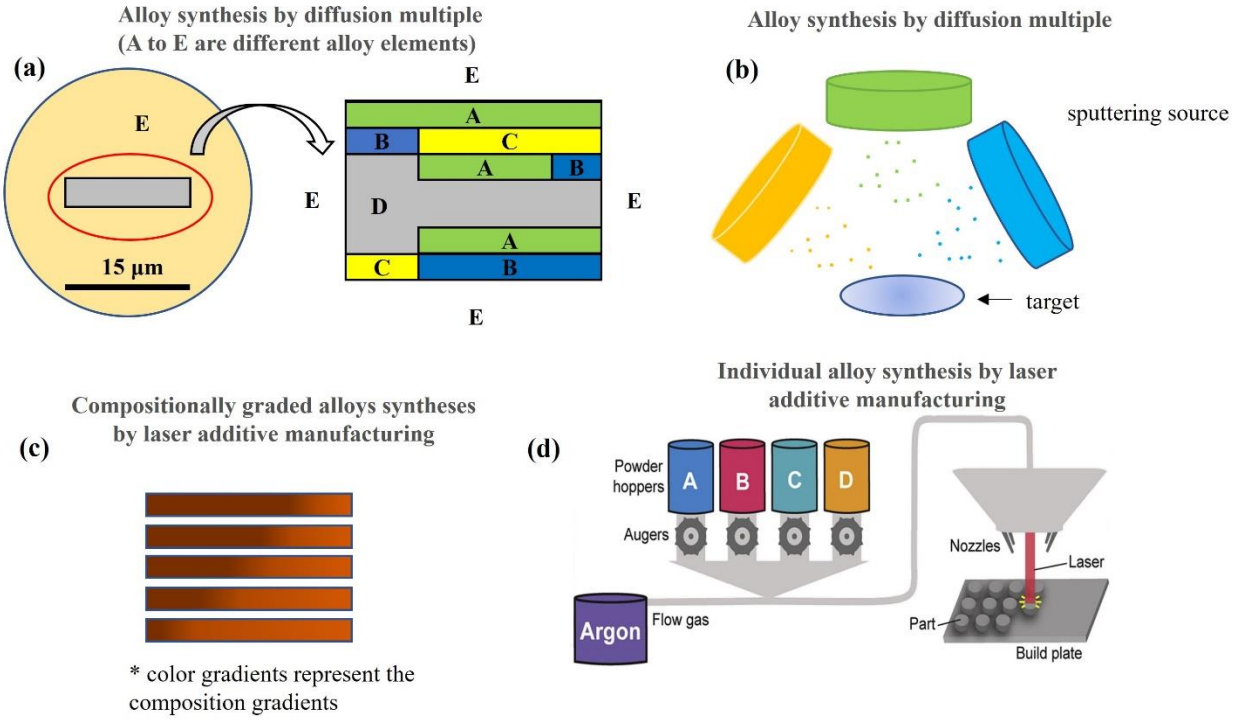

Figure 14. Schematic of different high throughput alloy synthesis technologies. (a) Diffusion multiple synthesis technique[159], *(b) thin film deposition technique*[163], *(c) compositional gradient alloy produced by LENS*[166], *and (d) in-situ alloying of bulk alloys by LENS*[167].

3. Hight-Throughput Electrochemical Methods for Corrosion Testing and Evaluation

Using the above HTP synthesis techniques, it is possible to study the corrosion of a large array of samples, enabling the use of electrochemistry in HTP alloy design, with large multi-dimensional features space. However, HTP corrosion testing, and monitoring can be somewhat challenging too. For instance, all the systems developed via the HTP synthesis techniques detailed above will suffer from galvanic corrosion if immersed in the same conductive electrolyte. In addition, if the system is only homogeneous and stable across small length scale (such as in the case of compositional gradients), monitoring the corrosion process in-situ requires local techniques, such that micro-electrochemical probe development is necessary.[170] On the other hand, one could also study the effect of electrolyte composition on alloy corrosion, but this requires the manufacturing of many independent corrosion cells and a proper sampling of electrolyte composition to vary redox potential, basicity, impurity content, etc. Thus, we will use “HTP”

to identify any methods that are significantly increasing the throughput relative to conventional approaches, where a single alloy is studied in a single electrolyte.

HTS can be designed through reducing the time per experiment or increasing the number of experiments per unit time, or both. In addition, one can either use the HTP approach to sample different electrolytes or to sample different alloy compositions, or both. As a first approach, rapid corrosion testing can be performed without any in-situ monitoring. For instance, Gateman et al utilized the scanning micropipette contact method, an electrochemical technique using a micropipette working electrode, to study the corrosion behaviors of different compositions in diffusion multiples.[162] As a tentative corrosion examination on compositionally homogenous bulk alloys, Muster et al incorporated nine pairs of different metallic wires of interest into a single multi-electrode assembly and immersed it into different inhibitor solutions, through which the corrosion resistances of the nine different metallic wires were evaluated by potentiodynamic scans simultaneously.[171] However, cross-contamination of the electrodes is likely during the electrochemical measurements. To solve this issue, HTP corrosion study of aluminum alloy exposed to multiple aqueous electrolytes was achieved based on the HTP corrosion test design (Figure 15(a)) by White et al.[172] Chambers et al designed a similar system (Figure 15(c)), consisting of 96 aluminum alloy 2024-T3 wires suspended into one of the reaction frame wells containing different electrolytes.[173] The corrosion of each cell can be evaluated independently using electrochemical techniques, such as potentiodynamic polarization scan and open circuit potential (OCP). Of course, in-situ corrosion monitoring can also be achieved through measuring the concentration of dissolved corrosion products by performing electrochemical tests such as cyclic voltammetry (CV) at different corrosion time. Relatively recently, Azmat et al. performed HTP corrosion study on zinc through depositing aqueous droplets of various chemistries and sizes on top of the sample.[174] In their design, a mini three-electrode (working, counter, and reference electrodes) assembly can be inserted into the salt droplet for the HTP in-situ corrosion monitoring through the quantification of dissolved corrosion products using electrochemical techniques. A more advanced design was reported by Joress et al by using a scanning droplet cell (SDC) as shown in Figure 15(d).[175] In their design, the SDC comprises a peristaltic pump, a fluid reservoir, and a scan head. During the experiments, the pump pushes the electrolyte into an isolated volume between the cell and substrate. The fluid passes by a counter and reference electrodes when the fluid enters and exits this volume, while the sample itself serves as the working electrode. Combined with a computer numerical control (CNC) system, the designed SDC can achieve HTP

in-situ corrosion monitoring. In addition to HTP approach to sample different electrolytes, or to sample different alloy compositions, HTP corrosion study on redox potentials were also recently performed. For instance, bipolar electrochemistry was selected for HTP corrosion testing, in which the corrosion behavior of one alloy was examined through a wide potential range in a single experiment.[176], [177]

HTP corrosion studies at high temperature in extreme environments are quite challenging. Wang et al.[178] followed the SDC approach and pelletized small LiCl-KCl-2wt% $EuCl_3$ salt pills. HTP corrosion testing was performed on a broad range of additively manufactured bulk alloys (using the LENS technique above) by melting salt pills into molten salt droplets on top of each printed alloy at 500 ℃ as shown in Figure 15(b), in an inert glovebox to prevent any salt contamination. The molten pill in contact with the bulk alloy surface creates a mini-corrosion cell and many of those cells can be studied simultaneously, without the risk of galvanic corrosion or mass transport induced by dissimilar materials. To the authors' knowledge, this is the first time that corrosion of bulk alloys in high-temperature electrolytes is achieved through HTS. A series of automated material characterization techniques were utilized in their study such as glow-discharge optical emission spectroscopy (GDOES) to study the depletion depth of the post-corroded alloys and inductively coupled plasma mass spectrometry (ICP-MS) to analyze the concentrations of dissolved corrosion products in the post-corrosion molten salt solutions. Another strategy for HTS in high-temperature molten salts proposed by Hoyt et al uses small crucibles manufactured from the alloys of interests and perform automated electrochemical techniques such as cyclic voltammetry to in-situ monitor the dissolved corrosion products.[179] Another possibility is using a micro-electrochemical probe suspended into the molten salt droplet placed on top of each alloy as designed in the ex-situ corrosion experiments shown in Figure 15(d).[180] This type of automated SDC techniques are seen as a very promising tool for electrochemical HTS of alloys for applications in extreme environments.

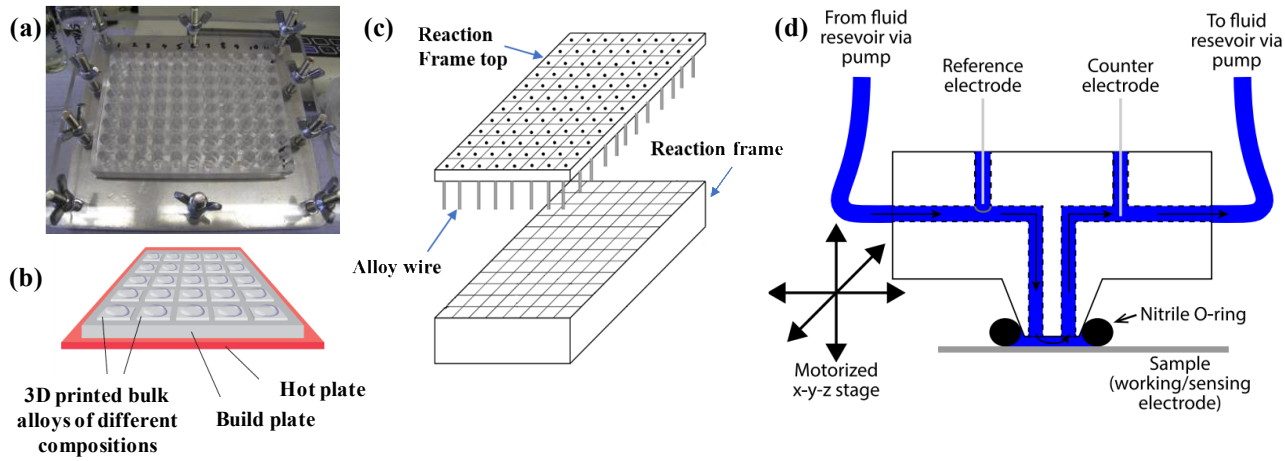

Figure 15. Schematic of different high throughput corrosion testing: a) HTP corrosion study of aluminum alloy exposed to multiple aqueous electrolytes, b) additively manufactured bulk alloys to perform HTP high-temperature corrosion testing, c) 96 aluminum alloy 2024-T3 wires suspended into one of the reaction frame wells containing different electrolytes, and d) scanning droplet cell design.

4. Successes and Opportunities in High-Throughput Corrosion Data Analysis

Motivation

It is understood that HTP methods enumerated in the previous section are the key to discovering high-performance alloys within a near-term time horizon. At the same time it is widely recognized that development of HTP experimentation and characterization gives rise to a bottleneck in the need to interpret/analyze large data sets on the order of hundreds [181]–[183]: given the scale of efforts in the collation and codification of materials databases, automation of experiments, and implementation of machine learning (ML) tools to accelerate detection of patterns in the processed data, efforts to automate the processing of raw data from HTP experiments, or even automating routine tasks of data interpretation are still sparse by comparison. Automating data reduction tasks frees the investigator to perform more high-level analysis tasks, and therefore the development of automated data reduction platforms in tandem with HTP experimentation is essential.

Successes

In the analysis of post-corrosion samples by Scanning Electron Microscopy (SEM) or Transmission

Electron Microscopy (TEM), computer vision has been demonstrated to quantify material porosity [184] with some success, as well as to identify and classify material defects [185]. Another major strategy for data reduction from SEM/TEM images is to use convolutional neural networks (CNN) to identify, classify and quantify such features [186]. In determining the phase-fractions of combinatorially-processed alloy samples by HTP X-Ray Diffraction, the implementation of CNN either on its own [187]–[192] or coupled to heuristic MATLAB scripts [193], [194] has proliferated in recent years. These serve to advance our understanding of the non-trivial problem of generating phase diagrams for novel materials generated by combinatorial methodologies. Compared to other ML algorithms, CNN were demonstrated to have the highest accuracy [195]. CNN have also been demonstrated to facilitate analysis [196]–[198] and even data reduction[199] from raw Electron BackScatter Diffraction (EBSD) data. To the end of storing and organizing large volumes of data generated by HTP methods[200], the National Institute of Standards Technology (NIST) has set up the Materials Resource Registry (MRR) to facilitate access to existing materials characterization data to end users [201], and the Materials Data Curation System (MDCS) to provide a customizable database indexing format for standardized organization of materials data of varied formats[202].

Challenges, Opportunities & Aspirational Perspectives

The attraction of ML methods is apparent: developing heuristic-based tools for data reduction often reveals some unspoken subjective liberties taken by the analyst, as will be highlighted in the next section of which ML methodologies tend to be far more forgiving. Indeed, the exercise of developing heuristic-based data reduction tools could ostensibly lead to deeper insights within the data. Regardless of whether data reduction is accelerated by ML-based or heuristic-based tools, the scale-up of data reduction processes is instrumental to HTP implementation capabilities to accelerate materials discovery. At the time of writing, there appears to be no published database for the collation of electrochemical (or other) data. This is likely due to the lack of standardized format for such a database but also the lack of standardized way of comparing pre-corrosion with post-corrosion changes to assess degradation performance. Despite the latter aspect being nontrivial, we recommend that the development of such a database include the following data of each alloy obtained from experiment to facilitate a comprehensive assessment of its degradation performance in extreme environments: pre/post-corrosion microstructure (phase fractions, texture, grain size, etc…) and microchemistry (surface composition, elemental depth profile in the substrate, etc…), oxide thickness and/or elemental dissolution, and information on thermodynamic/kinetic/of electrochemical reactions that can be gleaned

from electrochemical methods as discussed in greater detail in the following section. To combine data from various disparate characterization techniques to give a comprehensive representation of the degradation performance of a material, data reduction into a standardized, sparse format for storage, indexing and retrieval is essential.

5. Successes and Opportunities in High-Throughput Electrochemical Data Analysis

Motivation

Probing surface reactions by electrochemical methods provide invaluable information required to understand the rate and mechanism at which an alloy corrodes in a given medium. Information on the thermodynamic favorability of corrosion by dissolution (E_{corr}), the kinetics of surface corrosion (I_{corr}), behavior in passivation regions ($E_{pass,}$ I_{pass}), and ease of pitting (E_{pit}), can be gleaned from potentiodynamic polarization studies of the alloy. Information on the time-resolved dissolved quantities of corrosion products in a corrosion medium (related to peak current I_p) can be gleaned from CV. Interfacial mass and charge transfer mechanisms between the environment and the alloy can be probed by EIS to generate an equivalent-circuit model. It is anticipated that every alloy-environment combination will have a matrix of characteristic values [E_{corr}, I_{corr}, E_{pass}, I_{pass}, E_{pit}] from potentiodynamic polarization, [t, $C_{analyte}$] from CV, [R_{ct}, C_{dl}, Z_w CPE] from EIS, where R_{ct} is the charge transfer resistance in the equivalent circuit system, $C_{dl,}$ is the capacitance of a double-layer element, Z_w is impedence of the Warburg element and CPE is a constant phase element, to provide an electrochemical dataset that comprehensively describes the degradation performance of the alloy in the medium of interest. A map of the pathway of advancement from the current state-of-the art to the aspired scenario in HTP polarization and CV is presented in Figure 16. Automating the repetitive steps in data analysis will facilitate data reduction and in turn speed up database-building toward the critical capacity that enables the analyst to gain insights into any overarching patterns in degradation behavior of the novel alloys, which is ultimately the goal.

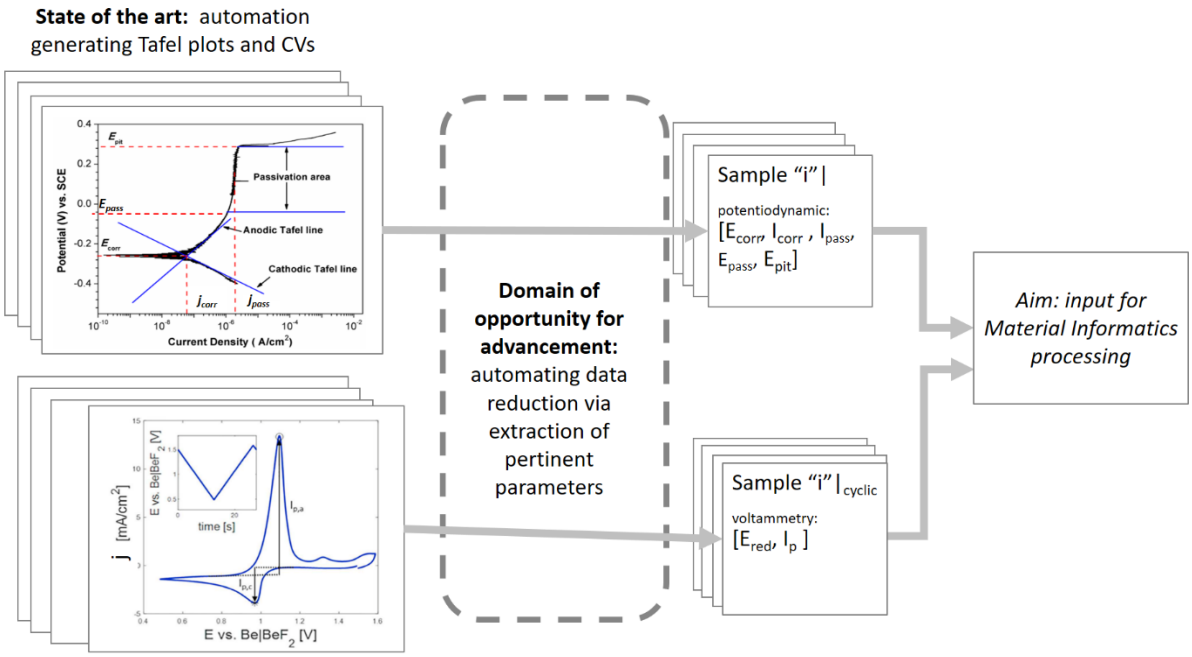

Figure 16: Schematic representing the pipeline through which potentiodynamic polarization and CV data is passed in order for it to be useful for material informatics: HTP experiments generating high volumes of Tafel plots and CV present a domain of opportunity to develop automated data reduction platforms to efficiently extract high volumes of desired parameters indicating alloy corrosion performance in the medium in a short period of time. It is expected that each alloy would be vectorized by the respective parameters extracted from its polarization and CV study results. These vectors representing each sample can then be applied to material informatics processing to glean high-level insights.

Successes

To the end of HTP electrochemical data analysis, batch analysis of CV peak-search (output peak value and centroid), as well as automating Tafel slope fits and corrosion current calculation are possible with, for instance, Nova® software from Autolab [203]. Parameters of interest for CV can be extracted automatically via least-squares fitting of a selected model using DigiElch® 8 software on individual CV. EIS and CV data can be automated for batch analysis using superimposition of modeled data onto experiment for ease of comparison using pyEIA[204]. As another example, Joress et. al. reported several useful scripts for automating the analysis of OCP, LPR, and Tafel

experiments.[205], [206] Polarization curves are more complex to model, as a good theoretical or empirical model that captures the nuances of the passivation process do not exist. Joress et. al. reported a relatively simple method for fitting polarization curves, assuming flat passivation plateaus, but the method is not robust to handle "plateaus" that curve, as is often observed experimentally[175], [207]. Bellezze et. al. provided an interesting method for attacking such types of curves, however, their code was not provided.[208] The autonomous fitting of EIS data is much more challenging, owing to both to there being an infinite number of equivalent circuits that could be used to fit the data and a lack of accepted best-practices that span multiple sub-fields. There are several interesting (semi-)automated pipelines currently available including EquivalentCircuits.jl and EISART.[209] The former is particularly interesting as it uses Gene Expression Programming to automatically generate potential equivalent circuits, performs the standard least squares fitting, and then iterates until it arrives at the optimal configuration. In our experience, this tends to generate an entire zoo of potential equivalent circuits which then require user intervention to narrow down to a physically reasonable subset of circuits for final human analysis.

Challenges, Opportunities & Aspirational perspectives

At this juncture it is important to draw a distinction between analysis by 'simulation' and analysis by 'modeling': where 'modeling' can be broadly applied to predicting the behavior of system mathematically, 'simulation' can be thought of as a subset of modeling in which the system is understood to have stochastic properties (eg. atomic-scale interactions in Molecular Dynamic Simulations, neutron-target interactions in Monte Carlo N-Particle Simulations) and it is necessary to address statistical metrics of reported results. Drawing such a distinction provides clarity when comparing results from various modes of analysis. By this distinction, strictly speaking, the analytical capabilities provided by, for instance, DigiElch® 8, is more accurately referred to as 'modeling' rather than 'simulation' per se. At the time of writing, Bongiorno et al have determined that the state-of-the-art in using ML methods to extract parameter values from an EIS system for which the model is known is on par with, but not exceeding, the accuracy of conventional heuristic ("hard-coded") fitting software [210]. By association, it is conceivable that this conclusion also extends to the efficacy of using ML to extract parameter values for potentiometric polarization or CV data for which a model is known.

Considering this, a primary challenge for batch analysis of large volumes of CV and EIS data (hereafter referred to as HTP analysis) is model selection. Conventionally the model is pre-selected for a given system. Making

the search for CV and EIS models autonomous or even quasi-autonomous is essential for the acceleration of CV and EIS data reduction. Generating optimal equivalent-circuit models (ECM) for EIS spectra, or EIS inversion, is a limiting factor in the speed with which EIS systems are analyzed. Bongiorno et al explored the obvious application of ML to solve EIS inversion by testing the effectiveness of a deep neural net classifier to sort a population of simulated EIS spectra into 3 ECMs, observing that classification accuracy suffers when differing models produce similar-looking spectra [210]. Such an outcome indicates that while naïve ML classifiers cannot yet exceed the accuracy of manual ECM identification, it can improve processing rate of EIS spectra if the objective is to know the representation proportion from a small set of possible ECMs of a large population of EIS spectra. However, the obvious limitation of naïve classifiers with EIS inversion is that they cannot suggest ECMs beyond those included in the training set. A technical advancement on the performance of the deep neural net classifier for EIS inversion would need to demonstrate the capability to suggest ECMs that are hitherto unknown.

That said, when considering or evaluating EIS inversion techniques that generate proposed ECMs without *a priori* knowledge from a bag of possible models to choose from, one must keep in mind it is often the case that the optimal ECMs are neither unique nor physically meaningful. To circumvent the need for ECMs to gain insight into the EIS data, functional fitting for distribution of relaxation times [211]–[213] and distribution of diffusion times [214], [215] are methods of interest, although determining these distribution functions is non-trivial. To this end, hierarchical Bayesian inference (HBI)[216] is a regression-like approach to determining underlying relaxation time distributions of an EIS spectrum without *a priori* knowledge of the system. In this approach, the experimentally measured impedance Z_{exp} is expressed as a discrete sum of Gaussian Radial Basis Functions (RBF) in $\ln(\tau)$ where τ is a time constant representing relaxation times and τ_k are basis time constants (typically equi-spaced), for each angular frequency ω_n measured (see Eq (1)).

$$Z_{DRT}(\omega_n) = R_\infty + i\omega L + \sum_{m=1}^{K} x_m \int_{-\infty}^{\infty} exp\ -[\mu \cdot ln\ (\frac{\tau}{\tau_k})]\ d[ln(\tau)] \qquad \textit{Eq (1)}$$

Here, "i" in this context is the imaginary number, R_∞ is the infinite resistance term, L is the inductance and μ is the inverse length scale of the RBF. The goal of the transform method is to obtain the values of weights x_i which can be used to fit the data for τ. The distribution of relaxation times is thereby obtainable. For this HBI methodology to be

made applicable for automated analysis of HTP electrochemical data, it is desired for HBI to be developed to the point where it is independent of *a priori* tuning. A schematic is drawn (Figure 17) codify all the components involved that make the development of HTP analysis of EIS a very non-trivial problem indeed.

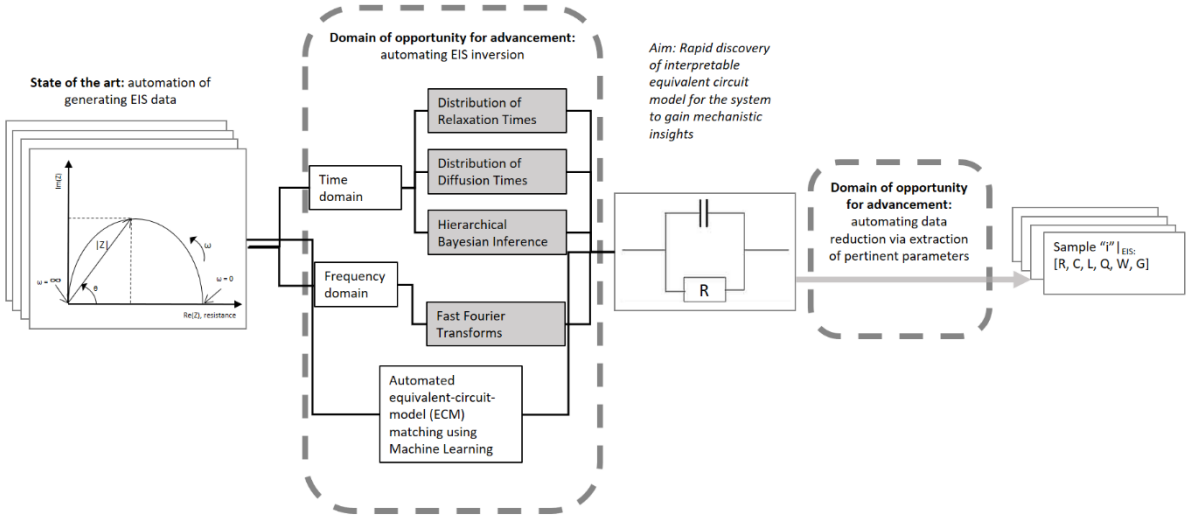

Figure 17: Schematic representing the pipeline through which EIS data passes for the experimenter to glean mechanistic insights into a system that lacks satisfactory understanding and thereafter to obtain the parameters representing various aspects of the mechanism. The simplistic equivalent circuit model (ECM) is shown for purposes of illustration, where the element labeled R represents a resistance element, but it is expected that unfamiliar systems would have a far more complex ECM. The data, once obtained, faces a process bottleneck to achieving mechanistic understanding which is the search for a satisfactory mechanistic model. Methodologies exist for EIS inversion to facilitate the discovery of plausible models, but the potential exists for these methodologies to be implemented in an automated process. The parameters anticipated in a complex ECM are represented by the following terms: R – resistance, C – double-layer

capacitance (ideal), Q – capacitance (non-ideal), W – circuit Warburg element, mechanistically representing diffusion processes, L – inductor, G – circuit Gerischer element, mechanistically representing an electrochemical chemical reaction with an irreversible component. It is expected that each alloy would be vectorized by the respective parameters extracted from its EIS results. These vectors representing each sample can then be applied to material informatics processing to glean high-level insights.

In the study of alloy corrosion by quantifying the time-resolved concentration of dissolved corrosion products in the corrosion medium using CVs measured in HTP fashion, chemometric analysis appears to be an appropriate analysis tool. However, chemometric methods still exhibit some obstacles to their application to material informatics: firstly, the chemometric model must first be calibrated for alloys in a particular element space, with the number of calibration curves equivalent to $\Sigma^{n}_{i}\,{}^{n}C_{i}$, where n is the number of elements present in the alloy including any impurities. This means implementing a chemometric model necessarily adds a laborious step of calibration in the data reduction process; the larger the element space and the non-negligible impurity species considered, the more laborious would be the calibration campaign. A cost-benefit consideration must be made as to whether the number of samples to be analyzed by CV in a sample space justifies the effort invested to calibrate the chemometric model. Secondly, the rigor and completeness of the chemometric model must be well-established before it can be applied to analyze HTP data as a routine; one has to consider that chemometric models are limited only to what is known about the system as there are no known 'smart chemometric' analysis routines at the time of writing capable of generating fitting parameters without *a priori* knowledge of the number and centroid values of the peaks of interest for the specific medium system of interest. This results in the third and final significant limitation of chemometric models as a basis for HTP analysis of HTP-generated CV data: the primary figure of merit to assess a chemometric model is the coefficient of determination (R^2), but this is no guarantee for the uniqueness or accuracy of the model – it is possible for different chemometric models to produce the same R^2 for the data. Therefore, the amount of effort invested into the calibration campaign for a compositionally complex alloy space may prove to introduce a new bottleneck in the HTP analysis process. The development of agnostic or automated chemometric calibration tools would be ideal for chemometric models to be efficiently used in the HTP electrochemistry space. A possible path forward in this regard is using generalized regressor neural networks (GRNN) and least absolute shrinkage and selection operator (LASSO)

techniques: Harefa et al have demonstrated an improvement in the quantitation accuracy of dissolved cations in aqueous media over the performance of conventional univariate regression of one emission spectral line by using active learning techniques to determine the most important lines from amongst all the emission lines for the analytes of interest[217]. Their work demonstrates that active learning techniques exhibit potential to overcome the need for *a priori* parametric tuning of multivariate linear regressors presented by chemometric methods to fit CV data.

6. Toward high-Throughput Autonomous Electrochemical Systems

Methods for automating electrochemical material synthesis and characterization are developed in parallel with the development of sophisticated AI/ML platforms for extracting knowledge and planning experiments. As an example, the use of HTP electrochemistry is being currently used to accelerate structural materials development for high-temperature molten salt technologies. As shown in Figure 18, HTP electrochemistry is inserted into the HTP processing/characterization/testing framework (i.e., all the steps interconnected in this study) detailed in [178], [218] using an automated mini-electrochemical probe.

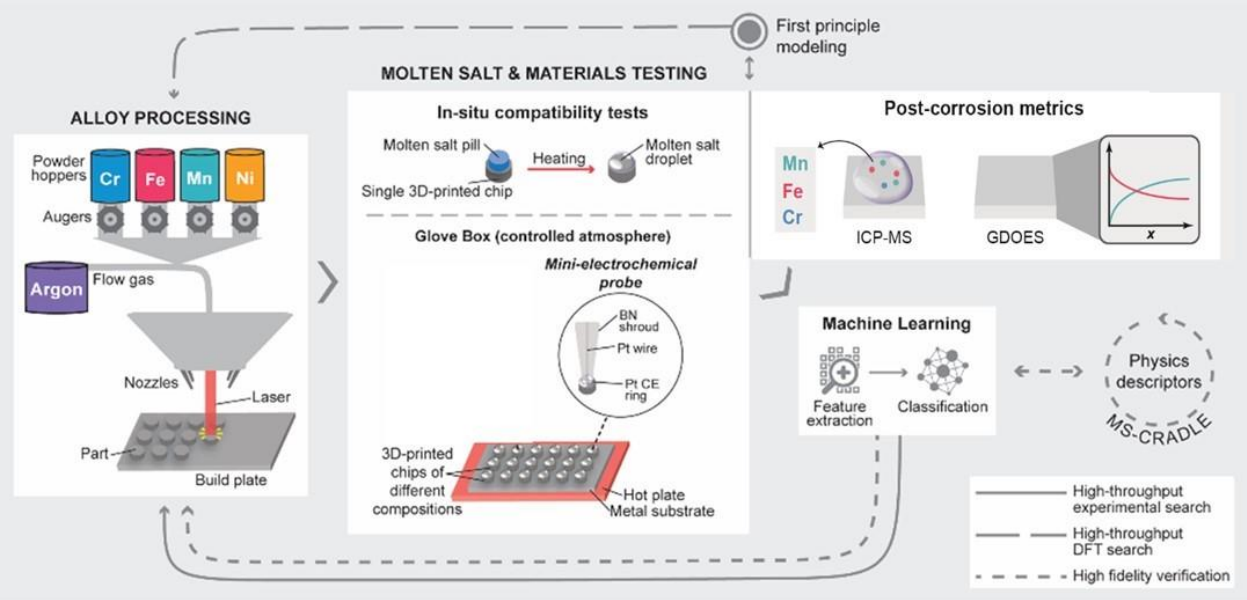

Figure 18: Schematic describing all the interconnected steps composing the HTP framework used to accelerate structural materials development for high-temperature molten salt technologies. In this case, HTP electrochemistry is used to obtain in-situ kinetics information of the corrosion process. This results

in an exceptionally rich output data set adding to the ex-situ post-corrosion metrics such as ICP and GDOES.

With these recent advancements, an opportunity for the development of autonomous platforms is presented. In these systems, a fully automated robot is responsible for planning experimental campaigns, performing the experiments recommended, and analyzing the results in a closed loop manner. Human scientists continue to engage with the scientific process at the outset by defining objectives, specifying constraints, and providing prior knowledge and heuristics to improve overall AI/ML exploration of complex spaces. Post hoc analysis and the generation of new knowledge is optimally performed via human-AI teaming using interactive data dashboards, identification of potentially interesting outliers, and flagging of unexpected correlations. For a review of the state of the art in autonomous materials science the interested reader is referred to a recent report by Stach et. al[157] and Ju et al[219].

To date, the field of autonomous electrochemistry is relatively unexplored with few demonstrated systems in the literature, as reviewed below. Dave et. al. demonstrated an autonomous platform for mixing and electrochemically testing different electrolyte compositions for battery applications.[220] The tool uses flow through mixing of different electrolyte compositions and measures the electrical conductivity and stability range of each mixture. One of the greatest challenges for effective autonomous experimentation is the effective orchestration of a hierarchical experimental loop. Rahmanian et. al. recently demonstrated hierarchical experimental laboratory automation and orchestration (HELAO) framework for performing autonomous electrochemistry[221] and have provided the software for the orchestrator online at GitHub[207]. DeCost et. al. recently demonstrated the first autonomous system capable of performing autonomous electrodeposition and corrosion measurements.[222] The tool is based off the established scanning droplet cell tool demonstrated by Kollender et. al.,[223] which has been reviewed earlier. They found that although automated characterization of the electrochemical corrosion was straightforward, effective evaluation of the success of an individual synthesis step was more complicated. Successful synthesis potentially requires a large number of additional observations including: deposition uniformity (thickness, coverage, and composition), capturing the appropriate phase (diffraction), and surface finish. Such measurements are typical in HTP pipelines but are typically delocalized from the synthesis platform and/or require human evaluation of a reasonable coating prior to being performed. Frankly, the concerns for successful synthesis span all conceivable

synthesis routes and thus careful selection of auxiliary measurement that can be co-located to provide at a minimum a pass-fail on the synthesis process is essential. In this context imaging can be a useful approach to estimate the density/success of a coating, the uniformity of an electrodeposited sample, or to identify spallation in a film deposited via physical vapor deposition.

In addition to the standard synthesis problems, extracting information from electrochemical data can vary from being relatively trivial to incredibly challenging, as detailed earlier. One of the most challenging aspects of these measurements is that during a HTP experiment, where experiments are optimally performed over a period of minutes rather than hours, the electrochemical response, such as the OCP, can drift as the electrolyte and material surface equilibrate. This can result in errors during further automated electrochemical analysis (LPR, Tafel, EIS), which in a truly intelligent autonomous agent would be flagged and the measurement re-preformed prior to truly destructive measurements. Consequently, the successful development of autonomous platform for non-steady-state systems, which are quite common in electrochemistry, is perceived as a formidable challenge for the next decade.

Conclusion

A relatively detailed overview of the motivation, successes, and opportunities in applying HTP electrochemical techniques to materials science, and in particular to the field of high-temperature alloy design, has been provided. A recent surge in HTP processing and testing methods development has been observed, resulting in unprecedented opportunities for HTP electrochemical techniques to benefit from/to this emerging field. While opportunities exist, significant new challenges are being offered to the scientific community. For instance, HTP electrochemical testing in extreme environments would provide an enormous amount of data needed to train ML models, but automated and reliable test methods are not yet developed for such aggressive environments. Accelerated electrochemical data analysis using ML methods still require significant research to properly identify and simulate the degradation mechanisms, accurately predict materials' behavior, and identify features of importance in materials' response. Nonetheless, in recent years, the scientific community has realized the needs to use ML-augmented HTP data analysis methods and an increase in scientific contributions on this topic is observed, as shown in this manuscript with the example of molten salt technologies. This is ultimately deemed necessary if autonomous research using electrochemical techniques are to be developed in the future.

3.6.2 Machine Learning Methods

Since the combinatorial space of a quaternary system is quasi-infinite, a systematic testing of alloys spanning a coarse-mesh representation of the space coupled to a predictive machine-learning model to accelerate the refinement of the mesh at each iteration of corrosion testing promises to be the most efficient approach to alloy composition discovery. High throughput computational screening has been demonstrated to be a viable strategy for exploring the space of hypothetical alloys [224], [225]

What defines a Machine Learning Method?

Machine Learning (ML) has been defined by Russell & Norvig in their 1995 textbook as the capability of a computer to a) react to new circumstances, b) detect and c) extrapolate patterns. The implied boundaries of this definition are "new circumstances" and "patterns" insofar as the scope boundaries are for the problem at hand for the computer to solve. Therefore the adaptability of the ML method to "new circumstances" heavily relies on how the problem is framed for implementation of the ML method. In other words, whether or not a problem can be solved by ML methods is limited only by the creativity of the analyst in engineering data structures to feed into the ML such that the outputs thereof can be interpreted to be meaningful.

As this thesis is multi-disciplinary, it is necessary to disambiguate the term "machine learning" from "artificial intelligence" from one another for the benefit of non-computer science practitioners among the scientific community. The term "artificial intelligence" as commonly invoked in mass media reflects the definition of "machines whose thought processes mimic human intelligence" by McCarthy [226] updated from Turing's original definition. We immediately find this definition difficult to adopt in this thesis since "human intelligence" does not have a globally standardized definition. Russell & Norvig's definition of ML, while quite open ended, has better-drawn parameters to qualify the various techniques that were feasibility-tested in this thesis work, therefore the usage of the term is adopted here.

It becomes evident during the literature review of ML methods applied to problems in Material Science that some methods commonly applied to solve Material Science problems do not qualify

as ML techniques by Russell & Norvig's definition. Linear regressions and their related models are one class of such methods commonly used to model behavior of materials if there exists no known functional relationship between the independent and dependent variables studied. Since modeling the system of interest as a linear combination imposes this functional form on the analysis framework, the method cannot be said to "detect" patterns, because the pattern of linear combination is assumed. Such an analytical framework is more accurately referred to as "Material Informatics" (MI) which has been defined as the application of data analytics methods to problems in Materials Science [225]. Material Informatics methods can often be found in the literature [227], [228] juxtaposed with ML methods to study similar/related problems. In this thesis, both ML methods and MI methods were utilized to study alloy corrosion in molten salts and their results were compared.

The following sections summarize several commonly utilized ML and MI techniques in contemporary literature used to analyze open questions in Materials Science. For the sake of convenience in this thesis, let us consider a sample population of size N (eg alloys). Each sample is defined by a vector of values (x_1, …, x_n) where each x_i denotes a sample "feature" (eg. "Mole fraction of Cr", "mole fraction Fe", "mole fraction Mn", "mole fraction Ni", etc) and n denotes the number of features used to describe a single sample. When samples are arrayed such that each row contains the feature values for a single sample, each column, X_i denotes a vector containing the values of a single feature over the whole sample population. Let Y represent the vector containing the target variable values of the sample population (eg. "Total corrosion concentration of Cr+Fe+Mn+Ni" in salt). Models are mathematical functions or algorithms relating the X's to the Y, for example the linear regression.

Definitions and Disambiguation of terms

At this juncture it is necessary to clarify that the term "model" as it is used in the field of ML is fundamentally different in nature to a mathematical model that describes a physical phenomenon. A mathematical model in general can be expressed as one or more series of related equations whereas by

contrast, under the hood, an ML model is generally expressed as a sorting routine governed by a series of "if…then" statements (or "rubrics"). Even regression-type ML algorithms are fundamentally a series of classification rubrics, they are simply a longer series such that continuous inputs/output variables can be approximated by very finely-subdivided discrete variables. In this regard, ML models perhaps have this characteristic in common with Monte-Carlo (MC)-type first-principles/ab initio particle simulation models. The central difference between a MC-type particle simulation model is that the rubrics are provided by the human programmer, whereas by contrast no rubrics are provided by the human programmer for ML at the start. The human programmer only provides a training set of data to the ML algorithm in which the inputs are matched to their respective outputs, and the ML algorithm produces the set of rubrics (aka "the model") upon completing the training. This contrast between MC and ML models highlights the potential of ML models to facilitate us to fill in knowledge gaps by producing models with the potential to reveal underpinning patterns in the data which were hitherto unobserved with conventional analysis; this is something MC simulations cannot do.

As a point of reference, we benchmark the performance of our ML methods against the Naive Mean, which is the average experimental result of our dataset. The "naive mean" approach assumes an out of bag sample will yield the same corrosion result as the average of all the experimental corrosion results in the trained dataset.

The concept of a "regressor" forms the basis of a major class of ML algorithms. In this section we describe the ML regressors' predecessors - the linear regressor. The standard form of a linear equation is shown in Eqn(1), which expresses output y as a linear combination of feature values (x_1, …, x_n), scaled by coefficients (a_1, …, a_n).

It assumes every feature is linearly independent. If two or more features are interdependent (for example the mole fraction of an element in the alloy is functionally related thermodynamics activity in the alloy), or if they are even spuriously correlated - they must be eliminated for the linear model to be

valid.

When using linear regression to analyze a dataset, it is necessary to ensure that all input variables ($x_i \ldots x_n$) are norm-scaled; this way the relative magnitudes of the coefficient a_i can be indicators of impact/importance of feature x_i assuming x_i is linearly related to y.

A fitted linear regression model takes the form:

$$y = a_0 + a_1 x_1 + a_2 x_2 + a_3 x_3 + \cdots + a_n x_n$$

In other words, for given matrices Y and X defined by the data, the underlying "pattern" we desire to uncover from the data is matrix a.

$$Y = aX$$

Solving for a entails minimizing the sum of errors squared (aka Ordinary Least Squares method)

$$min \, \|aX - Y\|^2$$

In theory, linear regression is able to incorporate new data into the model as it becomes available by refitting the coefficients ($a_0, \ldots, a_n$) iteratively with successive additions to the sample population. In spite of this the linear regression does not technically qualify as an ML technique because a pre-existing pattern - the linear relationship between inputs and output - cannot be varied on-the-fly as additional data is incorporated into the data set.

The basic linear regressor is the simplest model assumed if the data analyst is agnostic of the functional relationships between the input variables (the x's) and the output variable (the y). The size of the weight a_i on a variable x_i reflects the relative importance of a variable to the outcome, assuming all input variables are norm-scaled for the regression fit. It is commonly used in public medicine and social sciences to model impacts of social factors to the population. However, for more complex systems, the basic linear regressor is inadequate for accurate modeling or for understanding of mechanistic nuances.

For a linear regression model to be valid, the data needs to satisfy the following assumptions:

I. there exists a linear relationship between X and Y

II. the residuals (each element of ||aX-Y||)

   i) are uncorrelated to one another

   ii) have constant variance for all x in domain of study

   iii) are normally distributed for all x in domain of study

Based on the theory provided in the previous section, it is clear that corrosion cannot be modeled as a linear system. What follows in this section describes models commonly used in MI based on the linear regression in increasing levels of relaxing the above mathematical criteria for a simple linear regressor to accommodate the corrosion problem. Experimental corrosion data was modeled using these various MI methods to compare to ML methods to demonstrate that ML methods surpass these MI methods in modeling the system and a selection was made based on modeling figures of merit.

If the number of exogenous features is fewer than the number of samples, the problem is underdefined and the matrix a will have infinitely many solutions. This can occur if the domain knowledge of the problem is incomplete, or if there is muti-collinearity between input variables. Further constraints need to be placed on the least-squares optimization problem to limit the number of solutions - this is regularized least squares (RLS).

A simple form of is Tikhonov's regularization more popularly known as **Ridge regression**. It is named for the shape it takes along the along the diagonal of the matrix [229],. It takes the form of the beta parameter like so:

$$min\ \|aX - Y\|^2 + \beta\ \|a\|^2$$

RLS is also useful if the fitted model otherwise is not generalizable - that is, it performs well only for samples on which it was fitted, but it inaccurately predicts results for samples outside of the

training set (aka “out-of-bag” samples). Figure 19 shows that with larger beta, the values of the weights (a) are prevented from exponentiating, thereby maintaining the interpretability of the weights relative to one another.

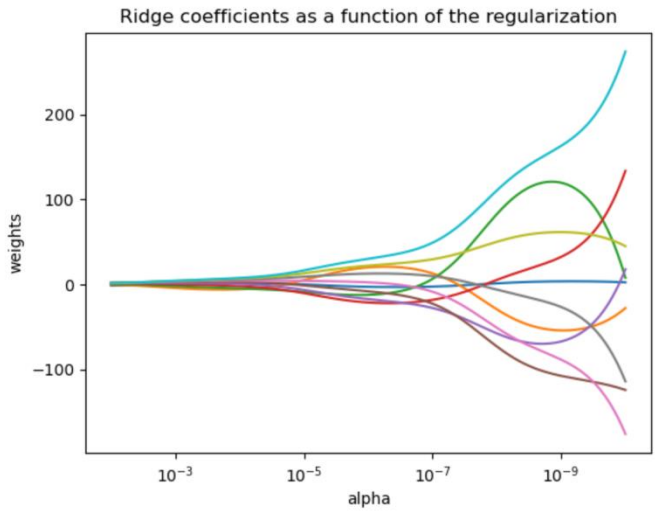

Figure 19: Ridge Coefficients as a function of regularization, image from [230]

In the opposite case where the problem is possibly over-defined, ie it is suspected that from the set of input variables only a small subset are significant to the output, **Lasso** is a linear model which estimates sparse coefficients [231], [232].

Mathematically, it is a linear model with an additional regularization term. The objective function to minimize is:

$$\min_{w} \frac{1}{2n_{\text{samples}}} ||Xw - y||_2^2 + \alpha||w||_1$$

Least Angle Regression LARS is based on forward stepwise regression [233] in which a model is built by adding variables and successively testing the fit with each variable added, in descending order of correlation coefficient. If two variables are equally correlated according to the optimization criteria, the variables are incorporated to the model at equi-angles to the two variables, hence the name

"least angles regressor". When the latest variable added results in no statistical improvement to the fit, the model is considered optimized.

One significant advantage of this model-building scheme is that it is robust against over-fitting because of its piecewise path, but a significant disadvantage is that it can also be over-sensitive to noise.

A numerically accurate model is one which returns exact values to ground truth. A numerically precise model is one where the uncertainty of the model prediction approaches zero. Any useful model is necessarily both accurate and precise to a satisfactory level. The uncertainty of the model can be thought of as a probability that the ground truth lies within the model's uncertainty bounds. From this perspective, the determination of a model's uncertainty bounds can be framed as a calculation of probabilities.

There are 2 broad paradigms to determine the probabilities associated with a model's output: frequentist and **Bayesian** [234] Assuming the model chosen to fit the problem at hand is known to be the most appropriate function (let's say linear regression, for argument's sake), a frequentist paradigm holds that the probabilities that the model's parameters (the model weights) are equal to ground truth approaches unity as the sample population on which the model is fitted approaches infinity [234]. The frequentist paradigm is so named because it is predicated on the frequency of observation.

The Bayesian paradigm contrasts to the frequentist paradigm in that given a finite sample population of size N with observations D, it is understood that D is in fact observed as a posterior distribution (D|w) of the maximum likelihood function w. In other words, the probabilities that the weights in the linear regression model at hand with values $\{a_1, \ldots, a_n\}$ are in fact ground truth are given by p(w|D). A Bayesian approach would then be to solve for w in order to determine the uncertainties on the weights $\{\{a_1, \ldots, a_n\}$. Solving for w using D entails knowing the form the function w takes and determining the values of the parameters of the function w (parameters of w are also known as

hyperparameters of the linear model).

$$p\ (w|D) = \frac{p(D|w)p(w)}{p(D)}$$

Notice that the application of a Bayesian approach is meant to improve upon the precision of a model's parameters when its form is already known (or at least established with a high level of certainty). For our corrosion problem at hand, we have yet to establish what form the prediction model will take, so delving into Bayesian methods for estimating parameters is premature at this juncture. The frequentist approach to determine model parameters is a necessary starting point at the stage of surveying the various models for their appropriateness. An overview of the Bayesian approach was included here simply because Bayesian methods are used in Material Informatics with sufficient prevalence as to warrant a mention that these methods have been considered.

For cases where there are multiple correlations between input variables, and we wish to recognize the importance of all those variables equally. **Elastic net regressor** provides a way to do this in a way that Lasso does not since lasso will only identify a single member of the correlated subset. Elastic net achieves this by combining L1 and L2 regularization. The objective function to minimize is then:

$$\min_{w} \frac{1}{2n_{\text{samples}}} ||Xw - y||_2^2 + \alpha\rho||w||_1 + \frac{\alpha(1-\rho)}{2}||w||_2^2$$

Python implementations of all these methods were obtained from sci-kit learn [235]. The various regressors described above are simply linear models with different regularization parameters. Ultimately a linear model is imposed on the data. To reiterate Russell & Norvig's definition, linear regressions and their regularization methods Ridge, LARS, Lasso and Bayesian Ridge cannot properly be called "ML" methods because their ability to "detect patterns" is severely constrained by the fact that they are inflexible if the data is ill-fitted to some linear combination of the input variables. However these methods are commonly applied in data analytics and therefore fall under the MI category. MI methods are

often applied as “first pass models” as a quick check as to whether the data can be conveniently fit to a linear model that is straightforward to interpret before resorting to more sophisticated bona fide ML techniques, which require some finesse to interpret.

Like the linear regressor, the “regressor class” of ML is the class of ML techniques that maps inputs to outputs which both take the form of continuous variables. That is the extent of their commonality as “regressors”. The following section discusses several regressor ML methods which are commonly implemented to solve open questions in Materials Science. In general, linear models are not suited to predicting corrosion problems because corrosion problems are time-series problems [236]

A **Decision Tree Regressor** [237] is a model which predicts a continuous dependent variable “y” based on a vector of input features ($x_1 \ldots x_n$) by building a series of sorting decisions. The tree begins with the universal set of the training population. At every juncture (“node”) a feature is randomly selected from the feature set to bifurcate into subsets (“branches”). An illustration of a decision tree is shown in the schematic of Figure 20 Schematic of a hypothetical decision tree.Figure 20

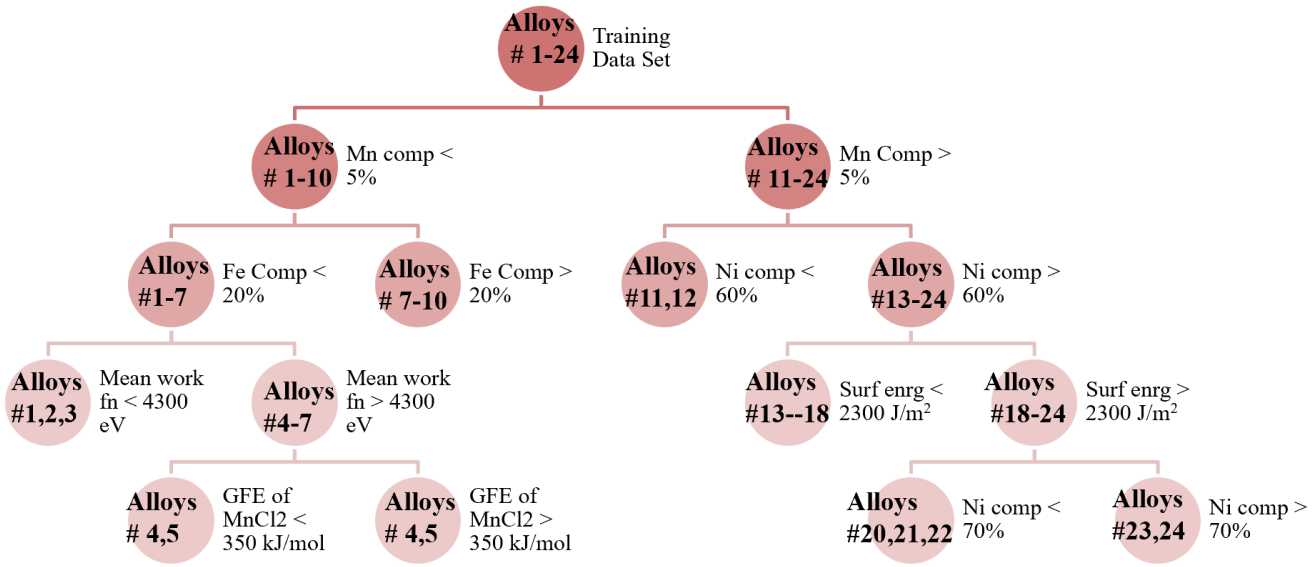

Figure 20 Schematic of a hypothetical decision tree.

During the construction of a decision tree, the bifurcation threshold is the value of that feature that minimizes the Gini impurity value for the populations in each branch. For a regressor, the Gini impurity is the variance of y-values in the branch [238] :

$$G = \frac{1}{N}\sum_{i}^{N}(y_i - \mu)^2 \qquad (15)$$

Where N is the total number of samples in the branch, y_i is the target variable value of the i^{th} sample and μ is the mean branch target variable value. During the training of each tree, the impurity decrease between branches for each feature is recorded.

Impurity decrease values determine Importance Scores for features: those features that yield consistently high Impurity decreases will have high importance scores. Bifurcation continues since no minimum tree depth is specified, until there is only one sample per terminal node ("leaf"). After the model is built, it is tested on the test samples, and the y-values the model assigns to these test samples based on their (x_i) values are the "predicted" values of the test samples. A predictive model is one whose predicted values show a low mean percentage error (m%e), with formula

$$m\%e = \frac{1}{N}\sum_{i}^{N} abs(y_{expt} - y_{pred}) \qquad (16)$$

Where N is the total number of samples, y_{expt} is the true y-value of the sample, and y_{pred} is the predicted y-value. Since the feature on which the node is split is determined randomly, it becomes apparent that a single decision tree may not represent the most optimum model for a given training set.

The Random Forest Regressor (RFR) [239] is a model in which many (~1000) decision trees (aka "estimators") are constructed for a given training set and their results are **bootstrap aggregated (aka "BAgged")** [240] in which M bootstrap training sets are generated from the universal training to

generate M bootstrap models. The expected error of the bootstrap model is proven to be lower than the expected error of the non-bootstrap model by M-fold [234]. An added benefit of bagging is that it ensures the prediction values from the model reflect a statistically reproducible pattern given the finite sample population, and to do so within a bounded number of trees to limit computational times to reasonable periods. **"Bootstrapping"** [241] is a statistical method designed to circumvent the need for a minimum critical sample size to apply normal distribution theory to the analyzed population by treating the original sample population as the universal set and two-thirds of the universal set are randomly selected with replacement for the building of each tree [239]. The predictions from regressor trees constructed from bootstrapped sample sets tend towards normal distribution in a smaller number of trees than without [241]. The final forest prediction of a sample's value is the aggregation of the predictions of all the trees in the forest, in the case of regressor trees, it is the mean prediction. The implication is that the forest's aggregated prediction for a sample's value is an unbiased estimator of the true mean of that sample's predictions from all possible trees constructed from an infinite number of samples. Therefore, bagging justifies the results from an RFR model in this thesis trained on a sample population where the logistics of physically processing and corrosion testing novel alloys limits the population size to ~100.

Gradient boosting is a meta-algorithm that can be used to reduce the bias and variance of ensemble models by iteratively estimating the bias of individual models within the ensemble and inserting a correction term into the ensemble [242] . Bias of a model can be thought of as the imposition of an ill-fitted pattern onto the data [243] for example imposing a linear model to fit data that shows a visibly more parabolic shape; greater bias often results in underfitting. The opposite problem, overfitting is where the model is overspecified to particularities in the training dataset to the point where it does not generalize well to out-of-training-set samples (aka "out-of-bag" samples). An example of an overfitted model is one in which "sample ID#" is used to fit the model among other variables and a correlation imposed where there is exists none. The best way to tell if a model is overfitted is to determine prediction errors for a test

set composed of entirely out-of-bag samples. A model is overfit when it shows extremely small prediction errors when the training set samples are used to test the model, but extremely large prediction errors when out-of-bag are used to test the model.

The obvious measures to avoid overfitting before the training stage are to 1) make sure to the best of one's knowledge, the inputs contain exclusively variables with deterministic relationships to the output and 2) make sure the training set samples are statistically well-distributed (as uniformly as possible) throughout the desired prediction domain. The first measure is difficult to achieve without complete *a priori* knowledge of the problem's defining parameters their bounds. Indeed, if domain knowledge is complete, the ML model would be unnecessary. The second measure is difficult to achieve with small training sets since obtaining large sample populations for the training dataset is difficult for ML models trained with experimental data since acquiring large datasets is limited by the logistics and lead times of preparing samples, performing experiments and post-experiment analysis/data reduction.

While it is clear that models with low average m%e are desirable as "predictive" or even "accurate", there is no consensus in the literature as to an acceptable threshold for m%e . Generally, a Gaussian distribution of the percentage errors about a mean of 0% is indicative that the model does not contain inherent biases.

In addition to these analysis tools to determine the robustness of an RFR model, the **Isolated Tree Regressor** is a method to determine whether out-of-bag samples are "in-model", that is they are statistically represented by the training set samples, or they are "out-of-model".
An Isolated Tree Regressor is a routine in which a regressor tree is constructed from each out-of-bag sample. It has been noted that out-of-model samples consistently produce trees with very short tree depths (generally two levels of branches) [244] whereas in-model samples consistently produce trees with maximum depths according to the training set. Samples are thereby sorted into binary classification of

"in-model" or "out-of-model".

After pruning the predictions to retain only those statistically supported by the training set representation, we now turn our attention to assessing the accuracy of the RFR model. In particular, the RFR method has demonstrated both high predictive power and interpretability in predicting material properties based on composition and microstructural features. The RFR has been mathematically proven to be suitable for ranking a large number of input variables in terms of importance [245]. RFR are suited to "tabular-style datasets where features are individually meaningful" [246]. Properties predicted with some success by RFR include superconducting properties [247] the onset of void swelling in irradiated metals [52] glass-forming ability [248] and elastic modulus [227]

The K-nearest-neighbors (K-NN) is a supervised learning technique predicated on the assumption that samples that are close to one another in feature space ($x_1,\ldots,x_n$) will be close to one another in target variable space ("y") [249]. In other words, it assumes continuous variation of the target variable in n-dimensional feature hyperspace. In a fundamental sense, the algorithm maps the multidimensional inputs to the outputs and computes the predicted value for an out-of-bag sample by finding the closest y-instance in feature space distance.

Kernel methods are supervised learning techniques that leverage the solution techniques of linear classifiers to solve nonlinear problems. They do this by assuming that for any problem in which the data are distributed in finite n-dimensional space ($x_1 \ldots x_n$) , there exists some hyperspace of n' dimensions ($x'_1,\ldots,x'_n,\ldots,x'_{n'}$) in which samples can be clustered into groups of "like" samples, and the boundaries between these clusters in the form of hyperplanes are the desired solutions to the problem Figure 21. Generally n' > n. The bounded sub-volumes in n'-dimensional hyperspace thereby each map to a value in target variable space ("y"). A kernel is therefore the mapping function of x—> x' that facilitates this kind of solution.

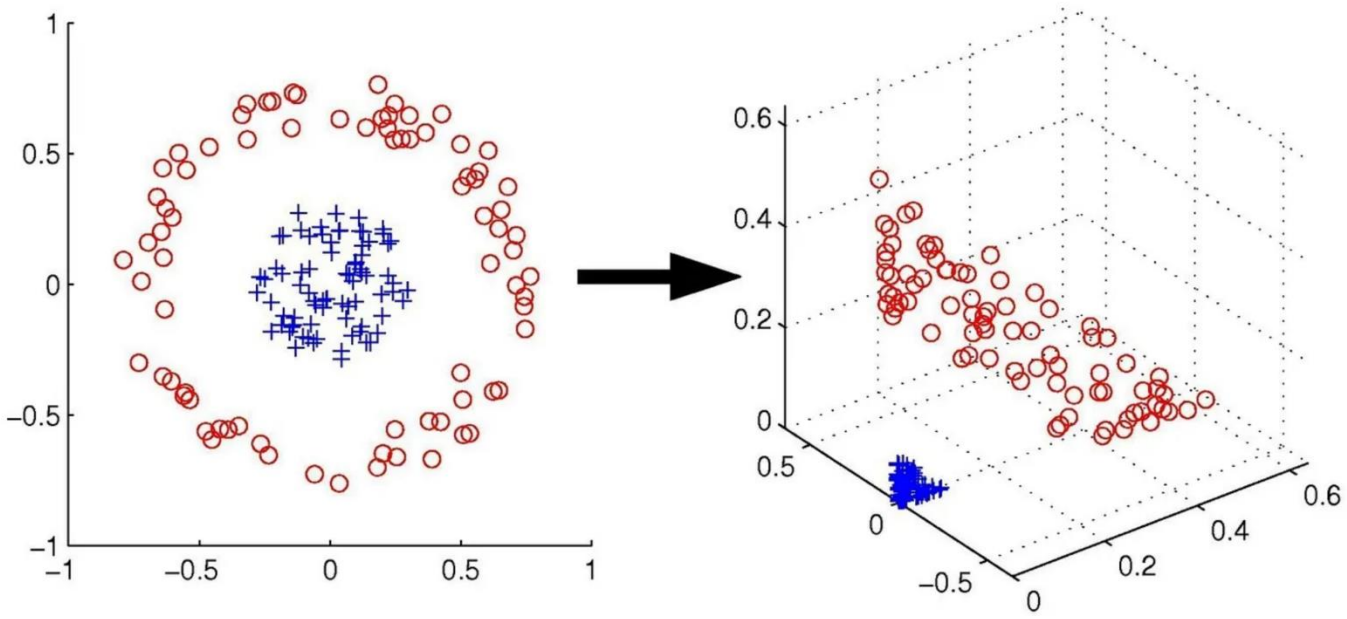

Figure 21: Illustration of "The Kernel Trick" transformation [250]

Support Vector Machine (SVM) is one of the higher profile of the kernel methods. It is useful in cases where the variables in the original problem are not linearly variable-separable, but an appropriate transformation into higher dimensional space can facilitate the problem to be variable separable. Support vectors define data points close to the hyperplane and they can strongly influence the position and orientation of the hyperplane. The optimum solution for the hyperplanes are the ones that maximize the distance between training data points the planes. In this way, confidence is maximized that an out-of-bag sample will have predicted values close to training samples that are "like it" [251].

Artificial Neural Networks (NNs) are perhaps the highest profile of the ML techniques in public consciousness, with the term "deep learning" being popularly used as synonymous with "machine learning", despite being unwarranted since there are many other ML techniques around. It is perhaps the fact that the structure of the algorithm most closely mimics the electrical network of the human brain, inspiring the hope that it will similarly most closely mimic human intelligence according to the Turing-McCarthy definition.

Consider the schematic of the algorithm shown in Figure 24: X is the matrix of inputs, fed directly into the first layer of neurons. At the first layer of neuron is an activation function, with the superscript denoting the layer, and the subscript denoting the index of the neuron in the layer. At each neuron, the ith element(s) of x are are operated on by activation function h(1)(i). The simplest form of activation function g(x) is the step function, defined thus:

$$g(x) = \begin{cases} 1, if\ x \geq 0 \\ 0, if\ x < 0 \end{cases}$$

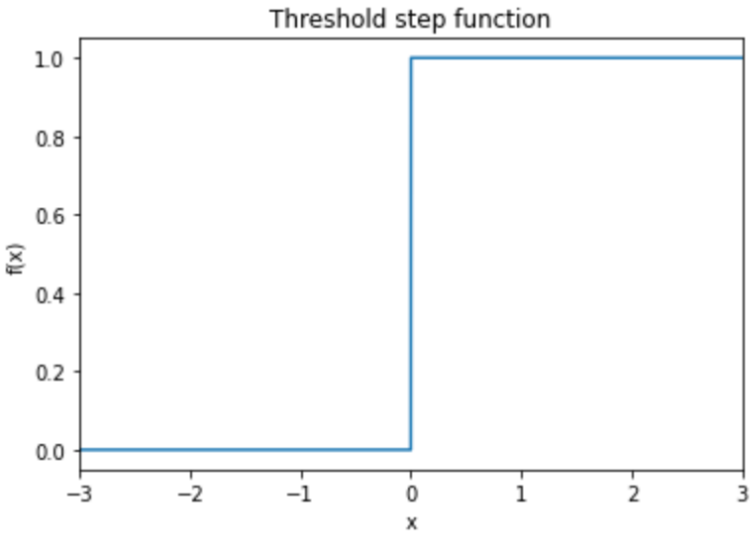

Figure 22: Illustration of a step function, [252]

Each node and activation function pair outputs a value of the form

$$h(x) = g(Wx + b)$$

In the case of a single layer neural network (aka “single layer perceptron”), the outputs of the activation function from h(1) are sufficient to map to output y (Figure 23).

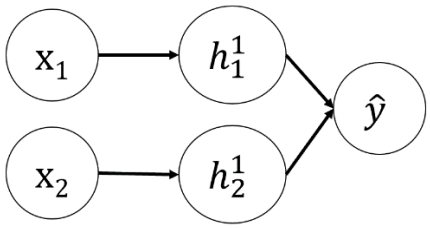

Figure 23: Schematic of single-layer perceptron, adapted from [252]

If inputs x1 and x2 are binary, the single layer perceptron reduces to a simple logic OR gate. In the case of a deep network, there is more than one layer of neurons, so the output from the first layer are fed as inputs into the second layer of neurons.

In the case where the input x and output y are both scalars, a deep neural network with two hidden layers can then be written as

$$\hat{y} = h^{(0)}\left(h^{(1)}(x)\right)$$

$$= g(W_1 \cdot g(W_0 x + b_0) + b_1)$$

where g is the activation function, W is the weight at that node, and b is the bias. The activation function g need not be a step function. It can theoretically be any non-linear function but common ones are sigmoidal, ReLU or PreLU[252]. A neural network in which the activation function is simply the identity function h(x) = x reduces to a linear regression. Tuning the NN entails tuning the weights and biases on the nodes.

In the case of a convolutional neural network (CNN), as illustrated in Figure 24, the output of $h^{(1)}{}_{(0)}$ does not necessarily only get fed into $h^{(2)}{}_{(0)}$ but it can be used as input into other neurons in the 2nd layer as well. CNNs have shown especial effectiveness in material science problems in which there is a strong spatial component such as with reconstructions of microscope/tomography imaging [253], texture and phase mapping [194], [196]. NN generally need training sets of size ~1000 for robust training statistics, so data in the form of images comprising thousands of pixels are deemed more suitable. ML

predictions of ~2% error have been demonstrated for problems in which NNs are trained on thousands of datapoints generated by computational simulations [254]–[258]. By contrast, cases which have "tabular-style datasets where features are individually meaningful and do not have strong multi-scale temporal or spatial structures" where RFRs are more suited [246].

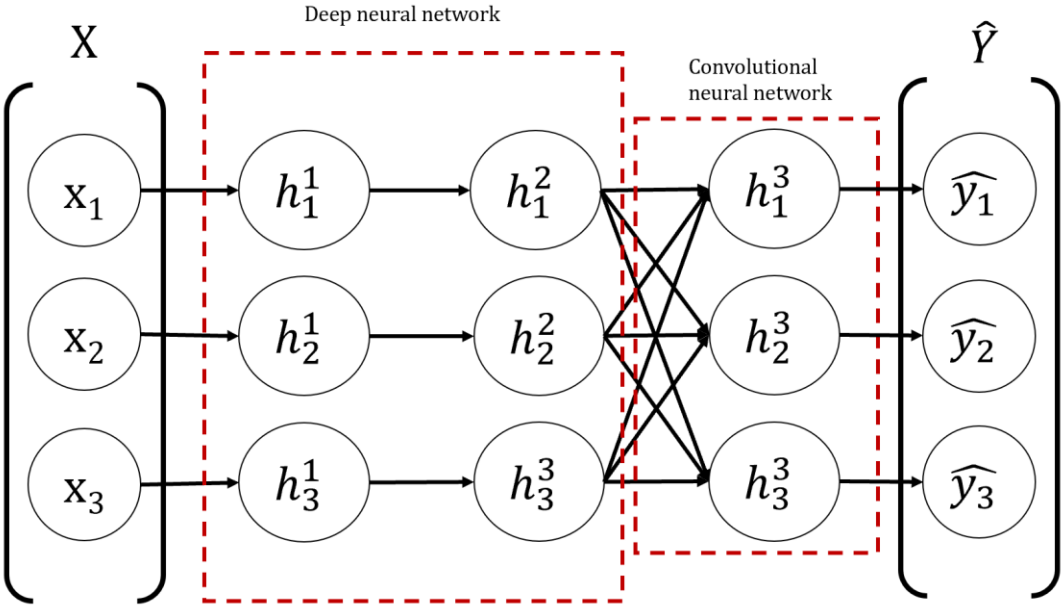

Figure 24: Schematic of deep convolutional neural network, adapted from [252]

It is important to establish whether or not the problem at hand has the following characteristics in order to select the appropriate ML technique to apply.

In general, MI and ML techniques are developed by inductive mathematical proof, so, strictly speaking, if the Material Science problem meets the prerequisite mathematical criteria, the solution produced by the technique can be considered mathematically validated. Unfortunately applied science is not as clear cut as pure mathematics or pure computer science. It is very often the case that despite every attempt to completely define the problem mathematically, some aspects of the problem can often defy mathematical definition. An example of such an aspect is the relationship between

microstructure and corrosion: the microstructure of an alloy can be described as an ordered data pair (phase category, phase fraction) but this data structure cannot be tested against the provided algorithm criteria. Additionally, in some cases of material science problems domain knowledge is incomplete. This limits the ability to select ML/MI techniques based on their meeting the mathematical criteria as originally laid out by the developers of the respective techniques. A survey of the literature of ML for materials science or material informatics finds that the lack of justification by satisfaction of mathematical criteria has not posed an insurmountable obstacle to utilizing MI or ML methods to find solutions to materials science problems. Justification in the literature generally comes by appeal to precedent and demonstration by figures of merit.

Despite this being common practice in the field, here I discuss the problem definition as pertains to common prerequisite mathematical criteria necessary for the application of ML/MI techniques:

Are all the features linearly independent in theory and practice?

As stated earlier, many MI methods are derived from the linear regressor. The applicability of a linear regression depends on all features being linearly independent in order for there to exist a unique solution to the coefficient matrix. As explained before, if this criterion is not met by the dataset, it is necessary to apply regularization techniques to determine/approximate a unique solution. If the features are even partially linearly dependent on one another, this can result in feature dilution in the model where the several independent features/variables in the model essentially represent the same one feature/variable.

Feature dilution in the model is of especial concern when some features may contain theoretical relationships to one another. For example, in our case, the activity of Ni in the alloy is often expressed as a linear function of mole fraction of Ni in the alloy for constant activity coefficient gamma:

$$a_{Ni} = \gamma_{Ni} C_{Ni} \qquad (17)$$

Non-linear functional relationships may exist between features, such as the Nernst Equation

that relates the activity of Ni in the alloy (and therefore its concentration) to the Gibbs Free Energy (GFE) of Ni corrosion product ($NiCl_2$) formation:

$$\Delta E_{Ni/NiCl_2} = \Delta E^{o}_{Ni/NiCl_2} - \frac{RT}{nF} ln\left(\frac{a_{NiCl_2} \cdot P_{Cl_2}}{a_{Ni,surf}}\right) \quad (18)$$

Non-linear relationships will be reflected in linear & related regressions as "low-impact" features by small coefficient magnitudes simply because the relationship is not linear. This scenario presents a false negative situation in which a feature such as GFE of a species falsely deemed to be unimpactful in predicting corrosion outcome despite there being a physical basis for there being so.

The propensity of linear & related regressions toward false negatives of this nature perfectly illustrates the crux of the problem we seek to solve with ML: if we do not know whether or not there exists a functional relationship between an input and an output, can the ML reveal to us a) whether this relationship exists, and b) the nature of this relationship (linear, square, log, exponential etc.)? Without turning to ML, a naive method to find a solution might be to iterate through all possible combinations of subsets of features S within the universal feature set F and all possible combinations of functions between them and determine the one with the highest coefficient of determination R^2. Even if the number of features n is small, this method is an inefficient use of computational resources. If an ML can help us sift through large numbers of hypothetical features and determine ones (or combinations of ones) with hitherto unknown relationships to the output at a decimal of the computation time, determining the functional relationship becomes trivial.

Even if there is no theoretical relationship between two features, the vectors of X_1 and X_2 may happen to be spuriously numerically correlated as a result of the logistics of performing the experiment. For example, there is no direct theoretical relationship between the tracer diffusion coefficient of Ni and the mole fraction of Ni in an alloy. However, as tracer diffusion is phase-dependent (Ni diffuses about 5 orders of magnitude faster in an FCC lattice than a BCC lattice) and high-Ni alloys

tend to form solid phases with high FCC fraction, therefore it is unavoidable in the dataset that Ni tracer diffusion is correlated to Ni mole fraction but only transitively due to FCC fraction.

If features are linearly related to one another or if these spurious correlations exist unavoidably within the dataset but the analyst desires for them to be represented within the ML model as distinct entities, then an appropriate ML technique must be selected which is able to handle the collinearity. As we have seen in this section, many ML models rely on the distribution of feature values in that dimension to relate the feature's impact on the target variable, so our choices are limited.

Alternatively an appropriate method of dimensional reduction must be implemented as a pre-training data processing step.

Principal Component Analysis (PCA) is a well-known method of dimensional reduction by orthogonalization of the basis feature vectors . PCA entails imposing a transformation on the datapoints in feature space of n dimensions to an orthogonal space also of n dimensions. The result is that the feature values in orthogonal space are assured to be linearly independent from other features, however each dimension contains the sum of components from several (or perhaps many) otherwise physically unrelated features. While PCA enables the implementation of regression methods which require linearly independent features, PCA sacrifices the physical interpretability of such a model by collapsing the parallel components of multiple physically-distinct features into a single orthogonal dimension.

An alternative method of dimensional reduction was developed as part of this dissertation: grouping numerically correlated features together according to the presence of a physically-established functional relationship. In this way, features groups are numerically independent from one another as far as the ML can discriminate, but the analyst is aware that a single feature group represents the impact of several physically related features with high collinearity.

Is the problem NP-complete?

As mentioned earlier, since the correctness of each possible solution to the most likely

corrosion mechanism at play with the CCAs cannot be easily verified by a brute force approach, this is a strong indication that our problem at hand is not NP-complete (Non-deterministic Polynomial-time complete). This means that some popular algorithms such as single Decision Trees will be unsuitable to solve this problem [259].

Does the problem call for supervised or unsupervised learning?

Since we desire to determine which features are most effective at predicting outputs, it calls for a supervised learning method to train the model on what the outcomes should be. That said, unsupervised learning techniques such as K-means clustering can still assist to search for patterns within the data irrespective of any consideration of a "correct answer" by grouping samples with other "like" samples in ways that may be unexpected.

We frame the corrosion problem thus:

I. features are unlikely to be linearly related to the target variable, either as individuals or linear combinations
II. the feature set contains many collinear features
III. our problem is NP-incomplete.

Corrosion events are time-series dependent, so motivating questions are what is the initiating event, and what are the propagated processes. Therefore it would be shrewd to incorporate a feature that reflects whether a process is slow or fast, whether it is rate-limiting, or some kind of indication of whether it happens first, second, etc in the sequence of events. It proved difficult to engineer a data structure which allowed the ML to distinguish the time scale at which the processes happen. Nonetheless, through shrewd ML interpretation methodologies in this thesis work, a feature that represented the rate-limiting step in the mechanism could emerge. Some features also have a timescale built in - for example, potentiodynamic experiments have told us that the corrosion current of Fe is faster than that of Cr in the same halide at the same temperature [126] and that the corrosion current of Mo is

faster than that of W in the same halide at the same temperature [115] therefore if it is found that the corrosion is dominated by thermodynamics Cr over all other features, we can infer that the timescale of the corrosion current of Cr, and all other processes are happening either too fast or too slow to matter.

1.6.4 Literature Review: Machine Learning in Material Science to predict hypothetical materials and their properties.

Applications of Machine Learning to Materials Science in General

In the last 10 years, MI and ML have facilitated the understanding of open questions in the field of Materials Science [260], [261], facilitating the prediction of the following properties for large sets of theoretical materials: ductile to brittle transition temperature [262], microstructure [190], [263]–[266] Surface morphology [267], [268], polymer dielectric constant [269], [270], superconductivity [247], [271] Amorphous Glass forming ability [248], discovering new catalyst materials [272], [273], mechanical properties [274]–[276], irradiation resistance [52], corrosion [236].

Of the ML methods, NNs in particular have been investigated for their feasibility in being computationally cheaper replacements for density functional theory (DFT) [255], [277]–[279] which is sometimes coupled to molecular dynamics (MD) simulations [280]–[283]. Using ML in this way results in no new knowledge gained, representing a missed opportunity to leverage the potential of ML methods to facilitate filling gaps in our understanding of structure-function-property relationships [261], [284]. Therefore a more effective way to exploit the potential of NNs is to use them to search for patterns that draw links between ab initio atomic simulations and surface characterization data as was done by [285], [286] for example, or association rule mining of NN model trained on DFT simulations to predict elastic modulus of materials [280]. By extension, other ML algorithms can theoretically be similarly leveraged.

Applications of Machine Learning to predict material properties of hypothetical Compositionally Complex Alloys

By now it should become clear that the predictive power of ML can be leveraged by training a model on material properties of interest for CCAs that have been studied in order to predict the material properties for hypothetical CCAs, or even to suggest CCAs that should be explored that are predicted to optimize the property of interest.

ML has been used to predict the phrases of theoretical CCAs [287]–[289] their phase transitions [266]. These implementations of ML methods are computationally cheaper replacements for DFT but lamentably do not add to scientific understanding. CALPHAD is already able to perform this task.

ML models have been developed by training on experimental data to predict mechanical properties of CCAs such as yield strength[56], hardness [276] and elastic modulus [280].

In addition to CCA investigation strategies in which the investigator defines the scope of the alloys (in terms of composition, microstructure etc.) for ML, the Genetic Algorithm [290] and Cuckoo Search are algorithms work by generating new hypothetical materials based on the inputs and iteratively testing them against the optimization criteria for down-selection [225]. The genetic algorithm has been used to find hypothetical CCAs with high hardness, whose performance was later verified by experiment [225]. Cuckoo Search, has been coupled to MD simulations to find CCAs that optimize tensile strength [291].

Of particular note is the study in which high temperature oxidation of CCAs in air, supercritical carbon dioxide, steam and water was modeled with ML by [227] using a standardized database from the existing literature as input. A similar study on high temperature oxidation on NiCr in atmospheric and aqueous environments was done by [292] with a standardized experimental dataset. The

target variable for prediction both cases was the parabolic rate constant of oxide growth. In addition, both publications had in common that the dataset was trained on multiple MI and ML models were trained including Linear Regression, Bayesian Regression, Support Vector Machine, Random Forest, as well as Neural Nets, and their predictive performance compared using the figures of merit R^2 and MSE. These works are the closest in scope to this thesis found in the literature. However, since the corrosion environment studied are oxygen-rich, the theoretical model of corrosion concerned is dominated by oxide thickness growth as opposed to one dominated by elemental dissolution as is the case with a molten halide corrosion environment. The practice of evaluating multiple ML methods was adopted in this thesis, but the methodology of interpreting the ML model to glean physical insight must consider the disparity in theoretical frameworks.

ML models to predict CCA properties are generally trained only on composition and thermodynamic data at most [56], [227], [292]. This presents a missed opportunity to test hypotheses linking physical parameters other than thermodynamics - such as kinetics, microstructure and surface energetics - to determine the desired property. Such a study needs to have a mechanism in place to rank the relative importance of input features to provide the basis for sifting through a large field of features to determine the most impactful one.

It is concluded from this survey of the literature that this work is the first of its kind to embark on a large standardized dataset of experimental corrosion test data in molten salts of CCAs in a quaternary element space to develop a validated ML model for corrosion prediction. Therefore this thesis represents an original contribution to the body of knowledge in materials science and informatics as well as molten salt corrosion chemistry.

3.6.3 Interpretation of ML methods

"Interpretability is the degree to which a human can understand the cause of a decision."

Tim Miller, Explanation in Artificial Intelligence: Insights from the Social Science

"Interpretability is the degree to which a human can consistently predict the model's result."

Been et al, Advances in Neural Information Processing Systems, 2016

This section contains some content from the following article first-authored by the PhD candidate:

Bonita Goh, Yafei Wang,Phalgun Nelaturu, Michael Moorehead, Thien Duong, Pikee Priya, Moorehead, Dan J. Thoma, Santanu Chaudhuri, Jason Hattrick-Simpers, Kumar Sridharan, Adrien Couet, **Nobility vs Mobility: Unlocking New Insights into Molten Salt Corrosion Mechanisms of High Entropy Alloys with High-Throughput Experiments and Machine Learning-enabled Analysis**

A model with a high coefficient of determination R^2 value close to unity is not sufficient proof that it can be trusted to a) correctly evaluate new samples outside of the training set (aka generalize to out of bag samples), and b) provide physically meaningful interpretation [293]

It is possible for a model to fit the data to a high R^2 by having learned overly specific but ultimately meaningless rules; the model may fit the training samples very well but return wildly inaccurate results on out-of-bag samples. In such a scenario, the model is said to be overfitted and it generalizes poorly [234]

There is the matter of how to define the accuracy of an ML model in Materials Science. "Accuracy" is generally understood as "how far away" the ML predictions are from their ground truth values, yet the Material Informatics community has yet to come to a consensus on how to measure distance between the ML predictions and their ground truth values. A critical evaluation of the various model validation metrics in common use will be made in the following section and the case will be made for Mean Absolute Percentage Error (MAPE) as singularly superior compared to the others.

Cross-Validation (X-Val, abbreviation chosen to avoid acronym confusion with "Cyclic Voltammetry") is a step that can be added to the training step such that the evaluated accuracy of the trained ML model with X-val provides a better indication of how well the model will generalize to out-of-bag samples than the trained ML model without X-val.

To build a 5-fold X-val ML model, the entire sample set is divided into 5 subsets where 4 subsets are used to train the model and the last one is used to test per fold. This procedure is repeated for each of the 5 sets so that all samples are used to test exactly once. In this way, the average of fitting errors for every sample over the folds is anticipated to reflect the fitting error of a sample just like it if it were an out-of-bag sample. By randomizing the samples within each subset and using each subset as a test set at least once, every sample is treated as an out-of-bag sample at least once during the x-val process. The accuracy of the x-val ML model thus reflects the expected generalization accuracy by utilizing all training samples were out-of-bag samples during the x-val process. Another benefit of randomizing the samples within each subset is that the training population for each fold is less likely to contain sufficient frequencies of incident patterns - any patterns that consistently appear over the x-val manifold can be deemed substantial patterns worth exploring for interpretation

3.6.3.1 Dimensional reduction that preserves physical interpretability using Spearman Pruning

Dimensional reduction is an essential step towards developing an interpretable ML model. A common in multivariate materials science problems to determine the most impactful variable to the observed phenomenology - hence the need for methods in dimensional reduction. Principal Component Analysis (PCA) is a common way to perform dimensional reduction in materials science problems , which entails orthogonalizing the n-dimensional feature space by defining the new bases vectors as linear combinations of the collinear components in each of the original variables [294]

The Pearson's correlation coefficient between two variables x_1 and x_2 is defined as the normalization of the covariance of x_1 and x_2 (cov (x_1,x_2)) by the product of their standard deviations σ_1 and σ_2 :

$$Pearson's\ Correlation\ Coefficient = \frac{cov(x_1, x_2)}{\sigma_1 \cdot \sigma_2} \quad (19)$$

Pearson's value of 1 indicates perfect collinearity, -1 indicates perfect counter-collinearity and 0 indicates complete non-linearity. Since the Pearson's correlation coefficient is an indicator of the degree of collinearity between two variables, it can be expected that variables with high magnitude of Pearson's correlation with one another will be conflated to a high degree with one another during the PCA transformation.

While PCA is effective at attributing explained variance in the model to orthogonal components [228], [295], it tends to obscure the interpretability of an MI/ML model for the fact the dimensional transformation conflates multiple physical features into the same dimension regardless of whether or not they are physically related to one another, rendering them mathematically convoluted. An interpretable model seeks to increase the degree of deconvolution/linear separability of features rather

than the opposite.

With this philosophy, this thesis work adopts an alternative method of dimensional reduction, here referred to as Spearman Pruning.

In the same spirit as Pearson coefficient, the Spearman correlation coefficient r_R is a useful metric for expressing the degree of monotonic correlation between two variables, where a pair of variables that are perfectly monotonic to one another will have a value of unity whereas a pair of variables with no monotonicity whatsoever will have a value of 0. A pair of variables that are perfectly anti-correlated will have a value of -1. The formula for the Spearman coefficient is:

$$r_R = \frac{6\sum_i d_i^2}{n(n^2-1)} \quad (20)$$

Where n is the number of data points and di is the difference in ranks of the i^{th} element. We use the Spearman coefficient throughout our paper to indicate the degree to which two variables are functionally related. For dimensional reduction, features with a high Spearman coefficient which did possess physical interrelationships with one another were grouped as a single feature and input into the model as a "single feature". In this way, the model treats the correlated features as a single entity mathematically, and they can be interpreted as a group of features linked by thermodynamics (eg. The Nernst equation) or kinetics etc.

3.6.4 Critical evaluation on validation metrics for ML in Materials Science.

It has also recently become more common among the machine learning community to use coefficient of determination R^2 [55], [56], [299], [300], [227], [228], [247], [274], [292], [296]–[298] to validate an ML model. Excellent R^2 values of >0.9 are often accompanied by magnitude of prediction

errors (eg. mean square error, MSE and absolute error, MAE) [56], [227], [302], [228], [247], [273], [274], [280], [299]–[301] as metrics to measure the accuracy of an ML's prediction in regression-type problems. Despite their common usage, MSE and MAE do not represent the relative distance of a prediction value from the parity line well, whereas Mean Absolute Percentage Error (MAPE) is a metric that is better able to represent the scatter of data about the parity line.

The comparison between the performance of various ML methods to solve corrosion problems by [236] (Figure 25a) finds R^2 to be >0.9 for NN and tree-based methods, justifying the choice of method used in this thesis. They find that R^2 of the model to be higher if the corrosion problem is treated as a time-series problem than (green) if the time-series component was ignored (red). MAPE is recommended here as a metric that is singularly superior to R^2 in unambiguously reflecting how tightly the predictions are scattered around the prediction-experiment parity line, and better than MSE at reflecting the relative accuracy of predictions. When data spans many orders of magnitude, it is possible for a relatively accurately predictive model to reflect an unfairly high MSE if the set contains one or two outliers in the high-magnitude domain that are inaccurately predicted. When R^2 and RMSE for multiple different ML models are tabulated and compared [227], it is not immediately clear which ML model is the most accurate because of the wide variance in R^2 and RMSE in different directions. It was also mentioned in the previous section that a high R^2 is no guarantee that a model is generalizable [293], RMSE is a flawed metric because it is possible to present it with a low value by a clever choice of units. In other words, a survey of the literature finds reports of R^2>0.9 and low RMSE to be overly flattering representations of the data since visual inspection finds data often exhibits more scatter around the parity line than one would expect based on the metrics.

Pearson's R is occasionally used as a substantiation of ML prediction accuracy [52], [254], [303] but since it is only a measure of linearity between two variables, it is not a singularly convenient indicator of how close the slope of linearity is to unity. A reader's inspection reveals the references cited

herein generally indicate MAPE values of ~40%, suggesting that ML prediction accuracy for material properties with MAPE ~40% for sample sets of hundreds of datapoints is considered acceptable to the community at the time of this writing for ML applied to materials science in general [299] and to corrosion problems in particular [236]Figure 25b.

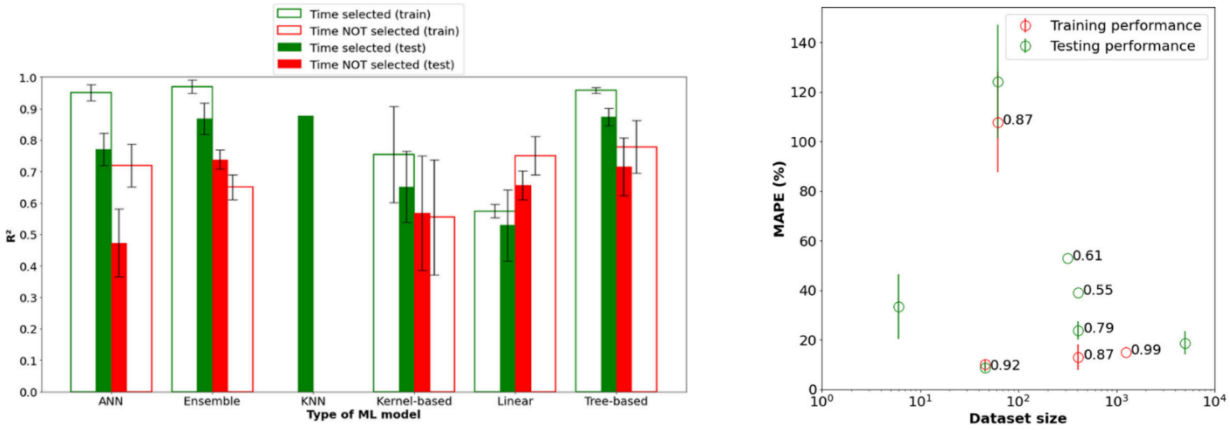

Figure 25: [236] *(a) The Mean R^2 as a function of the "Type of ML model", depending on whether time-series was accounted for or ignored in the problem (b) the mean MAPE as a function of dataset size.*

3.6.4.1 A general mathematical framework for the interpretation of ML results and the Shapley approach in particular

Having established that ML models are different in nature from conventionally understood mathematical models and MC simulation models, a different paradigm is needed to gain physically meaningful insights from ML models than the intuition applied to mathematical or MC simulation models.

This paradigm shift in mindset begins by accepting that we need a surrogate mathematical

function to express the interpretability of the ML model f(x') where x represents the physical feature values. Let us call this surrogate "explainer function" [304] g(z'), where z' denotes the feature value x' mapped into "explainer space". In an intuitively understandable model, f and g are equivalent and feature value x' maps directly onto z'. We therefore express the explainer function as a linear equation:

$$g(z') = \varphi_0 + \sum_{i=1}^{M} \varphi_i z'_i \qquad (21)$$

Where each φ_i is simply an arbitrary quantization of the impact of the i^{th} feature x'—> z' to the model; φ_i are normalized to the scale of the output distribution. The key to understanding the model is to determine the φ values for the various features. (the term "impact" tis used o avoid confusion with "Gini importance" on account of their mathematical distinctness from one another).

For linear models with a feature set containing multi-collinearity, it is efficacious to use Shapley regression to define values of φ_i in such a way that φ_i represents numerical impact on the model prediction for the inclusion of this feature. To calculate φ_i, a model using the universal set of all features fsU{i} is trained, and another model excluding feature i, fS, is trained. The difference between the results of the two models is the impact of withholding feature i from subset S. The aggregate impact of feature i on the model, φ_i , is computed by taking the aggregate impact of i over all possible feature subsets that exclude it.

$$\varphi_i = \sum_{S \subseteq F\{i\}} \frac{|S|!\,(|F| - |S| - 1)!}{|F|!} \left[f_{S\cup\{i\}}\left(x_{S\cup\{i\}}\right) - f_S(x_S) \right] \qquad (22)$$

S denotes the number all permutations of proper subsets within the universal set of F features.

This is the basis for the computation of SHapley Additive exPlanation (SHAP) values adopted in this thesis for analyzing any ML results. The larger the magnitude of the SHAP for a particular feature, the more impactful to the model it is.

4 Development of HTP platform for corrosion analysis

This chapter features direct content form the following article first-authored by the PhD candidate:

Bonita Goh, Yafei Wang,Phalgun Nelaturu, Michael Moorehead, Thien Duong, Pikee Priya, Moorehead, Dan J. Thoma, Santanu Chaudhuri, Jason Hattrick-Simpers, Kumar Sridharan, Adrien Couet, **Nobility vs Mobility: Unlocking New Insights into Molten Salt Corrosion Mechanisms of High Entropy Alloys with High-Throughput Experiments and Machine Learning-enabled Analysis**

It also contains some content from the following journal article co-authored by the PhD Candidate:

Yafei Wang, Bonita Goh, Phalgun Nelaturu, Thien Duong, Najlaa Hassan, Raphaelle David, Michael Moorehead, Santanu Chaudhuri, Adam Creuziger, Jason Hattrick-Simpers, Dan J. Thoma, Kumar Sridharan, Adrien Couet, **Integrated High-Throughput and Machine Learning Methods to Accelerate Discovery of Molten Salt Corrosion -Resistant Alloys,** *Advanced Science, 2022, 9, 20*

4.1 Sample Production: In Situ Alloying

110 alloys, 100 of which lie within the single phase FCC and FCC+BCC dual-phase fields of the CrFeMnNi CCAs, were successfully additively printed on a Laser Engineered Net Shaping (LENS) instrument, homogenized, aged, mirror-polished and corroded in molten salts following the method outlined in [178]. As shown in Figure 1, an Optomec LENS MR-7 system equipped with four hoppers filled with individual Cr, Fe, Mn, and Ni powders was utilized for the additive manufacturing fabrication

of the 110 CrFeMnNi alloys. During the alloy fabrication, flowing Ar gas carried the powder from the hoppers into the laser beam path. Following calibration, the printed alloy composition was controlled by the hoppers' auger RPM. The nominal printed alloy dimensions were 11mm x 11mm x 2mm with 25 alloys printed on each SS316 build plate. Each printed alloy comprised five print layers, with two remelting passes after each print layer to minimize unmelted powder fraction [167].The hatch spacing was 0.381 mm for the print layers and 0.19 mm for the remelting layers, with a 90° rotation of the hatch pattern between each subsequent print/remelt layer. Detailed description regarding the additive manufacturing process can be found in [178]. The 25 alloys on a build plate were simultaneously homogenized at 1000°C for 24 hours in a vacuum furnace, and heat treated at 700 °C for 24 hours to obtain a thermodynamically stable microstructure. Figure 26a

Prior to corrosion testing, printed alloys were ground with SiC abrasive papers from 400-1200 grit following which they were polished with polishing pads and 3μm, 1μm diamond suspensions, as well as 0.04μmcolloidal silica suspension. Finally they were cleaned by ultrasonication with water, ethanol, and acetone in succession [178].

4.2 The Experimental Platform

4.2.1 Standardized Pill Testing Procedure

As illustrated in Figure 1, a high throughput molten salt corrosion experiment was used as detailed in [178]. LiCl-KCl eutectic salt (in ratio 59:41 wt%) with 2 wt% $EuCl_3$ addition was used. To perform the corrosion experiment, small salt pills, about 0.37 g in mass, were pelletized in a custom-fabricated tungsten carbide die and compacted using a manual hydraulic press at a constant load of 2.5 tons for 2 minutes. The salt pellets were placed on the surface of each printed alloy. Then the entire plate

was heated on a heating plate at 500°C resulting in a molten salt droplet on each printed alloy. While the entire printed alloy surface was wetted by the salt, the salt droplet remained on the surface of each printed alloy due to surface tension. About 5% of the test set experienced salt spillage and in these cases the corrosion tests were redone. The inclusion of 2wt% $EuCl_3$ served to maintain a relatively high and constant chloride potential in each salt pill during the exposure [305]–[307]. The corrosion experiment was performed for 96 hours after which the heating plate was shut down, the salt droplet solidified, and the salt removed from the surface of each alloy for ICP-MS analysis at the Wisconsin State Hygiene Laboratory, following procedure detailed in [107].

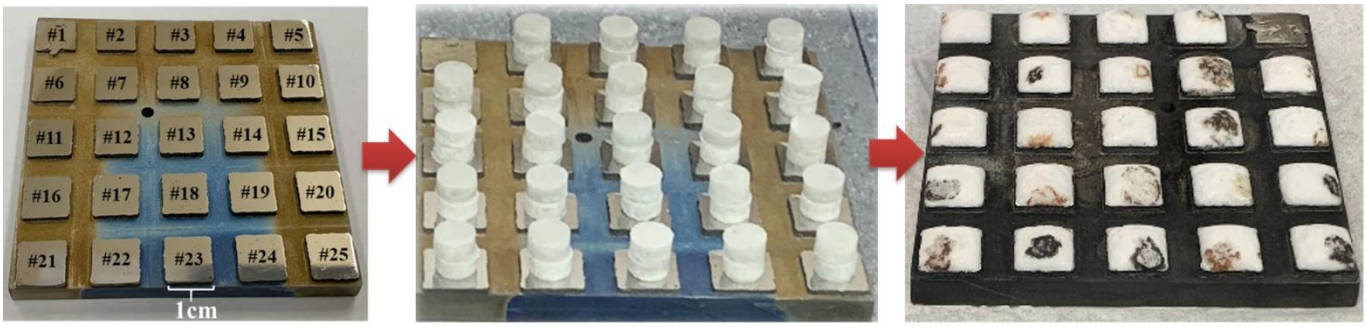

(a) *(b)* *(c)*

Figure 26 (a) Build plate with alloys after printing and heat treatment using the processes developed by (b) Standardized salt pills arranged on build plate prior to start of corrosion experiment. (c) Post corrosion salt pills. Photo credit: Dr Yafei wang [178]

4.2.2 Maintaining chlorine potential of each pill corrosion environment

The chlorine potential of the salt is controlled by the equilibrium of the Eu^{3+}/Eu^{2+}:

$$EuCl_3\ (m) \rightleftharpoons EuCl_2\ (m) + Cl^-\ (m) \qquad \Delta E^o_{Eu3+/Eu2+} \qquad (23)$$

The Nernst equation for this reaction can therefore be used as a proxy to determine chlorine potential:

$$\Delta E_{Eu3+/Eu2+} = \Delta E^{o}_{Eu3+/Eu2+} - \frac{RT}{nF} ln(\frac{a_{EuCl2} \cdot a_{Cl-}}{a_{EuCl3}}) \quad (24)$$

Where $\Delta E^{o}_{Eu3+/Eu2+}$ is the standard reduction potential of Eu^{3+} to Eu^{2+}, T is the temperature in K, R is the ideal gas constant in $[J \cdot K^{-1} \cdot mol^{-1}]$, a_{EuCl2} is the activity of $EuCl_2$ in the salt, a_{EuCl3} is the activity of $EuCl_3$ in the salt, and a_{Cl-} is the activity of chloride anion in the salt. The chlorine potential for every salt pill at the start of the experiment is uniform since they were prepared from the same large batch of LiCl-KCl-2%$EuCl_3$ eutectic.

With a conservative assumption that the corrosion of Cr, Fe, Mn, Ni all occurs as oxidation to the divalent state, balanced by monovalent reduction of Eu^{3+} according to equation (23), the chlorine potential at the end of the corrosion period was calculated for each salt pill by:

$$\Delta E_{Eu3+/Eu2+} = \Delta E^{o}_{Eu3+/Eu2+} - \frac{RT}{nF} ln(\frac{c_{tot} \cdot a_{Cl-}}{(2\% - c_{tot})}) \quad (25)$$

Where c_{tot} is the total corrosion concentration of analytes (Cr+Fe+Mn+Ni). As shown in the results section, the total corrosion concentration of analytes in the salt determined by ICP-MS is on the order of 0.1%, therefore the 2nd term in equation (7) is very small, and the calculated *perturbation* to the chlorine potential across all corrosion samples is ± 0.05 V.

4.2.3 Verifying the Repeatability of the Pill Corrosion Experiments

The repeatability of the pill corrosion tests was verified by experiment. Six replicates of the molten salt droplet corrosion experiments were performed using SS316 coupons purchased from McMaster-Carr. These SS316 coupons were prepared for the corrosion experiment as detailed above. The objective of the

replicate experiment was to estimate the experimental variance in the corrosion tests by measuring the total concentration of corrosion products in the replicates.

The average total concentration of (Cr+Fe+Mn+Ni) corrosion products measured in post-corrosion salt by ICPMS from the SS316 samples was found to be (1194 ± 163) ppm giving an experimental standard deviation of about 13.7%. Pre-corrosion and post-corrosion XRD were compared, and the microstructure did not change after corrosion with only a slight lattice parameter extension. The typical post-corrosion surface morphology can be seen in the SEM in Figure 27

Method development was done by the PhD candidate. Acknowledgment for performing the pill corrosion repeatability experiments goes to lab intern Isabelle Baggenstoss.

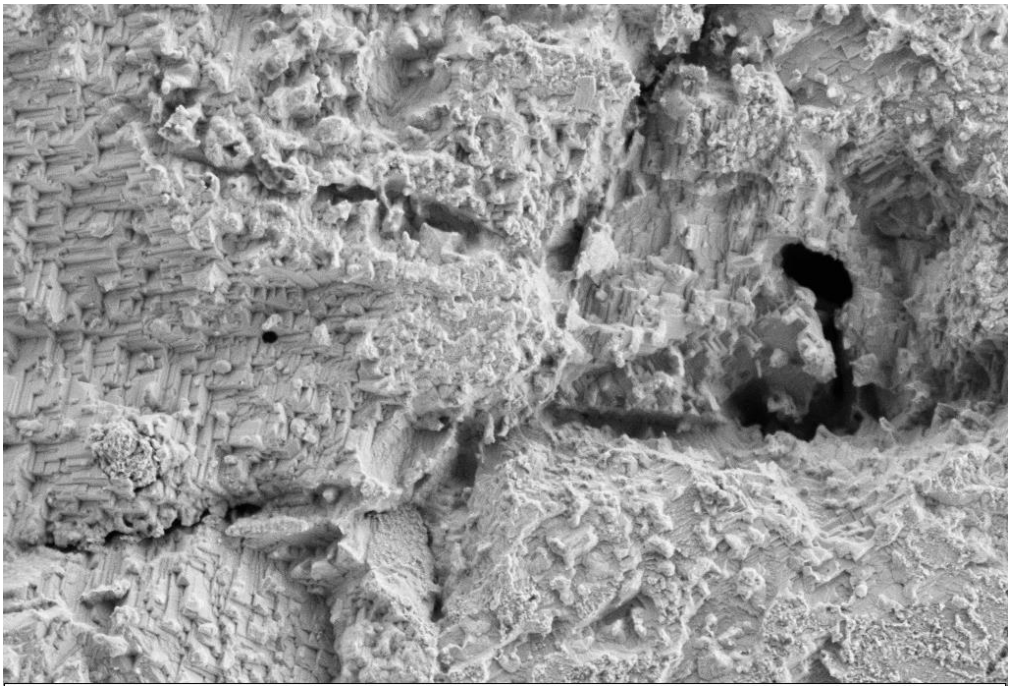

Figure 27 SEM of post-corrosion SS316 taken by Dr Yafei Wang.

4.3 Collation of the ML input matrix

4.3.1 Data sourced from databases: CALPHAD: MS-CRADLE, PANDAT & HSC.

Each of the alloys printed is featurized by quantified thermodynamic, kinetic, surface energetic parameters derived from their composition. These features were organized in a matrix. This data was sourced from various databases: MS-Cradle which is owned and maintained by Dr Santanu Chaudhuri, Pan HEA)v. 2021, both of which are CALPHAD-based databases, and HSC v.6.

CALculation of PHAse Diagrams (CALPHAD) utilizes a computational method of extrapolating thermodynamic and kinetic parameters of higher order alloy systems based on experimental data for binary and ternary alloy systems [308] The database contains sufficient data on thermophysical and thermochemical properties and their phase equilibria on relevant binary and ternary alloys to the one of interest. The calculation scheme then entails determining phase equilibria for the higher-order - CCA- composition of interest from which the thermophysical or thermochemical properties of interest can be derived using a model with built-in adjustable parameters. Further details can be found in [308].

The following thermophysical/thermochemical features were obtained for each alloy from the PanHEA database at 500 ^{o}C: solid solution phase fraction, elemental surface activity, Gibbs Free Energy of alloy formation, Enthalpy of formation of alloy, elemental chemical diffusion, and tracer diffusion coefficients. Diffusion coefficients are specified by phases, so they are strongly influenced by phase fraction.

Texture-specific surface energy and work function for the planes (100), (110), (111) were obtained for each alloy from the MS-Cradle database. MS-Cradle couples CALPHAD to DFT for first-principles derivation of parameters of interest [309] and ML to decrease computational cost of performing the prediction [bokeh plot].

Gibbs Free Energy (GFE) of formation for the corrosion products of interest, $CrCl_2$, $FeCl_2$, $MnCl_2$

and $NiCl_2$ were calculated using standard free energy of formation ΔG^o for these products obtained from HSC v.6 and the Nernst equation. This represents the thermodynamic favorability of an alloy to form corrosion products in Cr, Fe, Mn and Ni, and it is strongly influenced by the activity of the metal on the surface eqn *(2)*

$$\Delta G_{M/MCl_2} = \Delta G^{o}_{M/MCl_2} + RTln\left(\frac{a_{MCl_2} \cdot P_{Cl_2}}{a_{M,surf}}\right) \quad (2)$$

It was hypothesized [178]that a possible sacrificial corrosion relationship may occur between pairs of elements if their ratio meets some threshold value. In this vein, mole fractions of the reactive alloying elements were calculated and included as features.

Since some particular mechanical properties observed in CCAs have been attributed to entropy of mixing S_{mix} [39], [310], it was also desired to study whether S_{mix} had any impact on corrosion performance. ΔS_{mix} was estimated for each alloy by $\Sigma\, x\ln x_i$ where x_I is the mole fraction of the i^{th} element in the alloy, for inclusion in the input matrix.

The entire list of features is included in the next section for convenient reference.

4.3.2 Contribution of EBSD endearments to the input matrix

The texture fraction of (100), (110) and (111) planes were measured for 7 of the alloys in the total dataset by Electron Backscatter Diffraction (EBSD) on a Zeiss LEO 1530-1 FESEM. The EBSD data was collected using an accelerating voltage of 20 kV and a current of 51 nA. A step size of 3 μm was used to scan a nominal area of 700 μm × 900 μm on the sample surface. The EBSD data was analyzed using the Crystal Direction function on OIM Analysis Software v.8. Color-coded texture fractions for (100) in red, (110) in yellow and (111) in blue are shown in Figure 27, representative of the data from 7 samples. The average texture fractions are found to be (0.17 ± 0.06) for (100), (0.50 ± 0.11) for (110), (0.23 ± 0.06) for (111). Texture fractions have a fairly low variance between samples and the (110) fraction is the most

prevalent, even visibly so. These texture fractions are used to calculate the texture-fraction weighted surface energy γ and work function φ for each sample.

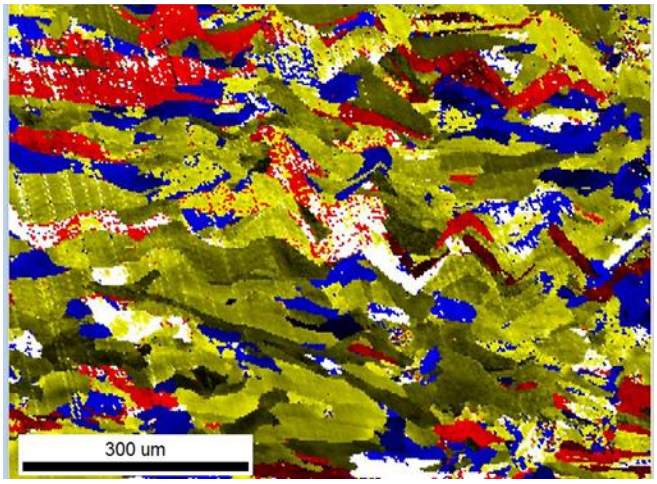

Figure 28: EBSD analysis on the alloy samples was performed by Dr Phalgun Nelaturu. Data reduction for this section was performed by the PhD candidate.

4.3.3 Complete list of features for ML input

Table 15: Complete list of features for ML input

Feature index no	**Feature**
1	No of Measured phases
2	(100) Surface Energy
3	(110) Surface Energy
4	(111) Surface Energy
5	(100)Work Function
6	(110)Work Function
7	(111)Work Function
8	Sample Surface Energy (texture-fraction weighted surface energy of the alloy)
9	Sample Work Function (texture fraction weighted work function of the alloy)
10	atomic fraction (Cr)
11	atomic fraction (Fe)
12	atomic fraction (Mn)
13	atomic fraction (Ni)
14	atomic fraction (Cr+Fe+Mn)
15	atomic fraction (Cr+Fe)
16	ratio Fe:Mn
17	ratio Cr:Mn
18	ratio Fe:Cr

19	ratio (Cr+Fe):Mn
20	ratio Fe:Ni
21	mixing entropy
22	bond probability(Cr-Cr)
23	bond probability(Cr-Fe)
24	bond probability(Cr-Mn)
25	bond probability(Cr-Ni)
26	bond probability(Fe-Fe)
27	bond probability(Fe-Mn)
28	bond probability(Fe-Ni)
29	bond probability(Mn-Mn)
30	bond probability(Mn-Ni)
31	bond probability(Ni-Ni)
32	activity(Cr)
33	activity(Fe)
47	activity(Mn)
35	activity(Ni)
36	GFE_formation of alloy
37	GFE_formation of corr pdt(CrCl2)
38	GFE_formation of corr pdt(FeCl2)
39	GFE_formation of corr pdt(MnCl2)
40	GFE_formation of corr pdt(NiCl2)
41	phase fraction (Bcc)

42	phase fraction (Fcc)
43	phase fraction (L12-FCC)
44	phase fraction (H-L21)
45	phase fraction (Sigma)
46	Enthalpy of alloy formation
47	Tracer Diffusion coefficient of Cr in the BCC phase
48	Tracer Diffusion coefficient of Cr in the FCC phase
49	Phase-weighted Tracer Diffusion coefficient of Cr
50	Tracer Diffusion coefficient of Fe in the BCC phase
51	Tracer Diffusion coefficient of Fe in the FCC phase
52	Phase-weighted Tracer Diffusion coefficient of Fe
53	Tracer Diffusion coefficient of Mn in the BCC phase
54	Tracer Diffusion coefficient of Mn in the FCC phase
55	Phase-weighted Tracer Diffusion coefficient of Mn
56	Tracer Diffusion coefficient of Ni in the BCC phase
57	Tracer Diffusion coefficient of Ni in the FCC phase
58	Phase-weighted Tracer Diffusion coefficient of Ni
59	Mean Electronegativity of alloy
60	Chemical diffusion coefficient of Cr in FCC & BCC phase
61	Cross-diffusion coefficient of Cr vs Fe in FCC & BCC phase
62	Cross-diffusion coefficient of Cr vs Mn in FCC & BCC phase
63	Cross-diffusion coefficient of Cr vs Ni in FCC & BCC phase
64	Chemical diffusion coefficient of Fe in FCC & BCC phase

65	Cross-diffusion coefficient of Fe vs Cr in FCC & BCC phase
66	Cross-diffusion coefficient of Fe vs Mn in FCC & BCC phase
67	Cross-diffusion coefficient of Fe vs Ni in FCC & BCC phase
68	Chemical diffusion coefficient of Mn in FCC & BCC phase
69	Cross-diffusion coefficient of Mn vs Cr in FCC & BCC phase
70	Cross-diffusion coefficient of Mn vs Fe in FCC & BCC phase
71	Cross-diffusion coefficient of Mn vs Ni in FCC & BCC phase
72	Chemical diffusion coefficient of Ni in FCC & BCC phase
73	Cross-diffusion coefficient of Ni vs Cr in FCC & BCC phase
74	Cross-diffusion coefficient of Ni vs Fe in FCC & BCC phase
75	Cross-diffusion coefficient of Ni vs Mn in FCC & BCC phase

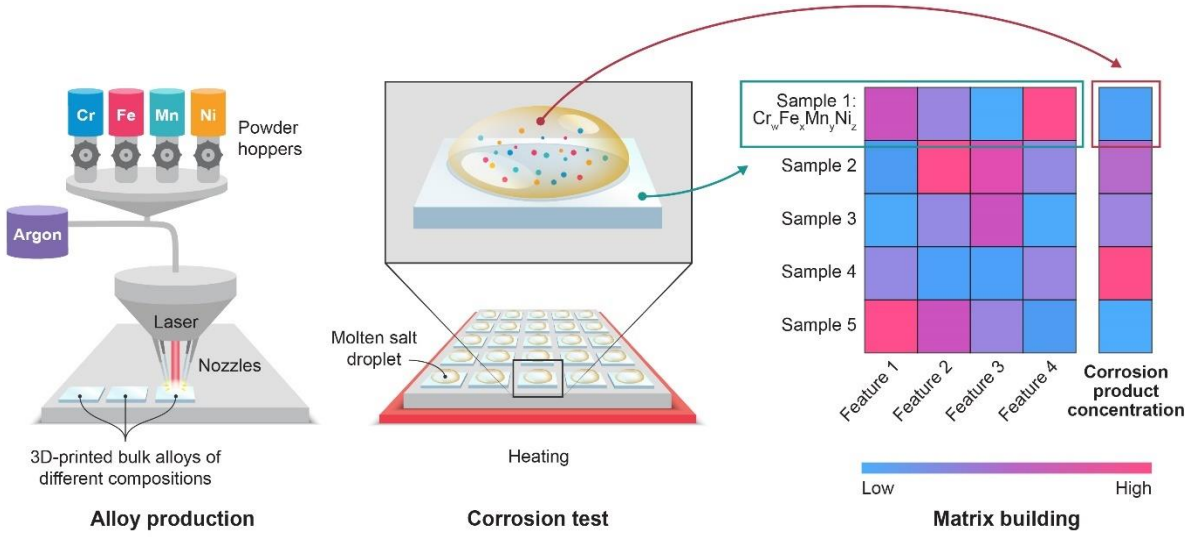

Figure 29. Schematic of the process from additive manufacturing of CrFeMnNi alloys, then corrosion testing of the alloys with molten salt droplets in individually isolated corrosion environment and, in parallel, featurization of each alloy by thermodynamic, kinetic and otherwise physical parameters for organization into a matrix for training/testing machine learning model.

4.3.4 A critical comparison of ICPMS and GDOES for quantifying molten salt corrosion products

This section contains direct content from the following articles first-authored by the PhD candidate:

Investigation of Alloy's Surface Recession in Molten Salt Corrosion by the comparative assessment of GDOES and ICPMS analyses

Bonita Goh[1], Yafei Wang[1], Phalgun Nelaturu[1], Michael Moorehead[1], Louis Bailly-Salins, Raphaelle David[1], Kumar Sridharan[1,2], Adrien Couet[1,2]

[1]Department of Engineering Physics, University of Wisconsin-Madison, WI 53706, USA

[2]Department of Materials Science and Engineering, University of Wisconsin-Madison, WI 53706, USA

1. Introduction

Nuclear power is an indispensable component of the global energy production portfolio. This paradigm becomes ever truer as the pressures of anthropogenic climate change mount for the world to replace fossil fuels as its primary energy source. As of 2021, 2,500 TW[4] of the 170 000 TW total global energy burden [311] is shouldered by nuclear power, primarily utilizing Gen III light water reactors (LWR)[312]. For the next generation of reactor designs, the Gen IV Molten Salt Reactor (MSR) concept aims to improve upon reactor fuel utilization and reactor efficiencies as well as inherent safety by employing molten alkali-metal/halide eutectic salts as fuel media and/or coolant media[312]. Unfortunately, despite their favorable heat transfer and hydraulic properties, molten halides are notoriously harsh corrosive environments to structural alloys. Therefore, understanding the basic science governing corrosion resistance against molten halides at high temperature [313]–[316] is imperative to the development of structural materials suitable to

be licensed for MSRs.

Corrosion modes are largely understood from the perspective of thermodynamically favorable species for forming corrosion products. In the case of molten halide salts, where the oxide layers are not stable, the main corrosion mode is dissolution. Preferential dissolution of the most susceptible element results in a depletion profile in the substrate. This understanding generally holds until about 53% of the alloy is made of one main noble element (i.e., known as the room temperature parting limit), below which de-alloying can occur. In addition, Fe, and even Ni, may not be stable in molten salt environments of MSRs due to the presence of oxidizing impurities or fission products, causing alloy surface recession. The recent increase in interest in High-Entropy Alloys (HEAs)[70], [317] as promising MSR structural materials [42], [52], [115], [120], [145], [152], [318] renders the former paradigm of analyzing corrosion mode from a single base element obsolete. Novel approaches are required to systematically study HEAs to understand the primary drivers behind their corrosion modes.

The first critical question to be answered relative to corrosion modes is if these alloys systematically experience significant and observable surface recession. If surface recession occurs at a relatively high rate in a particular alloy, all other corrosion modes (relative elemental depletion, grain boundary corrosion, phase separation, etc.) can be understood as secondary processes, that further degrade the material beyond uniform thinning of the material thickness.

Several characterization methods are commonly applied to study material degradation in molten salts:

- Energy Dispersive Spectroscopy (EDS) is used in the analysis of differential elemental depletion [91], [315], [319]; however it has several shortcomings, such as i) difficult to obtain quantitative data, ii) difficult to do a systematic comparison with large datasets due to time consuming sample preparation, and iii) analysis limited to a localized area;
- Inductively-Coupled Plasma Mass Spectrometry / Optical Emissions Spectroscopy (ICPMS/OES) are

prevalently used in the community to determine total loss by element [320], [321] but also have several shortcomings, such as i) heterogeneous analyte sampling on the order of 1g salt aliquots chiseled off bulk frozen salt from corrosion experiments, b) does not account for certain species of salt-impurity driven corrosion - in particular Cr_2O_3 - that are notoriously difficult to completely digest by common acid preparations such as concentrated HNO_3 and HCl or even aqua regia;

- Glow Discharge Optical Emissions Spectroscopy (GDOES) is a technique with the capability to analyze alloy samples post-corrosion in molten salts [322]–[327] resulting in differential elemental depletion, but its shortcomings are i) it is not a high throughput (HTP) method, and more importantly ii) GDOES analysis does not account for the effects of surface recession.

To this end, this study investigates the corrosion results of 90 unique HEAs in the CrFeMnNi quaternary compositional space. The dissolved Fe, Cr and Mn into the salt from each alloy was quantified by standardized ICPMS analysis. The results are compared to the integration of diffusion depletion profiles determined by a standardized GDOES analysis of the post-corrosion alloy surfaces. The purpose of this study is twofold. It aims at demonstrating that surface recession is broadly observed in 90 unique CrFeMnNi alloys mostly distributed over the FCC phase space, and that common digestion procedures for salt elemental analysis for ICPMS/OES comprising HCl and HNO_3 leave some corrosion products undigested; instead, samples must be digested by concentrated H_2SO_4 to completely digest all possible chemical forms of corrosion species of alloy components.

2. Methods

2.1. Sample preparation and corrosion experiments

90 unique alloy compositions within the CrFeMnNi quaternary composition space were additively manufactured on a Laser Engineering Net Shaping (LENS) system, each as 1cmx1cmx2mm samples on a

316 stainless steel buildplate. This was performed on an Optomec LENS MR-7 system using gas-atomized elemental powders of Cr, Fe, Mn, and Ni with a size distribution of 45-150um. Detailed description on the manufacturing process can be found in [167]. Before the corrosion experiment, the top surface of each alloy was leveled and polished with SiC abrasive papers up to 1200 grit and then with polishing pads using 3 µm, 1 µm diamond suspensions and 0.04 colloidal silica suspension. Based on the high-throughput corrosion experimental method outlined in our previous study [178], each of these 90 unique alloys was corroded by a ~0.37g droplet of LiCl-KCl eutectic salt, with 2wt% $EuCl_3$ added, at 500 °C. LiCl-KCl was purchased as anhydrous from Sigma Aldrich at 99.9% purity and only opened and used in glovebox for the corrosion experiments in an inert environment with O_2<1ppm and H_2O<0.1ppm [178]. During the corrosion testing, the top surface of each alloy sample was completely covered by the molten salt droplet as evidenced by post corrosion examination. After a corrosion period of 96 hours, the molten salt droplet was allowed to refreeze at room temperature, and was then removed from the top surface of each alloy.

2.2. ICPMS analysis

Pre-corrosion LiCl-KCl was analyzed by ICPMS for 55 elements for baseline concentrations. Table 16 shows the results of this analysis for specific elements of interest:

Table 16: Analysis of pre-corrosion salt by ICP-MS for analytes of interest in [µg of analyte / g of salt]

Analyte	Cr	Fe	Mn	Ni	P	S
Concentration [µg/g]	0.161	0.88	0.035	0.08	0.18	8.31
Uncertainty [µg/g]	0.008	0.28	0.006	0.02	0.04	0.26

The pre- and post-corrosion LiCl-KCl salt pills are prepared for ICP-MS analysis [328] by dissolving the

entire salt pill in 2.00mL of 12M aqueous HCl with the addition of 0.50 mL of 16M aqueous HNO_3. They are then refluxed at 95°C for 4 hours on a hot block. Afterwards each sample digest is volumetrically diluted with deionized (DI) water up to 50.0mL. Prior to loading on the ICP-MS instrument (Thermo-Finnegan 2XR Magnetic Sector ICP-MS), each sample's aqueous solution is further diluted in 1:20 ratio, which enables the analytes' concentration of interest to fall within the mass detector's dynamic range for quantification according to the instrument's maximum precision. Results are corrected by subtracting sample preparation method blanks prior to reporting. The calibration of the ICP-MS was performed by measuring series of multi-element calibration standards containing Cr, Mn and Ni at (0, 0.4, 2, 20)ppb and Fe at (0, 80, 400, 5000)ppb and ascertaining an $R^2 > 0.995$, according to the procedure in [107].

Due to the sample preparation procedure, which entails dissolution in aqueous media where there is an abundance of H and O, baseline H and O impurities in the anhydrous salt cannot be accurately and directly measured by ICP-MS. This is a significant disadvantage of the technique, as it does not allow the investigation of moisture and oxide driven corrosion mechanisms. Instead, P and S impurities may be used a proxy indication of the presence of O in the salt as PO_4^- and SO_4^{2-} [329], [330]. From the results in Table 16, it may be inferred that the O concentration from O-bearing P and S impurities has an upper limit of 33 [μg/g]; This concentration of S impurities is low enough such that its impact on sample weight loss is negligible [331]. Furthermore stoichiometrically this suggests an upper limit of 132ppm of elemental O present in the salt from phosphate and sulphate anions. Of course this does not account for impurities due to oxides or other oxygen containing species.

The mass of each post-corrosion salt droplet was measured such that the total quantity of each element dissolved in salt can be precisely calculated from the ICP-MS analysis results. Assuming all corrosion products dissolved in the salt are soluble in the acidic aqueous solution required for ICP-MS analysis, the total quantity of each element dissolved in the salt can be obtained by simply multiplying the concentration of the dissolved elements of interest from the ICP-MS by the mass of each salt droplet. The quantification

uncertainty for ICP-MS is taken as the Root Sum Square (RSS) of standard deviations for i) instrumental sensitivity for the analyte; ii) measurement uncertainty for analytical and digestion dilution factors; iii) quadruplicate method blank measurements; and iv) triplicate measurements for each sample. In general, the quantification uncertainty for ICP-MS measurements of each analyte is ~5%.

2.3. GDOES analysis

By contrast to ICP-MS, elemental analysis by GDOES needs no sample preparation. The post-corrosion sample is loaded directly onto the instrument with the surface to be analyzed facing a cylindrical copper anode; the sample acts as the cathode. A pulsed radiofrequency is applied between the anode and cathode, forming a plasma. The plasma sputters the atoms off the sample and the plasma characteristic elemental photon emissions plasma are quantified by polychromators. The depth-resolved elemental concentrations of Cr, Fe, Mn, and Ni is analyzed through a depth of 40μm (as measured by profilometry) with a circular sputtered area of 4mm diameter. The spatial resolution of the depth profile is $9x10^{-3}$ μm. To study the present set of samples, the flushing time was 80s, preintegration time 200s, background 5s, pressure 550 Pa, RF power was 40W, with module 7V and phase 4V.

The GDOES instrument used in this study is a Horiba GD-Profiler 2 located at the Nanoscale Imaging and Analysis Center at the University of Wisconsin - Madison. Calibration was performed by determining the values of the constants k_i, e_i, and q_{rel} relating light intensity I_i detected (number of photons) for element i to the amount of the element (number of atoms) c_i, as shown in Equation 1 [332]:

$$I_i = k_i e_i q_{rel} c_i + b_i \qquad (26)$$

where k_i is the instrumental detection efficiency for the element i and e_i is the emission efficiency for the element i, defined by the number of photons at characteristic energies emitted per mole of element. As a general rule, k_i and e_i are element dependent but not material dependent.

q_{rel} is the relative sputtering rate in mg/m^2/s of material compared to a reference and is assumed to be constant between elements in the same sample. It is as defined as:

$$q_{rel} = \frac{q}{q_{ref}} \tag{27}$$

where q is the absolute (measured) sputtering rate determined by measuring crater depth with a Zygo New View 9000 Profilometer, and q_{ref} is the sputtering rate of a reference sample.

The measured intensity I_m must be drift-corrected prior to plugging into equation (26) to determine c_i. The drift correction accounts for the drift in emission intensity detected by the instrument due to changes in conditions (spectrometer drift over time, plasma instability) over time between calibration measurement and sample measurement. The relationship between I_m and the drift-corrected intensity I_c can be expressed as:

$$I_c = \alpha I_m + \beta \tag{28}$$

where the correction coefficients α and β are calculated from the intensities of a sample with relatively high intensity (I_H), and relatively low intensity (I_L), at the moment of calibration (I^0_H and I^0_L) and at the moment of drift correction (I'^0_H and I'^0_L) [332]:

$$\alpha = \frac{I_H^0 - I_L^0}{I'_H - I'_L} \tag{29}$$

$$\beta = \frac{I_L^0 I'_L - I_H^0 I'_L}{I'_H - I'_L} \tag{30}$$

The multi-element calibration was performed with calibration standards that included Ni 200, Ni201, SS315H, Hastelloy-N, Inconel-625, $Cr_{15}Fe_{35}Mn_{15}Ni_{35,}$ and $Cr_{18}Fe_{27}Mn_{27}Ni_{28}$ alloys to determine the constants in the calibration curve in equation (26). Using this approach, the uncertainty for the depth-resolved concentration of element M, σ_M (x), at distance x from the surface is determined using an error-propagation of the uncertainties in:

- elemental concentration in the calibration standard σ_c;
- calculation of the relative sputtering rate σ_{qrel};
- the measured intensity of the element σ_I;
- the detection limit of the element $\sigma_{DL.}$

Calibration uncertainties are automatically performed in the instrument software (QUANTUM) to report goodness-of-fit metrics. For an in-depth discussion on the GDOES quantification and the calculation of uncertainties performed in this study, the reader is referred to [332]. Figure 30(a) shows a representative example of the depth-resolved concentrations of the alloying elementss for one sample using the quantification approach detailed above. A shaded area representing the respective uncertainty based on the error propagation calculation is also added. Specific plots were generated for each of the 90 samples analyzed using an in-house batch analysis algorithm.

Based on the depletion profiles for each of the 90 samples (see Figure 30(a)) the total number of moles per element depleted was calculated for each sample by numerical integration. Figure 30 (b) illustrates the depletion depth X_d^M for elements M (Cr, Fe, Mn) in the alloy for the same sample shown in Figure 30 (a). X_d^M is determined as the distance from the surface at which the elemental concentration has asymptotically approached the bulk concentration. The uncertainty in quantity of depleted element M, σ_d^M, was determined by:

$$\sigma_d^M = \int_{X_d^M}^{0} \sigma_M(x)\, dx \qquad (31)$$

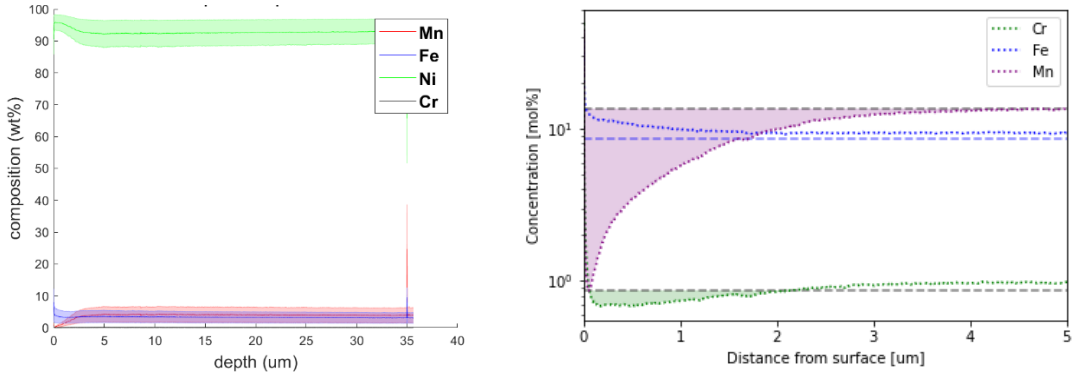

(a) *(b)*

Figure 30 (a) Example of elemental depletion depth profile for one sample $Cr_2Fe_{1}Mn_{15}Ni_{73}$ with associated instrumental quantification uncertainty at each point (shaded region), red (Mn), black (Cr), blue (Fe), green (Ni). As-printed alloy compositions of alloys independently verified for all samples by x-ray fluorescence and electron dispersive x-ray spectroscopy).(b) Example of elemental depletion depth profile (solid line) for the same sample with a focus on Mn, Fe and Cr (note that the word "depletion" is generically used although Fe shows a relative enrichment). The integration region used to estimate elemental depletion quantity is represented by the shaded areas: purple (Mn), green (Cr), blue (Fe). Ni has been omitted due to negligible dissolution.

2.4. Data analysis

If the alloy surface recession is negligible the total integrated elemental depletion depth from GDOES should equal the total amount of the element corroded into the salt as soluble corrosion product as measured by ICPMS. Figure 31(a) shows the quantification comparison for Fe in sample with composition $Cr_{0.2}Fe_{70}Mn_{6.2}Ni_{23.6}$ where it is evident that there is no statistical difference present between the quantification result by GDOES (red) and ICPMS(blue) since their ±2SD intervals (96% confidence intervals) overlap. Figure 31 (b) shows the quantification comparison for Fe in sample with composition $Cr_{12.5}Fe_{8}Mn_{0.5}$-

$Ni_{79}$where there is evidently a statistical difference between the quantification result by GDOES (red) and ICPMS(blue) since their ±2SD intervals do not overlap. These two samples were chosen to highlight the two cases where elemental quantification by ICPMS and GDOES agree or disagree.

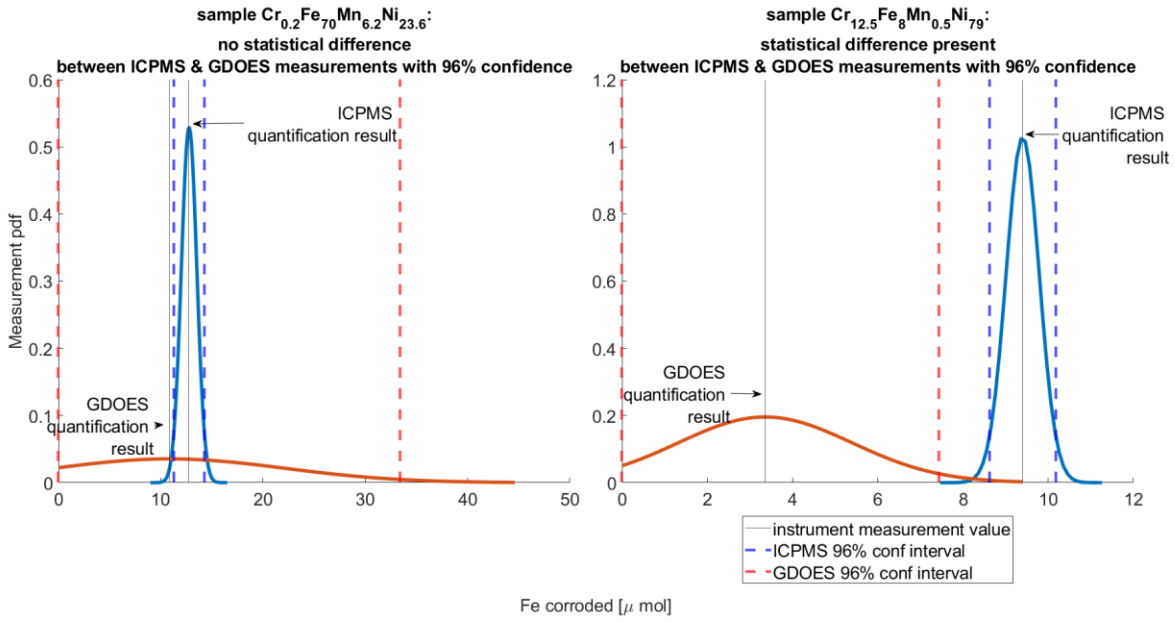

Figure 31: (left, a) Quantification comparison for Fe in sample with composition $Cr_{0.2}Fe_{70}Mn_{6.2}Ni_{23.6}$ where it is evident that there is no statistical difference present between the quantification result by GDOES (red) and ICPMS(blue) since their ±2SD intervals (96% confidence intervals) overlap. (right, b) Quantification comparison for Fe in sample with composition $Cr_{12.5}Fe_8Mn_{0.5}Ni_{79}$, where it is evidently a statistical difference between the quantification result by GDOES (red) and ICPMS(blue) since their ±2SD intervals (96% confidence intervals) do not overlap.

Results & Discussion

The elemental corrosion is thereby determined independently by ICPMS and GDOES with the methods outlined above for each of the 90 samples. Figure 30(b) illustrates the case where Mn and Fe dissolution strongly dominate the total corrosion compared to Cr and Ni. This was generally observed for all 90 samples

in the dataset. While it is expected that Ni corrosion into the salt is generally minimal because of Ni thermodynamic nobility, Cr depletion in the alloys in this dataset was not observed to be as dominant compared to Fe even though it is comparably thermodynamically active: for the 90 samples, ΔG_f for CrF_2 was calculated to be in the range (-374, -337)kJ/mol and ΔG_f for FeF_2 was calculated to be in the range (-367,-328)kJ/mol so there is significant overlap in the ΔG_f of the respective corrosion products. This is because the alloy compositions were primarily confined to the single phase FCC, meaning that almost all compositions had a Cr concentration lower than 10%.

The ICPMS and GDOES results are shown in Figure 32 under the form of a parity plot of measured (a) Cr, (b) Fe, (c) Mn by ICPMS on the x-axis and GDOES on the y-axis. The double-log scale was used for clarity because quantities span 5 orders of magnitude. Uncertainty bars shown are ±2SD as illustrated in Figure 31, for each of the respective analytical techniques on its respective axis. The mole fraction of alloying element composition in the alloy is indicated in the accompanying color bar to each plot: blue points have lower mole fraction and pink points have higher mole fraction of the respective element. It is immediately clear from Figure 32(a) and (c) that, overall, the corroded amounts of Cr and Mn tend to increase as function of their mole fraction in the alloy. This is generally expected from thermodynamics Mn and Cr chlorides in molten salt are thermodynamically stable relative to the other elements in the alloy. In light of this, the corrosion behavior of Fe indicated in Figure 32(b) is more complex as alloys spanning a large Fe composition range experience a large variety of corrosion rate, without clear trends. This is surprising because according to the Ellingham diagram [82], Fe and Cr redox potentials are relatively close, so the corrosion behavior of Cr is expected to closely mirror that of Fe.

Since this study was mostly confined to alloys in the single FCC region (with a few in the single BCC and BCC+FCC regions), all samples in this dataset can be loosely considered “Fe-based” (Fe composition greater than 50% with any balance of Cr, Mn and Ni) or “Ni-based” (Ni composition greater than 50% with

any balance of Cr, Fe, Mn). If surface recession was prevalent among the Fe based alloys in this dataset, Figure 32 would unambiguously show the quantification of corroded Cr, Mn and Fe by GDOES as under-quantified compared to ICPMS, i.e., the majority of the points should lie below the parity line. Indeed in Figure 32(b) and (c), most data points lie below the parity line, suggesting that surface recession could represent a main corrosion degradation mechanism in CrFeMnNi HEAs.

The parity plot in Figure 32a shows that Cr is mostly overquantified by GDOES compared to ICPMS. An investigation of the ICPMS samples indicated that during acidic digestion of the post-corrosion salt, undigested residue was observed in the bottom of the majority of the sample digests.

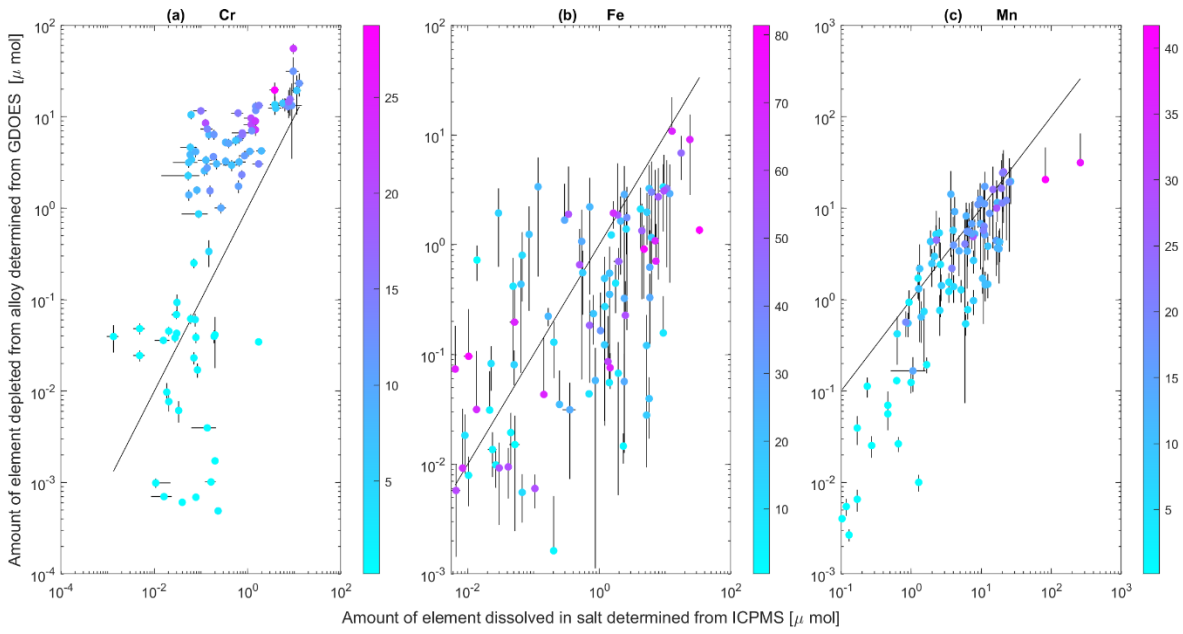

Figure 32: Parity plot of corroded (a) Cr, (b) Fe, (c)Mn quantified by ICPMS (x-axis) vs. that quantified by GDOES (y-axis). Log-log scale was used for clarity because quantities span 5 orders of magnitude. Uncertainty bars shown are ±2SD each in the respective analytical techniques for the respective axis. Error bars that result in negative values were omitted due to log scale. By inspection of the numerical data, all Fe points that lie above the parity line possess negative uncertainty bars in the y-direction that

cross the parity line, indicating that all Fe (blue) points that lie above the parity line show no statistical difference between ICPMS and GDOES analysis values at 96% confidence.

The residue was recovered by vacuum filtration followed by overnight desiccation of the filter paper, pictured in Figure 33. An estimation by gravimetry found the solid recovered from the digest of a single salt pill to weigh about 5 ± 2.5 mg. The undigested residue is of green color as shown in Figure 33 and is hypothesized to be Cr_2O_3, which is notoriously resistant to dissolution in aqueous media, having a K_{sp} of ~10^{-31} .at rtp. This is consistent with the wide body of literature indicating that oxygen-bearing impurities such as oxides and sulphates exacerbate corrosion to alloy constituents [333]. Assuming the 5mg of undigested residue was 100% Cr_2O_3, this translates to about 30 µmol of Cr that was missed by the first ICPMS analysis. A procedure to fully dissolved Cr_2O_3 was developed and consist in further dissolving the sample with 8mL concentrated H_2SO_4 and microwaving at 550W for 2h was found to completely digest the residue. Unfortunately, the new digestion procedure could not be scaled up to incorporate vacuum filtration of the Cr-bearing residue and re-digestion with H_2SO_4 for ICPMS analysis of 90 samples. Nevertheless, if one adds this Cr_2O_3 amount to the ICPMS analysis the ICPMS results become much larger compared to GDOES. With this consideration, the corrosion data for Cr is also consistent with evidence that surface recession is occurring.

Figure 33: Photograph of vacuum filtered solid residue from acidic digest of post-corrosion salt pills. Sample 1 (B2318-24): $Cr_{14}Fe_{27}Mn_{8}Ni_{51}$, Sample 2 (B2339-09): $Cr_{13}Fe_{59}Mn_{24}Ni_{4}$

Conclusion

Total element depletion by corrosion in molten LiCl-KCl at 500 ºC of Cr, Fe, Mn from 90 alloys in the quaternary CrFeMnNi composition space was determined by two independent analytical techniques: GDOES and ICPMS, and compared for parity. ICPMS is demonstrated to be a precise method to quantify total Fe and Mn corroded into salt when the entire sample can be digested for analysis. Based on the corrosion results form 90 alloys, it is concluded that surface recession is a significant effect in high-Ni alloys in molten halide environments. Deviation from parity for quantification of Fe and Mn between the two techniques was observed , with ICPMS being the more precise technique between the two compared. Regarding analyzing Cr corrosion products by analytical techniques that rely on aqueous acid digestion sample preparation steps (ICPMS), care must be taken that the acid digestion completely dissolves the highly resistant Cr_2O_3. We have found that concentration H_2SO_4, microwaved at 550W for 2h is sufficient for the purpose.

Overall, comparison of the quantification precision by ICPMS and GDOES generally indicates that total dissolution of the sample salt and analysis of the digest by ICPMS is a more precise analytical technique to quantify total Fe and Mn loss from the alloy by corrosion.

Visual inspection of the representative sample shown in Figure 30 reflects that GDOES does not accurately reflect the bulk elemental compositions in the alloys as-printed, independently verified by x-ray fluorescence and electron dispersive x-ray spectroscopy. The low precision of GDOES measurements suggest that its primary utility is to indicate qualitative relative surface compositional changes to anticipate surface microstructural changes as a result of local compositional changes.

It must also be noted that separate from instrumental uncertainty inherent in GDOES quantification, an additional source of uncertainty in quantification of elemental depletion by GDOES is that the GDOES measurement indicates the *relative* depletion of the elements, therefore an apparent non-deviation from bulk elemental concentration is no indication of non-depletion, rather it is possible to arise due to simultaneous depletion coupled to relative enrichment compared to another element. This is an inherent weakness of using GDOES to determine total elemental depletion by depletion profile integration. The low precision of GDOES measurements suggest that its primary utility is to indicate the extent of relative preferential dissolution mode of corrosion. GDOES analysis also does not reflect effects of re-deposition that may occur according to some identified molten salt corrosion mechanisms [95], [98]. Additionally, GDOES still has value as a high-throughput analytical technique.

GDOES is an analytical technique better suited for the analysis of compositional changes induced at the alloy surface as a result of corrosion attack to anticipate corollary corrosion effects such as associated microstructure destabilizations, rather than quantification of elemental corrosion. We intend for this study to shed light on the specific challenges associated with interpreting element-specific mass-loss data in

corrosion analysis, having demonstrated that it is crucial to implement analytical techniques that decouple the chemical species of corrosion products for quantification in order to accurately study corrosion mechanisms (say impurity-driven corrosion versus chemical attack by solvating species) of alloys in high-temperature molten salt systems.

Acknowledgments

We acknowledge Martin Schafer and Christa Dahman at the Wisconsin Hygiene lab for their contribution in analyzing the 90 salt pill samples by ICPMS. Additionally we acknowledge the efforts of Christa Dahman for assisting us to develop and test the Cr2O3 targeted digestion procedure.

5 Methods to Accelerate the Acquisition of element-resolved molten salt corrosion products

5.1 Cyclic Voltammetry-based mini-electrochemical probe

This section contains direct content from the following journal article co-first-authored by the PhD candidate:

Yafei Wan[†], Bonita Goh[1†], Kumar Sridhara[2], Adrien Couet, **In-situ Corrosion Monitoring of T91 alloy in Molten Chloride Salt using miniaturized electrochemical probe for High Throughput Applications,** *Anal. Chem.* 2022, 94, 9, 4012–4020 († These two authors contributed equally to this work)

Abstract

Corrosion sensing is essential to monitor and safeguard the materials' health in molten salts. The present study developed a three-electrode array mini sensor for the high temperature molten salt corrosion monitoring. By using the developed sensor, the impurity driven corrosion of T91 by a fission product, europium, in LiCl-KCl eutectic molten salt has been studied. The developed mini sensor was validated to be an ideal probe for in-situ corrosion monitoring in high temperature molten salt via the comparisons on concentrations of the dissolved corrosion products detected by this device and Inductively Coupled Plasma Mass Spectroscopy (ICP-MS). To analyze the large-volume of data measured by the mini sensor during in-situ corrosion experiments, an algorithm has been developed to achieve the high-throughput data analysis. The well designed mini sensor can be potentially used for high-throughput corrosion experiments. Combined with the developed algorithm for high-throughput analysis, this study provided a platform to explore the application of electrochemical sensor for the in-situ corrosion monitoring of materials in high-throughput molten salt corrosion experiments.

1. Introduction

Because of their atmospheric pressure operation at high temperatures, high thermal conductivity, large heat capacity, and compositional stability, molten salts are being considered for a wide range of applications for clean energy production, for example as coolants and solvent for fuel in advanced nuclear reactors [334] extraction media for pyroprocessing of spent nuclear fuel [335] thermal energy storage and heat transfer fluid of concentrated solar power [336], [337]], and battery electrolytes [338]. However, the corrosion of structural materials in molten salts continues to present a challenge [82], [339]. The protective oxide films relied upon for reducing the corrosion in most aqueous solutions or oxidative environments are readily dissolved in molten salt environment [340]Structural alloy corrosion has been recognized as one of the main concerns in the deployment of molten salt technologies, and, as a result, corrosion studies of structural alloys in molten salts have been performed extensively in recent years [82], [341], [342]. Although molten salt-based technologies are recognized and expected to play a crucial, transformative role in energy and industrial applications in the future, the developments and selections of corrosion-resistant structural materials, as well as producing pure and non-corrosive salts, have lagged behind, which has prevented the fast development and deployment of these technologies. Consequently, there is a need to develop high-throughput techniques to accelerate material testing for molten salt technologies. A key to the accelerated development of alloy design for molten salt applications is the ability to continually monitor in-situ the compositional changes and corrosion potential of the molten salt. Unlike the corrosion of alloy occurring in aqueous solutions or oxidative environments, the constituent elements of the alloy typically get oxidized and dissolve into molten salt in the form of ions (e.g., Cr^{2+}, Fe^{2+}, etc.) during the exposure to molten salt environments. At the same time, the molten salt itself is an ionic conductor. Hence, electrochemical methods, such as cyclic voltammetry (CV), hold promise to achieve in-situ measurements of the dissolved alloy constituents and the corrosion of alloys themselves in molten salts can be monitored as a function of time.

In the present study, a three-electrode array mini sensor for the high temperature molten salt corrosion monitoring has been developed. As the extraction media for pyroprocessing of spent nuclear fuel [335] , LiCl-KCl eutectic molten salt (44 wt% LiCl-56 wt% KCl) was selected to demonstrate the feasibility of the developed mini sensor on the corrosion monitoring. Using the developed mini sensor, the impurity driven corrosion of T91 ferritic steel by

europium, a fission product present in spent nuclear fuel, was evaluated. Considering the small dimensions of the designed mini sensor, it can be potentially applied for the high-throughput in-situ corrosion monitoring of molten salt droplet test on small samples, such as arrays of additively manufactured alloys [178]. At the same time, to handle the large volume of electrochemical data obtained by the mini sensor during the in-situ corrosion experiments, an algorithm has been developed to fit the experimental data to an electrochemical model, and the automated data analysis has been achieved. This study could form the basis to explore the application of electrochemical sensor for in-situ corrosion monitoring of materials in high-throughput experiments.

2. Experimental Methods

2.1. Mini sensor development

The mini sensor developed in this study (Figure 34) is based on a three-electrode system consisting of one tungsten working electrode (WE) (1.0 mm diameter, 99.95% impurity, Alfa Aesar), one platinum counter electrode (CE), and one platinum reference electrode (RE) (1.0 mm diameter, 99.95% impurity, Surepure Chemetals LLC). The Pt counter electrode is shaped into a coil as shown in Figure 34 to increase the surface area when immersed into molten salt. An 8.0 mm diameter alumina tube with three bores in the center was used to hold the three electrodes. The size of the bore is slightly larger than that of electrodes such that the three electrodes can be sealed tightly in the alumina tube at high temperature due to thermal expansions.

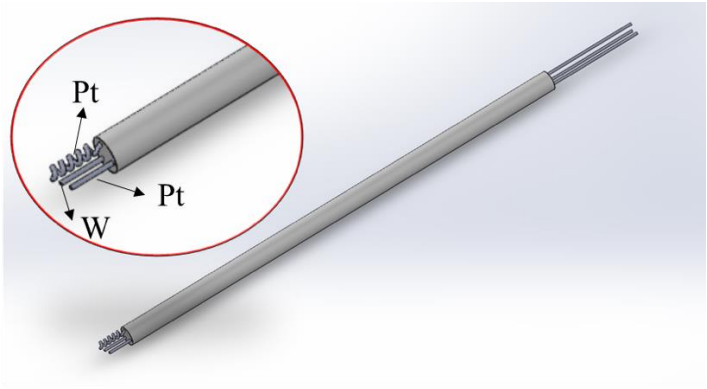

Figure 34. Schematic illustration of the mini sensor developed in this study.

2.2. Material preparations and corrosion experiments

The LiCl-KCl eutectic salt used in this study was prepared by 44 wt% of anhydrous LiCl salt powder (≥ 99% purity, Sigma Aldrich) and 56 wt% of anhydrous KCl salt powder (≥ 99% purity, Sigma Aldrich). Given that the oxidizing products generated from the nuclear fission reaction may cause severe structural material degradation. For instance, based on the calculation from the thermodynamic database, such as HSC Chemistry 6.0 ® [343] the standard potential of Eu^{3+}/Eu^{2+} at 500 ℃ is -0.40 V (vs Cl_2/Cl^-), which is found to be much higher than that of Cr^{2+}/Cr (-1.48 V vs Cl_2/Cl^-) and Fe^{2+}/Fe (-1.44 V vs Cl_2/Cl^-). At the same time, the high corrosiveness of Eu^{3+} in chloride salts was also reported in a previous study [344] Therefore, to simulate fission product driven corrosion, 2 wt% $EuCl_3$ of anhydrous $EuCl_3$ (99.99% purity, Sigma Aldrich) was added into the LiCl-KCl eutectic molten salt in this study. The impurities of the salt mixture were identified by ICP-MS test, the main impurity elements and their concentrations are listed in Table 17. As a mature structural material that is widely used in advanced power plants [345] but is also known to be susceptible to molten salt corrosion, T91 ferritic steel was selected and procured from American Alloy Steel Inc and sectioned into the dimension of 12.5 mm×12.5 mm×1mm. The nominal chemical composition of T91 is shown in Table 18.

Table 17. Main impurity elements and their concentrations in LiCl-KCl-2wt% $EuCl_3$ salt mixture identified by ICP-MS.

Na	Mg	Al	P	S	Ca	Cr	Fe	Mn	Ni
16.5	7.5	1.1	3.8	11.2	32.3	0.2	1.0	0.02	0.1

Table 18. Nominal chemical composition of T91 (in wt%, bal. Fe).

C	Mn	P	S	Si	Ni	Cr	Mo	Cu	N	Cb	Al	V
0.1	0.45	0.009	0.003	0.28	0.21	8.37	0.90	0.17	0.048	0.076	0.022	0.216

Before the corrosion experiments, the T91 steel sample was ground with silicon carbide abrasive papers of different grit sizes up to 1200 grit followed by ultrasonic cleaning with deionized water and ethanol. The in-situ corrosion

experiment was performed inside a glovebox filled with argon atmosphere (O_2<3ppm, H_2O<0.1ppm) at 500 ℃ using a muffle furnace, as shown in Figure 35. The salt mixture used in this study was baked at 200 ℃ for 15 hours to purge out moisture and oxygen before heating up to 500 ℃. In the corrosion experiment, the T91 steel sample was suspended through a 316 stainless steel wire and partially immersed in 100 g LiCl-KCl-$EuCl_3$ molten salt contained in a glassy carbon crucible (SPI supplies). The 316 stainless steel wire was electrically isolated through the quartz tube on the top of the muffle furnace. Based on the measured distance between the molten salt surface and muffle furnace, the immersion depth of the T91 sample in molten salt was fixed by using an alligator clamp. A schematic illustration of the experimental system used for electrochemical tests is shown in Figure 35. The muffle furnace was fixtured with quartz tubes on the top to allow the mini sensor to pass through the lid. The electrode parts between the tip of the mini sensor and the tip of the alumina sheath were partially immersed into molten salt to avoid salt creeping-up into potential tiny gap between the alumina bore and electrodes, although the tight design made such a gap quite unlikely. To verify the validity of the data acquired by the designed mini sensor, a classic three-electrode system with the same material as used in the mini sensor was also installed in the test cell. All the electrodes used in this study were well polished and ultrasonically cleaned before the test. The mini sensor and the equipped three-electrode system were connected to a VersaSTAT 3F potentiostat to obtain the electrochemical signal. Electrochemical measurements were conducted at different time intervals to monitor the concentration variations of ionic corrosion products in molten salt during the corrosion test. Before the electrochemical measurements were performed, a small oxidation current of 5 mA was applied on the working electrode for 10 s to remove the potential pre-contamination on the electrode.

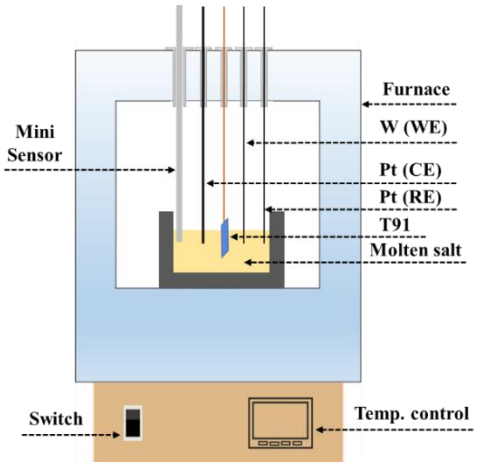

Figure 35. Schematic illustration of the in-situ corrosion test cell used in this study.

3. Results

3.1. Mini sensor validation

Before performing the corrosion experiment, the data acquired by the developed mini sensor needs to be validated. First, open circuit potential (OCP) measurements were carried out for about 10 hours as shown in Figure 36(a). A stable OCP value can be observed as function of time with a steady state being reached after about 10,000s. That initial transient may be due to the homogenization and equilibria process of the molten salt solution at the beginning of the experiment. The OCP measurement shows that the mini sensor is quite stable during electrochemical measurements. CV scans were also conducted using the mini sensor and the obtained cyclic voltammogram is shown in Figure 36(b) in which the cathodic/anodic limits at the left of the electrochemical window are attributed to the redox reaction of Li^+/Li [346] while the ones at the right side result from the redox reaction of Eu^{3+}/Eu^{2+}. The cyclic voltammogram obtained on the mini sensor is substantially similar to those obtained in studies using the well-established three-electrode system with Ag/AgCl reference equipped [347], [348] . It is also found that the potential differences between Li^+/Li and Eu^{3+}/Eu^{2+} measured by the mini sensor and those observed in references [347], [348] are both about 2.8 V. This demonstrates that the developed mini sensor is an effective tool for the electrochemical measurements in LiCl-KCl-$EuCl_3$ molten salt.

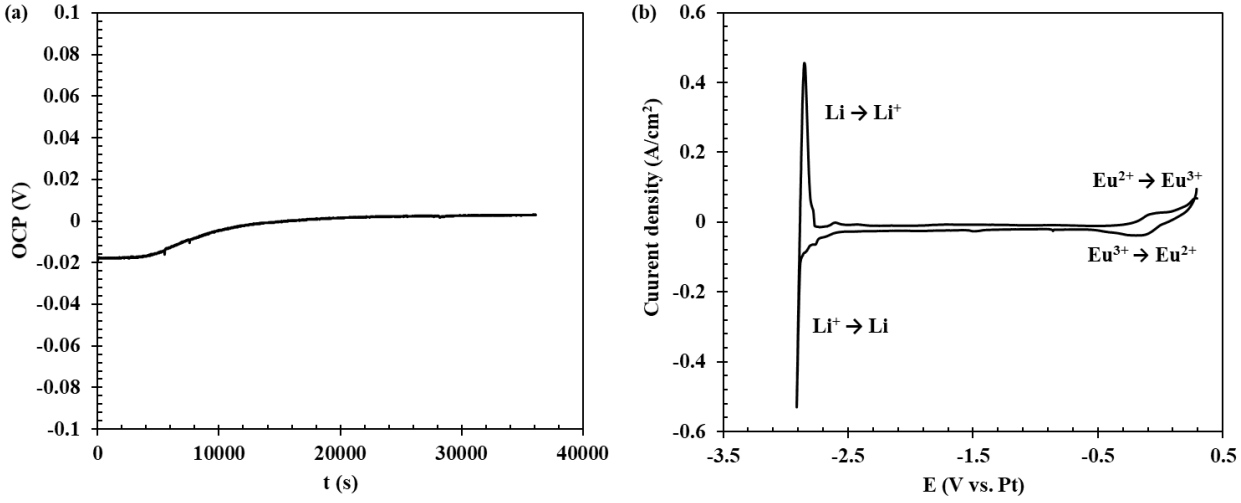

Figure 36. Electrochemical tests performed on the mini sensor: (a) OCP and (b) CV. Scan rate for CV is 0.1V/s.

3.2. In-situ corrosion monitoring

During the corrosion in molten chloride salt, alloys typically will suffer from active dissolution. Therefore, the measurement of the concentrations of the dissolved ions by CV at different time intervals provides an ideal way to monitor the corrosion of alloy in-situ in LiCl-KCl-2wt% $EuCl_3$ molten salt. The corrosion test of T91 in LiCl-KCl-2wt% $EuCl_3$ molten salt was performed for 96 hours and the CV measurements were taken throughout this whole exposure period. Only one extra CV redox peak appeared after the immersion of T91 sample in LiCl-KCl-2wt% $EuCl_3$ molten salt, and the intensity of the reduction peak increases with time, as shown in Figure 37. There was a slight potential shift among different CV scans which probably resulted from the Pt quasi-reference electrode potential drift. For direct comparison, all the cyclic voltammogram scans were corrected to the same potential as the one measured at the 4-hour exposure. In Figure 37, the anodic peak was also observed to shift for different scans, which is due to the different switching potential set in the CV scans [349].. Considering that T91 sample mainly consists of two elements: Fe and Cr, the extra redox peak should be attributed to the redox reaction of Cr^{2+}/Cr or Fe^{2+}/Fe. Based on previous studies [124], [350] the equilibrium potential of Cr^{2+}/Cr is about 0.3 V lower than that of Fe^{2+}/Fe in LiCl-KCl eutectic molten salt. However, this difference between the two equilibrium potentials was based on the conditions of equal concentrations of Cr^{2+} and Fe^{2+} in molten salt and equal activity of Cr and Fe on the inert electrode (activity is unity, assuming pure metals). During the corrosion of T91, there is likely a significant discrepancy between the dissolved concentrations (and activities) of Cr and Fe in molten salt. The activity of Cr and Fe in T91 are also different. For instance, if extracting the activity of Cr and Fe in T91 using the PanHEA database of Pandat software (version 2020) [351] , the values are 0.599 and 0.921 respectively, and assuming the activity of Cr^{2+} and Fe^{2+} in molten salt is 10^{-6} (i.e. dilute solution approximation) [352], the equilibrium potentials of Cr^{2+}/Cr and Fe^{2+}/Fe calculated by equation (1) are -1.92 V and -1.90 V (vs Cl_2/Cl^-), respectively.

$$E_{eq} = E^o_{MCl_2/M} + \frac{RT}{nF}\ln\left(\frac{\alpha_{MCl_2}}{\alpha_M}\right) \quad (1)$$

where M represents Cr, and Fe, MCl_2 is the metal chloride formed in molten salt during corrosion, $E^o_{MCl_2/M}$ is the standard potential which can be compiled from the thermodynamic database, such as HSC Chemistry 6.0 ® [343] n is the electron transfer number, F is the Faraday constant, R is the gas constant, T is the temperature, α_{MCl_2} is the

activity of metal chloride in molten salt, and α_M is the activity of M in T91.

Overall, the equilibrium potentials of Cr^{2+}/Cr and Fe^{2+}/Fe are quite close to each other. Therefore, the thermodynamic driving force for Cr and Fe depletion into molten salt should also be close. To further identify the extra redox reaction observed in CV scans, the ICP-MS analysis on the post-corrosion molten salt after 96 hours corrosion test was conducted, and the results are shown in Table 19. It can be seen Fe is the main depleted element and its concentration is more than ten times higher than that of Cr. In a cyclic voltammogram [349] the reduction peak is linearly related to the concentration of the dissolved species in the electrolyte. Under this scenario, the only significant redox peak detected by the mini sensor should be from the redox reaction of Fe^{2+}/Fe instead of Cr^{2+}/Cr, since the low concentration of Cr, and the extreme close equilibrium potentials of Cr^{2+}/Cr and Fe^{2+}/Fe, likely result in a negligible Cr^{2+}/Cr redox peak convoluted to the Fe^{2+}/Fe peak.

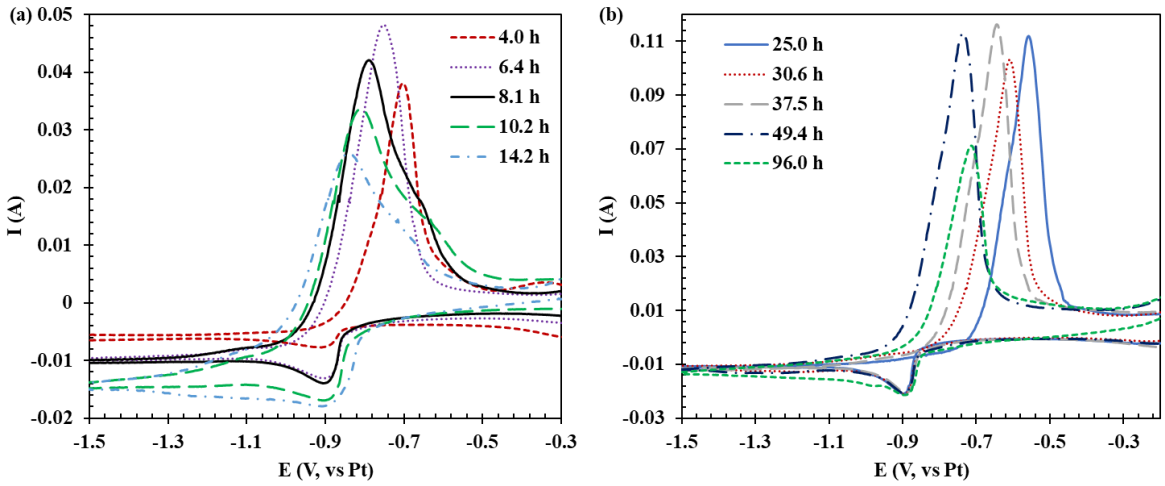

Figure 37. Cyclic voltammograms obtained from the mini sensor during the corrosion of T91 steel in LiCl-KCl-$EuCl_3$ molten salt, electrode area=0.4789 cm^2, scan rate=0.1V/s.

Table 19. Concentrations of Cr and Fe in the post-corrosion molten salt.

Test ID	Cr (ppm)	Fe (ppm)
#1	97.6±0.6	1282±14
#2	99.1±1.3	1248±21
#3	109±2.0	1438±30

The reversibility of the electrochemical reaction of $FeCl_2$/Fe in LiCl-KCl eutectic molten salt has been confirmed by the linear regression of the cathodic peak current changes with the square root of the scan rate as reported by Park et al [124] If assuming the redox peak shown in Figure 37 is only attributed to the redox reaction of Fe^{2+}/Fe (soluble/insoluble), the concentration of the dissolved Fe during the corrosion of T91 can be calculated from the Berzins-Delahay equation [122] below, based on the reduction peak obtained from CV.

$$i_{p,c} = -0.6105sC\left(\frac{n^3F^3Dv}{RT}\right)^{1/2} \quad (2)$$

where $i_{p,c}$ is the reduction peak in A, C is the concentration in mol/cm^3, n is the number of electrons exchanged in the redox couple, F is the Faraday constant of 96500 C/mol, D is the diffusion coefficient in cm^2/s, v is the scan rate in V/s, s is the electrode area in cm^2.

The diffusion coefficient of Fe^{2+} ions in LiCl-KCl eutectic molten salt at 500 °C has been reported in previous studies, and is equal to 1.5×10^{-5} cm^2/s using the CV technique [124] and $2.08\sim2.26\times10^{-5}$ cm^2/s using the chronopotentiometry technique [353] The reported smallest diffusion coefficient, 1.5×10^{-5} cm^2/s, and the largest diffusion coefficient, 2.26×10^{-5} cm^2/s, were chosen in this study to calculate the range of possible concentration of Fe^{2+} in the molten salt using equation (2). The calculated concentration of Fe^{2+} at different exposure periods is plotted in Figure 38. The ICP-MS results obtained on the post-corrosion salt (i.e. after the 96-hour corrosion test) are also plotted. The concentration of Fe^{2+} ions in the molten salt for the corrosion test of T91 increases gradually with the exposure time and approaches a steady value after about 24 hours. The concentration of Fe^{2+} ions at steady state measured by the mini sensor agrees quite well with the results measured for the post-corrosion salt after the 96-hour corrosion test. This is quite remarkable since both the electrochemical and spectroscopy measurements are totally independent from one another.

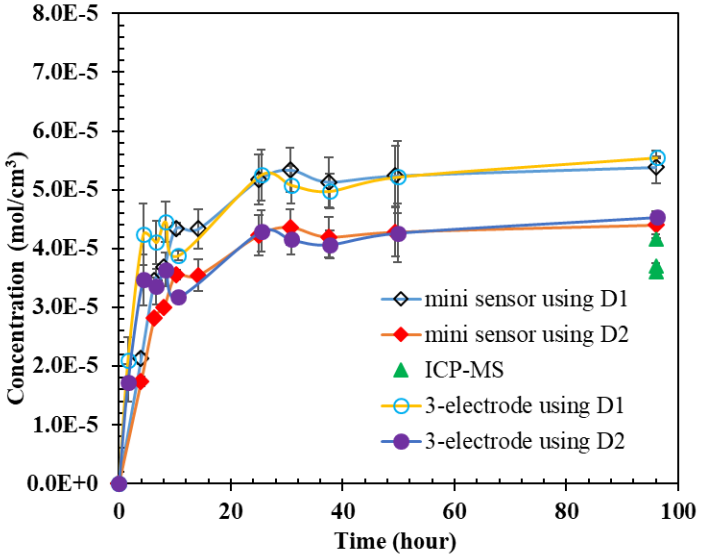

Figure 38. Concentration of Fe^{2+} ion in molten salt at different time intervals during the corrosion of T91 steel. D1 represents the diffusion coefficient of 1.5×10^{-5} cm^2/s reported by [124] D2 represents the diffusion coefficient of 2.26×10^{-5} cm^2/s reported by [353].

To further validate the results obtained with the developed mini sensor, a three-electrode system consisting of platinum reference electrode, platinum counter electrode, and tungsten working electrode (surface area is around 0.35 cm^2) was also used to perform the in-situ CV test at different interval times during the corrosion of T91. The calculated concentrations of Fe^{2+} ions in LiCl-KCl molten salt based on the measured reduction peak of CV were compared with the ones obtained by the developed mini sensor as shown in Figure 38. The results show excellent consistency between the two setups. This further validates that the effectiveness of the mini sensor to be a probe for in-situ corrosion monitoring in high temperature molten salt corrosion experiments.

3.3. Material characterization

After the 96-hour corrosion test, the T91 sample was removed and ultrasonically cleaned for Scanning Electron Microscopy (SEM) and Energy Dispersive X-Ray Spectroscopy (EDS) analysis. Figure 39 shows the typical SEM image of the T91 surface after 96 hours of exposure in LiCl-KCl-2wt% $EuCl_3$ molten salt. A dramatic uniform corrosion damage can be observed, along with some shallow pitting corrosion which is rarely observed in the corrosion of other alloys in molten salts [82].

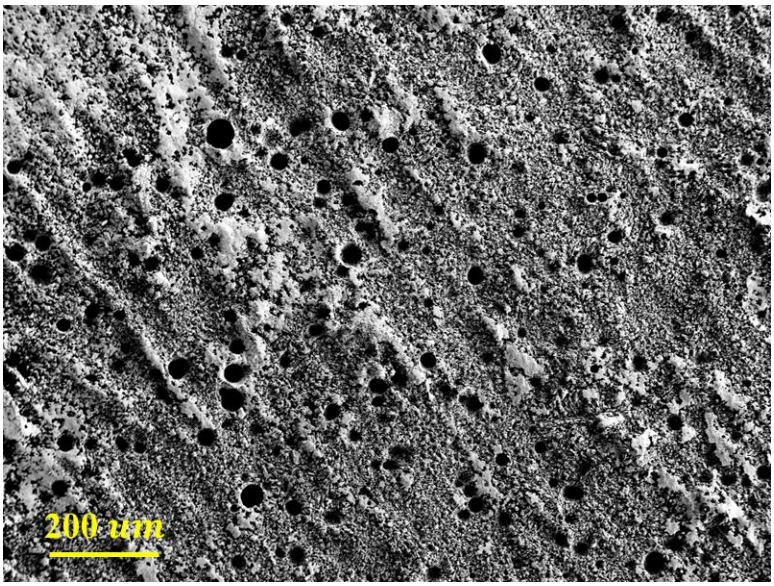

Figure 39. SEM image of the T91 surface after 96 h corrosion test in LiCl-KCl-2wt% $EuCl_3$ molten salt at 500 ℃.

To study the cross-sectional microstructure of the post-corrosion T91 steel, the corroded sample was cut through the center, mounted, and then polished for SEM and EDS compositional mapping. As can be seen from Figure 40, the post corroded interface is quite rough and severe corrosion attacks had occurred. However, no grain boundary corrosion, and/or depletion, was observed. The EDS mapping shows that there is a homogenous dissolution during the corrosion process, which results from the relatively close equilibrium potentials of Fe^{2+}/Fe and Cr^{2+}/Cr for T91 steel in molten chloride salts. It should be noted that although both Fe and Cr dissolved into molten salt during the corrosion process, the concentration of Cr^{2+} (see Table 19) in the post-corrosion salt is small because of the relatively low composition of Cr in T91 alloy. This also explains why only one pair of redox peaks were identified in the CV tests. The pits observed in Figure 6 were not observed in Figure 7 because of the difference in scale. Additional pit characterization using surface SEM/EDS did not reveal a different chemistry at the bottom of the pit. Comparing the characterization data to the CV results in Figure 5, it appears that dissolution kinetics should be linear as function of time (not diffusion limited since Fe is readily available at the surface). The fact that the dissolution rate decreases significantly after 24 hours would mean that the activity of Fe^{2+} in the salt is high enough that the electrochemical reaction would stop, because of the higher Fe equilibrium potential in the salt (Equation (1)). In addition, T91 corrosion

consumes Eu^{3+} such that the salt potential decreases as well. When both potentials are equal, the Fe electrochemical reaction will stop.

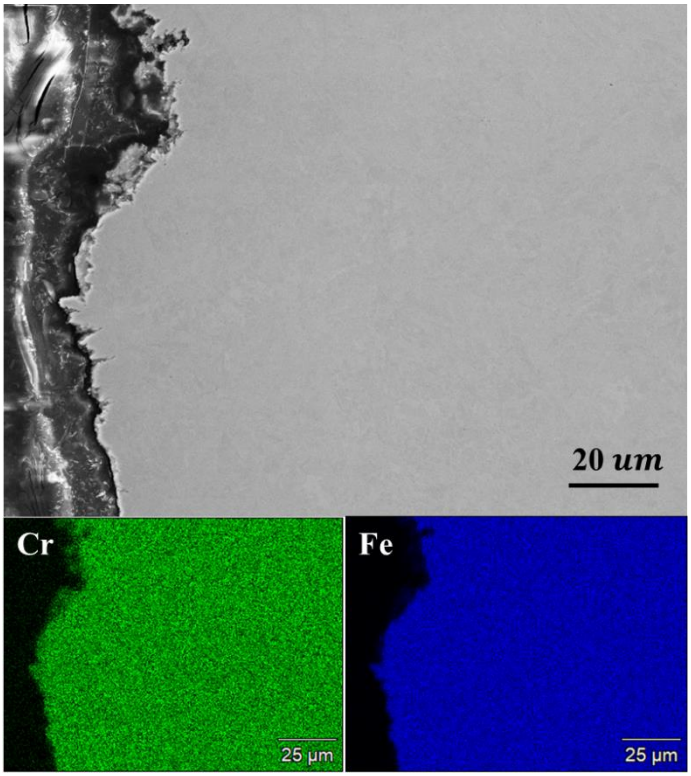

Figure 40. Cross sectional SEM image of the post-corrosion T91 alloy and the corresponding EDS maps.

3.4. CV automated fitting for high-throughput applications

To handle a relatively large volume of CV data anticipated from the in-situ corrosion experiment using the designed mini sensor, an algorithm, named Cyclic Voltammetry Automated Analysis (CVAA), was developed to automate the routine extraction of parameters of interest in a CV scan. An example of the different stages of processing a CV by the CVAA algorithm is shown in Figure 41. Considering that the oxidation peak will be affected by the reversal potential set in CV test [349]. and the concentration of the dissolved cation in electrolyte is more relevant to cathodic peak in cyclic voltammogram, the cathodic scan of CV is the focus of the CVAA code to save computational time. In Figure 41, dash line indicates the experimental CV data points acquired in LiCl-KCl-2wt% $EuCl_3$ molten salt at 500°C for the dissolved corrosion products from T91. To process the data, first, the CVAA algorithm locates the peak current value of the cathodic scan as the marked "X" shown in Figure 41 and the $i_{p,c}$ value is recorded. The background

charging current for cathodic scan in CV is normally determined by drawing a linear fit extrapolation line from the pre-peak of the cathodic scan to the edge of the cathodic peak [349]. In conventional CV analysis, the choice of the data points covering the pre-peak is rather arbitrary and can bring significant uncertainties in the peak fitting. To remove any subjectivity, in CVAA, the segment of the CV cathodic scan denoting the redox peaks, sectioned off (dark shaded area) as shown in Figure 41, is determined by one full width at half-maximum (FWHM) on either side of the peak marked "X". The data between the beginning of CV scan, far away from the peak, and the start of the peak, as defined above, is designated as the background charging current (grey shaded area) and a linear fit is used to approximate it.

In the CVAA algorithm, the Berzins & Delahay analytical solution [122].for charge transport at the electrode surface for soluble-insoluble reaction was developed in equation (3) to fit the cathodic scan of the CV obtained from experiment using non-linear least square fitting method.

$$i(\eta) = -\frac{2}{\sqrt{\pi}} C n^{3/2} F^{3/2} s \left(\frac{Dv}{RT}\right)^{\frac{1}{2}} exp\left(-\frac{nF}{RT}\cdot\eta\right) \int_0^{\left(\frac{nF}{RT}\cdot\eta\right)^{\frac{1}{2}}} \exp(z^2)\,\mathrm{dz} \tag{3}$$

where $i(t)$ is the current at time t during the CV scan in A, C is the bulk concentration of the dissolved cation in mol/cm^3, D is the diffusion coefficient in cm^2/s, s is the electrode surface area in cm^2, η is the overpotential in V, v is the scan rate in V/s.

Equation (2) is derived from Equation (3) by rewriting Equation (3) as:

$$i_{p,c} = \Phi(n,F,T,v) C n^{3/2} F^{3/2} s \left(\frac{Dv}{RT}\right)^{\frac{1}{2}} \tag{4}$$

where

$$\Phi(n,F,T,v) = \max\{|\frac{2}{\sqrt{\pi}} exp\left(-\frac{nF}{RT}\cdot\eta\right) \int_0^{\left(\frac{nF}{RT}\cdot\eta\right)^{\frac{1}{2}}} \exp(z^2)\,\mathrm{dz}\,|\} \tag{5}$$

Strictly speaking, $\Phi(n,F,T,v)$ is defined for electrons exchanged per reaction n, temperature T and scan rate v [122]. Numerically, $\Phi(n,F,T,v)$ evaluates to 0.61 as stated in Equation (2), and it was observed to vary by 0.1% by perturbing arguments within the range of v = (0.01,1) V/s, T = (298,773) K, n = (1,2). Therefore, 0.61 is a widely applicable conversion factor to calculate $i_{p,c}$ for commonly studied systems where n, C and D are known. The CVAA methodology serves to reinforce the theoretical basis of the existing literature on high-temperature molten salt cyclic voltammetry [124], [346] and provides improved precision and accuracy. To eliminate uncertainty with regard to $\Phi(n,F,T,v)$ for a particular system, CVAA calculates $\Phi(n,F,T,v)$ using the arguments provided for each analysis.

Based on the extracted background charging current as discussed above and the parameters n = 2, T = 773K, v = 0.1 V/s input by the experimenter, if taking the diffusion coefficient, $D_{Fe^{2+},LiCl-KCl}$=2.26×10^{-5} cm^2/s for instance, as reported from the literature [353] , the Equation (3) developed in the CVAA algorithm can be used to fit the experimental CV data. An example of the simulated CV cathodic scan with the experimental cyclic voltammogram is shown in Figure 41. The R^2 for this model is calculated in CVAA, found in this example to be 0.87. It provides a metric for the goodness-of-fit as an indicator of the appropriateness of a particular model for analyzing experimental data.

In high-throughput application of CVAA for analyzing multiple CV scans, with the previous reported $D_{Fe^{2+},LiCl-KCl}$ of 2.26×10^{-5} cm^2/s from the literature [353] the concentration of Fe^{2+} at different exposure periods during the corrosion experiment was extracted out through fitting equation (3) with the CV captured at intermediate timestamps during the 96-hour corrosion period.

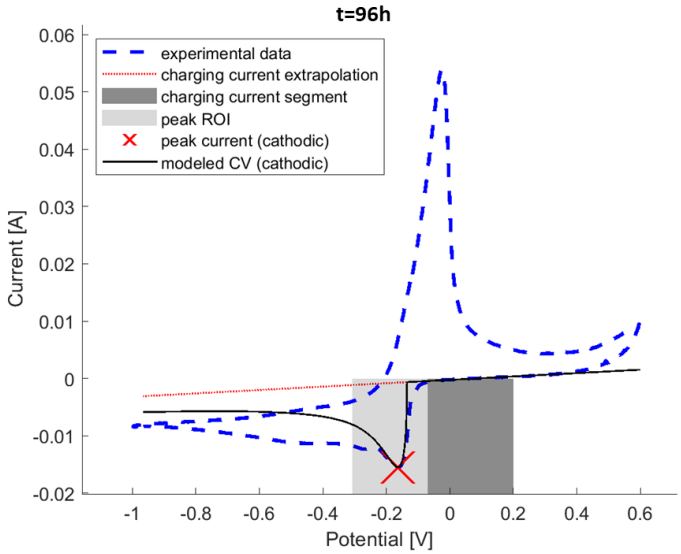

Figure 41. CVAA processed cyclic voltammogram obtained from in-situ corrosion experiment. Dash line indicates experimental CV data. The cathodic peak range of interest (ROI) is highlighted with grey shaded area while the charging current segment is highlighted with dark shaded area. The straight red dot line is the charging current estimation based on linear fit extrapolations using the charging current segments on the reduction reaction. The cathodic peak current is marked with 'X'. Solid line indicates the modeled CV cathodic scan. Potential shift correction was not performed in the CVAA. The R^2 for this modeled CV to the experimental data is 0.87.

CVAA is used to extract data for the CVs obtained by both the three-electrode control setup and the mini sensor at every timestamp up to the full corrosion period of 96 hours and generate simulated CV cathodic scans for each of them. These simulated CV cathodic scans with the experimental cyclic voltammogram are provided in the Supplementary Document. CVAA processes every CV in about 5 seconds, which is much faster than analyzing it manually and does not require dedicated attention, and eliminates sources of subjectivity in charging current estimation from an analyst. The CVAA estimated Fe concentration dissolved in LiCl-KCl as a function of time is shown in Figure 42 along with the manual estimation already shown in Figure 5. The results obtained by CVAA are very close to the ones obtained by the conventional CV analysis method. This means the developed CVAA algorithm could be used for the quick and accurate analysis of a large volume of experimental CV data. This open-source

software [354] will greatly accelerate CV data analysis especially in for high throughput applications [355] CVAA code architecture is modularized so that it is an easily generalizable, computationally inexpensive, automated analysis tool for any CV mathematical model [356] has either a closed-form solution or can be approximated by numerical methods.

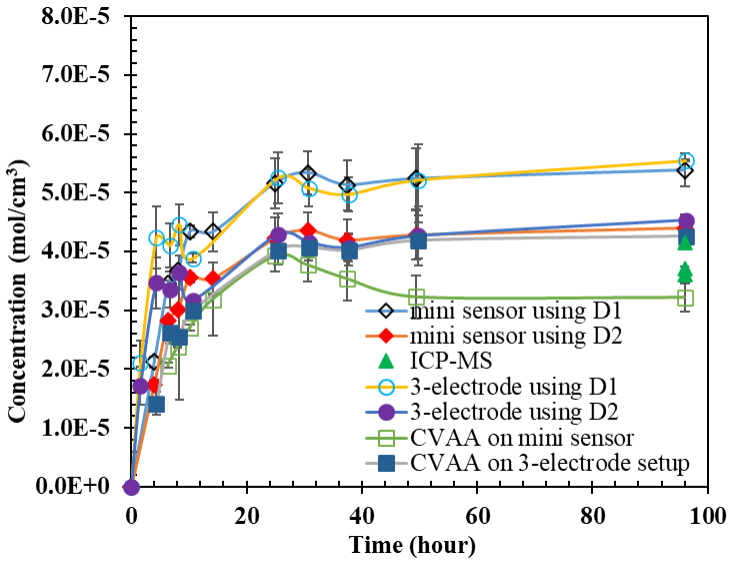

Figure 42. Concentration of Fe^{2+} ion in molten salt at different time intervals during the corrosion of T91steel obtained by different analysis methods.

3.5. Applications of mini sensor in high throughput tests

Compared with the regular three-electrode, the designed electrochemical mini sensor is more compact and convenient to use in electrochemical measurements, especially when small corrosion cells are considered, such as the high-throughput corrosion monitoring of different arrays of alloys in high-temperature molten salt droplets. Indeed, by suspending the mini senor into a molten salt droplet placed on each alloy surface, as designed in our previous study[178], the in-situ corrosion monitoring of a broad range of alloys in molten salts can be performed simultaneously. Coupling the sensor to an automated XYZ motion controller, such as a computer numerical control (CNC), as shown in the schematic in Figure 43, the high-throughput in-situ corrosion monitoring of tens of alloys in high-temperature molten salts can be performed automatically. To confirm that the self-designed mini sensor can be used for the high-throughput in-situ corrosion monitoring as sketched in Figure 43, an in-situ corrosion test was

performed on a T91 coupon (12.5 mm×12.5 mm×1mm) using a molten salt droplet. Before the corrosion experiment, 0.53 g of LiCl-KCl-2wt% $EuCl_3$ salt mixture, similar to the molten salt used in the corrosion experiment discussed above, was weighed and then pelletized as a solid salt pill with a diameter of 5 mm and a height of about 5 mm. The salt pill was pelletized inside the glovebox by placing the salt mixture powder into a custom-fabricated tungsten carbide die and then compacting using a Pike Pixie Manual Hydraulic Press at a constant load of 2.5 tons for 2 minutes. The pelletized solid salt pill was placed on top of the mirror polished T91 coupon. The salt pill was melted at 500 ℃ inside the glove box and remained as a droplet. The contact angle of the molten salt droplet on T91 alloy surface is found to be larger than 90° during the test, guaranteeing the non-spillage of salt droplet [357] After inserting the mini sensor into the molten salt droplet, CV scans were performed at different time intervals. Figure 44 shows the CV scans obtained. The reduction peak increases steadily over the first hour and remains relatively stable afterwards This means the Fe corrosion in T91 achieves equilibrium relatively quickly during the molten salt droplet experiment, the equilibrium concentration of Fe^{2+} in the salt was analyzed to be 4.3×10^{-5} mol/cm^3 if using Berzins & Delahay analytical solution and the previous reported diffusion coefficient $D_{Fe^{2+},LiCl-KCl}$=1.5×10^{-5} cm^2/s [353]. At the same time, this demonstrates that the designed mini sensor can be used for the high-throughput in-situ corrosion monitoring of different alloys in molten salt to accelerate the discovery of molten salt corrosion-resistant alloys, as highlighted in [218]

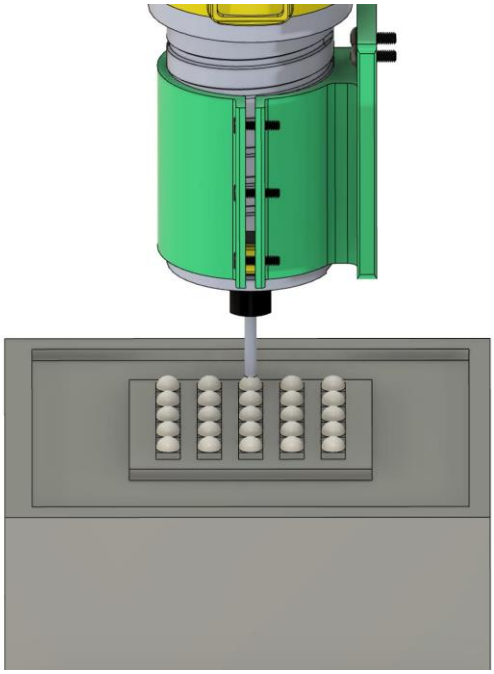

Figure 43. Schematic of automatic high-throughput in-situ corrosion monitoring.

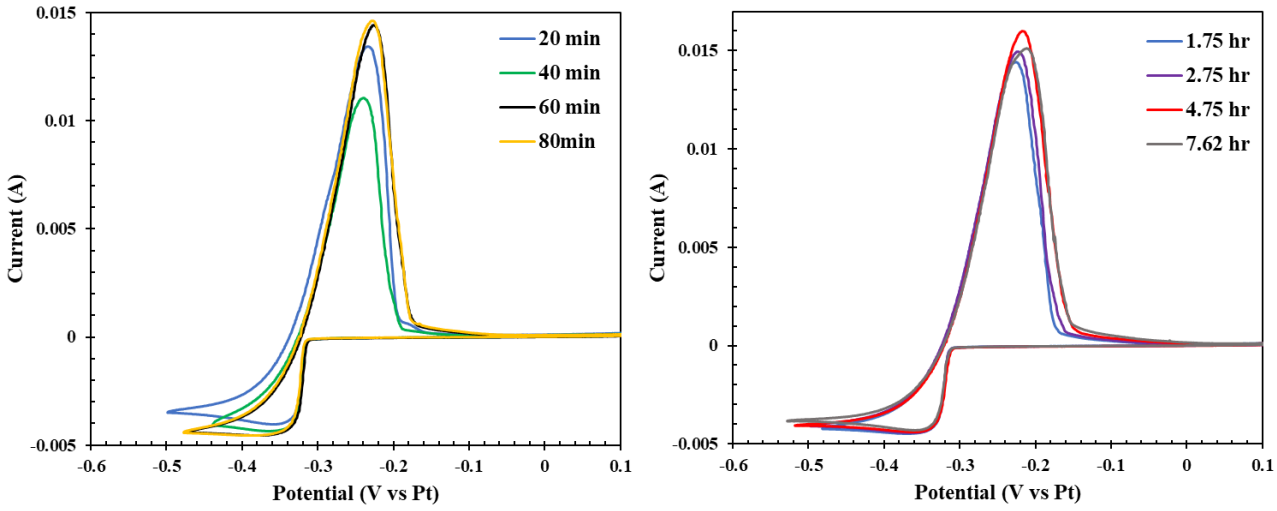

Figure 44. Cyclic voltammograms obtained on mini sensor in the molten salt droplet corrosion test of T91 coupon, electrode area=0.1335 cm^2, scan rate=0.1V/s.

4. Conclusions

In this study, a mini sensor was designed which could be used for the in-situ corrosion monitoring of different alloys in molten chloride salts. The feasibility of the designed mini sensor for the in-situ corrosion monitoring was validated by comparison with a well-accepted three-electrode system for high-temperature molten salt cyclic voltammetry. Based on the designed mini sensor, the impurity driven corrosion on T91 steel by a fission product, europium, in LiCl-KCl eutectic molten salt has been studied. It was observed that Fe is the elemental constituent that most predominantly dissolves into molten salt during the corrosion of T91. The concentration of Fe^{2+} in the salt increased gradually with the immersion time and approached a steady value after about 24 hours which indicates the corrosion of T91 steel reaches saturation thereafter. Characterization of the post-corroded T91 steel showed that shallow pitting corrosion occurred in the corrosion of T91 in LiCl-KCl molten salt, which was typically not observed in the corrosion of other alloys in molten salts. The designed mini sensor can also be used for the high throughput corrosion experiments and its feasibility has been demonstrated in this study through the salt droplet corrosion test on a T91 stud. To analyze the large-volume of data measured by the mini sensor during in-situ corrosion experiments, an algorithm based on an electrochemical model has been developed to achieve the high-throughput data analysis. The results obtained by the automated algorithm are in excellent agreement with the ones calculated by more conventional, manual, and potentially subjective, methods. This algorithm will greatly accelerate the data analysis process for the experimental CV. The present study could help support a platform to explore the application of electrochemical sensors for in-situ high-throughput corrosion monitoring and accelerate the material development for molten salt technologies.

Acknowledgements

This study is funded by the Advanced Research Projects Agency-Energy (ARPA-E) award number DE-AR0001050. The electron microscopy was carried out using facilities and instrumentation at the UW that are partially supported by the NSF through the Nanoscale Imaging and Analysis Center (DMR-1121288 and DMR-1720415). The authors also would like to Thank Cody Falconer and William Doniger for the helpful discussion of this study.

5.2 High throughput LIBS

A series of calibration samples is made by weighing out~0.3g of LiCl-KCl eutectic composition in a glovebox with Ar atmosphere. The salt is inserted into a tiny glassy carbon crucible (Figure 45) spiked separately with ~5000 [wt ppm] of Mn, Fe, Cr chloride, determined by gravimetry. The crucible is inserted into muffle furnace for salt to melt & analyte to homogenize over 30min and refreeze.

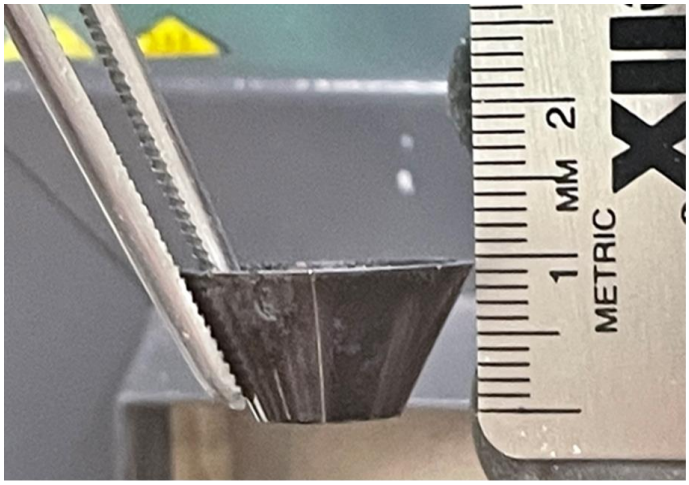

Figure 45: Tiny glassy carbon crucible in which calibration samples are melted to improve homogeneity of sample distribution.

Sample is loaded onto analysis cell to analyze on a TX 1000 LIBS instrument from Iumtek. Laser energy of 7mJ and delay time of 200ns was used. These parameters were determined as optimal by calibrating the instrument on the sample in the calibration series with the highest concentration of analyte from which the most intense signals could be expected.

After each sample is analyzed, it is returned to the glovebox, broken in approximately half and melted with an equivalent mass of clean LiCl-KCl eutectic. The process of serial dilution and sequential analysis on the LIBS is performed until the analyte signals fall below the limit of detection. In total there were 15 samples analyzed, 5 per analyte series for Cr, Fe, Mn. Each sample is analyzed by LIBS in a 10x10 grid of points (Figure 46a). One is generated per point (Figure 46b)

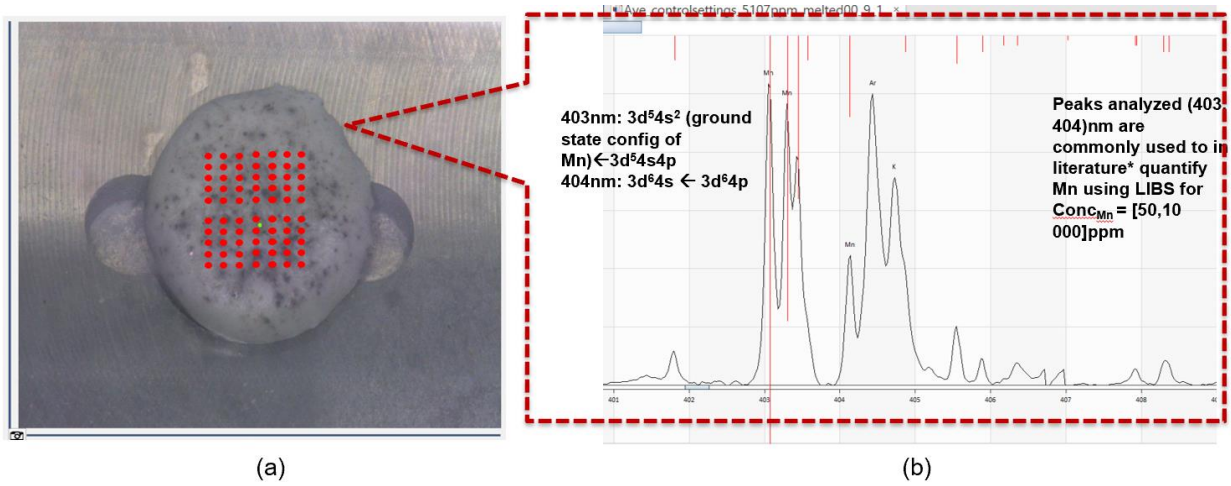

Figure 46: (a) Photo of sample in LIBS analysis cell. Sample was prepared by melting 0.3g LiCl-KCl eutectic in tiny glassy carbon crucible spiked with ~5000ppm of MnCl2 as determined by gravimetry Red spot grid is a representation of that traced by the laser for spot-analysis. Green spot is the laser cursor. (b) Spectrum obtained from single spot analysis on sample. Red lines denote Mn peaks expected by NIST database, length is proportional to expected relative intensity .[358]

Each spectrum is identified by (x,y) coordinate relative to green spot pointer. Each x-/y- value differs from its neighbor by 0.5mm in each direction Figure 46a.

A Python code was written to plot (x,y,Intensity$_\lambda$) as a heatmap directly from the excel sheet (Figure 47). Heat maps were generated for each of the 15 samples.

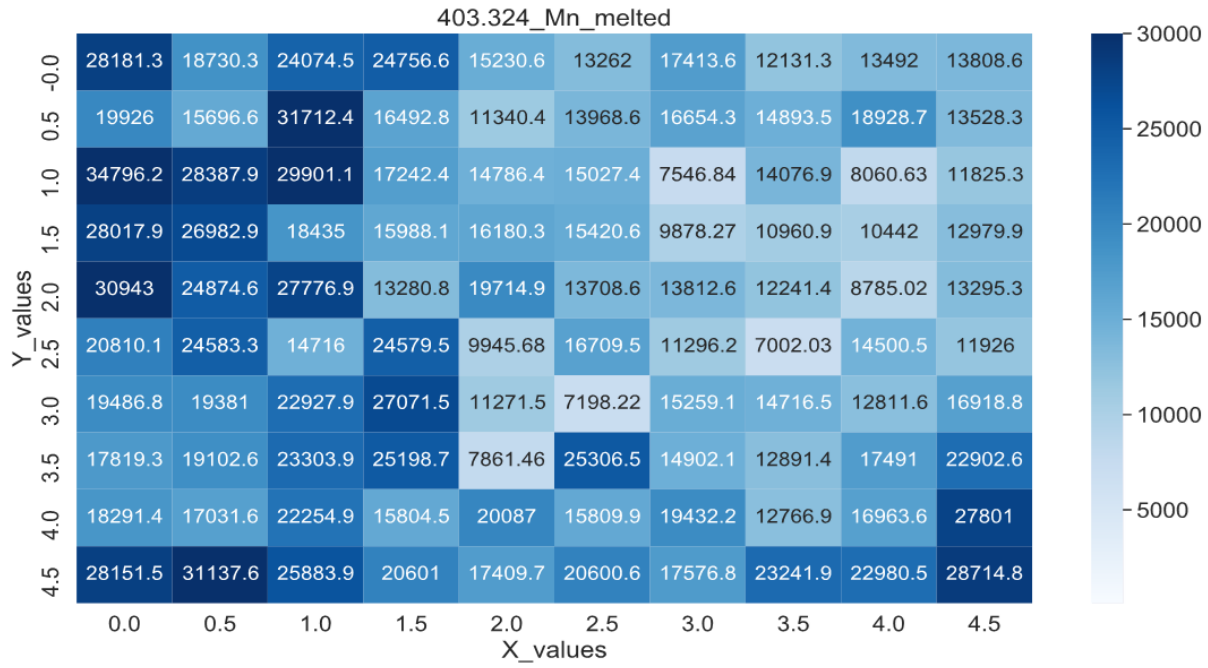

Figure 47 Heat map of signal intensity. Heat map demonstrates LIBS capability to spatially map the distribution of elements in solid salt. Total grid background-corrected signal intensity: 1.18 x 10^6

Heat map demonstrates LIBS capability to spatially map the distribution of elements in solid salt.

4 emission lines for Mn, 9 lines for Fe, 7 lines from Cr were selected from the NIST database for their intensity coefficient C. A linear model was determined for each line per analyte to determine the linearity over the desired dynamic range (100,5000)ppm. A chemometric model (linear regression) for each analyte was generated using its selected emission lines. Chemometric model was found to be equivalent to the linear model for a single selected line of each element (Figure 48 - Figure 50) ie. Other lines were rejected by the chemometric model.

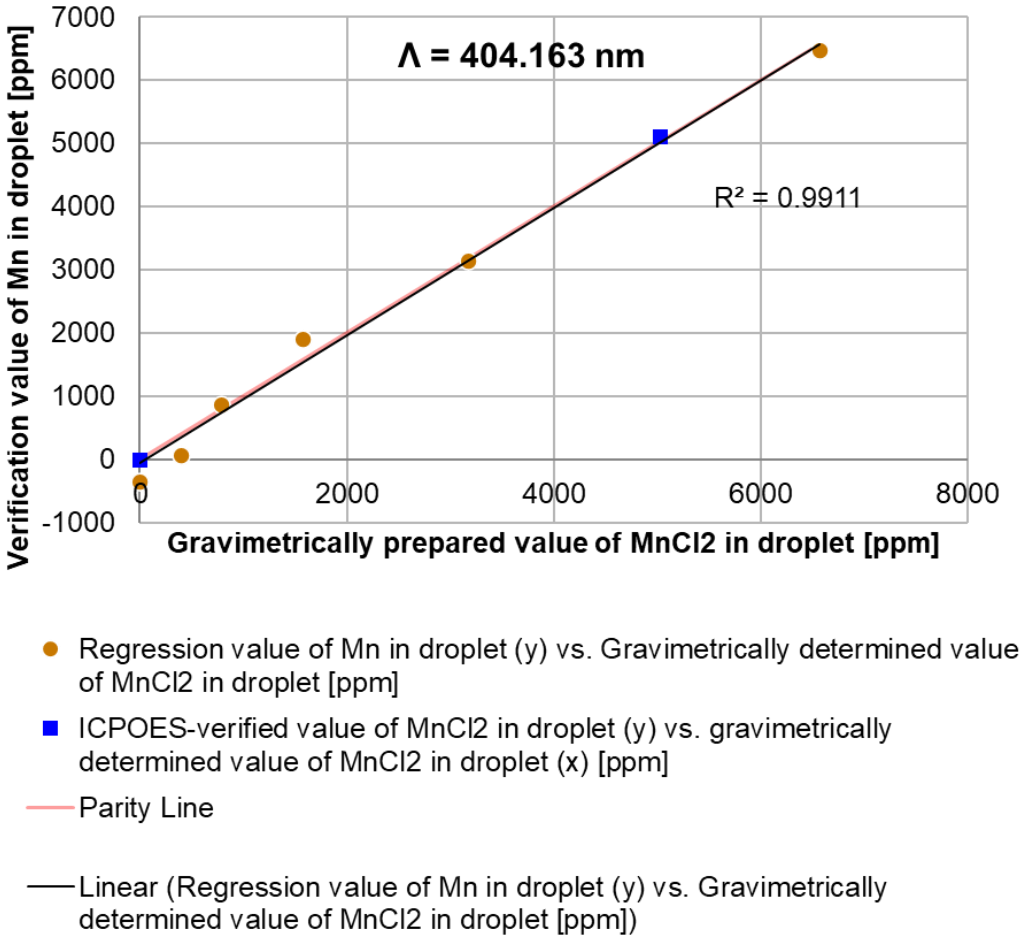

Figure 48 Mn Chemometric curve.

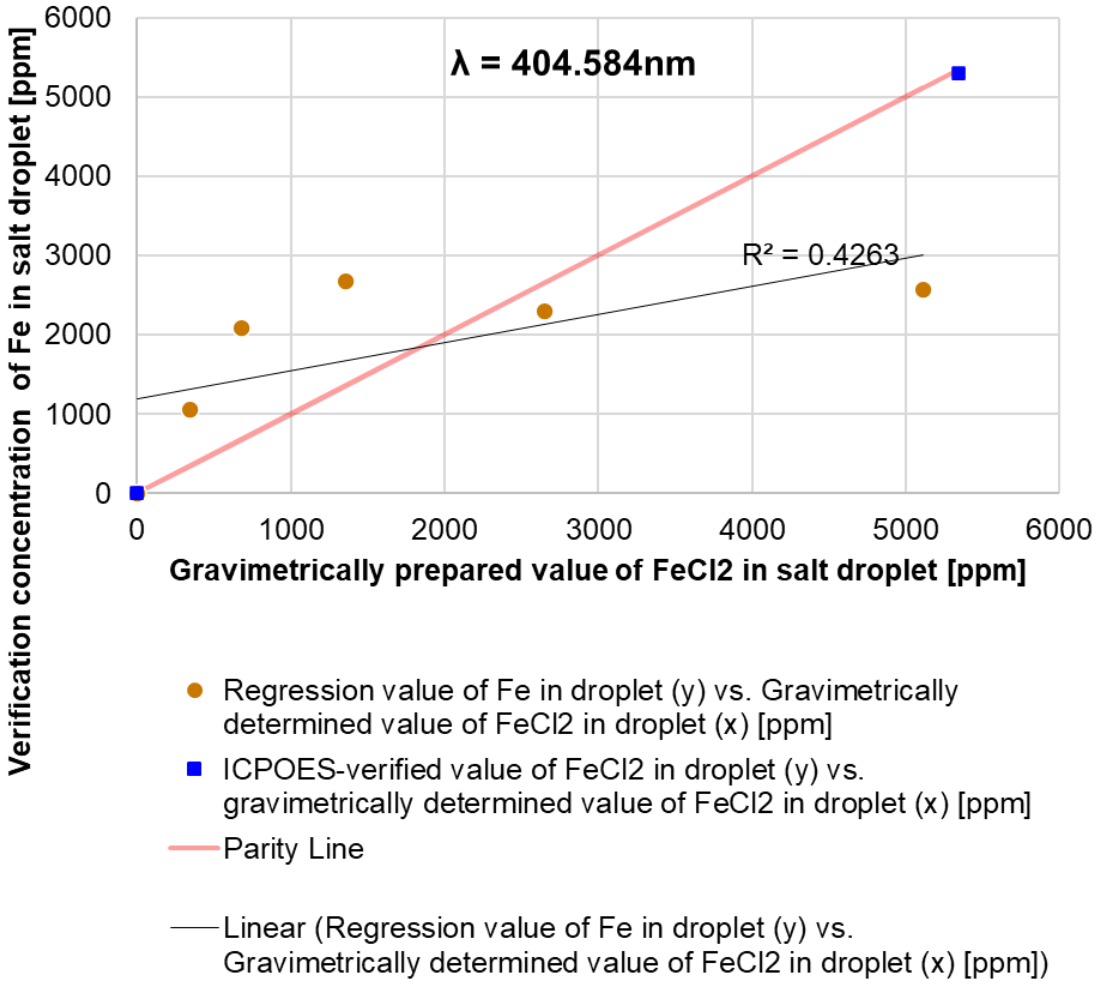

Figure 49 Fe Chemometric curve.

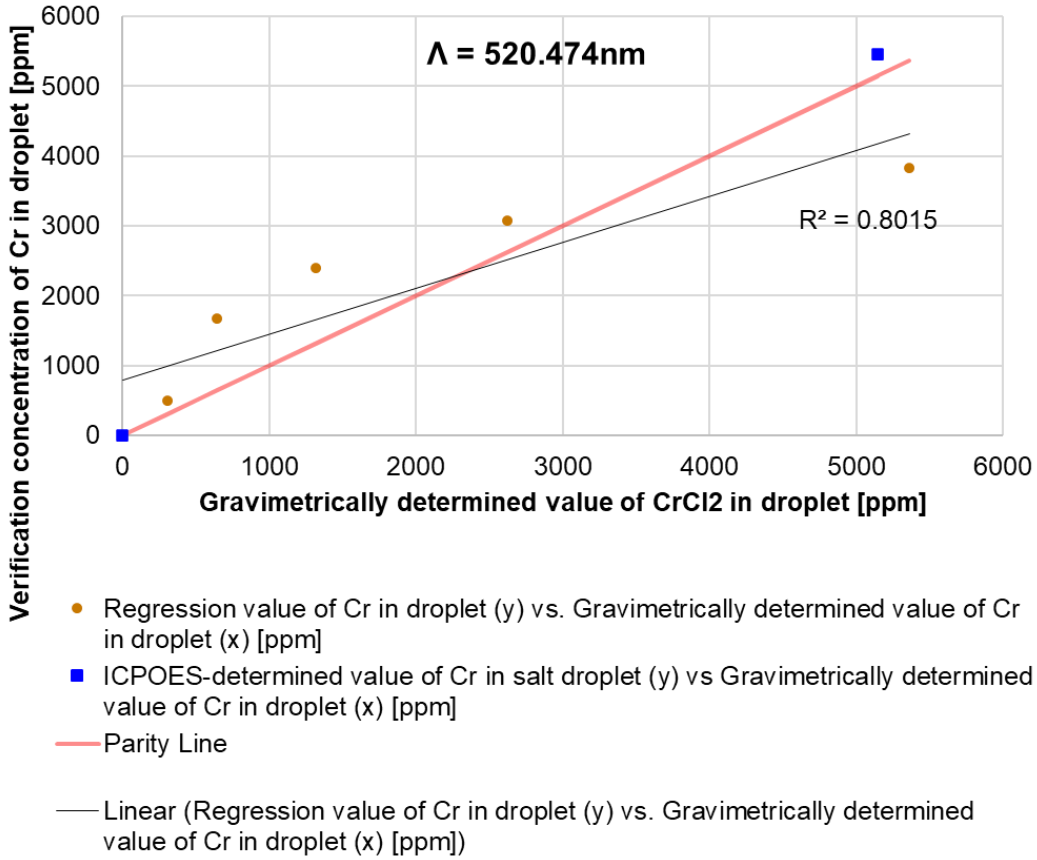

Figure 50 Cr Chemometric curve.

Mn and Cr show good linearity in the range (400,5500)ppm for their respective optimal emission lines (404nm for Mn and 520nm for Cr), determined independently by individual linear fit and chemometric linear regression.

It is demonstrated that even with chemometric modeling, results are consistent with single-emission line linear models shown for Mn by [359], [360]and for Cr by [361], [362]. Fe lines have yet to be fitted in a satisfactory manner[362].

It is concluded from this study that chemometric models developed for optical emission lines of Mn and Cr by LIBS are equivalent to the single-line linear model. Optical emission lines of Fe remain obstinate to a first-pass attempt at chemometric modeling; continued efforts in progress. LIBS is a

promising avenue to increase turnaround rate of analysis of molten salt corrosion products to serve structural alloy development.

Method development was done by the PhD candidate. Acknowledgment for performing the repetitive sample preparation and analysis on the instrument goes to lab intern Isabelle Baggenstoss.

5.3 High Throughput Synchrotron XAS

Synchrotron X-Ray Analysis techniques have been identified as an underutilized technique for studying alloy corrosion in molten salt [130], but the HTE platform developed as part of this thesis work can be leveraged to accelerate the analysis of alloy corrosion in molten halides by developing a process for high-throughput analysis of samples. The high-throughput corrosion experiments described in this section were designed in such a way as to enrich the body of literature in the field with a parametric study on the impact of salt basicity, Eu concentration and corrosion period on an Ni-based alloy in molten chloride.

64 Pill corrosion experiments were performed on Ni-20Cr plates and brought to the Brookhaven National Laboratory (BNL) synchrotron for X-Ray Fluorescence (XRF) and X-Ray Absorption Near Edge (XANES) analysis.

Circular wells each measuring 9mm in diameter and 1.5mm in depth were milled in a 4x4 grid formation into 10cm x 10cm square Ni-20Cr plates. The alloy surface inside each well was corroded by an LiCl-KCl salt pill of 0.2g. Every 16 of these well-corrosion experiments on a single plate is isolated from one another. The pills were varied in the x-direction by LiCl-KCl composition in the range (30,35,40,50)at%, and the pills were varied in the y-direction by spiking with EuCl3 in the range (0, 0.6,1.25, 2)wt%. This gives 16 combinations of LiCl-KCl-EuCl3 compositions on a single plate. Each plate was corroded for varying periods of time at 500 ^{o}C: (for t = 0h Temperature was raised to 500 ^{o}C and the heater was immediately shut off. This plate is the corrosion period control plate. Other plates were

corroded for (6, 12, 48)h in an Ar atmosphere with <1ppm O_2, H_2O. This 3D experiment matrix is represented in an infographic, Figure 51a. After the corrosion period is concluded and the plate is cooled to room temperature, post-corrosion salt adheres to their respective milled wells (Figure 51b).

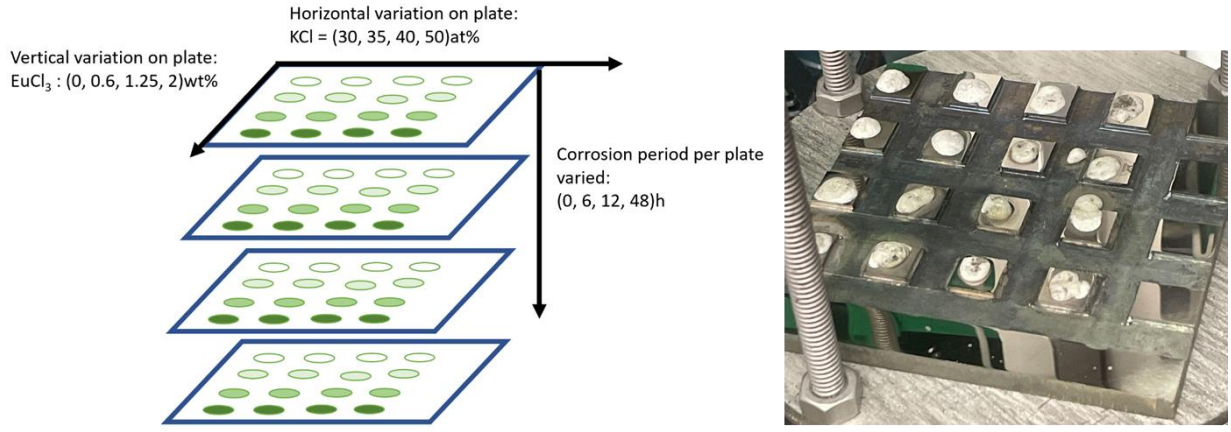

(a) *(b)*

Figure 51:(a)Infographic of the experimental matrix; (b) Photograph of the pill corrosion experiments.

An airtight X-ray analysis chamber was designed and constructed to hold the sample-bearing NiCr plates upright and maintained in an inert Ar atmosphere during exposure to the X-Ray beam. This is necessary to avoid exposure to atmosphere which contains oxygen and water vapor ingress into the chloride salt that can alter the

At the BNL synchrotron, for each sample, the K-edge was analyzed for Cr and Ni, and the L3 edge was analyzed for Eu. Within the allotted beamtime, we were able to acquire data for all samples in the 48h plate as well as samples on the 6h plate with KCl=35,40at% for all values of EuCl3, 24 samples in total.

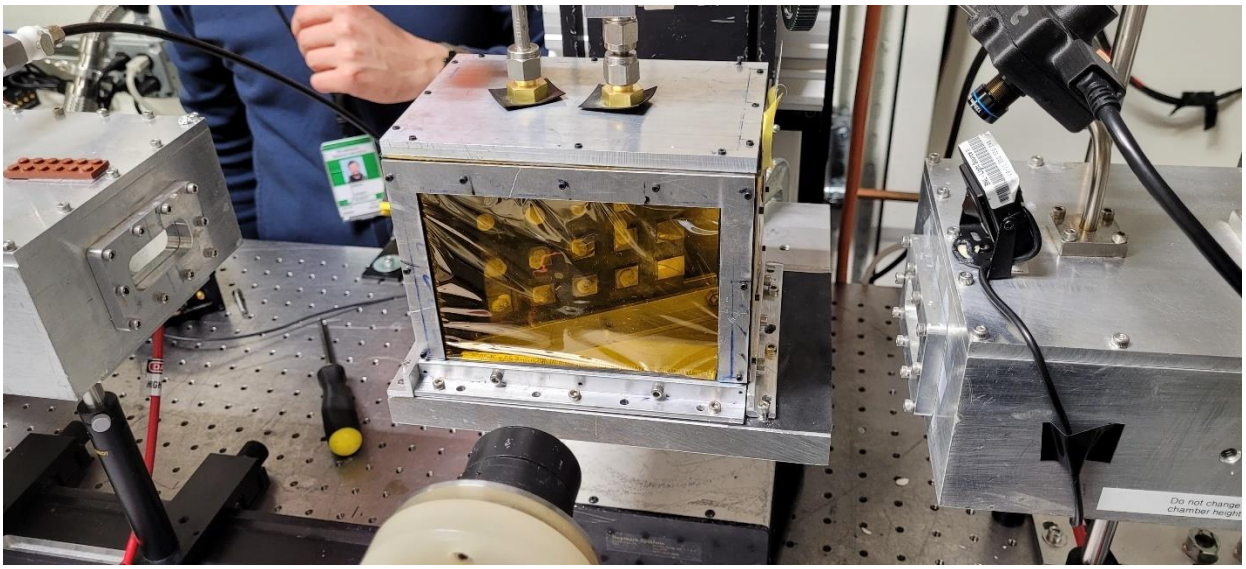

The assistance of Isabelle Baggenstoss, Kailee Buttice, Shea McCarthy, Nathan Curtis, Nate Eklof, Nick Czrnkovich and Gabriel Paramucchio on various aspects of sample preparation and fabrication of XAS chamber parts is acknowledged.

6 Interpretable Machine Learning for Mechanistic Insights into CCA corrosion phenomenon in Molten Salts

This chapter features direct content form the following article first-authored by the PhD candidate:

Bonita Goh, Yafei Wang, Phalgun Nelaturu, Michael Moorehead, Thien Duong, Pikee Priya, Moorehead, Dan J. Thoma, Santanu Chaudhuri, Jason Hattrick-Simpers, Kumar Sridharan, Adrien Couet, **Nobility vs Mobility: Unlocking New Insights into Molten Salt Corrosion Mechanisms of High Entropy Alloys with High-Throughput Experiments and Machine Learning-enabled Analysis**

Visual Abstract

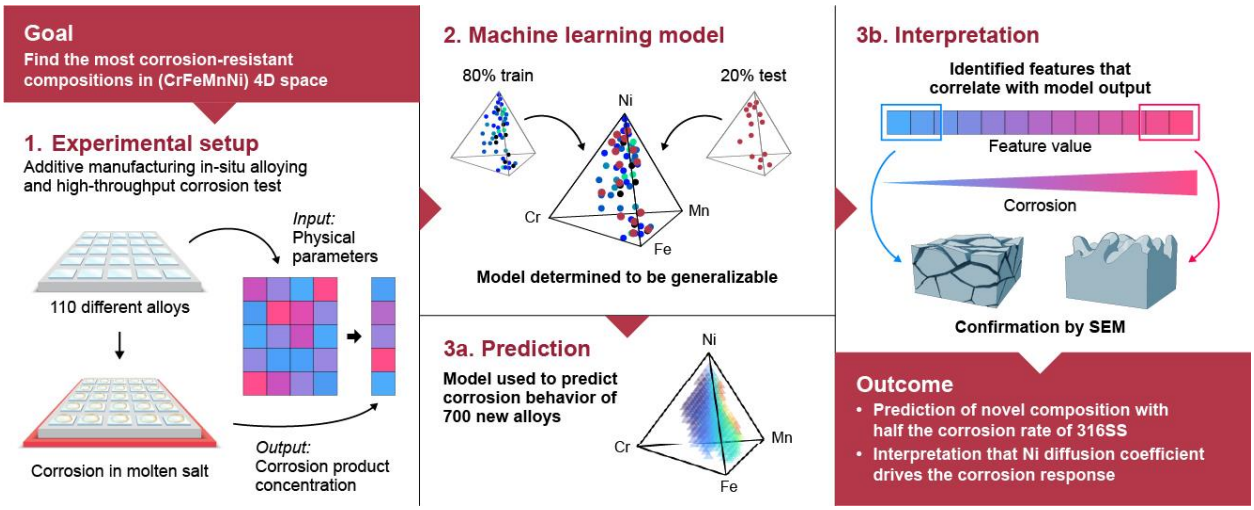

6.1 Critical Evaluation of ML algorithms & Model Selection

Machine Learning Model

A representative set of top Spearman correlation coefficients of physical features for each element in an alloy with the corrosion product concentration of that element into the salt have been calculated, Table 20

Table 20 Spearman Coefficient between single feature and corrosion outcome.

Pair of variables	**Spearman Coefficient**
Activity of Cr, Corrosion Concentration of Cr	0.650
Activity of Fe, Corrosion Concentration of Fe	0.303
Activity of Mn, Corrosion Concentration of Mn	0.534
Activity of Ni, Corrosion Concentration of Ni	0.512
Gibbs free energy of formation of corrosion product $CrCl_2$, Corrosion Concentration of Cr	-0.651
Gibbs free energy of formation of corrosion product $FeCl_2$, Corrosion Concentration of Fe	-0.303
Gibbs free energy of formation of corrosion product $MnCl_2$, Corrosion Concentration of Mn	-0.534
Gibbs free energy of formation of corrosion product $NiCl_2$, Corrosion Concentration of Ni	-0.513
Tracer Diffusion coefficient (Cr), Corrosion Concentration of Cr	-0.454
Tracer Diffusion coefficient (Fe), Corrosion Concentration of Fe	-0.440
Tracer Diffusion coefficient (Mn), Corrosion Concentration of Mn	0.611
Tracer Diffusion coefficient (Ni), Corrosion Concentration of Ni	-0.093

As expected, it is evident that not one feature exhibits a monotonic relationship with corrosion product concentration in the salt, suggesting that multiple features, and their coupling, are driving the corrosion response. This further demonstrates the usefulness of scientifically guided ML models to develop prediction and interpretability.

Algorithm Selection

Several ML techniques were assessed for suitability for the purposes of this study. The corrosion data of 88 samples each parametrized by 75 features were used to train the model with target variable being the total corrosion product concentration in salt (Cr+Fe+Mn+Ni) in ppm measured by ICP-MS. All input features were norm-scaled to allow for ML algorithm comparison. Scaled features are also crucial for K-means clustering to analyze for interpretability of the model [363]. Target variables were left unscaled. 5-fold cross-validated (x-val) predictions [364] for the target variable for each of the samples was obtained. The Mean Absolute Percentage Error (MAPE) of the sample predictions for each of these models was calculated and used as a metric to assess which model is expected to have the lowest error for an out-of-bag sample. A comparison of the MAPE from multiple ML algorithms was performed and compared to a naïve mean. The results (Figure 52) show the Random Forest Regressor (RFR) [239], [365] is promising with one of the lowest MAPE only bested by the Bayesian Ridge. In addition, the RFR has been demonstrated to accurately predict material properties based on multivariate input of parametrized physical features [247], [248], [366] and is also known to be physically interpretable. Consequently, RFR was used as the ML algorithm in this study.

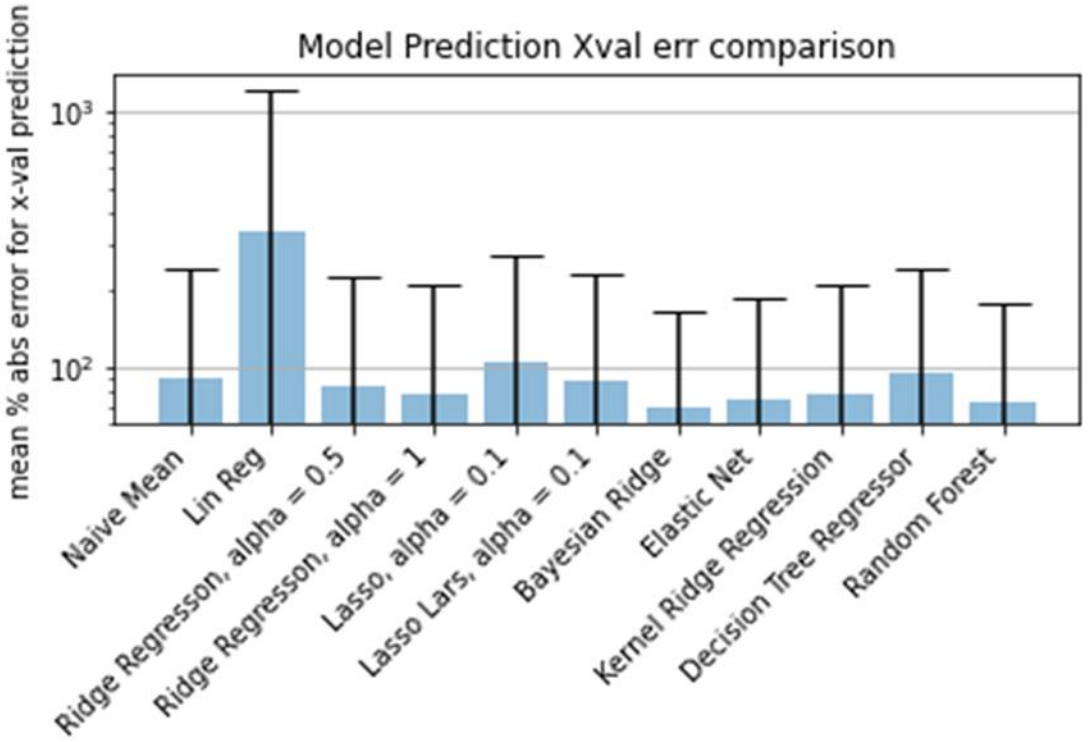

Figure 52 Comparison of training MAPE between popular ML methods for the current dataset.

6.2 Training on 80% of experimental dataset and Validation by testing on remaining 20% of dataset.

The Random Forest Regressor Model

Using the code package from sci-kit learn [367] the RFR model was trained on 88 samples using 1000 estimators, with no restriction on tree depth, 2 minimum samples per split and 1 maximum sample per leaf. Branch impurity was measured by branch population variance. All samples were assigned equal weighing. The MAPE of the 5-fold cross validated fitted values for the training set was used to estimate the expected error for an out-of-bag sample without overfitting. The trained RFR model was then tested on a set of 22 out-of-bag alloys featurized in the same format as the training set. The predicted corrosion values of the

test set were then compared with experiment. To improve ML-guided interpretability, it is necessary to orthogonalize the features as much as possible. The Spearman coefficient is a useful metric for expressing the degree of monotonic correlation between two variables, where a pair of variables that are perfectly monotonic to one another will have a value of unity whereas a pair of variables with no monotonicity whatsoever will have a value of 0. A pair of variables that are perfectly anti-correlated will have a value of -1. We use the Spearman coefficient throughout this study to indicate the degree to which two sets of values are numerically correlated. After the Spearman pruning of the feature set, random seed perturbation was performed by training 100 RFR models, and in each instance the random seed was varied. A random number was inserted as a benchmark "extra feature" to the Spearman-pruned feature set. The ranking order of these features by RFR Gini importance score was recorded in each instance of RFR The ordinal rank of each feature and standard deviation was recorded. Only features that consistently ranked above the random number in the random seed perturbation study were deemed meaningful to the model [368].

6.3 Evaluation of the RFR model.

The parity plot in Figure 53a shows the fitted values of the 88 samples from the training set to the RFR model versus their experimental values. The 5-fold cross-validated MAPE for the fitted values of the training set is ~75% over 3 orders of magnitude. The shaded area represents the 95% confidence interval of the predicted values of the RFR model. A probability density histogram of the fitting errors in the training set is shown in blue in Figure 53c. Clearly, the majority of samples have an error lower than 75% and outliers (~21.6% of the trained data set) have errors greater than 100%. While one could reduce the overall MAPE of the RFR model by sample pruning, such pruning can only be justified by physical considerations. K-means clustering analysis indicated that none of the outliers belong to a specific features' cluster, preventing physically based sample pruning to lower the MAPE on a subset of samples. The 22 out-of-bag samples from the test set, spanning three orders of magnitude in their corrosion response, are also shown

on the parity plot in Figure 53b. The MAPE of the test set predictions is ~56%, which is lower than the expected error for an out-of-bag sample of the trained model. Overall, this indicates that the test set was statistically well-represented by the training set. The probability density histogram in Figure 53c shows that the bin containing the lowest error (<20%) emerges with the highest probability density. A lower MAPE of the testing set shows that the RFR model prediction accuracy can be improved by adding more samples to the library. Therefore, it is expected that by doing so the RFR model MAPE will approach the experimental error of ~14% as determined by the repeatability study.

CCA comparison to 316SS and confusion matrix

Samples predicted by the RFR model to have a better corrosion resistance, on average, than SS316 are marked in red in Figure 53d. Samples rejected as predicted to have poorer corrosion resistance than SS316 are marked in black. The confusion matrix is also superimposed. The stark minority of false positives or negatives show that the model is conservative toward 316SS. The alloy selection accuracy from the confusion matrix is (91±7) %.

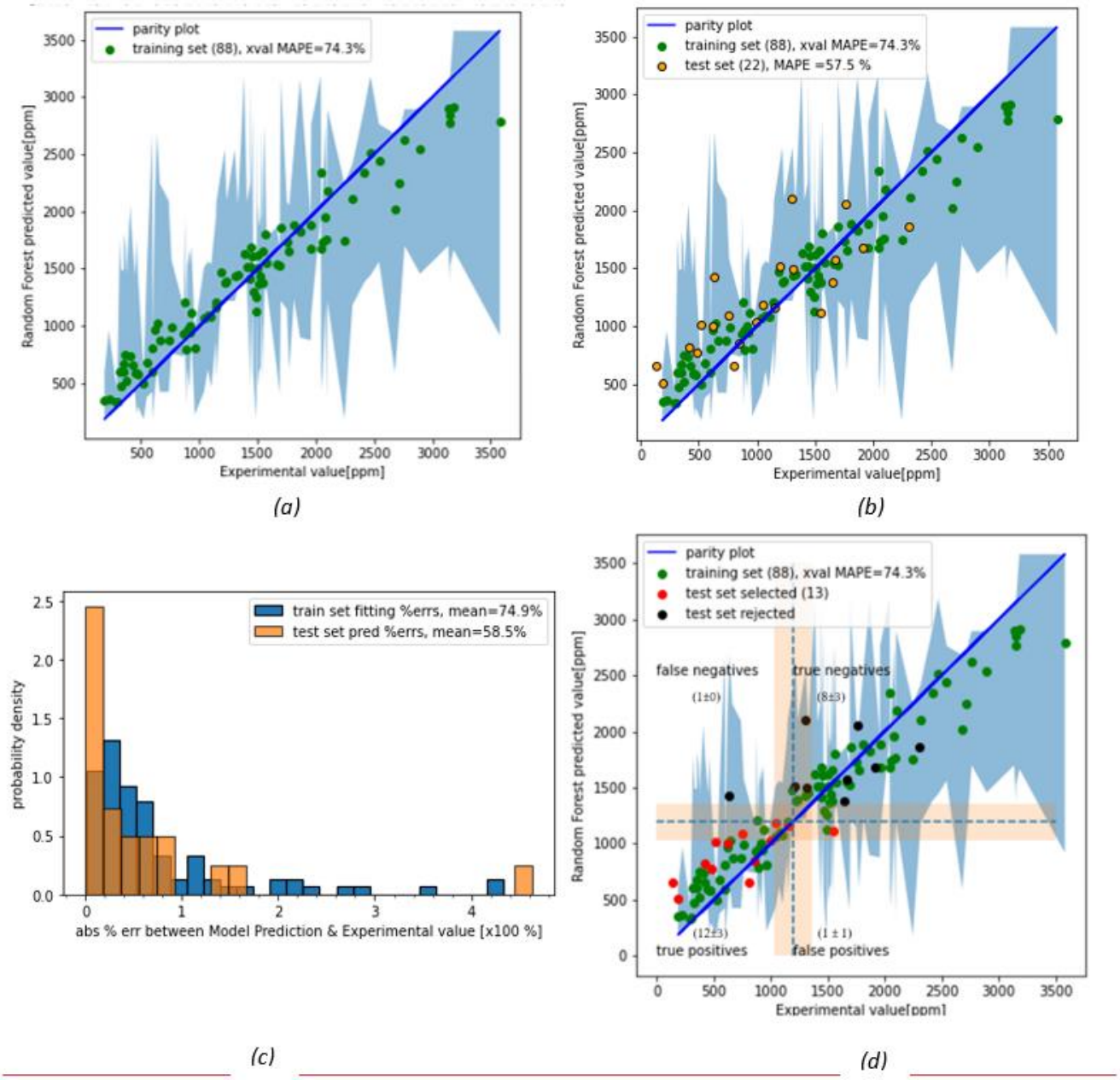

Figure 53 (a) Random Forest Regressor training set fitted values (y-axis) vs their experimental total corrosion concentration values measured by ICPMS (x-axis) on 88 samples in green, parity line in blue. Mean average percentage error of the model estimated by 5-fold cross-validation to be 74.3%; (b) trained

Random Forest Regressor model's predictions of 22 out-of-bag test samples vs. their experimentally measured total corrosion concentration values by ICPMS in orange. Mean Average Percent Error of the prediction for the test set is 57.5%; (c) Histogram of probability density for RFR absolute % fitting errors for training set (blue) & prediction errors of test set (orange); (d) Parity plot of training fit and test predictions superimposed with confusion matrix of sorting function with criterion placed that test samples predicted to have less corrosion than SS316 performance in the same experiment at 1194ppm (blue dotted line) are selected (red). If corrosion is predicted to be >1194ppm they are rejected (black) by the sorting function. The experimental uncertainty band (orange) of width 163ppm was determined by an experimental repeatability study on SS316 pill corrosion tests as outlined in the methodology by [178]

To our knowledge, the present work is the first attempt to predict the high-temperature corrosion rate of CCAs across a large compositional field. While a MAPE of ~56% may seem relatively high to predict materials' physical response relative to the accepted 40%, the improvement of the MAPE from ~75% to ~56% by the addition of only ~25% data is an encouraging sign that the model's predictability can be further improved. More importantly, the ML model can be used to determine compositional space of interest to design alloys with predicted low corrosion rate relative to commercial alloys, such as SS316. However, it is well known that ML models extrapolate poorly. To analyze the ML model performance, an Isolated Tree Regressor [244], [369] was used to highlight test samples that fell outside of the statistically well-represented trained ML model domain. These samples are circled in purple in the parity plot in Figure 54a and their corresponding location in Gibbs tetrahedron are shown in Figure 54b. As expected, model outliers from the test set lie in the high-Fe region, since it is more sparsely represented in the training set. Using Isolated Tree Regressor, the composition fields where domain knowledge is lacking can be identified, paving the way for autonomous uncertainty reduction [370], [371].

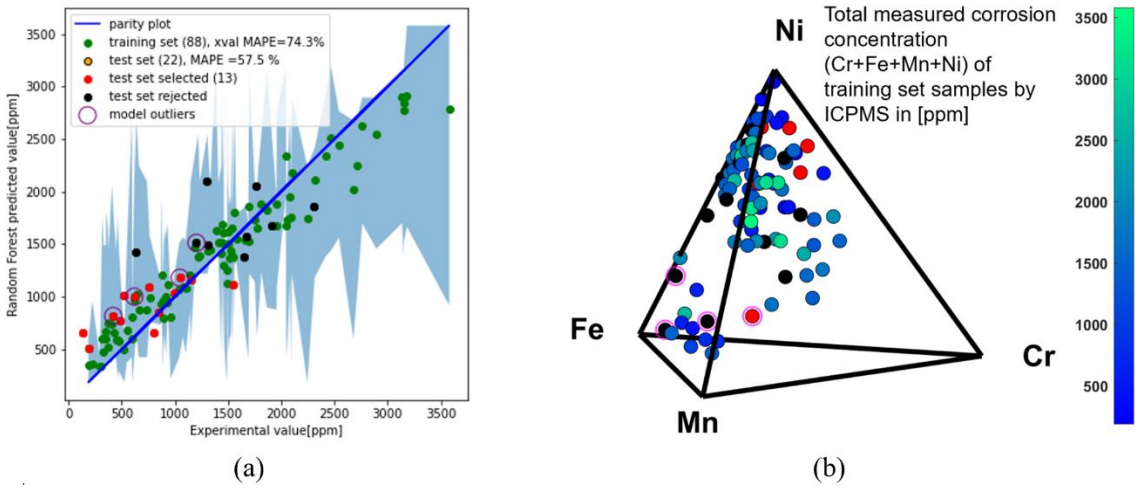

(a) (b)

Figure 54(a) parity plot from Figure 53c but with model outliers marked in purple, as determined by Isolated Tree Regressor; (b) model outliers are circled in purple in composition space.

6.4 Dimensional Reduction to improve interpretability

To date, corrosion phenomena in CCAs are primarily understood case-by-case often relying on relative concentrations of reactive vs. noble elements [83]. Knowledge gained from this paradigm of analysis is not conducive to elucidation of mechanisms whose principles may or may not be extensible to systems involving other compositions. Having established that the RFR model robustly predicts corrosion performance for out-of-bag samples within a statistically reliable compositional field, the RFR model is interrogated for the patterns underpinning the prediction. To improve interpretability, features were grouped together based on Spearman coefficients. The grouping was performed by reducing the Spearman coefficient until non-physical correlations appeared between features (Table 21), and a Spearman coefficient threshold of 0.94 was selected. Features that did not have a wide distribution in values over the training set population were also eliminated. With this "Spearman pruning", feature dimensionality was decreased from 75 to 62. This method of dimensional reduction preserves physical interpretability of the RFR model in a way that Principal Component Analysis [228], [294] does not. In this way, we can better

decouple the features' mathematical impact from one another on the ML model for interpretability. After Spearman pruning, the RFR model was re-trained with the same 88 samples of the training set, but with a reduced parametrization with 62 feature groups and no change in MAPE was observed, confirming that this set of 62 feature groups describes the training set to the same degree as the original set of 75 individual features. In addition, all members of the pruned set of features survived random seed perturbation pruning process, as detailed in Methods, thereby lending confidence that the RFR corrosion model is robustly interpretable. The reduced feature set is shown in Table 21, (where ^{g} denotes a feature group).

Table 21 Spearman-Pruned feature set

Feature Index	Spearman-pruned features/ groups	**Label**
1	Phase fraction of FCC No. of measured phases	$f(FCC)^{g}$
2	(100) Surface Energy	γ_{100}
3	(111) Surface Energy	γ_{111}
4	(100)Work Function	φ_{100}
5	(111)Work Function	φ_{111}
6	Sample Surface Energy (110) Surface Energy	$\gamma_{sample}{}^{g}$
7	Sample Work Function (110) Work Function	$\varphi_{sample}{}^{g}$
8	atomic fraction (Cr) Bond probability (Cr-Cr)	$X_{Cr}{}^{g}$
9	atomic fraction (Fe)	$X_{Fe}{}^{g}$

10	atomic fraction (Mn) [g]	X_{Mn} [g]
11	ratio Fe/Mn	Fe:Mn
12	ratio Cr/Mn	Cr:Mn
13	ratio Fe/Cr	Fe:Cr
14	ratio (Cr+Fe)/Mn	(Cr+Fe):Mn
15	ratio Fe/Ni	Fe:Ni
16	mixing entropy	S mix
17	bond probability(Cr-Fe)	P_{bond} (Cr-Fe)
18	bond probability(Cr-Mn)	P_{bond} (Cr-Mn)
19	bond probability(Cr-Ni)	P_{bond} (Cr-Ni)
20	bond probability(Fe-Mn)	P_{bond} (Fe-Mn)
21	bond probability(Fe-Ni)	P_{bond} (Fe-Ni)
22	bond probability(Mn-Ni)	P_{bond} (Mn-Ni)
23	Activity(Cr) Gibbs free energy of formation of corrosion product $CrCl_2$	α(Cr) [g]
24	Activity(Fe) Mole fraction of Fe Bond probability (Fe-Fe) Ratio of Fe/Ni Gibbs free energy of formation of corrosion product $FeCl_2$	α (Fe) [g]
25	Activity(Mn) Gibbs free energy of corrosion product formation $MnCl_2$	α (Mn) [g]
26	Activity(Ni)	α (Ni) [g]

	Mole fraction of Ni Mole fraction of (Cr+Fe+Mn) Bond probability (Ni-Ni) Gibbs free energy of formation of corrosion product $NiCl_2$ Mole fraction of (Cr+Fe)	
27	Gibbs Free Energy of formation of alloy	ΔG_{form}
28	Gibbs free energy of formation of corrosion product, $CrCl_2$ (CrCl2)	$\Delta G_{f,CrCl2}$
29	Enthalpy of alloy formation	ΔH_{form}
30	Tracer Diffusion coeff(Cr)	$D^t_{,Cr}$
31	Tracer Diffusion coeff(Fe)	D^t_{Fe}
32	Tracer Diffusion coeff(Mn)	D^t_{Mn}
33	Tracer Diffusion coeff(Ni)	D^t_{Ni}
47	Mean Electronegativity of alloy	χ (capital Greek letter 'chi')
48	Chemical diffusion coefficient of Cr in FCC & BCC phase	D^C_{Cr}
49	Cross-diffusion coefficient of Cr vs Fe in FCC & BCC phase	$D^C_{Cr,Fe}$
50	Cross-diffusion coefficient of Cr vs Mn in FCC & BCC phase	$D^C_{Cr,Mn}$
51	Cross-diffusion coefficient of Cr vs Ni in FCC & BCC phase	$D^C_{Cr,Ni}$
52	Chemical diffusion coefficient of Fe in FCC & BCC phase	D^C_{Fe}
53	Cross-diffusion coefficient of Fe vs Cr in FCC & BCC phase	$D^C_{,Fe,Cr}$
54	Cross-diffusion coefficient of Fe vs Mn in FCC & BCC phase	$D^C_{Fe,Mn}$
55	Cross-diffusion coefficient of Fe vs Ni in FCC & BCC phase	$D^C_{Fe,Ni}$

56	Cross-diffusion coefficient of Mn vs Cr in FCC & BCC phase	$D^{C}_{,Mn,Cr}$
57	Cross-diffusion coefficient of Mn vs Fe in FCC & BCC phase	$D^{C}_{Mn,Fe}$
58	Cross-diffusion coefficient of Mn vs Ni in FCC & BCC phase	$D^{C}_{Mn,Ni}$
59	Chemical diffusion coefficient of Ni in FCC & BCC phase	D^{C}_{Ni}
60	Cross-diffusion coefficient of Ni vs Cr in FCC & BCC phase	$D^{C}_{,Ni,Cr}$
61	Cross-diffusion coefficient of Ni vs Fe in FCC & BCC phase	$D^{C}_{Ni,Fe}$
62	Cross-diffusion coefficient of Ni vs Mn in FCC & BCC phase	$D^{C}_{Ni,Mn}$

6.5 Prediction of corrosion performance of CrFeMnNi for FCC+BCC phase field of composition space & Evaluation of model according to current understanding of corrosion phenomena

The RFR model was then used to predict the corrosion performance of ~360 theoretical quaternary compositions within the FCC, BCC, and BCC+FCC, quadrants of the (Cr,Fe,Mn,Ni) composition space (at 500ºC) at a mesh size of 5at%. Isolation Forest confirmed that 95% of these compositions fell within the statistical representation of the trained RFR model. The 360 in-model predictions are shown in the Gibbs tetrahedron in Figure 55a. The projections of the compositions of Hastelloy N (in high-Ni quadrant) and SS316 (in high-Fe quadrant) are provided for reference. The ML model predicts relatively low corrosion rate close to the Ni apex of the quadrant and higher corrosion rate toward Mn apex of the tetrahedron, as expected by their relative thermodynamic favorability of corrosion. However, it is notable that the model predicts high corrosion resistance close to the CrFeNi ternary plane, which is not expected due to the stability of Fe and Cr chlorides. This may suggest corrosion-resistant phenomena that are more complex

such as those observed in low temperature aqueous systems [70], [372], which is of interest for further investigation as detailed later. For alloy design perspective, it is interesting to note that a composition field close to the CrFeNi composition space (Mn not exceeding 10%) is predicted to exceed the corrosion performance of SS316 by a margin of 2 standard deviations (Figure 55b), meaning, as expected, that the model rejects Mn for best corrosion performance. This space is shown as a projection in the FeCrNi ternary diagram in Figure 55c. The space is roughly delimited by a minimum of 25% Ni, and a maximum of 55%Cr and 30% Fe, although the interdependence of the alloying element concentrations is more complex. A marker on Figure 55c indicates the projection of the SS316 composition. The CCA compositions predicted by the RFR to exceed the corrosion resistance of SS316 with 96% confidence are not within proximity to SS316 in composition space. It is important to note here that the redox potential of Cr^{2+}/Cr and Fe^{2+}/Fe are quite close in steels immersed in molten chlorides [180] resulting in a similar thermodynamic driving force for Cr and Fe. Using the ASME Section III Division 5 of the BPVC code qualified SS316H as an industry standard, the RFR model thus demonstrates the ability to predict CCA compositions that exhibit relatively high level of confidence of being worth exploring for molten salt technology industrial applicability and commercial viability. In the next section we describe analyses used to interrogate the model for important features which suggest mechanisms of corrosion-resistant phenomena unique to CCAs.

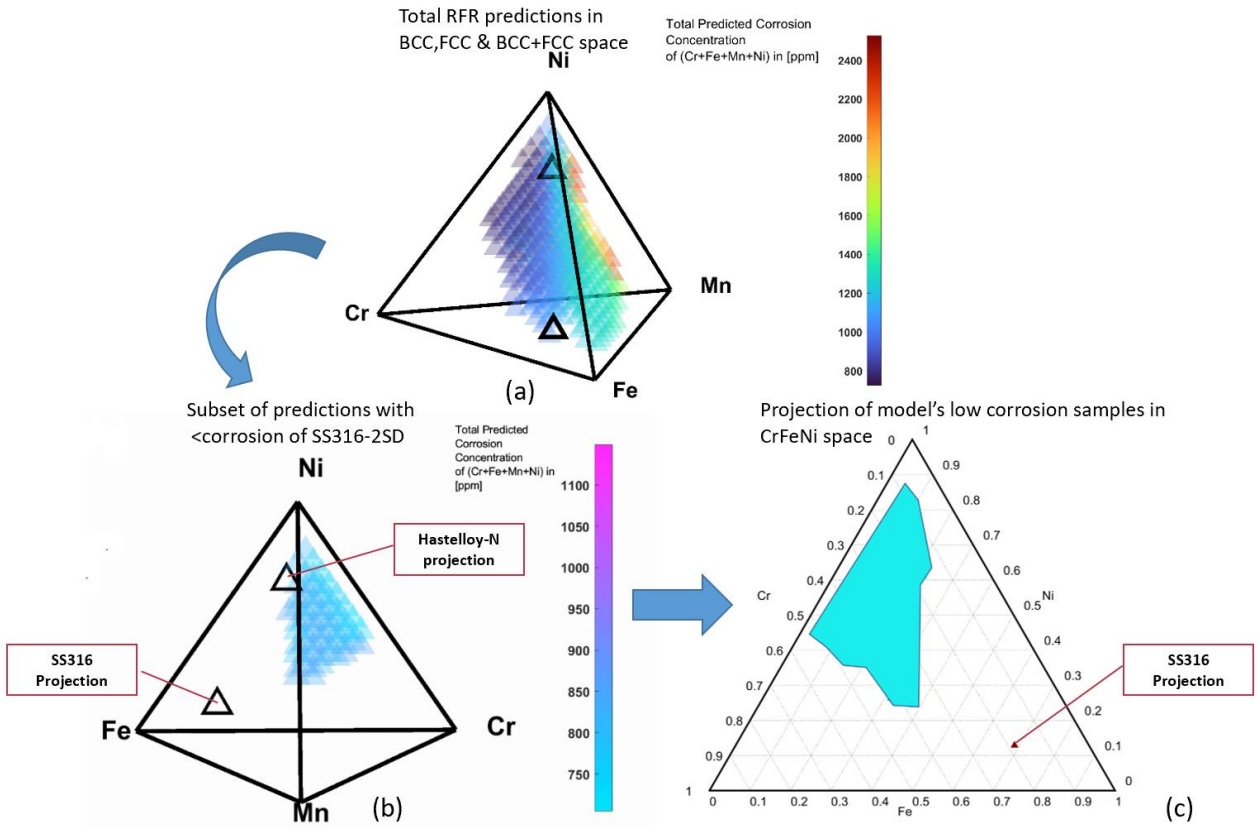

Figure 55(a) RFR prediction for compositions within statistically representative space of 4D CrFeMnNi tetrahedron; (b) RFR prediction for compositions within statistically representative space of 4D CrFeMnNi tetrahedron reflecting corrosion <2sd below that of SS316 with points marking projections of SS316 and Hastelloy-N compositions for reference. These compositions are expected to exceed SS316 performance with 95% confidence interval; (c) Blue patch represents on ternary grid shows compositions predicted by the RFR to have superior corrosion resistance than SS316 by 2 standard deviations. Mn content for all compositions within blue patch does not exceed 10%. The dark point shown at Fe~70% is the projection of the composition of SS316.

6.6 SHAP analysis to glean underpinning patters behind ML predictions

The RFR model was interrogated using Shapley Additive exPlanation (SHAP) analysis python package [373] for interpretability. Figure 56a lists the features in descending order of average SHAP magnitude, with the features or groups with average SHAP magnitudes lower than 10 omitted as least impactful. The magnitude of average SHAP value (Figure 56b in decreasing order of average SHAP magnitude) indicates the impact of a feature on the final prediction value according to the model [246], [304]; the larger the impact of a feature, the larger the magnitude of its SHAP values. From (Figure 56a and Figure 56b, we note that several of the expected features are shown to have a consistent and expected influence on the CCAs' corrosion resistance. For instance, alloys with higher Cr-Mn bond ($P_{bond}(\mathrm{Cr}-\mathrm{Mn})$) probabilities (both of which form the most stable chlorides) exhibit higher corrosion rates. Similarly, alloys with higher (111) surface energy (γ_{111}) also exhibit higher corrosion rates because of their less thermodynamically stable surfaces. Alloys with lower mean electronegativity (χ) have a higher driving force for electron exchange resulting in higher corrosion rates. On the other hand, electron exchange is facilitated on alloys with lower work functions also resulting in higher corrosion rates. These observations are consistent with expectations based on current fundamental understanding of corrosion mechanism in molten salts. The fact that the ML model interprets these features correctly brings confidence in how ML can isolate the effect of Spearman pruned features. What is indeed surprising though is these features are not quite as impactful to corrosion according to the RFR model, as evidenced by their mean |SHAP| magnitudes being ~10 (eg. mean |SHAP| for χ = 12). The sum of mean |SHAP| of those features account for a mere 10% of the impact on corrosion according to the RFR model. Figure 56b shows the spider-beeswarm plot of the top 18 most influential features on the model, and the distribution of the samples' SHAP values. The trends for the top 2 most influential features are consistent and clear: high $D^{\mathrm{t}}_{\mathrm{Ni}}$ and $D^{\mathrm{c}}_{\mathrm{Ni}}$ values (red) strongly correlate with high

SHAP, which means higher corrosion rate predicted by the model.

Figure 56c shows the spider-beeswarm plot of the top 18 most influential features groups on the model, and the samples' distribution in feature group space, with the redness of hue indicating average SHAP magnitude per feature group. We can see that most of the samples are well-distributed in each of the respective feature spaces. This means that their SHAP values obtained are meaningful because they were obtained from a well-distributed sampling of the feature group space. By contrast, the feature groups $D^{\mathrm{c}}_{\mathrm{Fe}}$, $D^{\mathrm{c}}_{\mathrm{Cr}}$, $D^{\mathrm{c}}_{\mathrm{Cr,Fe}}$, $D^{\mathrm{c}}_{\mathrm{Cr,Ni}}$, and Fe:Mn, are not very well distributed throughout the feature space, so one should remain careful in interpreting their SHAP values. With such a large 62-dimensional feature group hyperspace, it is inevitable that some features cannot be well-represented, especially with constraints in confining the study to CrFeMnNi elements and FCC, BCC, and (FCC+BCC) solid phase space.

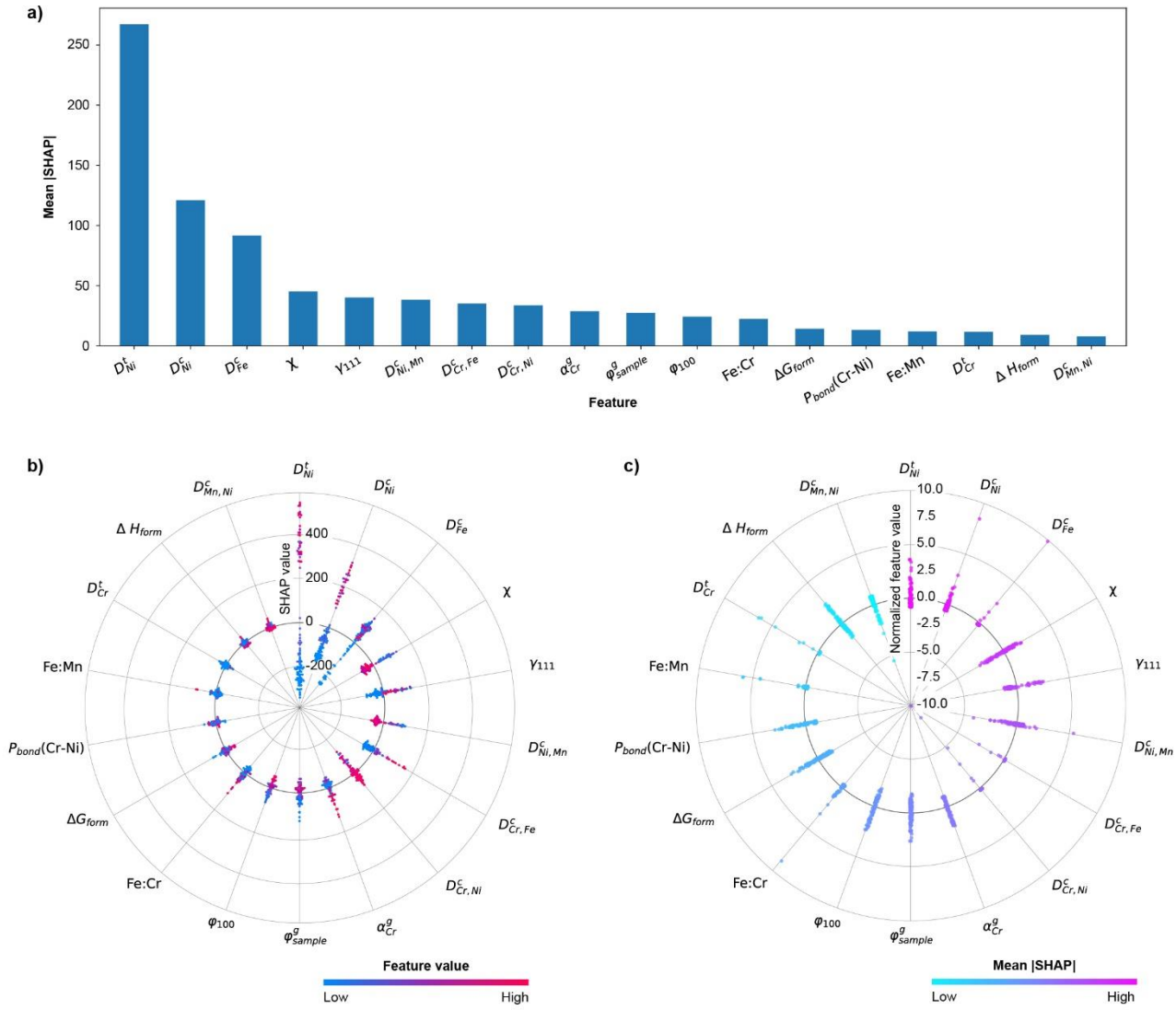

Figure 56(a) Waterfall plot of top 18 features with the average SHAP magnitude across samples. All of these features also exhibit >0.5 in Spearman coefficient between SHAP and feature value. By this quantitative criteria, the impact of these features values on the RFR model are deemed consistent over the feature domain. These 18 features account for 75% of each sample's ML prediction value. (b) Spider-Beeswarm plot to show the distribution of feature values in 18-dimensional feature hyperspace. Color

indicates the magnitude of average SHAP value: features which are more red have higher SHAP value than features that are more blue. Ideally, all features are distributed uniformly throughout the feature space with a high standard deviation for the SHAP value to be meaningful. (c)Spider-Beeswarm plot to show the SHAP values of the samples for each of their 18 most-important values. Color indicates feature values: more red indicates higher feature value and more blue indicates lower feature value.

Bulk diffusion coefficients (both tracer diffusion and chemical diffusion) of the most noble element Ni are not only the most dramatic Figure 56a) but also the most consistent (Figure 56b) predictors of corrosion performance in the FeCrMnNi CCA space explored in this study. By mean |SHAP| magnitude, these two features alone account for 42% of the impact on corrosion according to the RFR model, outstripping the combined impact of the expected features mentioned above by fourfold. As further confirmation of the importance of these top 18 features, the RFR model was retrained with data from all samples featurized by only the top 18 features in Figure 56b, resulting in a 5-fold cross-validation MAPE of 64%, which is only slightly higher than the original MAPE. This implies that the feature space dimensionality can be significantly decreased (in this case from 62 to 18) using SHAP scores without losing in RFR model's prediction accuracy over the 110 samples. A close numerical inspection of the data reflected in Figure 56a reveals that the corrosion performance gradient predicted by the RFR model is guided by the gradient in Ni bulk diffusion.

Since $D_{\mathrm{Ni}}^{\mathrm{t}}$ and $D_{\mathrm{Ni}}^{\mathrm{c}}$ features have such importance in the corrosion model's predictions, it is important to investigate if alloys with feature values at opposite ends of the dimension spectrum exhibit markedly different post-corrosion surface morphologies. The SEM images in Figure 57are shown in descending order of total ion corrosion. Figure 57c and Figure 57d show SEM surface morphology of samples with high D_{Ni}^{t}, and high total corrosion. Surface coarsening morphologies, as evidenced by ligaments that are isotropic in direction, which could either be isotropically contiguous (Figure 57c , total ion corrosion equals to 2300ppm) or unidirectionally contiguous (Figure 57d, total ion corrosion equals to 1400ppm), are clearly

observed. Both these morphologies have recently been associated with surface-diffusion-mediated dealloying in molten salt [100]. These two samples are Ni-rich compositions. Surprisingly, they incurred more quantifiably severe corrosion than the ones shown in Figure 57a (total ion corrosion equals to 762ppm) and Figure 57b (total ion corrosion equals to 620ppm), which were both Fe-rich compositions and have low D^{t}_{Ni}. These two Fe-rich alloys exhibited lower corrosion product formation than SS316 (Figure 27, total ion corrosion equals to 1194 ± 163 ppm) by more than two standard deviations. The surface morphologies in Figure 57a and Figure 57b exhibit a lack of clear ligand formation. Varying degrees of surface and grain faceting which is commonly associated with intergranular attack [96] are observed. Our results suggest that the bulk diffusion coefficients of noble element Ni, in a majority of CCAs, rather than the reactive elements Mn, Cr, and Fe, strongly impact the corrosion rate. The RFR model can therefore be interpreted as implying that the formation of ligament morphology is associated with high Ni bulk diffusion, and that samples with low Ni bulk diffusion exhibit noticeably different faceted surface and grain morphology. Element-wise analysis of corrosion products indicated that dissolved Fe and Mn generally made up more than 98% of the total corrosion of Ni-based compositions in the set. Coupling this to the RFR interpretation, the corrosion mechanism would be driven by the ease with which Ni bulk diffusion facilitates the exposure of Fe and Mn to corrosion attack.

The occurrence of faceting corrosion and dealloying mechanisms are not mutually exclusive. We postulate that faceting corrosion is present from low levels of corrosion attack through high levels, but it is only morphologically apparent at low levels of corrosion attack simply due to the absence of visible dealloying-mediated ligand formation. Conversely for samples with higher levels of corrosion attack, which also happen to be samples with higher Ni bulk diffusion, ligand-bearing morphologies characteristic of the dealloying mechanism predominate over any faceted morphology. This assessment draws a link between the findings of Bawane et al [90] and the findings of Liu et al [99]. In both studies, synchrotron X-ray nanotomography was used to monitor the morphology evolution of Ni-20Cr in binary KCl-$MgCl_2$. In the

former study, the alloy was corroded at 500°C and intergranular corrosion leading to faceted morphology was observed as predominant, and in the latter study the alloy was corroded at 800°C and dealloying leading to ligament morphology was observed as predominant. Increasing temperature increases Ni bulk diffusion which "switches on" the Ni-bulk diffusion-mediated dealloying. However, bulk diffusion of all species is expected to rise with temperature, therefore this simple conclusion is an incomplete description of the mechanism. Our systematic HTE approach indicates that the differential bulk diffusion of Ni compared to other species predicts the corrosion rate, and that whether faceting morphology is observed as opposed to ligament morphology is a matter of corrosion extent rather than a differentiation in corrosion mechanisms. Further supporting this case is the observation that SS316 (Figure 27) corroded under the same conditions exhibits not only total ion corrosion intermediate between Figure 57a and d but the morphology of post corrosion SS316 also appears intermediate between Figure 57a and d: the SS316 shows clear surface faceting akin to that observed in Figure 57a but these facets are much smaller scale than those in Figure 57c, and it also exhibits the beginnings of ligand-like morphology akin to Figure 57d.

A possible explanation for the significant effect of Ni diffusion coefficient on corrosion is that bulk tracer diffusion coefficient is a proxy for surface diffusion coefficient, since they are related by a first-order approximation [374], [375]. Indeed, a high Ni surface diffusion could facilitate exposure of more salt corrodible elements in the atomic layers underneath the surface, such as Fe and Mn. Higher surface diffusivity results in a higher probability for active elements underneath the noble atomic layers to be exposed to, and react with, the electrolyte. Thus, reducing the surface diffusion of noble elements in CCAs is likely a promising path forward to reduce corrosion rates in high-temperature molten salts, a discovery that was facilitated by the utilization of HTE and modeling coupled to ML techniques. Another possible interpretation is that a high D^{t}_{Ni} would result in more Ni-vacancy exchange probability, such that the corrosion induced vacancy flux into the alloy bulk would result in a relatively higher Ni flux toward the alloy surface. This would ultimately lead to a lower corrosion rate as the surface becomes enriched in more

noble elements, but it is unclear how this latter mechanism would lead to the ligament surface morphology. While our approach using HTE coupled to ML highlight the features of importance, physics-based simulations, such as phase-field modeling, are now critically needed to connect these features to surface morphology evolutions [376].

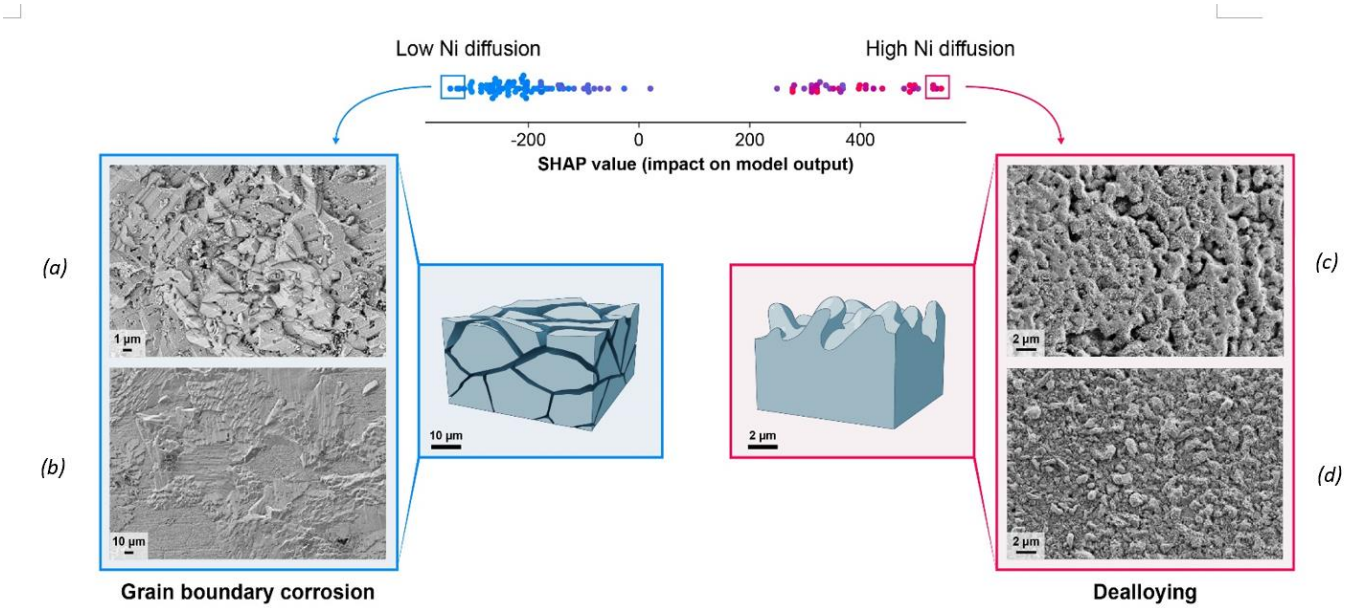

Figure 57(a) Surface SEM of $Cr_{1\mu}Fe_{54}Mn_{28}Ni_6$ corrosion 762ppm (b) Surface SEM of $Cr_{13}Fe_{60}Mn_{17}Ni_{10}$, corrosion 620ppm (c) Surface SEM of $Cr_{0.5}Fe_{27}Mn_{17}Ni_{55}$, corrosion 2300ppm (d) Surface SEM of $Cr_{0.5}Fe_{26}Mn_{15}Ni_{59.5}$, corrosion 1400ppm

Conclusion

We have presented a study in which 110 alloys were processed, corrosion tested and analyzed in a high-throughput standardized platform. To our knowledge it is the largest single body of standardized corrosion data in high-temperature extreme environment presented to date. We tested a field of ML algorithms and found the RFR provides an optimal balance of prediction accuracy and interpretability for our dataset. Anticipating the interpretation of our ML model to yield scientifically meaningful insights, alloys were parametrized such that each feature represented specific mechanisms of interest; care was taken

to decouple the spurious correlations between features so that the features and their represented mechanisms could be compared for their impact on the model without feature endogeneity convoluting the analysis. We have used this standardized body of experimental data to train an RFR model and on the basis of MAPE ~40%, determined that our model is predictive to the current state-of-the-art within the ML for materials science community. In addition, we have presented a case for the community to adopt MAPE as an appropriate single metric for quickly assessing the accuracy of an ML model for materials science applications.

It was demonstrated that our RFR model would approach a MAPE of ~14%, the value on par with the experimental uncertainty of the corrosion testing platform, with a practically finite number of samples added to the training population. Having demonstrated that the model was generalizable and conservative, showing 95% alloy selection accuracy, it was then used to find alloy compositions promising to exceed the corrosion performance of SS316H under the same conditions with 96% confidence. This method of using ML to accelerate the search for materials with desirable properties is widely applicable. SHAP analysis was used to interpret the RFR model and while it showed some expected features on the energetics of the alloy to be impactful in predicting corrosion such as the bond probability of Cr-Mn, the surface energy and work function, it was surprising that the most dramatically impactful features were the kinetics of the noble element, Ni. Prompted by these features highlighted by the RFR, we selectively identified representative samples of interest for SEM and found them to exhibit morphologies consistent with noble-element-diffusion-mediated processes, namely surface diffusion driven dealloying and/or driven vacancy injection. These results are by recent research in the community as primary drivers of corrosion in selected alloys in molten halides. Our investigation has demonstrated that despite the emergence of machine learning, the human intellect is indispensable in scientific inquiry. Nevertheless, the benefits of ML of should not be overlooked. By leveraging the complementary strengths of human intuition and machine speed and accuracy, we have unlocked new insights on the high-temperature corrosion mechanism of

CCAs.

7 Future Push towards HTP Data Acquisition in Corrosion Testing of CCAs in Molten Salts

7.1 In-Situ Electrochemistry

The feasibility of a mini-probe on the molten salt pill corrosion experiments was demonstrated in. The possibility remains for the further miniaturization of the electrochemical-based probe via nanowires. In addition, development of high-temperature in-situ auto-sampling capability for the pill corrosion experiments will enable time-series corrosion data to be acquired in order to study element-resolved interfacial corrosion reaction kinetics.

7.2 In-Situ Sampling for LIBS

In-situ quantification of oxygen in molten halides remains a frontier of molten salt technology research [377]. Even accurate quantification of oxygen in halide salts ex-situ remains relatively inaccessible because the capability is confined to the LECO oxide detector instrument [377]. In this vein, it is desired to develop methods for quantifying oxygen in halides by LIBS.

It was observed during the LIBS method development for this thesis that O experiences spectral interference with Ar in the inert cell environment, but it is expected that calibrating the laser power & delay time settings can overcome this issue. In addition, multi-element (Cr, Fe, Mn, O) calibration matrix in development.

7.3 Further Optimization of the Machine Learning Model

The RFR model in this work predicted corrosion is expected to decrease in the direction of the Cr corner

of the CrFeMnNi compositional domain studied. This prediction runs counter to thermodynamic intuition which suggests that corrosion should decrease and be minimized in the Ni corner of the CrFeMnNi domain because Ni is the most thermodynamically noble element in the space. Inference from SHAP analysis implies that the ML model prioritizes minimizing Ni diffusion as an alloy design parameter for minimizing corrosion in the CrFeMnNi composition space. Further experimental work is needed to verify whether Ni diffusion indeed supersedes Cr corrodibility in predicting total corrodibility of CrFeMnNi alloys.

7.4 Analysis of Ex-Situ Synchrotron XAS data and Method development for In-Situ Synchrotron XAS analysis of an actively corroding alloy sample

Ex-situ synchrotron XAS analysis was performed on Ni-20Cr corrosion in 16 different LiCl-KCl salt compositions varying in KCl=(30,35,40,50)at% and $EuCl_3$= (0,0.6,1.25, 2)wt% for corrosion periods (6,12,48)h.

In-situ synchrotron XAS analysis was performed on Ni-20Cr corrosion in eutectic composition LiCl-KCl salt compositions (LiCl: KCl= 60:40at%) and $EuCl_3$= (0,0.6,1.25, 2)wt% at about 30-min intervals from 0-8h, until a plateau in corrosion products (Ni,Cr) was observed by in-situ XRF.

Corrosion products Cr and Ni are currently being analyzed for oxidation state. Eu spike is currently being analyzed for oxidation state in relation to the role of Eu^{3+} as a corrosion mediator and the extent of its disproportionation in-situ. Comparisons are drawn between oxidation states ex-situ and in-situ.

Future work entails the conclusion of this analysis for timely publication.

8 References

[1] A. Ahlström *et al.*, "The dominant role of semi-arid ecosystems in the trend and variability of the land CO2 sink," *Science (80-.).*, vol. 348, no. 6237, pp. 895–899, May 2015.

[2] R. J. Andres *et al.*, "A synthesis of carbon dioxide emissions from fossil-fuel combustion," *Biogeosciences*, vol. 9, no. 5, pp. 1845–1871, 2012.

[3] P. Friedlingstein *et al.*, "Global Carbon Budget 2022," *Earth Syst. Sci. Data*, vol. 14, no. 11, pp. 4811–4900, Nov. 2022.

[4] Hannah Ritchie, Max Roser, and Pablo Rosado, "Nuclear Energy - Our World in Data," *OurWorldInData.org*, 2020. [Online]. Available: https://ourworldindata.org/nuclear-energy. [Accessed: 19-Jul-2022].

[5] "Nuclear Fuel Cycle -- ANS / About Nuclear / Nuclear Energy." [Online]. Available: https://www.ans.org/nuclear/energy/fuel/. [Accessed: 11-Apr-2023].

[6] A. P. Society, "The Development of the First Chain Reacting Pile Author (s): Enrico Fermi Source : Proceedings of the American Philosophical Society , Vol . 90 , No . 1 , Symposium on Atomic Energy and Its Implications (Jan ., 1946), pp . 20-24 Published by : America," vol. 90, no. 1, pp. 20–24, 2013.

[7] "Nuclear Power Reactors | How does a nuclear reactor work? - World Nuclear Association." [Online]. Available: https://www.world-nuclear.org/information-library/nuclear-fuel-cycle/nuclear-power-reactors/nuclear-power-reactors.aspx. [Accessed: 11-Apr-2023].

[8] N. S. Patel, V. Pavlík, and M. Boča, "High-Temperature Corrosion Behavior of Superalloys in Molten Salts–A Review," *Crit. Rev. Solid State Mater. Sci.*, vol. 42, no. 1, pp. 83–97, 2017.

[9] D. Mohr, L. K. Chang, E. E. Feldman, P. R. Betten, and H. P. Planchon, "Loss-of-primary-flow-without-scram tests: Pretest predictions and preliminary results," *Nucl. Eng. Des.*, vol. 101, no. 1, pp. 45–56, Apr. 1987.

[10] H. P. Mohr, D; Chang, L.K.; Feldman, E.E.; Betten, P.R.; Planchon, "Results, Loss of Primary Flow without Scram Tests: Pretest Predictions and Preliminary," *Nucl. Eng. Des.*, vol. 101, pp. 45–56, 1987.

[11] W. Grimes, "CHEMICAL RESEARCH AND DEVELOPMENT FOR MOLTEN-SALT BREEDER

REACTORS.,” 1967.

[12] “Power Distribution in Conventional Reactors | nuclear-power.net.” [Online]. Available: https://www.nuclear-power.net/nuclear-power/reactor-physics/neutron-diffusion-theory/power-distribution-conventional-reactors/. [Accessed: 24-Jun-2021].

[13] M. Kohler, G. P. Curtis, D. B. Kent, and J. A. Davis, “Experimental Investigation and Modeling of Uranium (VI) Transport under Variable Chemical Conditions,” *Water Resour. Res.*, vol. 32, no. 12, pp. 3539–3551, Dec. 1996.

[14] H. Peng, M. Shen, Y. Zuo, X. Tang, R. Tang, and L. Xie, “Electrochemical technique for detecting the formation of uranium-containing precipitates in molten fluorides,” *Electrochim. Acta*, vol. 222, pp. 1528–1537, 2016.

[15] S. Delpech, “Molten Salts for Nuclear Applications,” in *Molten Salts Chemistry*, Elsevier Inc., 2013, pp. 497–520.

[16] V. Ignatiev and A. Surenkov, “Alloys compatibility in molten salt fluorides: Kurchatov Institute related experience,” *J. Nucl. Mater.*, vol. 441, no. 1–3, pp. 592–603, Oct. 2013.

[17] I. Victor and S. Aleksandr, “Voltammetric measurements on the [U(IV)]/[U(III)] couple and embrittlement of high nickel alloys in fuel LiF-BeF2-UF4 salt with tellurium addition in application to molten salt reactor,” *Corros. Sci.*, vol. 160, p. 108164, Nov. 2019.

[18] D. F. Williams and K. T. Clarno, “Evaluation of salt coolants for reactor applications,” in *Nuclear Technology*, 2008, vol. 163, no. 3, pp. 330–343.

[19] M. S. Sohal, M. A. Ebner, P. Sabharwall, and P. Sharpe, “Engineering Database of Liquid Salt Thermophysical and Thermochemical Properties,” 2010.

[20] A. S. Basin, A. B. Kaplun, A. B. Meshalkin, and N. F. Uvarov, “The LiCl-KCl Binary System PHYSICOCHEMICAL ANALYSIS OF INORGANIC SYSTEMS,” *Russ. J. Inorg. Chem.*, vol. 53, no. 9, pp. 1611–1613, 2008.

[21] W. D. Powers and G. C. Blalock, “ENTHALPY AND HEAT CAPACITY OF LITHIUM CHLORIDE, POTASSIUM CHLORIDE EUTECTIC,” Oak Ridge, TN (United States), Aug. 1953.

[22] D. . Ballard and H. Yakowitz, “Mechanisms Leading to the Failure of Point Pleasant, West Virginia

Bridge," 1969.

[23] C. Parkin *et al.*, "Phase stability, mechanical properties, and ion irradiation effects in face-centered cubic CrFeMnNi compositionally complex solid-solution alloys at high temperatures," *J. Nucl. Mater.*, vol. 565, Jul. 2022.

[24] R. C. Briant, A. J. Miller, and W. B. Cottrell, "Aircraft Nuclear Propulsion Project Quarterly Progress Report," 1953.

[25] A. S. . Khanna, *Introduction to High Temperature Oxidation and Corrosion*. ASM International, 2002.

[26] M. L. Deanhardt and K. H. Stern, "Solubility Products of Metal Oxides in Molten Salts by Coulometric Titration of Oxide Ion Through Zirconia Electrodes," *J. Electrochem. Soc.*, vol. 128, no. 12, p. 2577, Dec. 1981.

[27] R. Grimes, "Molten Salt Reactor Chemistry," *Nucl. Appl.*, no. February, 1970.

[28] K. A. Romberger, J. Braustein, and R. E. Thoma, "New electrochemical measurements of the liquidus in the lithium fluoride-beryllium fluoride system. Congruency of lithium beryllium fluoride (Li2BeF4)," *J. Phys. Chem.*, vol. 76, no. 8, pp. 1154–1159, Apr. 1972.

[29] T. L. . Wright, R.N. ; Sham, "Status of Metallic Structural Materials for Molten Salt Reactors," Argonne, IL, 2018.

[30] J. W. Koger, "ORNL-TM-4188 EFFECT OF FeF 2 ADDITION ON MASS TRANSFER IN A HASTELLOY N-LiF-BeF 2-UF 4 THERMAL CONVECTION LOOP SYSTEM."

[31] K. Sridharan, "Understanding How Materials Corrode in Nuclear Reactors," no. January, 2014.

[32] K. Sridharan and T. R. Allen, "Corrosion in Molten Salts," *Molten Salts Chem.*, pp. 241–267, Jan. 2013.

[33] G. E. Lucas, "The evolution of mechanical property change in irradiated austenitic stainless steels," *J. Nucl. Mater.*, vol. 206, no. 2–3, pp. 287–305, Nov. 1993.

[34] J. R. Keiser, "Status of tellurium--hastelloy N studies in molten fluoride salts," Oct. 1977.

[35] D. B. Miracle and O. N. Senkov, "A critical review of high entropy alloys and related concepts," *Acta Mater.*, vol. 122, pp. 448–511, Jan. 2017.

[36] J. W. Yeh *et al.*, "Nanostructured high-entropy alloys with multiple principal elements: Novel alloy design concepts and outcomes," *Adv. Eng. Mater.*, vol. 6, no. 5, May 2004.

[37] J. W. Yeh *et al.*, “Formation of simple crystal structures in Cu-Co-Ni-Cr-Al-Fe-Ti-V alloys with multiprincipal metallic elements,” *Metall. Mater. Trans. A Phys. Metall. Mater. Sci.*, vol. 35 A, no. 8, pp. 2533–2536, 2004.

[38] B. Cantor, I. T. H. Chang, P. Knight, and A. J. B. Vincent, “Microstructural development in equiatomic multicomponent alloys,” *Mater. Sci. Eng. A*, vol. 375–377, no. 1-2 SPEC. ISS., pp. 213–218, Jul. 2004.

[39] Y. Zhang *et al.*, “Microstructures and properties of high-entropy alloys,” *Prog. Mater. Sci.*, vol. 61, no. September 2013, pp. 1–93, 2014.

[40] J.-W. Yeh, “Physical Metallurgy of High-Entropy Alloys,” *Miner. Met. Mater. Soc.*, vol. 67, no. 10, 2015.

[41] R. C. Reed, T. Tao, and N. Warnken, “Alloys-By-Design: Application to nickel-based single crystal superalloys,” *Acta Mater.*, vol. 57, no. 19, pp. 5898–5913, Nov. 2009.

[42] Y. Lu *et al.*, “A promising new class of high-temperature alloys: Eutectic high-entropy alloys,” *Sci. Rep.*, vol. 4, no. 1, pp. 1–5, Aug. 2014.

[43] B. Chanda and J. Das, “An assessment on the stability of the eutectic phases in high entropy alloys,” *J. Alloys Compd.*, vol. 798, pp. 167–173, Aug. 2019.

[44] H. P. Chou, Y. S. Chang, S. K. Chen, and J. W. Yeh, “Microstructure, thermophysical and electrical properties in AlxCoCrFeNi ($0 \leq x \leq 2$) high-entropy alloys,” *Mater. Sci. Eng. B Solid-State Mater. Adv. Technol.*, vol. 163, no. 3, pp. 184–189, Jul. 2009.

[45] Y. F. Kao, S. K. Chen, T. J. Chen, P. C. Chu, J. W. Yeh, and S. J. Lin, “Electrical, magnetic, and Hall properties of AlxCoCrFeNi high-entropy alloys,” *J. Alloys Compd.*, vol. 509, no. 5, pp. 1607–1614, Feb. 2011.

[46] Y. Zhang *et al.*, “Influence of chemical disorder on energy dissipation and defect evolution in concentrated solid solution alloys,” *Nat. Commun.*, vol. 6, no. 1, pp. 1–9, Oct. 2015.

[47] D. J. Kok, “The Effect of FLiNaK Molten Salt Corrosion on the Hardness of Hastelloy N,” 2019.

[48] S. qin Xia, Z. Wang, T. fei Yang, and Y. Zhang, “Irradiation Behavior in High Entropy Alloys,” *J. Iron Steel Res. Int.*, vol. 22, no. 10, pp. 879–884, 2015.

[49] F. Granberg *et al.*, “Mechanism of Radiation Damage Reduction in Equiatomic Multicomponent Single Phase Alloys The accelerated development of new technologies for efficient energy production demands

new materials that are tolerant to extreme environments and can operate reliably at high temperatures. Operating thermal power plants-whether conventional or nuclear-at higher temperatures," 2016.

[50] K. Jin *et al.*, "Effects of compositional complexity on the ion-irradiation induced swelling and hardening in Ni-containing equiatomic alloys," *Scr. Mater.*, vol. 119, pp. 65–70, 2016.

[51] M. W. Ullah, D. S. Aidhy, Y. Zhang, and W. J. Weber, "Damage accumulation in ion-irradiated Ni-based concentrated solid-solution alloys," *Acta Mater.*, vol. 109, pp. 17–22, 2016.

[52] M. Jin, P. Cao, and M. P. Short, "Predicting the onset of void swelling in irradiated metals with machine learning," *J. Nucl. Mater.*, vol. 523, pp. 189–197, Sep. 2019.

[53] D. Oh, HS; Ma, DC; Leyson, GP; Grabowski, B; Park, ES; Koermann, F; Raabe, "Lattice Distortions in the FeCoNiCrMn HEA studied by Theory and Experiment," *Entropy*, vol. 18, no. 321, 2016.

[54] Z. Wang, Q. Fang, J. Li, B. Liu, and Y. Liu, "Effect of lattice distortion on solid solution strengthening of BCC high-entropy alloys," *J. Mater. Sci. Technol.*, vol. 34, no. 2, pp. 349–354, Feb. 2018.

[55] A. Roy, P. Sreeramagiri, T. Babuska, B. Krick, P. K. Ray, and G. Balasubramanian, "Lattice distortion as an estimator of solid solution strengthening in high-entropy alloys," *Mater. Charact.*, vol. 172, p. 110877, Feb. 2021.

[56] J. Wang, H. Kwon, H. S. Kim, and B. J. Lee, "A neural network model for high entropy alloy design," *npj Comput. Mater.*, vol. 9, no. 1, pp. 1–13, 2023.

[57] W. Y. Ching, S. San, J. Brechtl, R. Sakidja, M. Zhang, and P. K. Liaw, "Fundamental electronic structure and multiatomic bonding in 13 biocompatible high-entropy alloys," *npj Comput. Mater.*, vol. 6, no. 1, pp. 1–10, 2020.

[58] S. Zhao, T. Egami, G. M. Stocks, and Y. Zhang, "Effect of d electrons on defect properties in equiatomic NiCoCr and NiCoFeCr concentrated solid solution alloys," *Phys. Rev. Mater.*, vol. 2, no. 1, p. 013602, Jan. 2018.

[59] S. Mu *et al.*, "Uncovering electron scattering mechanisms in NiFeCoCrMn derived concentrated solid solution and high entropy alloys," *npj Comput. Mater.*, vol. 5, no. 1, pp. 1–8, Dec. 2019.

[60] S. Praveen, B. S. Murty, and R. S. Kottada, "Alloying behavior in multi-component AlCoCrCuFe and NiCoCrCuFe high entropy alloys," *Mater. Sci. Eng. A*, vol. 534, pp. 83–89, Feb. 2012.

[61] S. Guo, Q. Hu, C. Ng, and C. T. Liu, “More than entropy in high-entropy alloys: Forming solid solutions or amorphous phase,” *Intermetallics*, vol. 41, pp. 96–103, 2013.

[62] K. G. Pradeep, N. Wanderka, P. Choi, J. Banhart, B. S. Murty, and D. Raabe, “Atomic-scale compositional characterization of a nanocrystalline AlCrCuFeNiZn high-entropy alloy using atom probe tomography,” *Acta Mater.*, vol. 61, no. 12, pp. 4696–4706, Jul. 2013.

[63] F. Otto, Y. Yang, H. Bei, and E. P. George, “Relative effects of enthalpy and entropy on the phase stability of equiatomic high-entropy alloys,” *Acta Mater.*, vol. 61, no. 7, pp. 2628–2638, Apr. 2013.

[64] E. J. Pickering and N. G. Jones, “High-entropy alloys: a critical assessment of their founding principles and future prospects,” *Int. Mater. Rev.*, vol. 61, no. 3, pp. 183–202, Apr. 2016.

[65] B. Ren, Z. X. Liu, D. M. Li, L. Shi, B. Cai, and M. X. Wang, “Corrosion behavior of CuCrFeNiMn high entropy alloy system in 1 M sulfuric acid solution,” *Mater. Corros.*, vol. 63, no. 9, pp. 828–834, Sep. 2012.

[66] X. W. Qiu, Y. P. Zhang, L. He, and C. G. Liu, “Microstructure and corrosion resistance of AlCrFeCuCo high entropy alloy,” *J. Alloys Compd.*, vol. 549, pp. 195–199, Feb. 2013.

[67] S. P. Wang and J. Xu, “TiZrNbTaMo high-entropy alloy designed for orthopedic implants: As-cast microstructure and mechanical properties,” *Mater. Sci. Eng. C*, vol. 73, pp. 80–89, Apr. 2017.

[68] J. Jayaraj, C. Thinaharan, S. Ningshen, C. Mallika, and U. Kamachi Mudali, “Corrosion behavior and surface film characterization of TaNbHfZrTi high entropy alloy in aggressive nitric acid medium,” *Intermetallics*, vol. 89, pp. 123–132, Oct. 2017.

[69] C. H. Tsau, S. X. Lin, and C. H. Fang, “Microstructures and corrosion behaviors of FeCoNi and CrFeCoNi equimolar alloys,” *Mater. Chem. Phys.*, vol. 186, pp. 534–540, Jan. 2017.

[70] Y. Qiu, S. Thomas, M. A. Gibson, H. L. Fraser, and N. Birbilis, “Corrosion of high entropy alloys,” *npj Mater. Degrad.*, vol. 1, no. 1, pp. 1–17, 2017.

[71] H. Luo, Z. Li, A. M. Mingers, and D. Raabe, “Corrosion behavior of an equiatomic CoCrFeMnNi high-entropy alloy compared with 304 stainless steel in sulfuric acid solution,” *Corros. Sci.*, vol. 134, pp. 131–139, Apr. 2018.

[72] C. C. Yen *et al.*, “Corrosion mechanism of annealed equiatomic AlCoCrFeNi tri-phase high-entropy alloy in 0.5 M H2SO4 aerated aqueous solution,” *Corros. Sci.*, vol. 157, no. March, pp. 462–471, 2019.

[73] S. S. Nene *et al.*, “Corrosion-resistant high entropy alloy with high strength and ductility,” *Scr. Mater.*, vol. 166, pp. 168–172, Jun. 2019.

[74] M. A. Melia *et al.*, “Mechanical and Corrosion Properties of Additively Manufactured CoCrFeMnNi High Entropy Alloy,” *Addit. Manuf.*, vol. 29, p. 100833, Oct. 2019.

[75] V. Hasannaeimi and S. Mukherjee, “Galvanic corrosion in a eutectic high entropy alloy,” *J. Electroanal. Chem.*, vol. 848, p. 113331, 2019.

[76] L. Li *et al.*, “AlxCoCrFeNi high entropy alloys with superior hot corrosion resistance to Na2SO4 + 25% NaCl at 900 °C,” *Corros. Sci.*, vol. 187, no. December 2020, p. 109479, 2021.

[77] J. Apell, R. Wonneberger, M. Seyring, H. Stöcker, M. Rettenmayr, and A. Undisz, “Early oxidation stages of a Co-Cr-Fe-Mn-Ni-Si complex concentrated alloy with Cr, Mn, and Si contents matching those of 316L stainless steel,” *Corros. Sci.*, vol. 190, no. June, 2021.

[78] Y. Garip, “An investigation on the corrosion performance of Fe2CoCrNi0.5 based high entropy alloys,” *Corros. Sci.*, vol. 206, p. 110497, Sep. 2022.

[79] G. Zheng, “Corrosion Behavior of Alloys in Molten Fluoride Salts,” *2015 PhD thesis*, p. 168, 2015.

[80] K. H. Stern, “NRL Memorandum Report 4772: Metal Oxide Solubility and Molten Salt Corrosion,” Washington, DC, 1982.

[81] Z. Tong, W. Wan, W. Zhou, Y. X. Ye, J. Jiao, and X. Ren, “Tensile property and hot corrosion behavior of CrMnFeCoNi high-entropy alloy fabricated via laser melting deposition,” *Intermetallics*, vol. 151, no. April, p. 107710, 2022.

[82] S. Guo, J. Zhang, W. Wu, and W. Zhou, “Corrosion in the molten fluoride and chloride salts and materials development for nuclear applications,” *Prog. Mater. Sci.*, vol. 97, pp. 448–487, Aug. 2018.

[83] M. Elbakhshwan *et al.*, “Corrosion and Thermal Stability of CrMnFeNi High Entropy Alloy in Molten FLiBe Salt,” *Sci. Rep.*, vol. 9, no. 1, pp. 1–10, Dec. 2019.

[84] K. Y. Tsai, M. H. Tsai, and J. W. Yeh, “Sluggish diffusion in Co-Cr-Fe-Mn-Ni high-entropy alloys,” *Acta Mater.*, vol. 61, no. 13, pp. 4887–4897, Aug. 2013.

[85] F. Y. Ouyang, C. H. Chang, and J. J. Kai, “Long-term corrosion behaviors of Hastelloy-N and Hastelloy-B3 in moisture-containing molten FLiNaK salt environments,” *J. Nucl. Mater.*, vol. 446, no. 1–3, pp. 81–89,

Mar. 2014.

[86] X. X. Ye *et al.*, “The high-temperature corrosion of Hastelloy N alloy (UNS N10003) in molten fluoride salts analysed by STXM, XAS, XRD, SEM, EPMA, TEM/EDS,” *Corros. Sci.*, vol. 106, pp. 249–259, May 2016.

[87] K. Michel, “Anodic Dissolution,” in *Corrosion Mechanisms in Theory and Practice*, 2002, pp. 97–169.

[88] L. Cassayre, P. Chamelot, L. Arurault, and P. Taxil, “Anodic dissolution of metals in oxide-free cryolite melts,” *J. Appl. Electrochem.*, vol. 35, no. 10, pp. 999–1004, Oct. 2005.

[89] G. Zheng and K. Sridharan, “Corrosion of Structural Alloys in High-Temperature Molten Fluoride Salts for Applications in Molten Salt Reactors,” *JOM*, vol. 70, no. 8, 2018.

[90] K. Bawane *et al.*, “Visualizing time-dependent microstructural and chemical evolution during molten salt corrosion of Ni-20Cr model alloy using correlative quasi in situ TEM and in situ synchrotron X-ray nano-tomography,” *Corros. Sci.*, vol. 195, Feb. 2022.

[91] L. Jiang *et al.*, “Tellurium segregation-induced intergranular corrosion of GH3535 alloys in molten salt,” *Corros. Sci.*, vol. 194, p. 109944, Jan. 2022.

[92] W. Zhou *et al.*, “Proton irradiation-decelerated intergranular corrosion of Ni-Cr alloys in molten salt,” *Nat. Commun.*, vol. 11, no. 1, pp. 1–7, Jul. 2020.

[93] E. M. Lehockey, A. M. Brennenstuhl, and I. Thompson, “On the relationship between grain boundary connectivity, coincident site lattice boundaries, and intergranular stress corrosion cracking,” *Corros. Sci.*, vol. 46, no. 10, pp. 2383–2404, Oct. 2004.

[94] Y. Pan, B. L. Adams, T. Olson, and N. Panayotou, “Grain-boundary structure effects on intergranular stress corrosion cracking of alloy X-750,” *Acta Mater.*, vol. 44, no. 12, pp. 4685–4695, Dec. 1996.

[95] H. W. Pickering and C. Wagner, “Electrolytic Dissolution of Binary Alloys Containing a Noble Metal,” 1967.

[96] T. Ghaznavi, M. A. Bryk, S. Y. Persaud, and R. C. Newman, “Alloying effects in high temperature molten salt corrosion,” *Corros. Sci.*, vol. 197, Apr. 2022.

[97] J. Erlebacher, M. J. Aziz, A. Karma, and N. Dimitrov, “Evolution of nanoporosity in Dealloying,” *Nature*, vol. 410, no. March, pp. 5–8, 2001.

[98] Q. Chen and K. Sieradzki, “Mechanisms and Morphology Evolution in Dealloying,” *J. Electrochem. Soc.*, vol. 160, no. 6, pp. C226–C231, 2013.

[99] X. Liu *et al.*, “Formation of three-dimensional bicontinuous structures via molten salt dealloying studied in real-time by in situ synchrotron X-ray nano-tomography,” *Nat. Commun.*, vol. 12, no. 1, pp. 1–12, Jun. 2021.

[100] T. Ghaznavi, S. Y. Persaud, and R.C. Newman, “The effect of temperature on dealloying mechanisms in molten salt corrosion,” *J. Electrochem. Soc.*, vol. 169, no. 11, p. Accepted, 2022.

[101] B. C. Kelleher, K. P. Dolan, P. Brooks, M. H. Anderson, and K. Sridharan, “Batch-Scale Hydrofluorination of Li 2 7 BeF 4 to Support Molten Salt Reactor Development,” *J. Nucl. Eng. Radiat. Sci.*, vol. 1, no. 4, p. 041010, Sep. 2015.

[102] S. Bell, T. Steinberg, and G. Will, “Corrosion mechanisms in molten salt thermal energy storage for concentrating solar power,” *Renew. Sustain. Energy Rev.*, vol. 114, no. July, p. 109328, 2019.

[103] A. G. Fernández and L. F. Cabeza, “Corrosion evaluation of eutectic chloride molten salt for new generation of CSP plants. Part 1: Thermal treatment assessment,” *J. Energy Storage*, vol. 27, no. November 2019, p. 101125, 2020.

[104] T. Liu, X. Xu, W. Liu, and X. Zhuang, “Corrosion of alloys in high temperature molten-salt heat transfer fluids with air as the cover gas,” *Sol. Energy*, vol. 191, pp. 435–448, Oct. 2019.

[105] B. Grégoire, C. Oskay, T. M. Meißner, and M. C. Galetz, “Corrosion mechanisms of ferritic-martensitic P91 steel and Inconel 600 nickel-based alloy in molten chlorides. Part II: NaCl-KCl-MgCl2 ternary system,” *Sol. Energy Mater. Sol. Cells*, vol. 216, Oct. 2020.

[106] D. C. Harris, *Quantitative Chemical Analysis*, 8th ed. 2016.

[107] J. Creed, C. Brockhoff, and T. D. Martin, “Method 200.8 Determination of Trace Elements in Waters and Wastes By Inductively Coupled Plasma-Mass Spectrometry,” 1994.

[108] *Agilent 5800 and 5900 ICP-OES User’s Guide*. Agilent Technologies, Inc, 2019.

[109] R. Cornelis and M. Nordberg, “General Chemistry, Sampling, Analytical Methods, and Speciation,” *Handb. Toxicol. Met.*, pp. 11–38, Jan. 2007.

[110] *TX 1000 ANALYZER User Manual*. Iumtek, 2021.

[111] D. A. Cremers and L. J. Radziemski, “Handbook of Laser-Induced Breakdown Spectroscopy: Second Edition,” *Handb. Laser-Induced Break. Spectrosc. Second Ed.*, Mar. 2013.

[112] T. Nelis and R. Payling, “Glow discharge optical emission spectroscopy,” in *RSC Analyticial Spectroscopy Monographs*, 2005, pp. 269–282.

[113] W. Struve, *Fundamentals of Molecular Spectroscopy*, vol. 1, no. 1. 1990.

[114] J.-M. Mermet and E. Poussel, “ICP Emission Spectrometers: 1995 Analytical Figures of Merit,” *Appl. Spectrosc.*, vol. 49, no. 10, pp. 12A-18A, 1995.

[115] H. Ai *et al.*, “On the possibility of severe corrosion of a Ni-W-Cr alloy in fluoride molten salts at high temperature,” *Corros. Sci.*, vol. 149, pp. 218–225, Apr. 2019.

[116] S. Fabre *et al.*, “Use of electrochemical techniques to study the corrosion of metals in model fluoride melts,” *J. Nucl. Mater.*, vol. 441, no. 1–3, pp. 583–591, Oct. 2013.

[117] S. J. Keny *et al.*, “CORROSION ASPECTS OF COMPATIBLE ALLOYS IN MOLTEN SALT (FLINAK) MEDIUM FOR INDIAN MSR PROGRAM IN THE TEMPERATURE RANGE OF 550-750˚C750˚C USING ELECTROCHEMICAL TECHNIQUES,” 2015.

[118] K. Vignarooban, P. Pugazhendhi, C. Tucker, D. Gervasio, and A. M. Kannan, “Corrosion resistance of Hastelloys in molten metal-chloride heat-transfer fluids for concentrating solar power applications,” *Sol. Energy*, vol. 103, pp. 62–69, May 2014.

[119] J. C. Gomez-Vidal and R. Tirawat, “Corrosion of alloys in a chloride molten salt (NaCl-LiCl) for solar thermal technologies,” *Sol. Energy Mater. Sol. Cells*, vol. 157, pp. 234–244, Dec. 2016.

[120] Y. Shi, B. Yang, and P. K. Liaw, “Corrosion-resistant high-entropy alloys: A review,” *Metals (Basel).*, vol. 7, no. 2, pp. 1–18, 2017.

[121] S. Guo, N. Shay, Y. Wang, W. Zhou, and J. Zhang, “Measurement of europium (III)/europium (II) couple in fluoride molten salt for redox control in a molten salt reactor concept,” *J. Nucl. Mater.*, vol. 496, pp. 197–206, Dec. 2017.

[122] T. Berzins and P. Delahay, “Oscillographic Polarographic Waves for the Reversible Deposition of Metals on Solid Electrodes,” *J. Am. Chem. Soc.*, vol. 75, no. 3, pp. 555–559, 1953.

[123] W. H. Doniger and K. Sridharan, “Application of voltammetry for quantitative analysis of chromium in

molten 2LiF-BeF 2 (FLiBe) salt," *J. Electroanal. Chem.*, vol. 838, no. April 2018, pp. 73–81, 2019.

[124] J. Park, S. Choi, S. Sohn, and I. S. Hwang, "Cyclic Voltammetry on Zr, Sn, Fe, Cr and Co in LiCl-KCl Salts at 500°C for Electrorefining of Irradiated Zircaloy-4 Cladding," *J. Electrochem. Soc.*, vol. 164, no. 12, pp. D744–D751, Aug. 2017.

[125] N. W. Shay, "Electrochemical Sensor Development for Fluoride Molten Salt Redox Control." 2017.

[126] M. M. Tylka, J. L. Willit, J. Prakash, and M. A. Williamson, "Method Development for Quantitative Analysis of Actinides in Molten Salts," *J. Electrochem. Soc.*, vol. 162, no. 9, pp. H625–H633, Jun. 2015.

[127] A. Bianconi, "Surface X-ray absorption spectroscopy: Surface EXAFS and surface XANES," *Appl. Surf. Sci.*, vol. 6, no. 3–4, pp. 392–418, Nov. 1980.

[128] J. Yano and V. K. Yachandra, "X-ray absorption spectroscopy," *Photosynth. Res.*, vol. 102, no. 2–3, pp. 241–54, Aug. 2009.

[129] Atenderholt, "Diagram showing which transitions contribute to X-ray absorption edges.," 2009. [Online]. Available: https://en.wikipedia.org/wiki/X-ray_absorption_spectroscopy#/media/File:XASEdges.svg. [Accessed: 09-May-2023].

[130] L. Jiang, X.-X. Ye, D.-J. Wang, and Z.-J. Li, "Synchrotron radiation-based materials characterization techniques shed light on molten salt reactor alloys," *Nucl. Scence Technol.*, vol. 31, no. 6, 2020.

[131] J. Moon *et al.*, "Application of in situ X-ray Absorption Spectroscopy to Study Dilute Chromium Ions in a Molten Chloride Salt," *ChemRxiv. Cambridge Cambridge Open Engag.*, 2019.

[132] S. Fayfar *et al.*, "In-situ analysis of corrosion products in molten salt: concurrent X-ray absorption and electrochemistry reveal both ionic and metallic species," 2022.

[133] N. S. Patel, V. Pavlík, B. Kubíková, M. Nosko, V. Danielik, and M. Boča, "Corrosion behaviour of Ni-based superalloys in molten FLiNaK salts," *Corros. Eng. Sci. Technol.*, vol. 54, no. 1, pp. 46–53, 2019.

[134] F. Y. Ouyang, C. H. Chang, B. C. You, T. K. Yeh, and J. J. Kai, "Effect of moisture on corrosion of Ni-based alloys in molten alkali fluoride FLiNaK salt environments," *J. Nucl. Mater.*, vol. 437, no. 1–3, pp. 201–207, Jun. 2013.

[135] L. C. Olson, J. W. Ambrosek, K. Sridharan, M. H. Anderson, and T. R. Allen, "Materials corrosion in molten LiF-NaF-KF salt," *J. Fluor. Chem.*, vol. 130, no. 1, pp. 67–73, Jan. 2009.

[136] C. C. Company, “HITEC ® Heat Transfer Salt Materials Data Sheet.” Brenntag, Houston, TX, 2009.

[137] J. R. Keiser, J. H. DeVan, and E. J. Lawrence, “Compatibility of molten salts with type 316 stainless steel and lithium,” *J. Nucl. Mater.*, vol. 85–86, no. PART 1, pp. 295–298, Dec. 1979.

[138] D. F. Williams, *Assessment of Candidate Molten Salt Coolants for the NGNP/NHI Heat-Transfer Loop*, no. June. 2006.

[139] J. R. Keiser, “Status of tellurium--hastelloy N studies in molten fluoride salts,” Oak Ridge, TN (United States), Oct. 1977.

[140] K. Sridharan, M. Anderson, T. Allen, and M. Corradini, “Liquid Salts as Media for Process Heat Transfer from VHTR’s: Forced Convective Channel Flow Thermal Hydraulics, Materials, and Coating,” Idaho Falls, ID (United States), Jan. 2012.

[141] M. Anderson, K. Sridhara, T. Allen, and P. Peterson, “Liquid Salt Heat Exchanger Technology for VHTR Based Applications,” Idaho Falls, ID (United States), Oct. 2012.

[142] G. Zheng, B. Kelleher, G. Cao, M. Anderson, T. Allen, and K. Sridharan, “Corrosion of 316 stainless steel in high temperature molten Li2BeF4 (FLiBe) salt,” *J. Nucl. Mater.*, vol. 461, pp. 143–150, Jun. 2015.

[143] I. N. Ozeryanaya, “Corrosion of metals by molten salts in heat-treatment processes,” *Met. Sci. Heat Treat.*, vol. 27, no. 3, pp. 184–188, Mar. 1985.

[144] S. S. Raiman and S. Lee, “Aggregation and data analysis of corrosion studies in molten chloride and fluoride salts,” *Journal of Nuclear Materials*, vol. 511. Elsevier B.V., pp. 523–535, 01-Dec-2018.

[145] A. Jalbuena, J. Logier, J. C. Nava, and V. Ravi, “Corrosion of High Entropy Alloys in Molten Salts,” *NACE Int. Corros. Conf. Expo*, no. 11664, pp. 1–8, 2018.

[146] K. Patel, M. Sadeghilaridjani, M. Pole, and S. Mukherjee, “Hot corrosion behavior of refractory high entropy alloys in molten chloride salt for concentrating solar power systems,” *Sol. Energy Mater. Sol. Cells*, vol. 230, no. June, p. 111222, 2021.

[147] K. Patel, V. Hasannaeimi, M. Sadeghilaridjani, S. Muskeri, C. Mahajan, and S. Mukherjee, “Molten Salt Corrosion Behavior of Dual-Phase High Entropy Alloy for Concentrating Solar Power Systems,” *Entropy*, vol. 25, no. 2, p. 296, Feb. 2023.

[148] K. Patel, C. Mahajan, S. Muskeri, and S. Mukherjee, “Corrosion Behavior of Refractory High-Entropy

Alloys in FLiNaK Molten Salts," *Metals (Basel).*, vol. 13, no. 3, p. 450, Feb. 2023.

[149] Y. Qiu, M. A. Gibson, H. L. Fraser, and N. Birbilis, "Corrosion characteristics of high entropy alloys," *Mater. Sci. Technol. (United Kingdom)*, vol. 31, no. 10, pp. 1235–1243, 2015.

[150] F. Ji, Z. Wang, and L. Wu, "High temperature oxidation and hot corrosion behaviors of Fe65.7Ni11.7Ti1Mo6.6Co15 high entropy alloy," *Mater. Today Commun.*, vol. 32, no. June, p. 104063, 2022.

[151] J. Moon, E. J. Schindelholz, M. A. Melia, A. B. Kustas, and D. Chidambaram, "Corrosion of Additively Manufactured CoCrFeMnNi High Entropy Alloy in Molten NaNO3-KNO3," *J. Electrochem. Soc.*, vol. 167, no. 8, p. 081509, May 2020.

[152] X. L. Li *et al.*, "High-temperature corrosion behavior of Ni-16Mo-7Cr-4Fe superalloy containing yttrium in molten LiF-NaF-KF salt," *J. Nucl. Mater.*, vol. 464, pp. 342–345, May 2015.

[153] Y. L. Wang, Q. Wang, H. J. Liu, and C. L. Zeng, "Effect of grain refinement on the corrosion of Ni-Cr alloys in molten (Li,Na,K)F," *Corros. Sci.*, vol. 109, pp. 43–49, Aug. 2016.

[154] D. B. Miracle, "High entropy alloys as a bold step forward in alloy development," 2019.

[155] D. T. W. Fei, M. C. Gross, J. L. Lofgren, M. Mora-Worms, and A. B. Chen, "Cyclic AMP response to recombinant human relaxin by cultured human endometrial cells—A specific and high throughput in vitro bioassay," *Biochem. Biophys. Res. Commun.*, vol. 170, no. 1, pp. 214–222, 1990.

[156] G. Wu and S. K. Doberstein, "HTS technologies in biopharmaceutical discovery," *Drug Discov. Today*, vol. 11, no. 15, pp. 718–724, 2006.

[157] E. Stach *et al.*, "Autonomous experimentation systems for materials development: A community perspective," *Matter*, vol. 4, no. 9, pp. 2702–2726, 2021.

[158] J. J. de Pablo *et al.*, "New frontiers for the materials genome initiative," *npj Comput. Mater.*, vol. 5, no. 1, pp. 1–23, 2019.

[159] J.-C. Zhao, X. Zheng, and D. G. Cahill, "High-throughput diffusion multiples," *Mater. Today*, vol. 8, no. 10, pp. 28–37, 2005.

[160] P. Wilson, R. Field, and M. Kaufman, "The use of diffusion multiples to examine the compositional dependence of phase stability and hardness of the Co-Cr-Fe-Mn-Ni high entropy alloy system,"

Intermetallics, 2016.

[161] G. C. Carter, “Applications of phase diagrams in metallurgy and ceramics,” United States, 1978.

[162] S. M. Gateman, N. S. Georgescu, M.-K. Kim, I.-H. Jung, and J. Mauzeroll, “Efficient Measurement of the Influence of Chemical Composition on Corrosion: Analysis of an Mg-Al Diffusion Couple Using Scanning Micropipette Contact Method,” *J. Electrochem. Soc.*, vol. 166, no. 16, pp. C624–C630, 2019.

[163] Y. Shi, B. Yang, P. D. Rack, S. Guo, P. K. Liaw, and Y. Zhao, “High-throughput synthesis and corrosion behavior of sputter-deposited nanocrystalline Alx(CoCrFeNi)100-x combinatorial high-entropy alloys,” *Mater. Des.*, vol. 195, p. 109018, 2020.

[164] T. Gebhardt, D. Music, T. Takahashi, and J. Schneider, “Combinatorial thin film materials science: From alloy discovery and optimization to alloy design,” *Thin Solid Films*, vol. 520, no. 17, pp. 5491–5499, 2012.

[165] K. Schlüter, C. Zamponi, A. Piorra, and E. Quandt, “Comparison of the corrosion behaviour of bulk and thin film magnesium alloys,” *Corros. Sci.*, vol. 52, no. 12, pp. 3973–3977, 2010.

[166] P. Tsai and K. M. Flores, “High-throughput discovery and characterization of multicomponent bulk metallic glass alloys,” *Acta Mater.*, vol. 120, pp. 426–434, 2016.

[167] M. Moorehead *et al.*, “High-throughput synthesis of Mo-Nb-Ta-W high-entropy alloys via additive manufacturing,” *Mater. Des.*, vol. 187, p. 108358, Feb. 2020.

[168] M. A. Melia *et al.*, “High-throughput additive manufacturing and characterization of refractory high entropy alloys,” *Appl. Mater. Today*, vol. 19, p. 100560, Jun. 2020.

[169] H. Springer and D. Raabe, “Rapid alloy prototyping: Compositional and thermo-mechanical high throughput bulk combinatorial design of structural materials based on the example of 30Mn-1.2C-xAl triplex steels,” *Acta Mater.*, 2012.

[170] Z. Lai *et al.*, “An Automated Test Platform for High-Throughput Micro-Electrochemical Characterization of Metallic Materials and Its Application on a Fe–Cr–Ni Combinatorial Materials Chip,” *J. Electrochem. Soc.*, vol. 168, no. 9, p. 91501, 2021.

[171] T. H. Muster *et al.*, “A rapid screening multi-electrode method for the evaluation of corrosion inhibitors,” *Electrochim. Acta*, vol. 54, no. 12, pp. 3402–3411, 2009.

[172] P. A. White *et al.*, “A new high-throughput method for corrosion testing,” *Corros. Sci.*, vol. 58, pp. 327–

331, 2012.

[173] B. D. Chambers and S. R. Taylor, “The high throughput assessment of aluminium alloy corrosion using fluorometric methods. Part II – A combinatorial study of corrosion inhibitors and synergistic combinations,” *Corros. Sci.*, vol. 49, no. 3, pp. 1597–1609, 2007.

[174] N. S. Azmat, K. D. Ralston, T. H. Muster, B. C. Muddle, and I. S. Cole, “A High-Throughput Test Methodology for Atmospheric Corrosion Studies,” *Electrochem. Solid-State Lett.*, vol. 14, no. 6, p. C9, 2011.

[175] H. Joress *et al.*, “A High-Throughput Structural and Electrochemical Study of Metallic Glass Formation in Ni–Ti–Al,” *ACS Comb. Sci.*, vol. 22, no. 7, pp. 330–338, Jul. 2020.

[176] S. Munktell, L. Nyholm, and F. Björefors, “Towards high throughput corrosion screening using arrays of bipolar electrodes,” *J. Electroanal. Chem.*, vol. 747, pp. 77–82, 2015.

[177] S. Munktell, M. Tydén, J. Högström, L. Nyholm, and F. Björefors, “Bipolar electrochemistry for high-throughput corrosion screening,” *Electrochem. commun.*, vol. 34, pp. 274–277, 2013.

[178] Y. Wang *et al.*, “Integrated High-Throughput and Machine Learning Methods to Accelerate Discovery of Molten Salt Corrosion-Resistant Alloys,” *Adv. Sci.*, vol. n/a, no. n/a, p. 2200370, May 2022.

[179] J. Guo, N. Hoyt, and M. Williamson, “Multielectrode Array Sensors to Enable Long-Duration Corrosion Monitoring and Control of Concentrating Solar Power Systems,” *J. Electroanal. Chem.*, vol. 884, p. 115064, Feb. 2021.

[180] Y. Wang, B. Goh, K. Sridharan, and A. Couet, “In Situ Corrosion Monitoring of the T91 Alloy in a Molten Chloride Salt Using a Miniaturized Electrochemical Probe for High-Throughput Applications,” *Anal. Chem.*, vol. 94, no. 9, pp. 4012–4020, Mar. 2022.

[181] R. K. Vasudevan *et al.*, “Materials science in the artificial intelligence age: High-throughput library generation, machine learning, and a pathway from correlations to the underpinning physics,” *MRS Communications*, vol. 9, no. 3. Cambridge University Press, pp. 821–838, 01-Sep-2019.

[182] H. S. Stein and J. M. Gregoire, “Progress and prospects for accelerating materials science with automated and autonomous workflows,” *Chem. Sci.*, vol. 10, no. 42, pp. 9640–9649, Oct. 2019.

[183] Y. Liu *et al.*, “High-throughput experiments facilitate materials innovation: A review,” *Sci. China Technol.*

Sci. 2019 624, vol. 62, no. 4, pp. 521–545, Feb. 2019.

[184] J. Chen, A. Balan, P. Masih Das, J. P. Thiruraman, and M. Drndić, "Computer vision AC-STEM automated image analysis for 2D nanopore applications," *Ultramicroscopy*, p. 113249, Mar. 2021.

[185] B. Gawlik, A. R. Barr, A. Mallavarapu, and S. V. Sreenivasan, "Spectral imaging and computer vision for high-Throughput defect detection and root-cause analysis of silicon nanopillar arrays," *J. Micro Nano-Manufacturing*, vol. 9, no. 1, Mar. 2021.

[186] W. Li, K. G. Field, and D. Morgan, "Automated defect analysis in electron microscopic images," *npj Comput. Mater. 2018 41*, vol. 4, no. 1, pp. 1–9, Jul. 2018.

[187] P. M. Maffettone *et al.*, "Crystallography companion agent for high-throughput materials discovery," *Nat. Comput. Sci.*, vol. 1, no. 4, pp. 290–297, 2021.

[188] A. Chakraborty and R. Sharma, "A deep crystal structure identification system for X-ray diffraction patterns," *Vis. Comput.*

[189] K. Vaddi and O. Wodo, "Metric Learning for High-Throughput Combinatorial Data Sets," *ACS Comb. Sci.*, 2019.

[190] J. W. Lee, W. B. Park, J. H. Lee, S. P. Singh, and K. S. Sohn, "A deep-learning technique for phase identification in multiphase inorganic compounds using synthetic XRD powder patterns," *Nat. Commun.*, vol. 11, no. 1, 2020.

[191] D. Jha *et al.*, "Enhancing phase mapping for high-throughput X-ray diffraction experiments using fuzzy clustering," *ICPRAM 2021 - Proc. 10th Int. Conf. Pattern Recognit. Appl. Methods*, pp. 507–514, 2021.

[192] J. W. Lee, W. B. Park, M. Kim, S. Pal Singh, M. Pyo, and K. S. Sohn, "A data-driven XRD analysis protocol for phase identification and phase-fraction prediction of multiphase inorganic compounds," *Inorg. Chem. Front.*, vol. 8, no. 10, pp. 2492–2504, May 2021.

[193] V. Stanev, V. V. Vesselinov, A. G. Kusne, G. Antoszewski, I. Takeuchi, and B. S. Alexandrov, "Unsupervised phase mapping of X-ray diffraction data by nonnegative matrix factorization integrated with custom clustering," *npj Comput. Mater. 2018 41*, vol. 4, no. 1, pp. 1–10, Aug. 2018.

[194] H. Dong *et al.*, "A deep convolutional neural network for real-time full profile analysis of big powder diffraction data," *npj Comput. Mater. 2021 71*, vol. 7, no. 1, pp. 1–9, May 2021.

[195] F. Oviedo *et al.*, “Fast and interpretable classification of small X-ray diffraction datasets using data augmentation and deep neural networks,” *npj Comput. Mater. 2019 51*, vol. 5, no. 1, pp. 1–9, May 2019.

[196] K. Kaufmann *et al.*, “Phase Mapping in EBSD Using Convolutional Neural Networks,” *Microsc. Microanal.*, vol. 26, no. 3, pp. 458–468, Jun. 2020.

[197] K. Kaufmann, C. Zhu, A. S. Rosengarten, K. S. Vecchio, and K. S. Vecchio, “Deep Neural Network Enabled Space Group Identification in EBSD,” *Microsc. Microanal.*, vol. 26, no. 3, pp. 447–457, Jun. 2020.

[198] K. Kaufmann *et al.*, “Crystal symmetry determination in electron diffraction using machine learning,” *Science (80-.).*, vol. 367, no. 6477, pp. 564–568, Jan. 2020.

[199] D. Steinberger, H. Song, and S. Sandfeld, “Machine Learning-Based Classification of Dislocation Microstructures ,” *Frontiers in Materials* , vol. 6. 2019.

[200] A. Dima *et al.*, “Informatics Infrastructure for the Materials Genome Initiative,” vol. 68.

[201] “GitHub - usnistgov/MaterialsResourceRegistry: Materials Resource Registry.” [Online]. Available: https://github.com/usnistgov/MaterialsResourceRegistry. [Accessed: 11-Mar-2022].

[202] “GitHub - usnistgov/MDCS.” [Online]. Available: https://github.com/usnistgov/MDCS. [Accessed: 11-Mar-2022].

[203] M. Autolab, “NOVA User manual,” 2013.

[204] J. L. Vishart, J. Castillo-León, and W. E. Svendsen, “pyEIA: A Python-based framework for data analysis of electrochemical methods for immunoassays,” *SoftwareX*, vol. 15, p. 100720, Jul. 2021.

[205] H. Joress, B. DeCost, N. Hassan, T. M. Braun, J. M. Gorham, and J. Hattrick-Simpers, “Development of an automated millifluidic platform and data-analysis pipeline for rapid electrochemical corrosion measurements: a pH study on Zn-Ni,” *arXiv Prepr. arXiv2204.06094*, 2022.

[206] “tafel-fitter.” .

[207] “No Title.” .

[208] T. Bellezze, G. Giuliani, and G. Roventi, “Study of stainless steels corrosion in a strong acid mixture. Part 1: cyclic potentiodynamic polarization curves examined by means of an analytical method,” *Corros. Sci.*, 2018.

[209] H. Li, Z. Lyu, and M. Han, “Robust and fast estimation of equivalent circuit model from noisy electrochemical impedance spectra,” *Electrochim. Acta*, vol. 422, p. 140474, 2022.

[210] V. Bongiorno, S. Gibbon, E. Michailidou, and M. Curioni, “Exploring the use of machine learning for interpreting electrochemical impedance spectroscopy data: evaluation of the training dataset size,” *Corros. Sci.*, vol. 198, p. 110119, Apr. 2022.

[211] E. IVERS-TIFFÉE and A. WEBER, “Evaluation of electrochemical impedance spectra by the distribution of relaxation times,” *J. Ceram. Soc. Japan*, vol. 125, no. 4, pp. 193–201, Apr. 2017.

[212] B. A. Boukamp and A. Rolle, “Analysis and Application of Distribution of Relaxation Times in Solid State Ionics,” *Solid State Ionics*, vol. 302, pp. 12–18, Apr. 2017.

[213] B. A. Boukamp, “Distribution (function) of relaxation times, successor to complex nonlinear least squares analysis of electrochemical impedance spectroscopy?,” *J. Phys. Energy*, vol. 2, no. 4, p. 042001, Aug. 2020.

[214] E. Quattrocchi, T. H. Wan, A. Curcio, S. Pepe, M. B. Effat, and F. Ciucci, “A general model for the impedance of batteries and supercapacitors: The non-linear distribution of diffusion times,” *Electrochim. Acta*, vol. 324, p. 134853, Nov. 2019.

[215] J. Song and M. Z. Bazant, “Electrochemical Impedance Imaging via the Distribution of Diffusion Times,” *Phys. Rev. Lett.*, vol. 120, no. 11, p. 116001, Mar. 2018.

[216] J. Huang, M. Papac, and R. O’Hayre, “Towards robust autonomous impedance spectroscopy analysis: A calibrated hierarchical Bayesian approach for electrochemical impedance spectroscopy (EIS) inversion,” *Electrochim. Acta*, vol. 367, p. 137493, Jan. 2021.

[217] E. Harefa, N. Li, and W. Zhou, “Application of laser-induced breakdown spectroscopy with a generalized regression neural network and LASSO-type methods for estimation of arsenic and chromium in soil,” *J. Anal. At. Spectrom.*, 2022.

[218] A. Couet, “Integrated high-throughput research in extreme environments targeted toward nuclear structural materials discovery,” *J. Nucl. Mater.*, vol. 559, p. 153425, 2022.

[219] D. Morgan, G. Pilania, A. Couet, B. P. Uberuaga, C. Sun, and J. Li, “Machine learning in nuclear materials research,” *Curr. Opin. Solid State Mater. Sci.*, vol. 26, no. 2, 2022.

[220] A. Dave *et al.*, “Autonomous Discovery of Battery Electrolytes with Robotic Experimentation and Machine Learning,” *Cell Reports Phys. Sci.*, vol. 1, no. 12, p. 100264, 2020.

[221] F. Rahmanian *et al.*, “Enabling Modular Autonomous Feedback-Loops in Materials Science through

Hierarchical Experimental Laboratory Automation and Orchestration," *Adv. Mater. Interfaces*, vol. 9, no. 8, p. 2101987, Mar. 2022.

[222] B. DeCost, H. Joress, S. Sarker, A. Mehta, and J. Hattrick-Simpers, "Towards automated design of corrosion resistant alloy coatings with an autonomous scanning droplet cell," *arXiv Prepr. arXiv2203.17049*, 2022.

[223] J. P. Kollender, A. I. Mardare, and A. W. Hassel, "Photoelectrochemical Scanning Droplet Cell Microscopy (PE-SDCM)," *ChemPhysChem*, vol. 14, no. 3, pp. 560–567, Feb. 2013.

[224] R. Gómez-Bombarelli *et al.*, "Design of efficient molecular organic light-emitting diodes by a high-throughput virtual screening and experimental approach," *Nat. Mater.*, vol. 15, no. 10, pp. 1120–1127, 2016.

[225] J. M. Rickman, G. Balasubramanian, C. J. Marvel, H. M. Chan, and M.-T. Burton, "Machine learning strategies for high-entropy alloys," *J. Appl. Phys.*, vol. 128, no. 22, p. 221101, 2020.

[226] J. Mccarthy, "WHAT IS ARTIFICIAL INTELLIGENCE?," 2007.

[227] C. D. Taylor and B. M. Tossey, "High temperature oxidation of corrosion resistant alloys from machine learning," *npj Mater. Degrad.*, vol. 5, no. 1, pp. 1–10, 2021.

[228] T. Olfatbakhsh and A. S. Milani, "A highly interpretable materials informatics approach for predicting microstructure-property relationship in fabric composites," *Compos. Sci. Technol.*, vol. 217, Jan. 2022.

[229] A. E. Hoerl and R. W. Kennard, "Ridge regression: Biased estimation for nonorthogonal problems," *Technometrics*, vol. 12, no. 1, pp. 55–67, 1970.

[230] "1.1. Linear Models — scikit-learn 1.2.2 documentation." [Online]. Available: https://scikit-learn.org/stable/modules/linear_model.html#ridge-regression-and-classification. [Accessed: 11-May-2023].

[231] S.-J. Kim, K. Koh, M. Lustig, S. Boyd, and D. Gorinevsky, "An Interior-Point Method for Large-ScalèScalè 1-Regularized Least Squares," *IEEE J. Sel. Top. Signal Process.*, vol. 1, no. 4, 2007.

[232] J. H. . Friedman, T. Hastie, and R. Tibshirani, "Regularization Paths for Generalized Linear Models via Coordinate Descent," *J. Stat. Softw.*, vol. 33, no. 1, pp. 1–22, 2010.

[233] B. Efron, T. Hastie, I. Johnstone, and R. Tibshirani, "Least Angle Regression," *Ann. Stat.*, vol. 32, no. 2, pp. 440–444, 2004.

[234] C. M. Bishop, *Pattern Recognition & Machine Learning*. 2006.

[235] sci-kit learn developers, "3.1. Cross-validation: evaluating estimator performance — scikit-learn 1.1.3

documentation.” [Online]. Available: https://scikit-learn.org/stable/modules/cross_validation.html. [Accessed: 18-Nov-2022].

[236] L. B. Coelho, D. Zhang, Y. Van Ingelgem, D. Steckelmacher, A. Nowé, and H. Terryn, “Reviewing machine learning of corrosion prediction in a data-oriented perspective,” *npj Mater. Degrad.*, vol. 6, no. 1, 2022.

[237] L. Breiman, J. H. Friedman, R. A. Olshen, and C. J. Stone, “Classification and regression trees,” *Classif. Regres. Trees*, pp. 1–358, Jan. 2017.

[238] A. Saabas, “Selecting good features – Part III: random forests | Diving into data,” 2014. [Online]. Available: http://blog.datadive.net/selecting-good-features-part-iii-random-forests/. [Accessed: 25-Jun-2021].

[239] L. Breiman, “Random Forests,” *Mach. Learn.*, vol. 45, no. 1, pp. 5–32, 2001.

[240] L. Breiman, “Bagging Predictors,” *Mach. Learn.*, vol. 24, pp. 123–140, 1996.

[241] B. Efron, “Computers and the Theory of Statistics: Thinking the Unthinkable,” *SIAM Rev.*, vol. 21, no. 4, 1979.

[242] L. Breiman, “Bias, variance, and arcing classifier,” 1996.

[243] T. P. Pagano *et al.*, “Bias and unfairness in machine learning models: a systematic literature review,” Feb. 2022.

[244] F. T. Liu, K. M. Ting, and Z.-H. Zhou, “Isolation-based anomaly detection,” *ACM Trans. Knowl. Discov. Data*, vol. 6, no. 3, p. 39, 2012.

[245] C. Strobl, A.-L. Boulesteix, A. Zeileis, and T. Hothorn, “Bias in random forest variable importance measures: Illustrations, sources and a solution,” 2007.

[246] S. M. Lundberg *et al.*, “From local explanations to global understanding with explainable AI for trees,” *Nat. Mach. Intell. 2020 21*, vol. 2, no. 1, pp. 56–67, Jan. 2020.

[247] B. Meredig *et al.*, “Can machine learning identify the next high-temperature superconductor? Examining extrapolation performance for materials discovery,” *Mol. Syst. Des. Eng.*, vol. 3, no. 5, pp. 819–825, Oct. 2018.

[248] L. Ward, S. C. O’Keeffe, J. Stevick, G. R. Jelbert, M. Aykol, and C. Wolverton, “A machine learning approach for engineering bulk metallic glass alloys,” *Acta Mater.*, vol. 159, pp. 102–111, Oct. 2018.

[249] T. M. Cover and P. E. Hart, “Nearest Neighbor Pattern Classification,” *IEEE Trans. Inf. Theory*, vol. 13, no. 1, pp. 21–27, 1967.

[250] C. Ranjan, “Understanding the Kernel Trick with fundamentals,” *Towards Data Science*, 2018. [Online]. Available: https://towardsdatascience.com/truly-understanding-the-kernel-trick-1aeb11560769. [Accessed: 08-May-2023].

[251] R. Gandhi, “Support Vector Machine — Introduction to Machine Learning Algorithms,” *Towards Data Science*, 2018. [Online]. Available: https://towardsdatascience.com/support-vector-machine-introduction-to-machine-learning-algorithms-934a444fca47. [Accessed: 08-May-2023].

[252] “Activation Function Definition | DeepAI.” [Online]. Available: https://deepai.org/machine-learning-glossary-and-terms/activation-function. [Accessed: 08-May-2023].

[253] E. W. Huang, D. Yu, J. W. Yeh, C. Lee, K. An, and S. Y. Tu, “A study of lattice elasticity from low entropy metals to medium and high entropy alloys,” *Scr. Mater.*, vol. 101, pp. 32–35, 2015.

[254] S. Feng, H. Zhou, and H. Dong, “Using deep neural network with small dataset to predict material defects,” *Mater. Des.*, vol. 162, pp. 300–310, Jan. 2019.

[255] M. S. Nitol, D. E. Dickel, and C. D. Barrett, “Machine learning models for predictive materials science from fundamental physics: An application to titanium and zirconium,” *Acta Mater.*, vol. 224, p. 117347, Feb. 2022.

[256] D. Dickel, D. K. Francis, and C. D. Barrett, “Neural network aided development of a semi-empirical interatomic potential for titanium,” *Comput. Mater. Sci.*, vol. 171, p. 109157, Jan. 2020.

[257] G. C. Sosso, V. L. Deringer, S. R. Elliott, and G. Csányi, “Understanding the thermal properties of amorphous solids using machine-learning-based interatomic potentials,” *https://doi.org/10.1080/08927022.2018.1447107*, vol. 44, no. 11, pp. 866–880, Jul. 2018.

[258] J. Wei *et al.*, “Machine learning in materials science,” *InfoMat*, vol. 1, no. 3, pp. 338–358, Sep. 2019.

[259] S. Kumar, T. Daniya, M. Geetha, and K. S. Kumar, “CLASSIFICATION AND REGRESSION TREES WITH GINI INDEX,” *Adv. Math. Sci. J.*, vol. 9, no. 10, pp. 1857–8438, 2020.

[260] J. P. Correa-Baena *et al.*, “Accelerating Materials Development via Automation, Machine Learning, and High-Performance Computing,” *Joule*, vol. 2, no. 8. Cell Press, pp. 1410–1420, 15-Aug-2018.

[261] M. Umehara, H. S. Stein, D. Guevarra, P. F. Newhouse, D. A. Boyd, and J. M. Gregoire, “Analyzing machine learning models to accelerate generation of fundamental materials insights,” *npj Comput. Mater.*, vol. 5, no. 1, Dec. 2019.

[262] D. Ferreño, M. Serrano, M. Kirk, and J. A. Sainz-aja, “Prediction of the Transition-Temperature Shift Using Machine Learning Algorithms and the Plotter Database,” *Metals (Basel).*, vol. 12, no. 2, pp. 1–24, 2022.

[263] K. T. Schütt, H. Glawe, F. Brockherde, A. Sanna, K. R. Müller, and E. K. U. Gross, “How to represent crystal structures for machine learning: Towards fast prediction of electronic properties,” *Phys. Rev. B - Condens. Matter Mater. Phys.*, vol. 89, no. 20, 2014.

[264] I. Takeuchi, “Dynamic Determination of Phase Diagrams by Active Machine Learning,” vol. 24, pp. 544–545, Aug. 2018.

[265] A. G. Kusne, T. Gao, B. Decost, J. Hattrick-Simpers, A. Mehta, and I. Takeuchi, “Autonomous Quantum Materials Research: Phase Mapping,” *APS*, vol. 2019, p. C62.004, 2019.

[266] T. Kostiuchenko, F. Körmann, J. Neugebauer, and A. Shapeev, “Impact of lattice relaxations on phase transitions in a high-entropy alloy studied by machine-learning potentials,” *npj Comput. Mater.*, vol. 5, no. 1, pp. 1–7, 2019.

[267] C. Ly *et al.*, “A new approach for quantifying morphological features of U 3 O 8 for nuclear forensics using a deep learning model,” *J. Nucl. Mater.*, vol. 517, pp. 128–137, Apr. 2019.

[268] H. Zhang *et al.*, “Nano-porosity effects on corrosion rate of Zr alloys using nanoscale microscopy coupled to machine learning,” *Corros. Sci.*, vol. 208, p. 110660, Nov. 2022.

[269] C. Kim, A. Chandrasekaran, T. Doan Huan, D. Das, and R. Ramprasad, “Polymer Genome: A Data-Powered Polymer Informatics Platform for Property Predictions,” *J. Phys. Chem*, vol. 122, pp. 17575–17585, 2018.

[270] A. Mannodi-Kanakkithodi *et al.*, “Scoping the polymer genome: A roadmap for rational polymer dielectrics design and beyond,” *Materials Today*, vol. 21, no. 7. Elsevier B.V., pp. 785–796, 01-Sep-2018.

[271] M. Matsubara, A. Suzumura, N. Ohba, and R. Asahi, “Identifying superionic conductors by materials informatics and high-throughput synthesis,” *Commun. Mater.*, vol. 1, no. 1, pp. 1–6, 2020.

[272] P. Schlexer Lamoureux *et al.*, “Machine Learning for Computational Heterogeneous Catalysis,”

ChemCatChem, vol. 11, no. 16, pp. 3581–3601, Aug. 2019.

[273] W. Xia *et al.*, "Materials informatics-guided superior electrocatalyst: A case of pyrolysis-free single-atom coordinated with N-graphene nanomesh," *Nano Energy*, vol. 94, Apr. 2022.

[274] A. Agrawal, P. D. Deshpande, A. Cecen, G. P. Basavarsu, A. N. Choudhary, and S. R. Kalidindi, "Exploration of data science techniques to predict fatigue strength of steel from composition and processing parameters," *Integr. Mater. Manuf. Innov.*, vol. 3, no. 1, pp. 90–108, Dec. 2014.

[275] B. O. Mukhamedov, K. V. Karavaev, and I. A. Abrikosov, "Machine learning prediction of thermodynamic and mechanical properties of multicomponent Fe-Cr-based alloys," *Phys. Rev. Mater.*, vol. 5, no. 10, pp. 1–9, 2021.

[276] Y.-F. Zhang *et al.*, "Interpretable hardness prediction of high-entropy alloys through ensemble learning," *J. Alloys Compd.*, vol. 945, p. 169329, Jun. 2023.

[277] N. Artrith and A. Urban, "An implementation of artificial neural-network potentials for atomistic materials simulations: Performance for TiO2," *Comput. Mater. Sci.*, vol. 114, pp. 135–150, Mar. 2016.

[278] J. Behler, "First Principles Neural Network Potentials for Reactive Simulations of Large Molecular and Condensed Systems," *Angew. Chemie Int. Ed.*, vol. 56, no. 42, pp. 12828–12840, Oct. 2017.

[279] H. Yan, G. Chen, S. Huang, Y. Dai, and K. Liao, "Simulation research on near-neutral electrochemical corrosion of ferrite-pearlite pipeline steel," *AIP Adv.*, vol. 12, no. 8, 2022.

[280] J. Zhang, C. Cai, G. Kim, Y. Wang, and W. Chen, "Composition design of high-entropy alloys with deep sets learning," *npj Comput. Mater.*, vol. 8, no. 1, pp. 1–11, 2022.

[281] V. L. Deringer, M. A. Caro, and G. Csányi, "Machine Learning Interatomic Potentials as Emerging Tools for Materials Science," *Adv. Mater.*, vol. 31, no. 46, p. 1902765, Nov. 2019.

[282] P. Friederich, F. Häse, J. Proppe, and A. Aspuru-Guzik, "Machine-learned potentials for next-generation matter simulations," *Nat. Mater.*, vol. 20, no. 6, pp. 750–761, 2021.

[283] M.-T. Nguyen, B. A. Helfrecht, R. Rousseau, and V.-A. Glezakou, "Actinides in Complex Reactive Media: A Combined Ab Initio Molecular Dynamics and Machine Learning Analytics Study of Transuranic Ions in Molten Salts," *J. Mol. Liq.*, p. 120115, Aug. 2022.

[284] J. R. Hattrick-Simpers, J. M. Gregoire, and A. G. Kusne, "Perspective: Composition-structure-property

mapping in high-throughput experiments: Turning data into knowledge," *APL Mater.*, vol. 4, no. 5, May 2016.

[285] J. Carrasquilla and R. G. Melko, "Machine learning phases of matter," *Nat. Phys.*, vol. 13, no. 5, pp. 431–434, 2017.

[286] M. Ziatdinov, A. Maksov, and S. V. Kalinin, "Learning surface molecular structures via machine vision," *npj Comput. Mater.*, vol. 3, no. 1, pp. 1–9, 2017.

[287] W. Huang, P. Martin, and H. L. Zhuang, "Machine-learning phase prediction of high-entropy alloys," *Acta Mater.*, vol. 169, pp. 225–236, 2019.

[288] J. Qi, A. M. Cheung, and S. J. Poon, "High Entropy Alloys Mined From Binary Phase Diagrams," *Sci. Rep.*, vol. 9, no. 1, pp. 1–10, 2019.

[289] P. Brown and H. Zhuang, "Quantum machine-learning phase prediction of high-entropy alloys," *Mater. Today*, vol. 63, no. March, pp. 18–31, 2023.

[290] A. Konak, D. W. Coit, and A. E. Smith, "Multi-objective optimization using genetic algorithms: A tutorial," *Reliab. Eng. Syst. Saf.*, vol. 91, no. 9, pp. 992–1007, 2006.

[291] A. Sharma, R. Singh, P. K. Liaw, and G. Balasubramanian, "Cuckoo searching optimal composition of multicomponent alloys by molecular simulations," *Scr. Mater.*, vol. 130, pp. 292–296, 2017.

[292] J. Peng *et al.*, "Data analytics approach to predict high-temperature cyclic oxidation kinetics of NiCr-based Alloys," *Nat. Mater. Degrad.*, vol. 5, no. 41, 2021.

[293] K. T. Butler, D. W. Davies, H. Cartwright, O. Isayev, and A. Walsh, "Machine learning for molecular and materials science," *Nature*, vol. 559, no. 7715, pp. 547–555, 2018.

[294] J. Lever, M. Krzywinski, and N. Altman, "Points of Significance: Principal component analysis," *Nat. Methods*, vol. 14, no. 7, pp. 641–642, Jun. 2017.

[295] I. Toda-Caraballo, E. I. Galindo-Nava, and P. E. J. Rivera-Díaz-Del-Castillo, "Unravelling the materials genome: Symmetry relationships in alloy properties," *J. Alloys Compd.*, vol. 566, pp. 217–228, Jun. 2013.

[296] F. A. Faber *et al.*, "Prediction Errors of Molecular Machine Learning Models Lower than Hybrid DFT Error," *J. Chem. Theory Comput.*, vol. 13, no. 11, pp. 5255–5264, Nov. 2017.

[297] S. A. Giles, D. Sengupta, S. R. Broderick, and K. Rajan, "Machine-Learning-Based Intelligent Framework

for Discovering Refractory High-Entropy Alloys with Improved High-Temperature Yield Strength," *npj Comput. Mater.*, vol. 235, pp. 1–11, 2022.

[298] F. Legrain, J. Carrete, A. Van Roekeghem, S. Curtarolo, and N. Mingo, "How Chemical Composition Alone Can Predict Vibrational Free Energies and Entropies of Solids," *Chem. Mater.*, vol. 29, no. 15, pp. 6220–6227, Aug. 2017.

[299] L. Qiao, R. V. Ramanujan, and J. Zhu, "Machine learning accelerated design of a family of AlxCrFeNi medium entropy alloys with superior high temperature mechanical and oxidation properties," *Corros. Sci.*, p. 110805, Nov. 2022.

[300] A. K. Hoffman *et al.*, "Elucidating Precipitation in FeCrAl Alloys through Explainable AI: A Case Study," 2022.

[301] J. Lee, A. Seko, K. Shitara, K. Nakayama, and I. Tanaka, "Prediction model of band gap for inorganic compounds by combination of density functional theory calculations and machine learning techniques," *Phys. Rev. B*, vol. 93, no. 11, p. 115104, Mar. 2016.

[302] A. Roy, M. F. N. Taufique, H. Khakurel, R. Devanathan, D. D. Johnson, and G. Balasubramanian, "Machine-learning-guided descriptor selection for predicting corrosion resistance in multi-principal element alloys," *npj Mater. Degrad. 2022 61*, vol. 6, no. 1, pp. 1–10, Jan. 2022.

[303] L. Ward *et al.*, "Strategies for accelerating the adoption of materials informatics," *MRS Bull.*, vol. 43, no. 9, pp. 683–689, Sep. 2018.

[304] S. M. Lundberg and S.-I. Lee, "A Unified Approach to Interpreting Model Predictions," *Adv. Neural Inf. Process. Syst.*, vol. 30, 2017.

[305] T.-J. Kim, A. Uehara, T. Nagai, T. Fujii, and H. Yamana, "Quantitative analysis of Eu2+ and Eu3+ in LiCl–KCl eutectic melt by spectrophotometry and electrochemistry," *J. Nucl. Mater.*, vol. 409, no. 3, pp. 188–193, Feb. 2011.

[306] A. Uehara, O. Shirai, T. Nagai, T. Fujii, and H. Yamana, "Spectroelectrochemistry and electrochemistry of europium ions in alkali chloride melts," *Zeitschrift fur Naturforsch. - Sect. A J. Phys. Sci.*, vol. 62, no. 3–4, pp. 191–196, 2007.

[307] J. Zhang *et al.*, "Redox potential control in molten salt systems for corrosion mitigation," *Corros. Sci.*, vol.

144, pp. 44–53, Nov. 2018.

[308] A. van de Walle, R. Sun, Q. J. Hong, and S. Kadkhodaei, “Software tools for high-throughput CALPHAD from first-principles data,” *Calphad Comput. Coupling Phase Diagrams Thermochem.*, vol. 58, pp. 70–81, Sep. 2017.

[309] T. Duong, Y. Wang, X. Yan, A. Couet, and S. Chaudhuri, “A First-Principles-Based Approach to The High-Throughput Screening of Corrosion-Resistant High Entropy Alloys,” 2021.

[310] M. H. Tsai, “Physical properties of high entropy alloys,” *Entropy*, vol. 15, no. 12. MDPI AG, pp. 5338–5345, 2013.

[311] N. Sönnichsen, “Global primary energy consumption 2000-2021,” *Statista*, 2022. [Online]. Available: https://www.statista.com/statistics/265598/consumption-of-primary-energy-worldwide/. [Accessed: 19-Jul-2022].

[312] S. Brinton, “The Advanced Nuclear Industry,” *The Third Way*, 2015.

[313] L. Ma, C. Zhang, Y. Wu, and Y. Lu, “Comparative review of different influence factors on molten salt corrosion characteristics for thermal energy storage,” *Sol. Energy Mater. Sol. Cells*, vol. 235, no. November 2021, p. 111485, Jan. 2022.

[314] Q. Liu, Z. Wang, W. Liu, H. Yin, Z. Tang, and Y. Qian, “Ni-Mo-Cr alloy corrosion in molten NaCl-KCl-MgCl2 salt and vapour,” *Corros. Sci.*, vol. 180, p. 109183, 2021.

[315] Y. Wu *et al.*, “Effect of high temperature molten salt corrosion on the microstructure of a Co-Mo-Cr-Si wear resistant alloy,” *Mater. Charact.*, vol. 179, p. 111377, Sep. 2021.

[316] C. J. Rao, P. Venkatesh, and S. Ningshen, “Corrosion assessment of 9Cr-1Mo steel in molten LiCl-KCl eutectic salt by electrochemical methods,” *J. Nucl. Mater.*, vol. 514, pp. 114–122, Feb. 2019.

[317] N. Birbilis, S. Choudhary, J. R. Scully, and M. L. Taheri, “PERSPECTIVE OPEN A perspective on corrosion of multi-principal element alloys,” *npj Mater. Degrad.*, vol. 14, 2021.

[318] Y. Lu, H. Jiang, S. Guo, T. Wang, Z. Cao, and T. Li, “A new strategy to design eutectic high-entropy alloys using mixing enthalpy,” *Intermetallics*, vol. 91, pp. 124–128, Dec. 2017.

[319] T. C. Ong, M. Sarvghad, K. Lippiatt, S. Bell, G. Will, and T. A. Steinberg, “Investigation of the corrosion of electro-less nickel-plated alloys in molten salt and its effect on phase change properties for energy storage

applications," *Sol. Energy*, vol. 236, pp. 512–521, Apr. 2022.

[320] S. Bell, M. de Bruyn, T. Steinberg, and G. Will, "C-276 nickel alloy corrosion in eutectic Na2CO3/NaCl molten salt under isothermal and thermal cycling conditions," *Sol. Energy Mater. Sol. Cells*, vol. 240, p. 111695, Jun. 2022.

[321] D. Sulejmanovic, J. M. Kurley, K. Robb, and S. Raiman, "Validating modern methods for impurity analysis in fluoride salts," *J. Nucl. Mater.*, vol. 553, p. 152972, Sep. 2021.

[322] A. G. Fernández, F. Pineda, M. Walczak, and L. F. Cabeza, "Corrosion evaluation of alumina-forming alloys in carbonate molten salt for CSP plants," *Renew. Energy*, vol. 140, pp. 227–233, Sep. 2019.

[323] Á. G. Fernández, F. Pineda, E. Fuentealba, D. Jullian, A. Mallco, and M. Walczak, "Compatibility of alumina forming alloys with LiNO3-containing molten salts for solar thermal plants," *J. Energy Storage*, vol. 48, p. 103988, Apr. 2022.

[324] B. A. Pint, C. . Parker, Y. F. Su, D. Sulejmanovic, M. J. Lance, and R. Pillai, "Assessing Stainless Steel Compatibility in Flwing Fluoride Salts," 2022.

[325] B. Pint, D. Suleijmanovic, C. G. Parker, and A. W. Willoughby, "Corrosion of 316H Stainless Steel Specimens in," 2022.

[326] M. Weinstein *et al.*, "Environmental degradation of electroplated nickel and copper coated SS316H in molten FLiNaK salt," *Corros. Sci.*, vol. 191, Oct. 2021.

[327] A. Królikowska, L. Komorowski, and P. L. Bonora, "Pitting Corrosion of Hot-Dip Galvanized Coatings," *Mater. 2020, Vol. 13, Page 2031*, vol. 13, no. 9, p. 2031, Apr. 2020.

[328] U. S. E.P.A., "Method 3050B: Acid Digestion of Sediments, Sludges, and Soils," 1996.

[329] J. Qiu *et al.*, "Effect of SO42− on the corrosion of 316L stainless steel in molten FLiNaK salt," *Corros. Sci.*, Sep. 2018.

[330] H. Xu *et al.*, "Non-uniform corrosion of UNS N10003 alloy induced by trace SO42- in molten FLiNaK salt," *Corros. Sci.*, vol. 192, no. July, p. 109802, 2021.

[331] Y. Zhu *et al.*, "Effects of SO42− ions on the corrosion of GH3535 weld joint in FLiNaK molten salt," *J. Nucl. Mater.*, vol. 492, pp. 122–127, 2017.

[332] L. Bailly-Salins, "Modeling the High-Temperature Corrosion of Zirconium Alloy Fuel Cladding and of

High Manganese Stainless Steel Exhaust Valves using Finite Elements in MOOSE," University of Wisconsin - Madison, 2021.

[333] T. C. Ong *et al.*, "Review of the solubility, monitoring, and purification of impurities in molten salts for energy storage in concentrated solar power plants," *Renew. Sustain. Energy Rev.*, vol. 131, Oct. 2020.

[334] J. Serp, R. J. M. Konings, R. Malmbeck, J. Rebizant, C. Scheppler, and J. P. Glatz, "Electrochemical behaviour of plutonium ion in LiCl - KCl eutectic melts," *J. Electroanal. Chem.*, vol. 561, no. SUPPL. 1, pp. 143–148, Jan. 2004.

[335] M. F. Simpson, "Developments of Spent Nuclear Fuel Pyroprocessing Technology at Idaho National Laboratory," Mar. 2012.

[336] S. Kuravi, J. Trahan, D. Y. Goswami, M. M. Rahman, and E. K. Stefanakos, "Thermal energy storage technologies and systems for concentrating solar power plants," *Prog. Energy Combust. Sci.*, vol. 39, no. 4, pp. 285–319, Aug. 2013.

[337] K. Vignarooban, X. Xu, A. Arvay, K. Hsu, and A. M. Kannan, "Heat transfer fluids for concentrating solar power systems – A review," *Appl. Energy*, vol. 146, pp. 383–396, May 2015.

[338] T. Ouchi, H. Kim, B. L. Spatocco, and D. R. Sadoway, "Calcium-based multi-element chemistry for grid-scale electrochemical energy storage," *Nat. Commun. 2016 71*, vol. 7, no. 1, pp. 1–5, Mar. 2016.

[339] V. Ignatiev and A. Surenkov, *Corrosion phenomena induced by molten salts in Generation IV nuclear reactors*. 2016.

[340] H. G. MacPherson, *Development of Materials and Systems for the Molten Salt Reactor Concept*. University of Tenessee, Knoxville, 1729.

[341] A.E. Danon *et al.*, "Molten salt corrosion (FLiNaK) of a Ni–Mo–Cr alloy and its welds for application in energy-generation and energy-storage systems," *Corros. Sci.*, vol. 164, 2020.

[342] B. D'Souza, A. Leong, Q. Yang, J. Z.-C. Science, and undefined 2021, "Corrosion behavior of boronized nickel-based alloys in the molten chloride Salt," *Elsevier*.

[343] "HSC Chemistry." [Online]. Available: https://hsc-chemistry.com/. [Accessed: 11-May-2023].

[344] S. Guo, W. Zhuo, Y. Wang, and J. Zhang, "Europium induced alloy corrosion and cracking in molten chloride media for nuclear applications," 2019.

[345] Y. Chen, K. Sridharan, and T. Allen, “Corrosion behavior of ferritic–martensitic steel T91 in supercritical water,” *Corros. Sci.*, vol. 48, no. 9, pp. 2843–2854, Sep. 2006.

[346] D. Yoon and S. Phongikaroon, “ Electrochemical Properties and Analyses of CeCl 3 in LiCl-KCl Eutectic Salt ,” *J. Electrochem. Soc.*, vol. 162, no. 10, pp. E237–E243, Jul. 2015.

[347] J. Ge, Q. Yang, Y. Wang, W. Zhuo, M. Du, and J. Zhang, “Selective Electrodeposition of Europium and Samarium in Molten LiCl-KCl with Copper and Aluminum Electrodes,” *J. Electrochem. Soc.*, vol. 167, no. 2, p. 022501, Jan. 2020.

[348] S. K. Min, S. E. Bae, Y. H. Cho, Y. J. Park, and K. Song, “Diffusivity and Absorptivity of EuCl 3 in a LiCl-KCl Molten Salt,” *Trans. Korean Nucl. Soc. Spring Meet. Jeju*, 2009.

[349] A. J. Bard, L. R. Faulkner, N. York, C. @bullet, W. Brisbane, and S. E. Toronto, *ELECTROCHEMICAL METHODS Fundamentals and Applications*. 1944.

[350] S. Yoon and S. Choi, “Spectroelectrochemical Behavior of Cr, Fe, Co, and Ni in LiCl-KCl Molten Salt for Decontaminating Radioactive Metallic Wastes,” *J. Electrochem. Soc.*, vol. 168, no. 1, p. 013504, 2021.

[351] “CompuTherm – Pandat, Calphad, ICME, MGE, Materials Design.” [Online]. Available: https://computherm.com/. [Accessed: 11-May-2023].

[352] Y. Wang, K. Sridharan, and A. Couet, “Method for identification of redox control parameters for corrosion mitigation in molten fluoride salts,” *J. Nucl. Mater.*, vol. 543, p. 152624, Jan. 2021.

[353] D. Inman, J. C. Legey, and R. Spencer, “I. A chronopotentiometric study of iron in LiCl-KCl,” *J. Appl. Electrochem. 1978 83*, vol. 8, no. 3, pp. 269–272, May 1978.

[354] “https://github.com/AtomicBonz/CVAA/.” .

[355] Y. Wang *et al.*, “Accelerated Discovery of Molten Salt Corrosion-resistant Alloy by High-throughput Experimental and Modeling Methods Coupled to Data Analytics,” Apr. 2021.

[356] and Y. W. Wentao Zhou, Jinsuo Zhang, “Review—Modeling Electrochemical Processing for Applications in Pyroprocessing,” *J. Electrochem. Soc.*, vol. 165, no. 13, pp. 712–724, 2018.

[357] Y. Grosu, L. González-Fernández, U. Nithiyanantham, and A. Faik, “Wettability Control for Correct Thermophysical Properties Determination of Molten Salts and Their Nanofluids,” *Energies 2019, Vol. 12, Page 3765*, vol. 12, no. 19, p. 3765, Oct. 2019.

[358] “NIST ASD Output: Lines.” [Online]. Available: https://physics.nist.gov/cgi-bin/ASD/lines1.pl?libs_req=1&spectra=Mn I-III,Cl I-III,Li I-III,K I-III&low_w=200&upp_w=600&unit=1. [Accessed: 11-May-2023].

[359] Q. Zeng *et al.*, “Quantitative analyses of Mn, V, and Si elements in steels using a portable laser-induced breakdown spectroscopy system based on a fiber laser,” *J. Anal. At. Spectrom.*, vol. 31, no. 3, pp. 767–772, Mar. 2016.

[360] Q. Zeng *et al.*, “Laser-induced breakdown spectroscopy using laser pulses delivered by optical fibers for analyzing Mn and Ti elements in pig iron,” *J. Anal. At. Spectrom.*, vol. 30, no. 2, pp. 403–409, Jan. 2015.

[361] M. Yao, L. Huang, J. Zheng, S. Fan, and M. Liu, “Assessment of feasibility in determining of Cr in Gannan Navel Orange treated in controlled conditions by laser induced breakdown spectroscopy,” *Opt. Laser Technol.*, vol. 52, pp. 70–74, 2013.

[362] G. S. Senesi *et al.*, “Heavy metal concentrations in soils as determined by laser-induced breakdown spectroscopy (LIBS), with special emphasis on chromium,” *Environ. Res.*, vol. 109, no. 4, pp. 413–420, 2009.

[363] sci-kit learn developers, “sklearn.cluster.KMeans — scikit-learn 1.1.3 documentation.” [Online]. Available: https://scikit-learn.org/stable/modules/generated/sklearn.cluster.KMeans.html. [Accessed: 18-Nov-2022].

[364] M. O. G. C. Garriga, “Permutation Tests for Studying Classifier Performance Markus Ojala,” *J. Mach. Learn. Res.*, vol. 11, pp. 1833–1863, 2010.

[365] P. Geurts, D. Ernst, and L. Wehenkel, “Extremely randomized trees,” *Mach. Learn.*, vol. 63, no. 1, pp. 3–42, Mar. 2006.

[366] L. Ward, A. Agrawal, A. Choudhary, and C. Wolverton, “A general-purpose machine learning framework for predicting properties of inorganic materials,” *npj Comput. Mater.*, vol. 2, no. 1, p. 16028, Nov. 2016.

[367] M. B. M. P. É. D. Fabian Pedregosa; Gaël Varoquaux; Alexandre Gramfort; Vincent Michel; Bertrand Thirion; Olivier Grisel; Mathieu Blondel; Peter Prettenhofer; Ron Weiss; Vincent Dubourg; Jake Vanderplas; Alexandre Passos; David Cournapeau, “Scikit-learn: Machine Learning in Python,” *J. Mach. Learn. Res.*, vol. 12, no. 85, p. 2825−2830, 2011.

[368] K. Lei, H. Joress, N. Persson, J. R. Hattrick-Simpers, and B. DeCost, “Aggressively optimizing validation

statistics can degrade interpretability of data-driven materials models," *J. Chem. Phys.*, vol. 155, no. 5, p. 054105, Aug. 2021.

[369] F. T. Liu, K. M. Ting, and Z. H. Zhou, "Isolation forest," *Proc. - IEEE Int. Conf. Data Mining, ICDM*, pp. 413–422, 2008.

[370] A. Talapatra, S. Boluki, T. Duong, X. Qian, E. Dougherty, and R. Arróyave, "Autonomous efficient experiment design for materials discovery with Bayesian model averaging," *Phys. Rev. Mater.*, vol. 2, no. 11, Nov. 2018.

[371] R. J. Murdock, S. K. Kauwe, A. Y. T. Wang, and T. D. Sparks, "Is Domain Knowledge Necessary for Machine Learning Materials Properties?," *Integr. Mater. Manuf. Innov.*, vol. 9, no. 3, pp. 221–227, 2020.

[372] Y. Y. Chen, T. Duval, U. D. Hung, J. W. Yeh, and H. C. Shih, "Microstructure and electrochemical properties of high entropy alloys-a comparison with type-304 stainless steel," *Corros. Sci.*, vol. 47, no. 9, pp. 2257–2279, Sep. 2005.

[373] Scott Lundberg, "SHapley Additive exPlanations," *Scott Lundberg*. 2018.

[374] C. Yao and T. Chen, "A new simplified method for estimating film mass transfer and surface diffusion coefficients from batch adsorption kinetic data," *Chem. Eng. J.*, vol. 265, pp. 93–99, Apr. 2015.

[375] R. L. Tseng, P. H. Wu, F. C. Wu, and R. S. Juang, "A convenient method to determine kinetic parameters of adsorption processes by nonlinear regression of pseudo-nth-order equation," *Chem. Eng. J.*, vol. 237, pp. 153–161, Feb. 2014.

[376] N. Bieberdorf, M. D. Asta, and L. Capolungo, "Grain Boundary Effects in Dealloying Metals: A Multi-Phase Field Study," Jun. 2022.

[377] B. Goh, F. Carotti, and R. O. Scarlat, "A Review of Electrochemical and Non-Electrochemical Approaches to Determining Oxide Concentration in Molten Fluoride Salts," *ECS Trans.*, vol. 85, no. 13, pp. 1459–1471, Jun. 2018.

9 Supplemental Material A: Summary of the Three Mile Island Nuclear Accident, 1979

The order of events in the Tree Mile Island Accident of 1979 were are summarized below, as reported by Collier and Davies.

Prior to the accident-initiating turbine trip, the reactor was operating under automatic control at 97% of rated output of 2772 MWt. There was an existing leakage from either the PROV or the ASME code safety valve on the pressurizer. Attempts to transfer clogged resins from an isolated condensate water system to a regeneration tank caused water to get into the service air system. Some water from the service air line entered the instrument air line, causing the condensate polishing isolation valves to shut and the condensate booster pump to trip because of the loss of suction pressure. The main feedwater pumps in the secondary circuit tripped, resulting in an instantaneous trip of the main turbine.

The turbine trip was the initiating event to the accident, which caused an interruption in the flow of feedwater to the steam generators and this led to a reduction in the heat removal from the primary system. The RCS pressure reached the PORV set point to 15.5 MPa and the valve opened to relieve the pressure but this was insufficient to reduce the pressure immediately and the RCS pressure continued to rise. Such undesirable operating conditions initiated a scram, after which residual heat needed to be removed. The reducing RCS pressure reached the point which called for automatic PROV closure but that failed. This failure of the PORV to close (ie. It was stuck open) was the crux of the course of events in the TMI accident, because it caused a loss of coolant accident.

RCS water was being lost through the open PORV. All the auxiliary feedwater pumps were running but the water level in the steam generators was continuing to fall and they were drying out. No water was being injected into the steam generators because of the closed valved between the pumps and the steam generators. The valves had been closed sometime before the incident for routine testing and had been inadvertently left in that position. This is the first of human errors that exacerbated accident conditions, additionally to that, status tags on other valves obscured some of the status lights.
During the first crucial period, the reactor coolant circuit was deprived of effective means of heat removal and could dispose of the energy only by blowing off water and steam. The temperature gradient between hot and cold legs was approaching zero with the steam generators drying out. RCS pressure was falling and the liquid level in the pressurizer rose rapidly.

The coolant loop continued to depressurize. In response to the observed conditions, the RC pumps in loops B and A were tripped to prevent damage to the pipes and pipework. However this caused steam and water phases in the circuit to separate in loop B, blocking the circulation in the loop. The core began a heat-up transient and eventually leading to core damage.

The events during the heat-up transient 2-6h after initiating events further exacerbated the severity of the accident. During this time, the PROV blocking valve was closed by operators but the indications as to its position were ambiguous to the operators. The high temperature in the pipework downstream of the valve was mistaken as being caused by the preexisting leak though the PORV or another code valve. Had the repressurization of the RCS using the HPIS been implemented at this point, the accident conditions could probably have been terminated. Closure of the PORV was achieved and RCS pressure rose, however at this point a significant fraction of the reactor core was uncovered and had sustained high temperatures, which could lead to fuel damage, release of volatile fission products into the

RCS and generation of hydrogen from a zirconium-steam reaction. (Incidentally this condition was the same condition faced with Fukushima Daiichi when the diesel-powered cooling pumps lost power and could not remove residual heat from the reactor after scram. Indeed the zirconium-steam reaction in the clad released large amounts of hydrogen which caused the secondary containment to explode. Because of this there was fear that volatile fission products would be released into the surrounding environment.)

Attempts were made to restart the RC pumps. One pump tripped again due to vapor binding and vibration alarms. Radiation monitor readings were rising throughout the reactor, auxiliary and fuel handling buildings.

Operators attempted to activate the core flooding system and establish heat removal through the low pressure heat removal system. The PORV blocking valve was opened and the RCS reached pressure level that was nominal in the core flood tank systems. The core flooding system was activated but only a small amount of water was injected into the reactor pressure vessel. Ultimately depressurization was unsuccessful, as all attempts to do so failed so the decay heat removal system could not be brought into operation. The PORV block valve was closed again.

After the accident the removal of hydrogen bubble and ultimate establishment of stable cooling mode were achieved. The void in the pressure vessel was due mainly to incondensible hydrogen and this was decreased by degassing with the PORV and the letdown system and operating recombiners. At this point, the decay heat was far below 1 MWt.

10 Supplemental Material B: Summary of Root Cause Analysis for the Nuclear Reactor Accident at Fukushima, 2011

Here follows a summary of the events leading to the accident at TEPCO's Fukushima Nuclear Power Stations (NPS), according to the Japanese Government's Nuclear Emergency Response Headquarters

With the arrival of the tsunami >10m (exceeding 10m seawall) a total of 561 km sq of land was inundated. There was infrastructure damage: gas supply shortages, electricity and telecommunications cutoff across the island, and damage to seawalls and harbor installations was sustained.

The ground around the bases of tidal embankments and seawalls were scoured by runups and rundowns and many of the bases were observed to have suffered collapses, lining of embankments and seawalls (concrete portions that cover rocks and ground inside embankments) suffered boring from the lower edge of bases and failed to play a role of lining. Given the situation, it was possible that the sand embankments would collapse through by scouring due to runups and rundowns and breakwater walls would be scoured or collapse if tsunamis breach the sand embankments when these are used as coastal defenses.

As evidenced by the above description, there great destructive force in the natural disaster of the earthquake and tsunami that hit Fukushima. Seizmic groundmotion: maximum horizontal motion was 550 Gal and vertical motion was 302 Gal at Unit 2 (1 Gal is equal to 0.01 m/s^2) causes automatic shutdown of all 3 reactors in operation (scram).

The design basis of the precautionary/protective infrastructure for pre-empted for tsunami water level of 3.1m. The highest water level of each Unit was set at 5.4-5.7m, suggesting that this qualifies as Beyond Design Basis Accident.

Earthquake caused damage to the breakers of the switchyards of Units 1 and 2. Cables were damaged too by undetermined causes.

The seismic intensity of the main shock caused disruption of power transmission from the 2 lines of 275kV systems and one line of the 66 kV system. Of the equipment receiving power on the MPS site, a startup transformer of Unit 1 failed. The power was switched to the external regular supply (275 kV) and the normal power supply system was returned. The result of all this power being knocked out and the fuel for the diesel generators being washed away is that the emergency pumps and cooling systems could not work to remove residual heat after scram from the reactor.

The water rose in the seawater pump room due to the tsunami and the water level in the underground intake pit also rose, caused by siphon phenomenon. This resulted in seawater overflowing through the opening of the tide gauge into the seawater pump room. Then the seawater flowed from the pump room, via the trench into the basement floors of the reactor buildings, causing the heat exchanger room of the CCWS in the second basement to be submerged. Additionally, the CCW pump of Unit 2 was submerged. Cooling function of the emergency diesel generators was lost, with 2/3 units stopped.